# Interaction and Control of Multiple Vortices over Double Delta Wings

Zhang, Jason

*Award date:*
2017

*Awarding institution:*
University of Bath

# INTERACTION AND CONTROL OF MULTIPLE VORTICES OVER DOUBLE DELTA WINGS

**Xizhe Zhang**

A thesis submitted for the degree of Doctor of Philosophy

Department of Mechanical Engineering

University of Bath

November 2017

# ABSTRACT

Double delta wing configurations are widely employed for jet fighters, supersonic aircraft and Unmanned Air Vehicles (UAVs) due to its superior aerodynamic performance at high angles of attack. The main feature of the flow is the presence of both strake and wing vortices. At low angles of attack the vortices remain separate, whereas for flows at higher angles of attack the two vortices interact, coil-up, merge, and vortex breakdown develops. Therefore, this study was carried out investigating vortex interactions over a 70˚/50˚ double delta wing (with kink at 50% chord location), and ultimately investigating active and passive flow control methods for their impact on double delta wing aerodynamics.

During the first phase of the study, interactions between strake vortex and wing vortex over a 70˚/50˚ double delta wing (with kink at 50% chord location) were investigated experimentally in a wind tunnel at Re = 2.34 x $10^5$ using particle image velocimetry (PIV) measurements for angles of attack from 4˚ to 32˚. When angle of attack increased, both strake and wing vortices gained strength and size, and moved further away from the wing surface; however, vortex breakdown also occurred earlier as a result. The time-averaged vorticity fields exhibited a very distinctive 'dual-vortex' pattern in the crossflow plane at *x/c* = 50% across all the angles of attack range, its relative spatial position moved in the clockwise direction as the wing incidence was increased. The same dual-vortex structure was not found on the simple delta wing with the same sweep angle, which suggested that the wing vortex may have upstream effect on the formation of the strake vortex. Meandering of the vortices was investigated from the instantaneous flow fields and characterised. Meandering probability plots showed that as angle of attack gradually increased to an optimum value, the meandering area decreased and peak probability increased; after passing the optimum angle of attack the meandering area expanded and the peak probability decreased. The normalised vortex meandering amplitude results also confirmed the findings from the probability plots. Coefficient of correlation showed generally low correlation between the displacements of the strake and wing vortices in both vertical and horizontal directions. The proper orthogonal decomposition (POD) displayed counter rotating

vortex pairs for the strake and wing vortices for the first few most dominant modes, which also contribute to most of the total energy. However, the POD analysis suggested that many modes are needed to describe the unsteady flow at this Reynolds number.

Second and third phase of this study was carried out in water tunnel at Re = 2.80 x $10^4$ over the same 70˚/50˚ double delta wing configuration investigating the effect of jet blowing and passive bleed. Comparisons between the water tunnel and the wind tunnel baseline cases were also made. It was found that the wing vortex broke down first in the water tunnel results tested at Re = 2.80 x $10^4$, whereas strake vortex broke down first in the wind tunnel results at Re = 2.34 x $10^5$. Higher Reynolds number also resulted in higher peak standard deviation and higher vortex meandering amplitude.

For the active blowing, depending on the jet location and yaw angle, the strake vortex and the wing vortex could be separated further away from each other thus resulting in weak interactions or the interactions between the strake and wing vortices could be intensified thus leading to an earlier merge. Ingestion of jet turbulence into the vortices appeared to promote merging. It was found that jet blowing could substantially modify the global vortex centroid over the double delta wing up to $\alpha$ = 24˚, which suggested that significant changes in forces/moments could be produced. However, as angle of attack increased the effect of jet blowing decreased. Passive bleed with estimated momentum coefficients of the order of 0.1% can also promote vortex merging. The secondary vortex can be strengthened and alter the vortical flow structure over the delta wing. It was found that bleed is more effective at lower wing incidences.

# ACKNOWLEDGEMENTS

This PhD research study was a self-funded project, I would like to express my gratefulness for the support and encouragement received over the years from my parents Leyan and Yan, without them I would not have the means to pursue this study. I would also like to thank my supervisors Dr. Zhijin Wang and Prof. Ismet Gursul for their invaluable advices and support through my study, they provided me with the best theoretical and experimental advices. Thanks is also expressed to Neys Schreiner, Joshua Horwood and Liam Wood for their effort proof-reading my thesis. Appreciation is given to the department technician team, especially Ian Trussler, Steve Thomas, Steve Coombes, Colin Brain and Vijay Rajput, they helped me building the experimental rigs and maintaining the testing facility.

I would also like to thank the friends and colleagues in the Aerodynamics research group: Nader Al-Battal, Chen Chen, Daniel Heathcote, Dinitha Bulathsinghala, Richard Jackson and Robin Jones and the rest of the people. I had great office memory working with them, and sharing support.

# CONTENTS

# LIST OF FIGURES

# NOMENCLATURE

$A_j$ = Cross-sectional area of the jet blowing hole

$a_M$ = Vortex meandering amplitude

b = Span

c = Wing root-chord length

$C_p$ = Pressure coefficient, $(p - p_\infty)/\frac{1}{2}\rho U_\infty^2$

$C_\mu$ = Jet blowing momentum coefficient, $\rho V_j^2 A_j/\frac{1}{2}\rho U_\infty^2 S_w$

Cr = Chordwise distance in relation to the tip of the wing section

P = Pressure

Re = Reynolds number, $\rho U_\infty c/\mu$

t = Wing thickness

$U_B$ = Bleed velocity

$U_{std}$ = Standard deviation of velocity fluctuations

$U_\infty$ = Freestream velocity

s = Local semi-span

$S_w$ = Wing surface area

$V_j$ = Jet blowing velocity

x = Chordwise distance

y = Spanwise distance

$y_i$ = The coordinate of instantaneous vortex location in the spanwise direction

$\bar{y}$ = The coordinate of time averaged vortex location in the spanwise direction

$y_b$ = Spanwise distance from the bleed hole centre the wing centreline

z = Distance from wing surface in the normal direction in the measurement plane

$z_i$ = The coordinate of instantaneous vortex location in the normal direction

$\bar{z}$ = The coordinate of time averaged vortex location in the normal direction

$\alpha$ = Angle of attack

$\beta$ = Jet blowing yaw angle

$\mu$ = Dynamic viscosity

$\nu$ = Kinematic viscosity

$\rho$ = Density

$\omega$ = Vorticity

$\Phi$ = Roll angle

dA = Grid area of PIV measurements

$\Gamma$ = Circulation

$\Lambda$ = Sweep angle

$\Lambda_1$ = Strake sweep angle

$\Lambda 2$ = Wing sweep angle

M = Mach number

N = Number of snapshots

r = Distance to the wing centerline

PIV = Particle image velocimetry

POD = Proper orthogonal decomposition

UAV = Unmanned air vehicle

# CHAPTER 1.

# INTRODUCTION

Double delta wings are commonly adopted in the aviation industry due to their superior aerodynamic performance at high angles of attack, and are utilised by military fighter jets, supersonic aircrafts and Unmanned Air Vehicles (UAVs) in particular [1, 2]. A double delta wing configuration contains two different sections, which are termed strake section (the front part) and wing section (the rear part). The flow pattern over a double delta wing is dominated by two counter rotating strake vortices and two counter rotating wing vortices that are formed by the roll-up of vortex sheets shedding from the leading-edges, as shown in Figure 1 [3]. The axial velocity of the strake vortices can reach much higher values than the freestream velocity and it is jet-like at low and moderate angles of attack, which creates low pressure regions on the wing upper surface. The low pressure regions enable additional suction and lift force to be generated, which is known as vortex lift; moreover, the strong strake vortex strengthens and stabilises the main wing vortex [4].

Despite the benefits of the double delta wing geometries, the interaction of the strake and wing vortices over a double delta wing could result in very complicated and unpredictable flow patterns when the angle of attack and/or sideslip angle exceeds certain limits, this will increase the difficulty in terms of flight control and aircraft stability [5-7]. Although several experimental and computational studies have been carried out previously, the governing mechanism behind the interactions, meandering, breakdown and merging of the vortices over double delta wing is still not well understood [8, 9], and there is less emphasis on the unsteady aspects of the vortical flow over double delta wing. The unsteady aspects of the vortical flow will impact aircraft stability, flight control system and cause wing/fin buffeting. For instance, vortex breakdown can introduce undesired structural vibrations and severe damage of the fins. The dynamic response of leading-edge vortices and breakdown is important for the flight of modern fighter aircraft, hence it is important to understand the unsteady vortical flow for successful, high performance aircrafts [10]. Furthermore,

with the proper use of flow control methods (active blowing, passive bleed.,etc.) over double delta wing, the interactions of multiple vortices can potentially be manipulated to maximise their benefits.

Therefore, the objective of this thesis is to understand the effects of angle of attack on double delta wing aerodynamics, and also the effectiveness of active and passive flow control methods. The geometric definitions used in this study can be found on Figure 2. This study will be divided into three stages: 1) Stage one will investigate the flow pattern over a 70˚/50˚ double delta wing in a closed-loop wind tunnel at Re = $2.34 \times 10^5$ for various angles of attack ranging from 4˚ to 32˚. For comparison purposes, additional test results carried out on a simple delta wing with $\Lambda = 70^\circ$ at the same experimental conditions will also be presented. 2) Stage two will examine the effect of active jet blowing on the same double delta wing configuration in a closed-loop water tunnel at Re = $2.8 \times 10^4$ and various angles of attack ranging from 8˚ to 28˚. In particular, effect of blowing hole location, effect of blowing jet yaw angle and effect of blowing momentum coefficient will be illustrated. In addition, comparison of the double delta wing vortical flow between Re = $2.8 \times 10^4$ and $2.34 \times 10^5$ will be presented. 3) Stage three will illustrate the effect of passive bleed for angle of attack ranging from 8˚ to 28˚ for the same double delta wing configuration in a closed-loop water tunnel at Re = $2.8 \times 10^4$. Bleed will be introduced from bleed holes and slots at different spanwise locations and x/c = 37.5%.

In this thesis, an overall review of the current literatures will be presented in the next chapter which covers different flow properties over slender delta wings, non-slender delta wings and double delta wings; various flow control methods will be also compared. The third chapter will introduce the experimental methods and the uncertainty analysis. The results chapters (chapter 4-6) will focus on the vortical flow over double delta wings on both high and low Reynold numbers, and the effects of active blowing and passive bleed on the interactions of multiple vortices. Future work and conclusion will be presented in chapter 7.

## 1.1 Figures

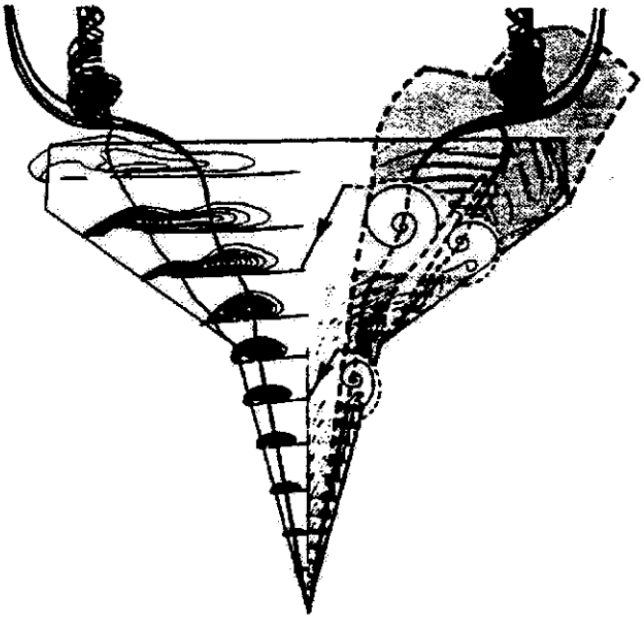

Figure 1. Solution for the flow over double delta wing by Ekaterinaris, et al [2] at M = 0.22, $\alpha = 19^{\circ}$ and Re = 4 x $10^6$

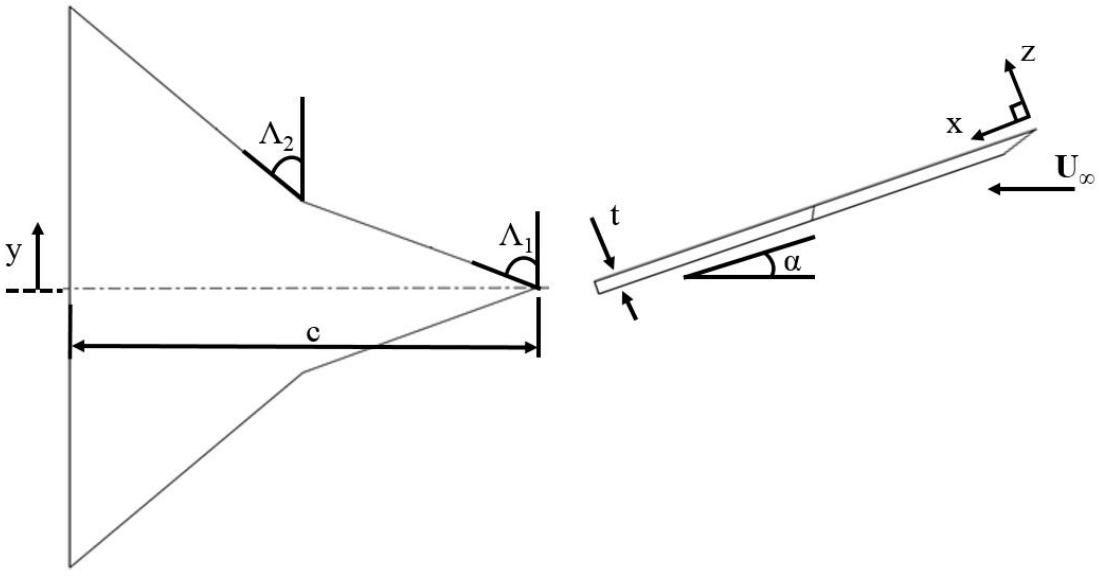


Figure 2. Geometric definitions of the double delta wing

# CHAPTER 2.

# LITERATURE REVIEW

## 2.1 Summary

This chapter provides an overview of the past studies carried out investigating the aerodynamic properties of different types of delta wings and double delta wings, furthermore, different flow control methods are also introduced. Section 2.2 focuses on the vortical flow over two types of delta wings: slender delta wing and non-slender delta wings. Section 2.3 then presents the characteristics of the flow pattern over double delta wing configurations, it emphasises on the need for further investigations on the vortex breakdown and interactions, especially the unsteady aspects. Section 2.4 summaries several vortex control methods, suggesting the potential benefits they could bring when implemented on the double delta wing configurations.

## 2.2 Vortical Flow over Delta Wing

Delta wings are normally divided into two types depending on their leading-edge sweep angle, they are slender delta wings ($\Lambda \geq 65^0$) and non-slender delta wings ($\Lambda \leq$ 55) respectively. Large amount of research effort has been put into understanding the vortical properties of both types of delta wings. It has been discovered that the flow around slender and non-slender delta wings has very different characteristics, which will be discussed in the following sections.

### 2.2.1 Slender Delta Wing

The development of vortical flow over delta wings includes the flow separation at the leading-edge and the formation of shear layers. Figure 3 [11] describes the flow characteristics over a slender delta wing. It can be seen that the flow separation occurs along the highly swept sharp leading-edges and wraps up in a spiral fashion, which forms one counter rotating vortex pair on the suction surface [12]. The stream surface which has separated at the leading-edge (primary separation line $S_1$) loops above the

wing and then reattaches along the primary attachment line (line $A_1$). One thing to notice in Figure 3 is the small secondary vortices separate at line $S_2$ near the main vortex reattachment points, they rotate in an opposite direction to the primary vortices and reattach at the secondary attachment line $A_2$, this is due to the lateral flow towards the leading-edge [12]. Verhaagen [8] describes that the primary vortices over slender delta wings have similar characteristics to a jet flow and the axial velocity in their cores can reach up to two or three times that of the free stream velocity. This results in a very low pressure region which enables additional lift to be generated [11]. As angle of attack increases, the primary vortex reattachment line moves inboard towards the centreline and reaches the wing centreline at a certain angle of attack. After passing this angle of attack the reattachments of the primary vortices will move along the wing centreline and away from the wing surface as shown in Figure 4 [3, 13]. Further increase the angle of attack, the primary vortices will go through a stage of sudden expansion, which is also known as vortex breakdown. Figure 5 illustrates the process of a vortex breakdown, for slender delta wings, vortex breakdown is the main flow phenomenon that causes lift loss, and it is the dominant source of wing and fin buffeting [13]. Previous studies on vortex breakdown phenomenon agree on two important parameters that affect the occurrence and movement of vortex breakdown: swirl level and pressure gradient, increase in either one of the parameters will result in the earlier onset of vortex breakdown. Moreover, the minimum swirl level required for breakdown decreases with increasing magnitude of the adverse pressure gradient [10, 13-15].

### 2.2.2 Non-Slender Delta Wing

On the other hand, as delta wing sweep angle decreases, it has been found that the portion of lift contributed by the primary vortices reduces [16]. This indicates that breakdown of the primary vortices is no longer a key factor of lift loss for non-slender delta wings with small sweep angle. Previous studies have revealed the differences in the vortical structures between slender delta wings and non-slender delta wings. On the non-slender delta wings, the reattachment of the separated flow is possible even after breakdown reaches the apex of the wing, however it is not possible at high angles of attack in the post-stall region, as completely stalled flows occurs on the wing [13].

Figure 6 shows the effect of delta wing sweep angle on the flow reattachment, vortex breakdown and stall angle. It can be seen that as the wing sweep angle increases, the onset of vortex breakdown occurs at higher angles of attack, but at the same time the flow reattachment is becoming more difficult [13, 17]. Stall angle is higher for larger sweep angle wings than small sweep angle wings [2, 13, 18, 19]. Ol et al [20] compared the vortical structure between a $50^0$ sweep angle non-slender delta wing and a $65^0$ slender delta wing. They discovered that when angle of attack is kept below $10^0$, similarities in the flow field were observed between the two, which were: 1) the geometry of the leading-edge shear layer, 2) the presence of a pair of primary vortices, 3) the axial velocity distribution, and 4) the gradual upstream progression of the vortex breakdown as angle of attack increases. However, as the angle of attack increases, the flow fields between the two delta wings behave quite differently, as the non-slender delta wing experiences vortex breakdown at much lower angles of attack, it also experiences a large-scale collapse of the rolled-up leading-edge vortex structure across a narrow angle of attack range, as shown in Figure 7 [20].

### 2.2.3 The Dual Vortex Structure

Another interesting vortical flow phenomenon is the dual vortex structure (the formation of an additional co-rotating vortex alongside primary vortex), which has been rarely documented and only studied on delta wing experimentally and computationally. Taylor and Gursul [19] firstly observed the dual-vortex structure experimentally on a $50^0$ sweep delta wing at $\alpha = 7.5^0$ and Re = 8700. It was found that the formation of the dual-vortex structure can be affected significantly by Reynolds number and angle of attack. At low angles of attack and Reynolds number, the primary vortex structure is relatively weak and closer to the wing surface, the secondary vortex splits the primary vortex into two separate regions of vorticity, which they then further develop into the dual-vortex structure, a pair of co-rotating vortices, as shown in Figure 8. As angle of attack or Reynolds number keeps increasing, the primary vortex gains both in strength and size, and moves away from the wing surface so that the secondary vortex will not be able to effectively split the primary vortex. Rockwell and Yaniktepe [21] also observed a well-defined dual vortex structure at sufficiently low angles of attack on a 38.7˚ sweep non-slender delta wing. Wang and Zhang [22] then

investigated the dual vortex structure further, they concluded that the conditions for the dual-vortex structure to form are such that the angle of attack needs to be within a very small range with the Reynolds number above a critical value. However, they also observed dual vortex structure on slender delta wing ($\Lambda = 65^0$). Computational evidences of the dual-vortex structure was provided by Gordnier and Visbal [23], they identified the dual-vortex structure at $\alpha = 5^0$, which faded away slowly as angle of attack increased and finally diminished by $\alpha = 15^0$ (Figure 9), it was then replaced by the more typical primary vortex.

## 2.3 Vortical Flow over Double Delta Wing

Numerous studies have been carried out both experimentally and computationally investigating the vortical behaviours over double delta wings. The formation process of the leading-edge vortices over double delta wings is similar to that of delta wings, it is initiated at the sharp leading-edges and includes flow separation and the formation of shear layer. One of the early studies [24] describes that the vortical flow over double delta wing is similar to that over delta wing, but it is more complicated due to the possible interactions between vortices. These interactions are mainly caused by the two primary vortices - strake vortex and wing vortex - and usually involve a starting phase in which the vortices spiral around each other [7]. At high angles of attack, the strong strake vortex stabilises the flow over the wing, enhances the lift-to-drag efficiency of the aircraft and delays the vortex breakdown [4, 25]. However, the interactions of multiple vortices, the vortex bursting and the complicated vortical structure are highly problematic vortical properties that require further investigations, especially the unsteady aspects of vortex interactions, it has gained little attention in the research field previously [26].

Gonzalez et al [27] summarised the vortical flow over double delta wing as follow: At low angles of attack, the strake and wing vortices are very distinctive and follow the strake and wing leading-edges. As angle of attack increases, the wing vortex starts to move inboard and closer to the strake vortex to interact. Depending on the wing sweep angle, the wing vortex might breakdown before interacting with the strake vortex. As angle of attack increases, the breakdown points of both strake and wing

vortices move upstream until they reach the apexes. Rom [28], Verhaagen and Maseland [29] initially suggested that the interactions between the two primary vortices, and the breakdown of them are affected by the angle of attack, the shape of leading-edge cross-section, Reynolds number and the leading-edge kink angle. It was concluded that the interaction point of the two vortices moves downstream as the angle of attack decreases, as leading-edge kink angle increases and as Reynolds number increases. Later in another study [30], two types of interactions were identified, which were the enveloping interaction and spiralling/coiling interaction. The enveloping interaction occurs at low angles of attack, during which the wing vortex 'pulled' the strake vortex outboard and underneath itself. While during the spiralling/coiling interaction, which occurred at high angles of attack, the wing vortex was drawn inboard and around the strake vortex. Sohn et al. [4] discovered that two adjacent vortices of the same rotating sense and unequal strengths will revolve around a centre which positioned on the connecting line between the two vortices centres, and at the point of zero induced velocity such that the centre is closer to the core of the stronger vortex. When the strengths of the two vortices are about the same, they tend to spiral around each other but still maintain their identities until merging occurs. Lopsided coiling will take place for unequal strengths of the vortices [31, 32].

### 2.3.1 Effect of Angle of Attack

One of the early studies carried out by Verhaagen et al. [8] investigated the effect of angle of attack and Reynolds number on the vortical flow over a 76˚/40˚ double delta wing configuration. Figure 10 illustrates part of their results from this study, it shows two coherent leading-edge vortices on the main wing section even beyond $\alpha$ = 20˚ without breakdown. With the absence of the strake vortex, a delta wing with 40˚ sweep would stall around $\alpha$ = 17˚ [13, 18]. Furthermore, the trajectories and the breakdown locations of the two vortices are greatly affected by angle of attack. As angle of attack increases, there is increased level of vortex interaction (due to the increase in size and strength of both vortices), also the location of vortex breakdown moves more upstream. Similar trend was also observed by Gai et al. on a 76˚/40˚ double delta wing configuration [30], they observed that the strake vortex firstly starts forming at $\alpha = 5^0$; at $\alpha = 10^0$, both strake and wing vortices are well developed but no

evidences of interactions or breakdown is observed; at $\alpha = 20^0$, the strake vortex moves outboard and its breakdown occurs at around x/c = 75%. Pamadi [33] describes the general vortical flow before and after passing the kink, it is suggested that as the strake vortex passes the kink, since it is no longer energised by the flow separation at the wing leading-edge, it tends to bend outboard and move closer to the wing surface; on the other hand the wing vortex is more energised hence it tends to bend inboard and move away from the wing surface. In addition, from Figure 10, it can be seen that the strake vortex breaks down just after the wing vortex breakdown point, which suggests that the breakdown of strake vortex might be triggered by the breakdown of the wing vortex. However, on the other hand, Hebbar et al. [34] investigated the double delta wing vortical properties in a water tunnel and found that the wing vortex breakdown occurs downstream of the strake vortex breakdown point.

### 2.3.2 Effect of Reynolds Number

With regards to Reynolds number, Hebbar et al. [35] and Gursul et al. [36] reported that the vortex interactions on double delta wings might be very sensitive to Reynolds number at low Reynolds number range. In the study from Hebbar et al., they investigated how the change in Reynolds number can affect vortex interactions and breakdown on a 76˚/40˚ double delta wing in water tunnel. Three different Reynolds numbers were tested: Re = $1.5 \times 10^4$, $4.5 \times 10^4$ and $7.5 \times 10^4$. As shown in Figure 11, when increasing the Reynolds number, they found that the coiling/spiral interaction between strake and wing vortices gradually disappeared; the vortex breakdown locations for both strake and wing vortices moved more forward towards the apex of the model; and the wing and strake vortex core locations moved outboard.

On the other hand, in one of the wind tunnel studies from Verhaagen et al. [8] over a 76˚/40˚ double delta wing configuration, it was observed that at $\alpha$ = 20˚, the breakdown location of strake vortex was unaffected by Reynolds number when it changed from $2.5 \times 10^5$ to $2.0 \times 10^6$. An early study from Erickson [17] also suggested that the onset of vortex breakdown is independent of Reynolds number. In addition, Verhaagen et al [8] noticed that the secondary separation lines vanished at Re = $1.5 \times 10^6$ and $\alpha$ = 10˚, which indicates that either no secondary vortices were

induced by the strake vortices at this Reynolds number, or the secondary vortices moved outboard and merged with the wing secondary separation lines. However, at the same angle of attack but lower Reynolds number Re = $0.5 \times 10^6$ and $1.0 \times 10^6$, the strake vortex secondary separation line is clearly visible. Later, Verhaagen et al [25] undertook another study investigating the effects of Reynolds number on vortical flow structure over the same 76˚/40˚ double delta wing configuration. It was concluded that for angle of attack up to $\alpha = 25^\circ$ and Reynolds number up to Re = $4.0 \times 10^6$, the flow over the strake section was little affected by the Reynolds number; at Reynolds number below Re = $1.0 \times 10^5$, strong Reynolds number effect was observed on the interaction between strake and wing vortices over the wing section; when Reynolds number kept the same, the interaction between the two vortices is weak at low angles of attack and strong if angles of attack are larger than $\alpha = 10^\circ$.

## 2.4 Vortex Control Methods

Controlling the vortical flow over delta wing can have several benefits, including enhancing the lift, generating forces and moments for flight control and attenuating the wing/fin buffeting. It is usually achieved by using active and passive flow control methods to manipulate one or more of the following flow phenomena: flow separation from the wing, separated shear layer, vortex formation, flow reattachment on the wing surface, and vortex breakdown [13]. This section will give a brief introduction of the commonly used active and passive control methods, such as deployment of control surface, modification of the wing geometry, blowing, suction and bleed.

### 2.4.1 Effect of Wing Geometries

In terms of wing geometries, Gonzalez et al [27] compared three 76˚/40˚ double delta wings with different fillets at the kink (Linear, Diamond and Parabolic) and the baseline model in a wind tunnel for angle of attack ranges between $\alpha = -4^\circ$ and 32˚, the wing geometries are shown in Figure 12. The linear and diamond fillets added more edges at the kink, therefore additional vortices were expected; while the parabolic fillet smooth out the edge at the kink. It was found that the flow field of the linear fillet case was dominated by the strake, fillet, and wing vortices. The strake vortex was

immediately entrained by the fillet vortex and possessed a much smaller footprint in the data. At $\alpha = 16^{\circ}$, all the vortices interacted with each other and resulted in a single vortex. For the diamond fillet case, four pairs of vortices were observed: two from the fillet, one from the strake and one from the wing. At low angles of attack, the two fillet vortices rapidly rolled up into a single vortex, and the vortical field displayed three distinct vortices. At higher angles of attack, the strake, fillet and wing vortices started to show a single vortex footprint. While for the parabolic fillet case, majority of the vorticity rolled up into a single pair of vortices. This single vortex pair ceased to follow the wing leading-edge and 'tear off' [37], a new vortex was then formed along the wing leading-edge after this 'tear off'. It was found that with the help of additional fillets at the kink, the lift increased for angles of attack between $\alpha = 8^{\circ}$ and $32^{\circ}$ when compared with the baseline model. Among them, the parabolic fillet generated significant higher maximum lift, while the linear and diamond fillets increased lift only to certain degrees.

Later on Sohn and Chung [4] investigated the effects of three different kinds of strake planforms on the vortical flow over double delta wing. The different strake platform shapes are presented in Figure 13, they are a $65^{\circ}/90^{\circ}$ sweep cropped delta; $79^{\circ}$ sweep single delta and $72^{\circ}/84^{\circ}$ sweep cropped delta. Their results indicated that the $79^{\circ}$ sweep single delta produced more concentrated vortical system at upstream locations than the other two planforms. However, this more concentrated vortical system found on the $79^{\circ}$sweep single delta planform tended to diffuse and break down much faster than the other two platforms, and it showed more advanced coiling interaction of the strake and wing vortices. It was concluded that the flow pattern over a double delta wing can be greatly affected by the shape of strake planform.

One of the early studies carried out by Gursul and Yang [38] investigated the control of leading-edge vortices and vortex breakdown over a pitching delta wing with variable sweep between $\Lambda = 60^{\circ}$ and $70^{\circ}$. It was found that when sweep angle variation and pitching motion are combined with a proper phase angle, the amplitude of the variation of vortex breakdown location becomes a minimum. The advantage of using variable sweep angle as control method is that the variation of vortex breakdown location with sweep angle is monotonic, therefore it is desirable for controlling purposes [13].

Another close family of the double delta wing geometry is the canard-wing configuration, it was shown that the vortex interactions take place over the canard wing configuration can delay the breakdown of wing vortex [39]. Myose et al. [40] investigated the effect of a canard wing on a 70˚ sweep delta wing vortical flow when placed at different locations, Figure 14 shows their experimental configurations. It was concluded that the presence of a canard produced a delay in the vortex breakdown location. The effect was the greatest when the canard was located close to the main delta wing (0.0c forward), it resulted in 19% delay in the full stall angle of attack. Furthermore, they also investigated the effect of canard sweep angle on the main wing vortex breakdown locations when it was placed next to the main delta wing (0.0c forward). Three different canard sweep angles with the same chord length were tested, which were $\Lambda = 45˚$, 60˚ and 70˚ respectively. It was found that increasing the canard sweep angle, area or span had a beneficial effect on delaying the vortex breakdown, but they could not determine which of the above-mentioned factors caused this delay on vortex breakdown. This effect of canard on delaying the vortex breakdown was also observed by Landahl and Widnall [41], by carefully positioning the canard above the main wing, the vortex breakdown was effectively delayed and a stall angle of 50˚ was achieved.

### 2.4.2 Control Surfaces

Control surfaces manipulate the vortical flow by changing the wing geometries, three examples have been discussed earlier regarding the effect of wing geometries - double delta wing kink fillet shapes, various strake platform shapes and canard-wing shapes. Gursul et al. [42] investigated the effect of leading-edge flap angles on vortex breakdown over simple delta wing with sweep angle of $\Lambda = 70˚$. Here the flap angle is denoted using the letter 'δ', as shown on Figure 15, $\delta = 180˚$ is when the flap is fully extended, and $\delta = 0$ is when the flap is folded on the wing surface. It was found that at low angles of attack ($\alpha = 16˚$ & 20˚), as the flap angle decreased from 180˚, the vortex breakdown location moved towards the trailing-edge. At higher angles of attack ($\alpha =$ 25˚ & 30˚), the breakdown location did not change much initially as the flap angle decreased from 180˚, however it then rapidly moved towards the wing trailing-edge.

Figure 15 summarises the effect of flap angle and vortex breakdown location. It can be seen that when $\alpha \leq 30^{\circ}$, the vortex breakdown location was monotonic, hence the breakdown location can be controlled by using flaps; however, at their highest tested angle of attack ($\alpha = 35^{\circ}$), as the flap angle decreased, the vortex breakdown location moved downstream first, then it moved upstream when flap angle $\delta < 65^{\circ}$, this means it is not suitable for control purpose.

Since majority of the vorticity in the vortex core originated from a small region near the apex of the wing, therefore an apex flap could be very beneficial in controlling the vortical flow [43]. Klute et al. [44] studied the effect of using apex flap on the vortical flow over a $\Lambda = 75^{\circ}$ delta wing in both a water tunnel and a wind tunnel. It was found that with the deployment of an apex flap in a drooping position, the vortex breakdown was delayed by an angle of attack of $8^{\circ}$ beyond the corresponding value of the unmodified fixed wing. The most effective drooping angle for the apex flap was found to be $15^{\circ}$, and it appeared to be equally efficient in controlling breakdown during pitch-up manoeuvres.

In another study, Lee et al. [45] successfully applied the micromachined actuators to control leading-edge vortices of a delta wing by manipulating the thin boundary layer before flow separation. Figure 16 illustrates the delta wing model and schematic of microactuators set up on the leading-edge that they used for this study. As shown in Figure 17, they placed the actuator on either the forward or the rear half-section of the leading-edge to achieve five different configurations (the thick black line represents actuators). It was found that the shear layer separated with a steeper angle if the actuator array was placed at or before the original separation point; hence, the vortex moved outboard and away from the surface, generating a positive rolling moment. On the other hand, the shear layer separated with a smaller angle if the actuator array was positioned downstream of the original separation point, this control forced the vortex to move inboard and closer to the surface, producing a negative rolling moment, as shown in Figure 18. By breaking up the symmetry of the main vortex pair using the actuators, it is possible to generate appreciable moments for flight control.

### 2.4.3 FLUIDIC CONTROL

#### 2.4.3.1 Blowing

Numerous studies have been carried out previously investigating the effect of mainly the following blowing configurations over delta wings, these are spanwise leading-edge blowing, tangential leading-edge blowing, parallel leading-edge blowing, vortex core blowing, recessed angled spanwise blowing and trailing-edge blowing [13, 46, 47].

Hong et al. [48] investigated the effect of spanwise leading-edge blowing on the vortical flow over a $\Lambda = 60^{\circ}$ delta wing with linearly varying thickness from the wing centreline, as shown in Figure 19. They found out that the flow from the blowing jet fed into the leading-edge vortex and strengthened it. Also, since a jet sheet can sustain pressure difference, the lateral blowing increased the effective span of the wing, the leading-edge vortices appeared to be more strengthened and moved outboard. The effectiveness of this blowing arrangement covered for the whole range of the angles of attack tested from $0^{\circ}$ to $30^{\circ}$, except for $\alpha = 20^{\circ}$, at which the normal force did not increase but decreased when blowing was applied. For low angles of attack, the lateral blowing increased the vortical lift by enhancing the vortices, however, it also encouraged the vortex breakdown location to move upstream and caused loss of lift. But it compensated this loss of lift by increasing the area where the vortex was effective. In addition, they also discovered that a partial slot was more effective than the full slot configuration in generating roll moment for a large range of blowing strengths and angles of attack.

Much earlier, Wood et al. [49] carried out research investigating the effect of tangential leading-edge blowing on the vortical flow over a $60^{\circ}$ sweep delta wing through a blowing slot. Their results showed that the co-flowing, tangential leading-edge mass injection was capable of extending the regime of stable, controlled vortical flow over the upper surface of a delta wing by approximately $30^{\circ}$ angle of attack. Increasing in maximum normal force coefficient by approximately 30% was achieved and significant rolling moment was produced at $\alpha = 35^{\circ}$ to $60^{\circ}$. At low angles of attack, the vortical flow may be removed entirely from the surface of the wing, recovering the

fully attached flow case. Gu et al. [50] then investigated the effect of steady blowing, steady suction and alternating suction-blowing in the tangential direction along the leading-edge over a $\Lambda = 75^{\circ}$ sweep delta wing. It was found that tangential injection from the leading-edge in the form of any of the three mentioned methods can retard substantially the onset of vortex breakdown and stall. Among them, alternating blowing-suction produced the largest downstream displacement of the vortex breakdown. Once this maximum downstream displacement was attained, it was maintained in a relatively steady position except for small fluctuations, irrespective of whether steady blowing, steady suction, or alternating blowing-suction was applied.

In one of the early researches, Bradley et al. [51] performed a study with blowing on a $80^{\circ}/40^{\circ}$ double delta wing at two different locations, one blew along the strake leading-edge and the other blew along the wing leading-edge. It was concluded that, in general, blowing tends to be effective in delaying vortex breakdown by intensifying and aiding the formation of the vortex system. They found that the wing blowing was effective at lower angles of attack, whereas the strake blowing was most effective at higher angles of attack, which was expected as vortex breakdown occurred at lower angle of attack for wings with low leading-edge sweep. They also discovered that, as angle of attack increased, the strake vortex turned outboard into the stalled outer-panel flow, where vortex breakdown occurred if angle of attack kept increasing. At $\alpha = 20^{\circ}$, wing blowing facilitated the turning of the strake vortex so that a single vortex was formed at the wing section, indicating merging of the wing and strake vortices. Figure 20 shows the force measurement data from their study, it described the findings of the effect of the wing blowing and strake blowing in terms of force.

Mitchell et al. [52] investigated the effect of along-the-core blowing on vortex breakdown locations over a $70^{\circ}$ sweep delta wing. They found that blowing along the core of the portside leading-edge vortex on the leeward surface of the delta wing was shown to be effective for controlling the vortex breakdown location. Depending on the blowing momentum coefficient, this asymmetric flow control technique was able to displace aft the portside vortex breakdown location more than 20% of the root chord at lower momentum coefficient, and permanently displace the vortex breakdown location to or after the wing trailing-edge at higher momentum coefficient (shown in Figure 21). As the portside vortex breakdown location was displaced downstream with

the blowing, the starboard vortex breakdown location shifted farther upstream than the no-blowing configuration, therefore asymmetric flow control influences both the controlled and uncontrolled leading-edge vortices.

Johari et al. [46] carried out a vortex control study via recessed angled spanwise blowing over a 60˚ sweep delta wing. The main difference between recessed angled spanwise blowing and spanwise blowing is that the blowing holes on recessed angled spanwise blowing were placed away from the leading-edge, Figure 22 illustrates the experimental model used by Johari et al. It was summarised that between $\alpha = 18^{\circ}$ and $\alpha = 32^{\circ}$, blowing at 20-30% chord locations upstream of the natural burst location tended to move the burst location forward, blowing downstream of the natural burst location tended to move it closer to the blowing port, and blowing at the burst location had little effect. Also, increasing the blowing coefficient beyond a certain value did not generally result in further improvement of the burst location.

As for the trailing-edge blowing, Wang et al. [53] investigated the effect of thrust-vectoring jets on both slender ($\Lambda = 50^{\circ}$) and non-slender ($\Lambda = 65^{\circ}$) delta wings, rectangular and circular blowing nozzles were used (as shown in Figure 23). It was found that for non-slender delta wing, the effect of the jet strongly depended on the spanwise location of the nozzle. Centreline blowing had small effect on non-slender delta wing, whereas for under-vortex blowing the maximum lift enhancement reached $\Delta C_{L,MAX} \approx 0.15$ near the stall angle of $\alpha = 20^{\circ}$. Flow visualization indicated that for under-vortex blowing near the stall incidence and post-stall region, earlier reattachment of the shear layer occurred and vortex breakdown was delayed. For slender delta wing, however, the effect of centreline blowing was relatively larger than non-slender delta wings, due to the relatively shorter span of the wing, and there was evidence that the effectiveness of trailing-edge blowing increased with the wing sweep angle. Their force measurements indicated that the effect of nozzle geometry was important due to its influence on the entrainment effect of the jet. There was also interaction between the wing vortex and the jet in the near wake, this interaction was much stronger for the rectangular nozzle and had a larger influence on the delta wing aerodynamics.

#### 2.4.3.2 Suction

In one of the early studies, Parmenter and Rockwell [54] investigated the re-stabilisation of a leading-edge vortex on a delta wing by using transient suction. They compared two different suction coefficients and their required time to stabilise the broken-down vortex. Four different stages, progression through time, of the stabilisation process of vortex breakdown due to suction were identified: 1) downstream movement of the breakdown location and insignificant change of the radius of the breakdown spiral; 2) continued downstream movement of the spiral pattern, accompanied by a decrease in radius of the spiral; 3) rapid decrease in radius of the spiral, eventually becoming indiscernible and leaving a breakdown bubble upstream of a turbulent wake; 4) achieve stabilisation of the turbulent breakdown region as it was drawn into the probe. The four stages can be seen from their visualisation results shown in Figure 24.

In addition, they also measured the time each suction configuration took to stabilise the vortex. It was found that for a given suction location, when the suction coefficient was sufficiently large, further increase of the suction coefficient would not significantly alter the re-stabilisation time. Decreasing the suction coefficient below this threshold value would increase re-stabilisation time noticeably. The re-stabilisation time was also very sensitivity to the suction locations, when the suction point was located at/or downstream of the wing trailing-edge within the low velocity recirculation zone of the vortex breakdown region, it could delay the vortex breakdown very effectively; however, when it was placed upstream of the trailing-edge, it was not as effective as the former one. They explained that the suction point drew fluid from essentially all directions when located at/or downstream of the wing trailing-edge, which created a different kind of sink flow pattern compared with when the suction point was located upstream of the trailing-edge.

In another study mentioned earlier, Gu et al. [50] investigated the effect of steady blowing, steady suction and alternate suction-blowing in the tangential direction along the leading-edge of a $\Lambda$=75˚ delta wing. They found that alternating blowing-suction produced the largest downstream displacement of the vortex breakdown, and steady

suction also delayed the vortex breakdown location very effectively. They tested the dynamic response of the vortex breakdown location to the on/off switch of the suction. It was noted that it took a much shorter time for the breakdown location to reach its maximum downstream point after switching on the suction than for it to return to its equilibrium after switching off the suction. This relatively longer time required for relaxation to the final equilibrium position was associated with a mild overshoot of the vortex breakdown position. Later on, McCormick and Gursul [55] also studied the effect of suction on leading-edge vortices with two different suction models - model A had the suction slot located at the shear layer separation location, whereas model B had the suction slot located inboard and away from the separated shear layer (as shown in Figure 25). It was found that model A could effectively delay the vortex breakdown to downstream location, suction allowed the shear layer to be manipulated at the point of separation along the leading-edge. However, for model B, since shear layer had already separated and begun its characteristic curvature over the wing surface before the suction slot was encountered, the vorticity fed into the shear layer did not change with suction but the shear layer could still be vectored inboard in a very effective manner. Their later study also confirmed that suction is more effective in delaying vortex breakdown for locations closer to the leading-edge [56].

One of the most recent studies published by Wang and Gursul [57] investigated the effects of suction on the aerodynamics of a flat-plate aerofoil, with emphasis on increasing the lift and delaying the stall of the aerofoil. Their force measurements data suggested that the effect of suction is negligible at pre-stall angles of attack, however the lift enhancement could be substantial at post-stall angles of attack. They observed a maximum of 65% increase in the maximum lift coefficient and a maximum delay of stall angle of 9 degree for suction coefficients less than 3%. The lift-to-drag ratio was increased by nearly 100% at post-stall angles of attack when compared with the baseline case. The best performance was observed when the time-averaged reattachment was achieved on the aerofoil surface and close to the trailing-edge, resulting in a large separation bubble. The optimal location of suction was around x/c = 40%, which resulted in the maximum lift coefficient; when suction was applied close to the leading-edge the separation could not be delayed, but reattachment further downstream was promoted, which caused a small separation bubble.

#### 2.4.3.3 Bleed

Passive bleed as a flow control method has been explored in several studies previously. In a typical application, fluid is bled from high pressure region to low pressure region through porous surface segments via internal passage or a plenum [58].

Glezer and Leonard [58] investigated the effect of bleed over an aerofoil for aero-effected flight control purposes, bleed was applied from both leading-edge and trailing-edge, as shown in Figure 26 ('a' is trailing-edge bleed and 'b' is leading-edge bleed). Various louvres opening angles were used in their study to control the bleed flowrate, $\Lambda$ represents the fractional opening of the louvres, which equals to 1 at maximum louvre displacement 2.12mm. For the trailing-edge bleed, it was found that the lift decreased linearly as the opening angle of the louvre increased, the decrease was more profound for lower angles of attack, their lift coefficient plot is shown in Figure 27a. For the leading-edge bleed, louver actuation was mostly effective between 8˚ and 20˚ angle of attack, and it was manifested by a large decrease in lift of $\Delta C_L$ = 0.7 at $\alpha = 16^{\circ}$, as shown in Figure 27b.

Later on Han and Leishman [59] applied bleed slots on helicopter blade to investigate their effect on rotor blade tip vortex, their model was shown in Figure 28. The tip vortices generated by helicopter rotor blade could be a source of adverse aerodynamics problems, such as blade – vortex interactions and vortex – airframe interactions. They found that slotted blade reduced the peak value of the swirl velocity components in the tip vortex by up to 60% relative to those of the baseline cases, the bleed slots were considered a highly effective method in diffusing vorticity and reducing the high velocity field that would otherwise be induced by a rotor tip vortex. As the rotor tip vortex formed and rolled up along the tip side edge, the bled flow at the bleed slots exit acted in such a way as to interact and promote turbulence inside the innermost region of the tip vortex, which would otherwise remain laminar, as shown on the schematic plot in Figure 29.

Hu et al. [60] also applied passive bleed techniques to attenuate self-excited roll oscillations of a low-aspect-ratio rectangular flat plate wing. They found that the

baseline wing model exhibited large-amplitude roll oscillations that began before the stall angle. For appropriate tip slots, these roll oscillations could be largely suppressed for all angles of attack, the effectiveness of the bleed slots depended on the width and spanwise location of the slot. The jet-like bleed through tip slots resulted in the formation of a counter-rotating vortex, which may interact with the shear layer separated from the tip, as shown in Figure 30. As a result of this interaction, the coherent tip vortex observed over the stationary baseline model was not formed and only patches of vorticity were shown.

## 2.5 Literature Review Summary

In this literature review, section 2.2 and 2.3 described the aerodynamic properties of slender delta wings, non-slender delta wings and double delta wings. It was shown that slender and non-slender delta wings have different vortical properties, by adopting a double delta wing geometry, it would combine the advantages of both types of delta wings. However, with the presence of multiple vortices over double delta wings, their interactions and breakdown can be problematic and raise challenges for aircraft flight control and stability. Moreover, there was lack of research emphasis previously on the unsteady aspects of vortex breakdown and interaction over double delta wing, therefore there is need to provide more insight into the conditions of these vortical behaviours.

Section 2.4 introduced some of the common flow control methods including adopting different wing geometries, deploying control surfaces, using blowing, suction and bleed. Deploying control surfaces such as flaps, micromachined actuators along the leading-edge of delta wings has been shown to be able to delay the onset of vortex breakdown and modify the position of the primary vortex. Several types of active blowing configurations were also presented, they are the spanwise leading-edge blowing, tangential leading-edge blowing, parallel leading-edge blowing, vortex core blowing, recessed angled spanwise blowing and trailing-edge blowing. Spanwise blowing was shown to be able to enhance the vortex but also aid early onset of vortex breakdown. Tangential leading-edge blowing, along-the-core blowing and trailing-edge blowing were shown to be very effective in delaying the vortex breakdown and enhancing the lift. Whereas the wing leading-edge parallel blowing could not only

delay the vortex breakdown but also facilitate the merging between the wing and the strake vortices at certain angles of attack. Recessed angled spanwise blowing, on the other hand, had different effect on the vortical flow depending on the relative location of the blowing port to the original vortex breakdown point. The diversity of different blowing methods and their impact on double delta wing vortical flow implied another potential way to investigate the effect of blowing – by placing rotatable blowing caps at different locations on the wing surface such that both the blowing jet yaw angle and its chordwise location can be studied. On the other hand, bleed is a novel passive concept that is generated by the pressure difference between the lower and the upper surfaces of the wing. Bleed has been shown to alter the structure of the wing tip vortex, manipulate lift and attenuate wing rock, these properties make it a desirable candidate for passive flow control study.

## 2.6 Aim and Objectives

The aim of this study is to investigate the interactions and control of multiple vortices over a 70º/50º double delta wing. The objectives of this study are the following:

1) Investigate the effect of angle of attack over a 70º/50º double delta wing using PIV technique, the interested angle of attack ranges between 4º to 32º. PIV data will be able to provide comprehensive measures of the flow field, which offers opportunity to extensively study the unsteady aspects of the interaction of multiple vortices.
2) Investigate the effect of various jet blowing configurations on the flow field over the same double delta wing configuration using PIV experimental technique. Combinations of several angles of attack, blowing jet yaw angles and blowing hole locations will be studied.
3) Investigate the effect of passive bleed on the flow pattern over the same double delta wing configuration using PIV technique. Different spanwise bleed hole locations and angles of attack will be studied.

The table on the next page summarises key objectives, the contributions from current study and their chapter numbers within this thesis.

| Objective | Contribution | |
|---|---|---|
| • Providing experimental data focusing on the unsteady aspects of double delta wing vortical flow | • Firstly observed the dual-vortex structure at x/c = 50% over double delta wing.<br>• Provided both time-averaged and unsteady results, such as time-averaged vorticity, standard deviation of crossflow velocity fluctuations, vortex meandering probability and amplitude, POD analysis.<br>• The meandering between the two vortices showed out-of-phase movement. | Chapter 4 |
| • Comparing the effect of Reynolds number on vortical behaviour | • Wing vortex breakdown first in water tunnel test, whereas strake vortex breakdown first in wind tunnel test.<br>• Dual vortex structure was not observed in the water tunnel test. | Chapter 5 |
| • Investigating the effect of active fluidic control method | • Blowing could either intensify or reduce the interaction between vortices depending on the configuration.<br>• Blowing could modify the global centroid significantly.<br>• The interaction between vortices could be effectively controlled by momentum coefficient. | Chapter 5 |
| • Investigating the effect of passive flow control method | • Depend on location, bleed had different effect on the vortical flow.<br>• Bleed enhanced the counter-rotating secondary vortex, which could interfere with the shear layer.<br>• Bleed increased turbulence level and meandering amplitude.<br>• Bleed is more effective at lower angle of attack. | Chapter 6 |

## 2.7 Figures

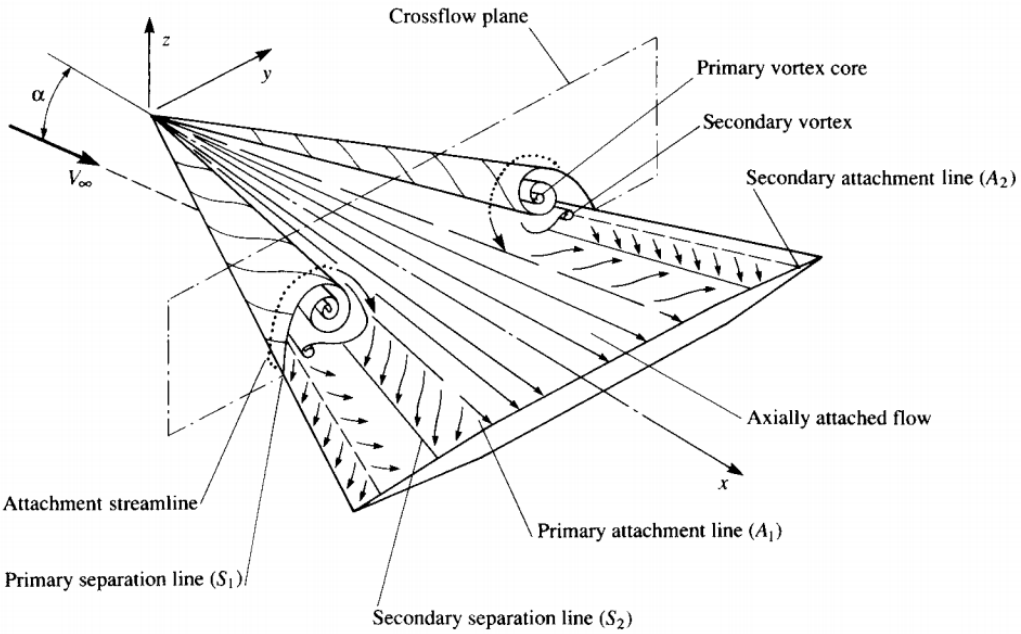


Figure 3.Schematic of the subsonic flow field over the upper surface of a highly swept delta wing [11]

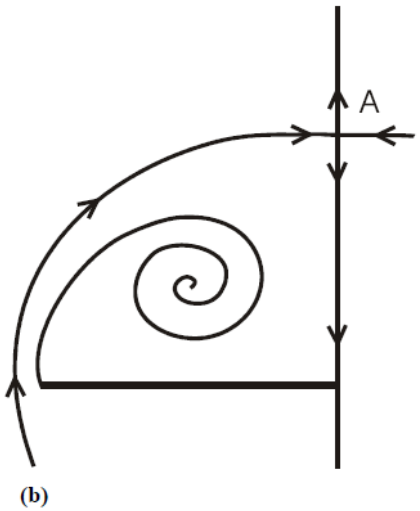


Figure 4. Schematic streamline patterns for slender delta wings no reattachment on wing surface [13]

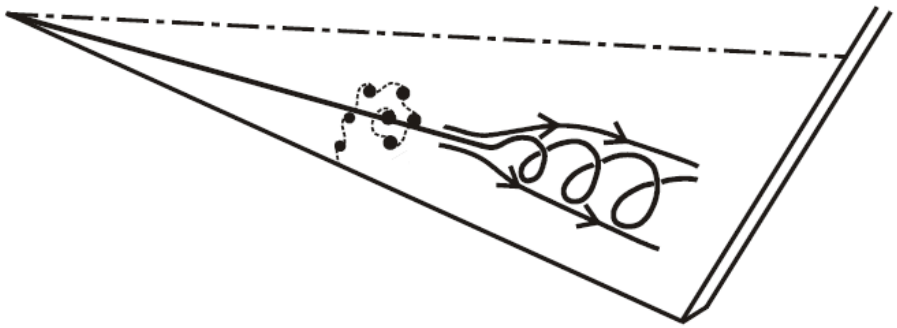

Figure 5. Schematic of vortex breakdown and shear layer instabilities [13]

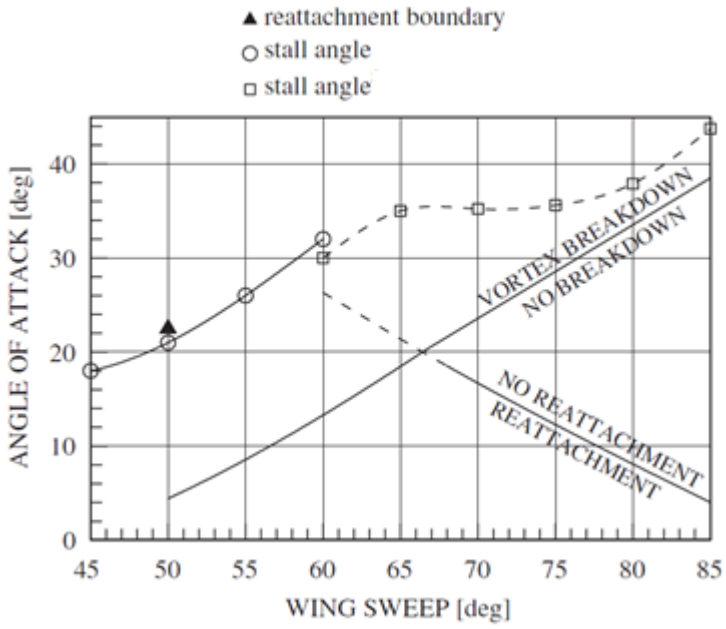


Figure 6. Effect of delta wing sweep angle on the flow reattachment [13]

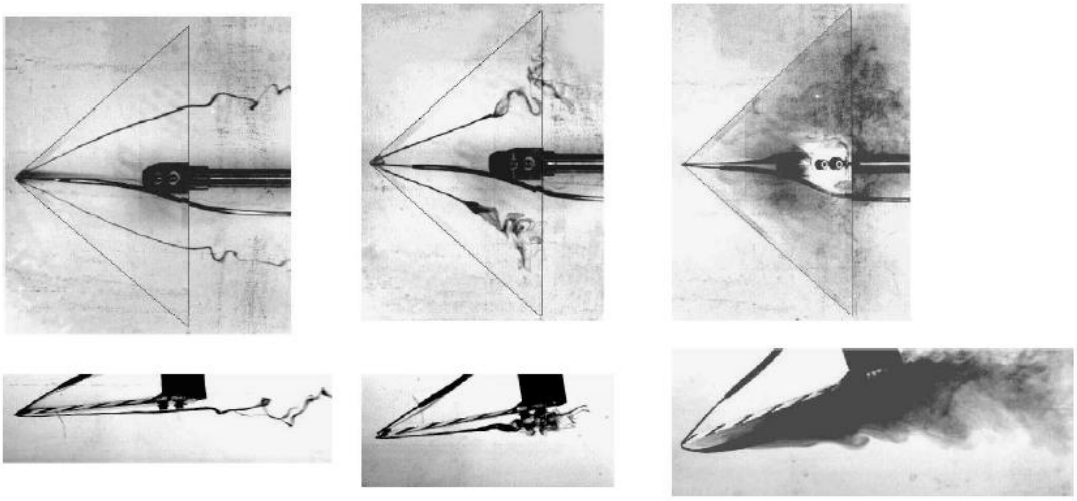

α = 5º α = 10º α = 20º

Figure 7. Dye streaks following primary LEVs for 50-deg wing; planform and side views [20]

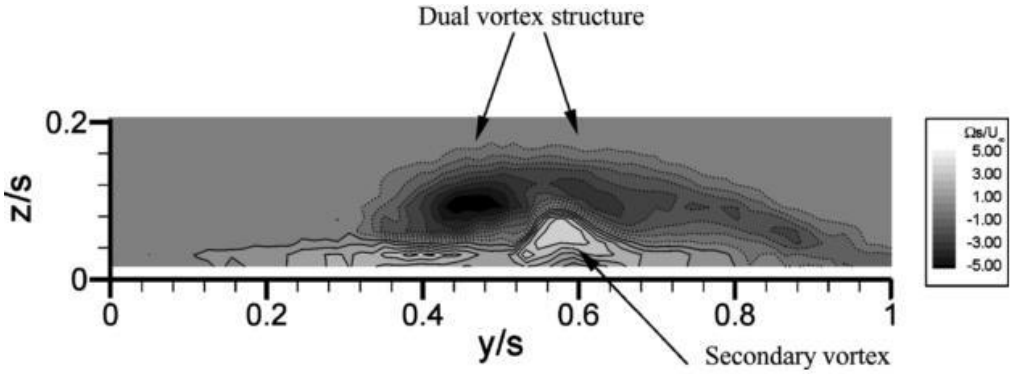


Figure 8. Crossflow vorticity field at x/c = 40%, α = 7.5 deg, Re = 8.7 x $10^3$, showing dual vortex structure [19]

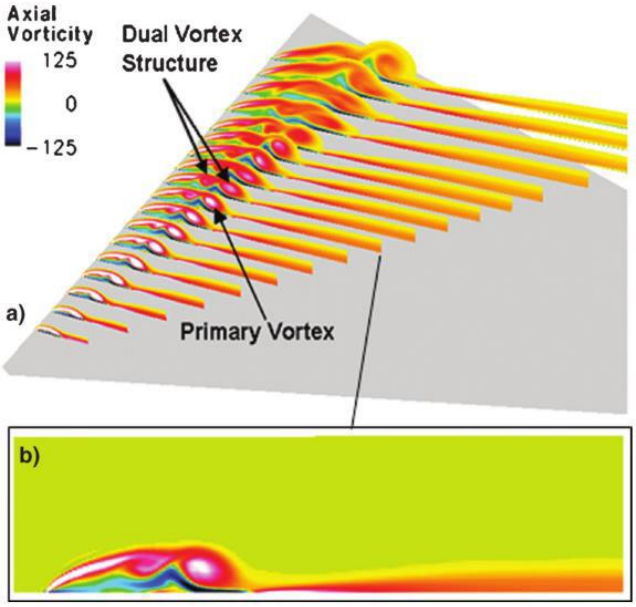


Figure 9. Mean vortex structure over delta wing at $\alpha = 5$ deg, $Re = 2.6 \times 10^4$ [23]

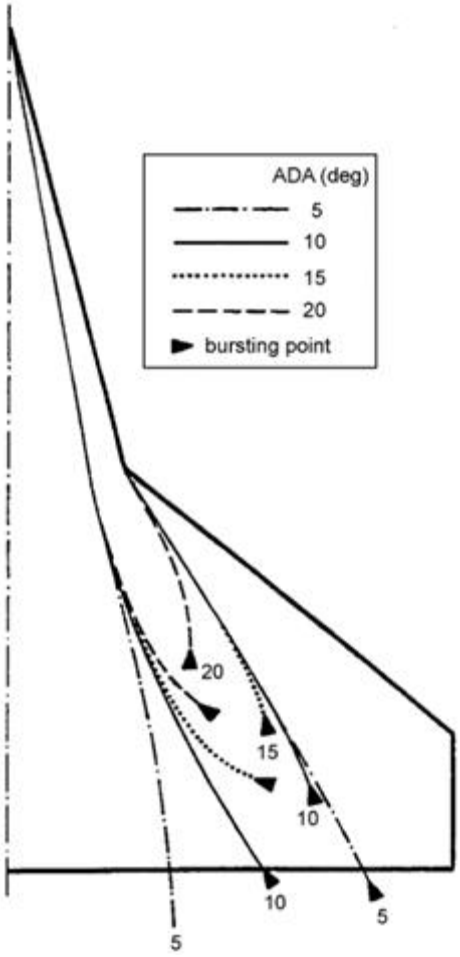


Figure 10. Effect of angle of attack on vortical flow over a 76˚/40˚ double delta wing [8]

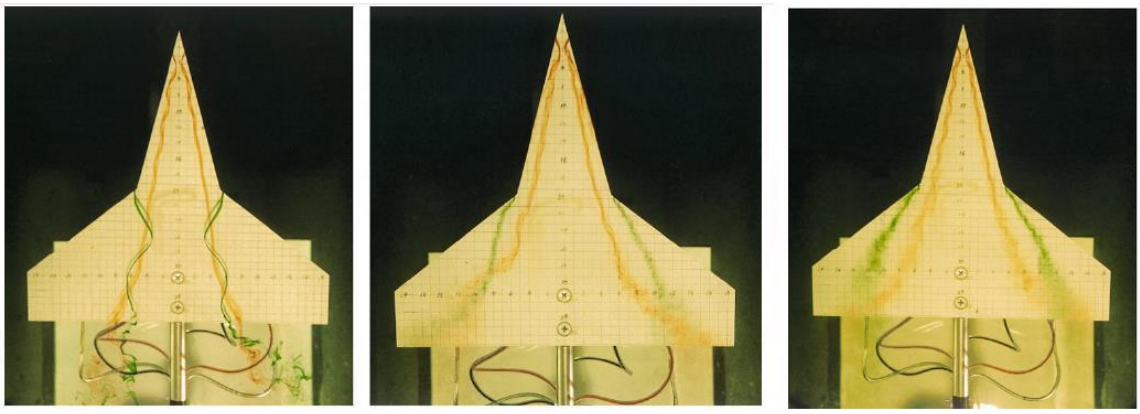

Figure 11. Effect of Reynolds number on double delta wing vortical flow. Re = 1.5 x $10^4$, 4.5 x $10^4$ and 7.5 x $10^4$ from left to right respectively [35]

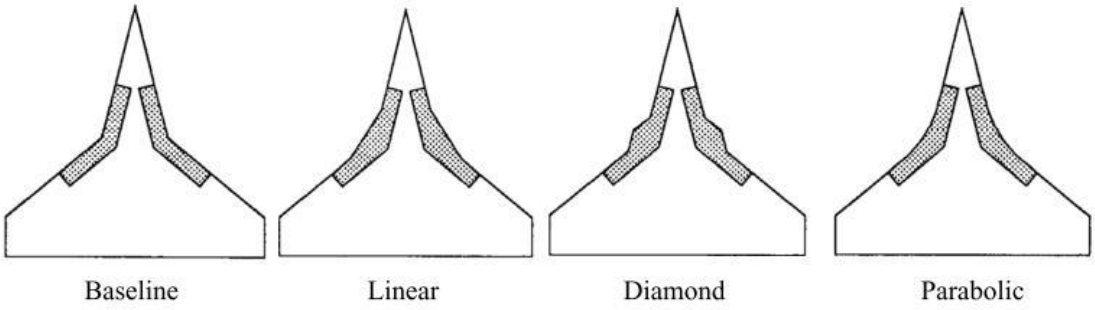


Figure 12. Different kink geometries investigated by Gonzalez et al [27]

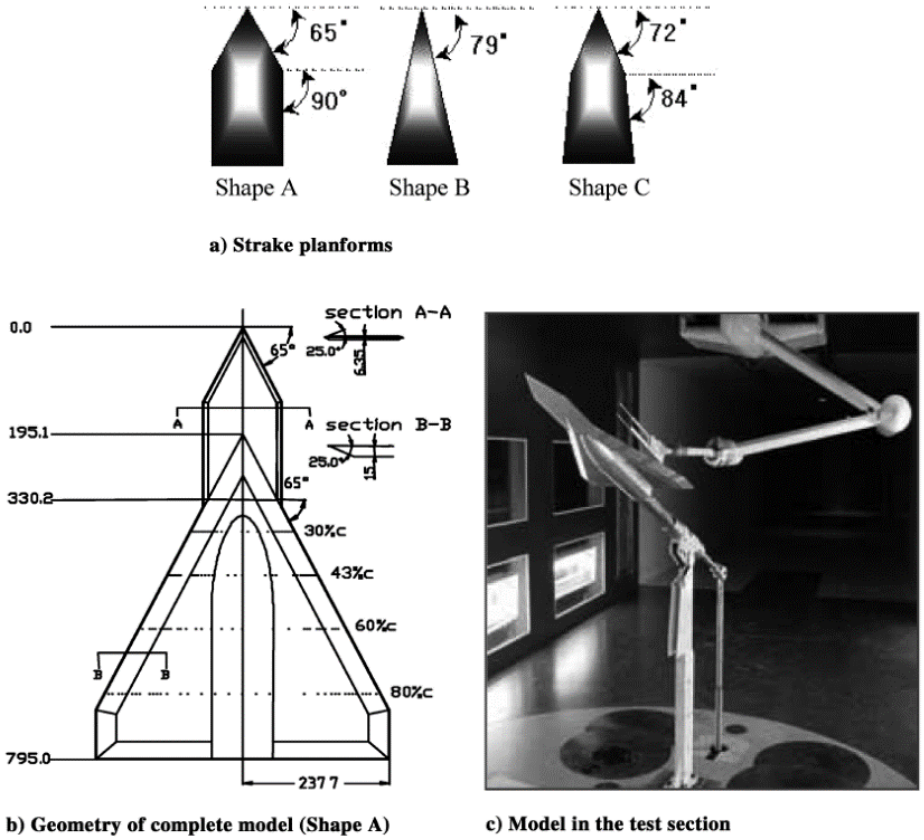


Figure 13. Different strake platforms investigated by Sohn and Chung [4]

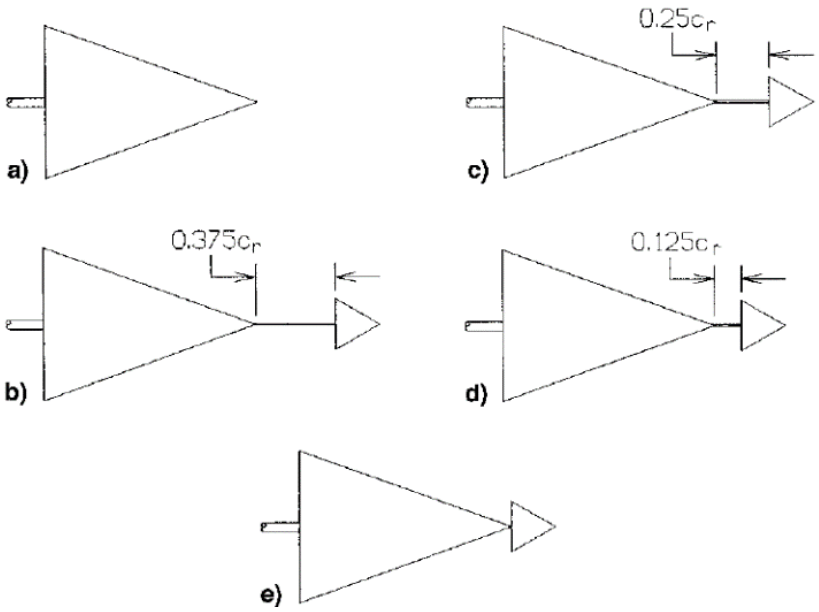


Figure 14. Test model canard configurations: a) no canard, b) canard 0.375Cr forward, c) canard 0.25Cr forward, d) canard 0.125Cr forward, and e) canard 0.0Cr forward [40]

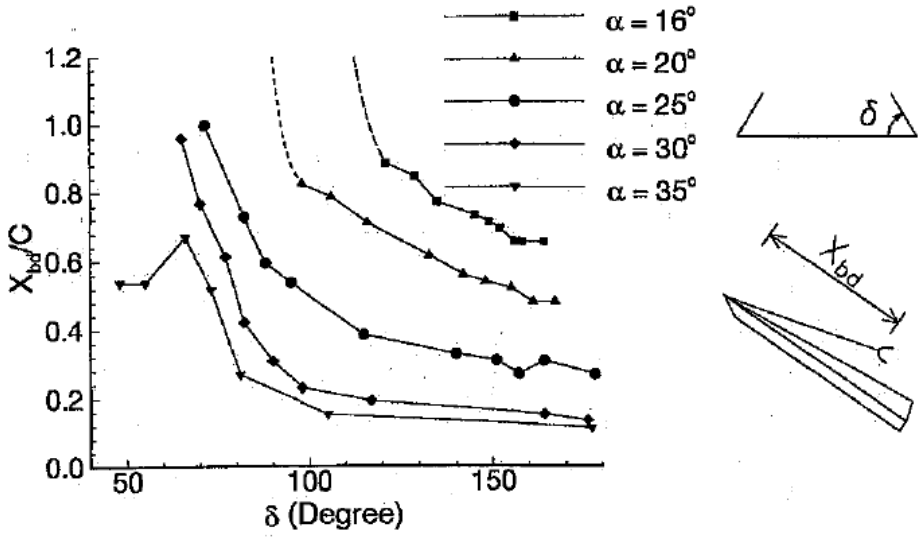


Figure 15. Variation of breakdown location as a function of flap angle for several values of angle of attack [42]

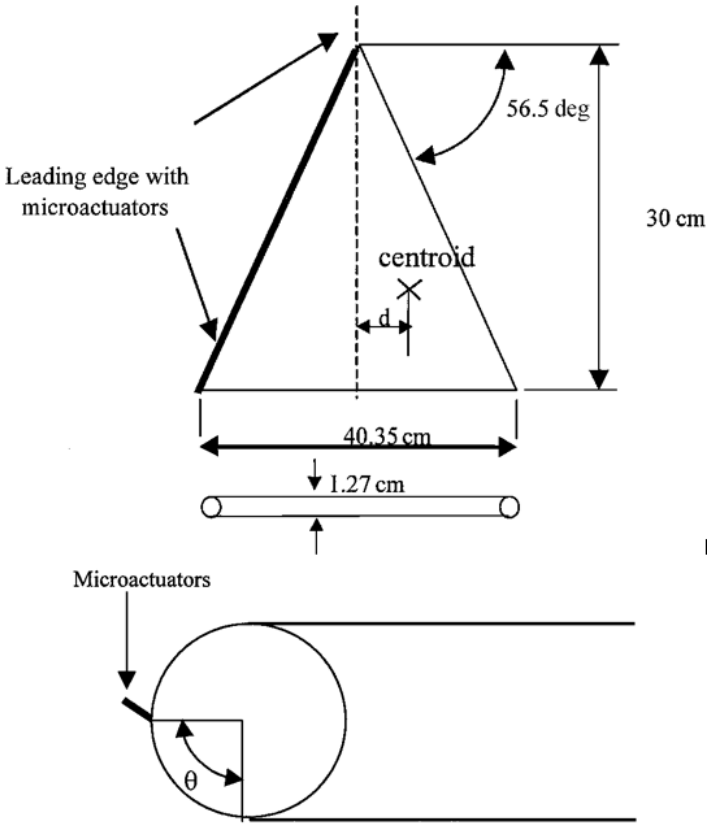


Figure 16. Delta wing model and schematic of microactuators set up on the leading edge used by Lee et al [45]

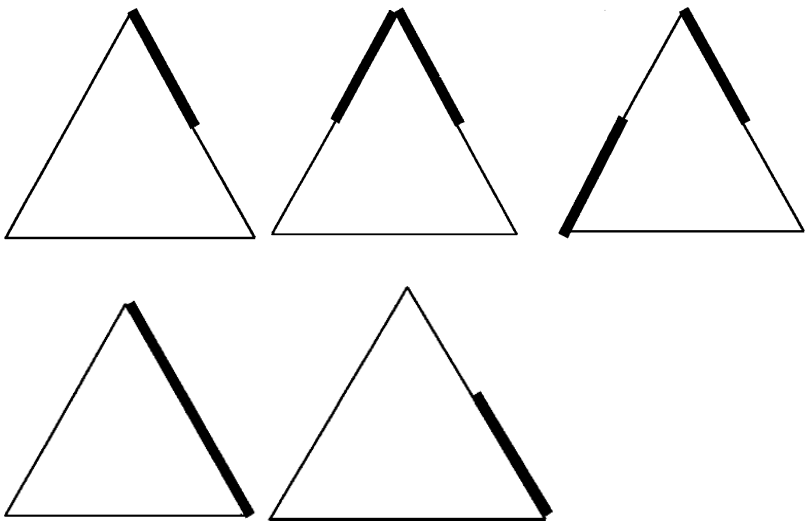

Figure 17. Different configurations of the leading-edge actuator used in the study from Lee et al [45]

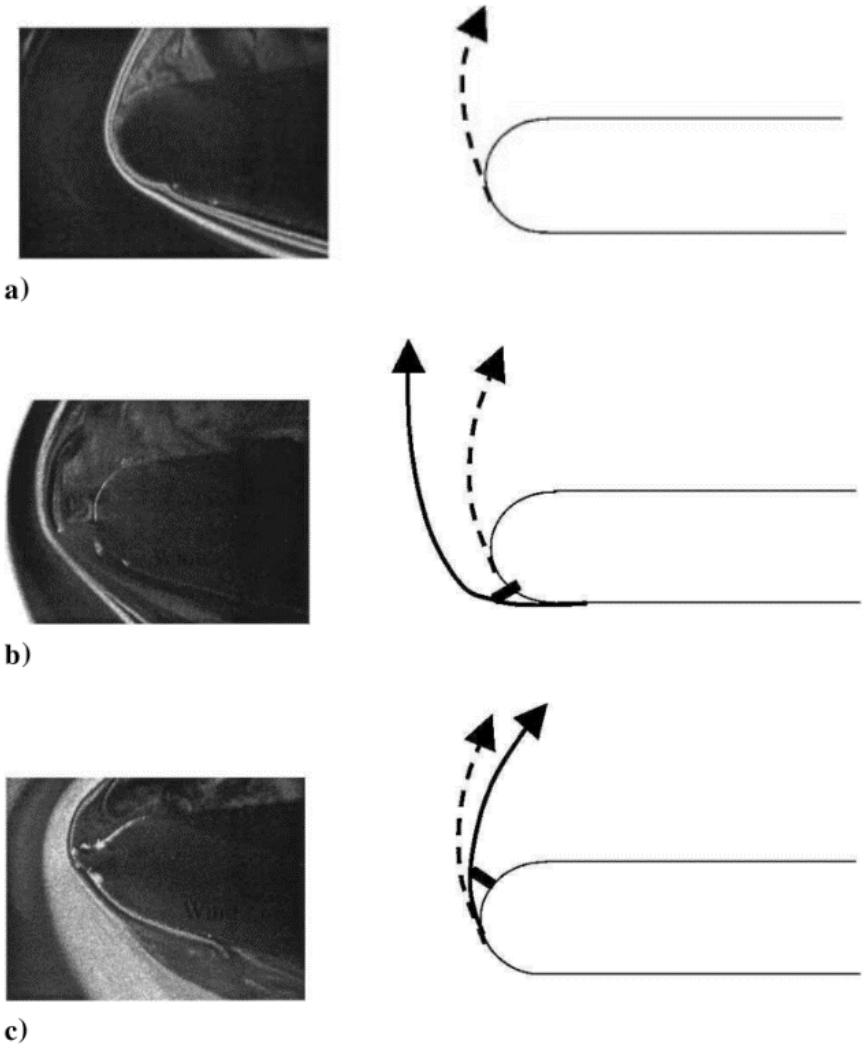


Figure 18. Streakline flow pattern near the leading edge: a) without any actuator, b) with actuators before the original separation line, and c) with actuators downstream of the original separation line. [45]

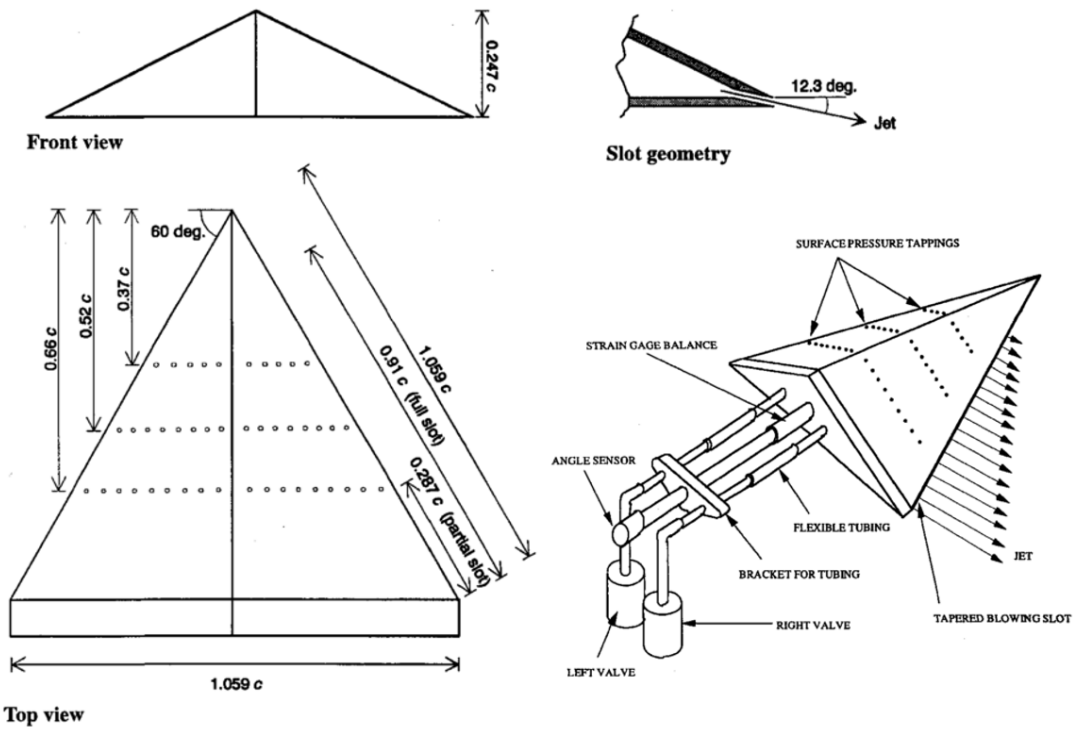


Figure 19. Spanwise leading-edge blowing delta wing model used by Hong et al [48]

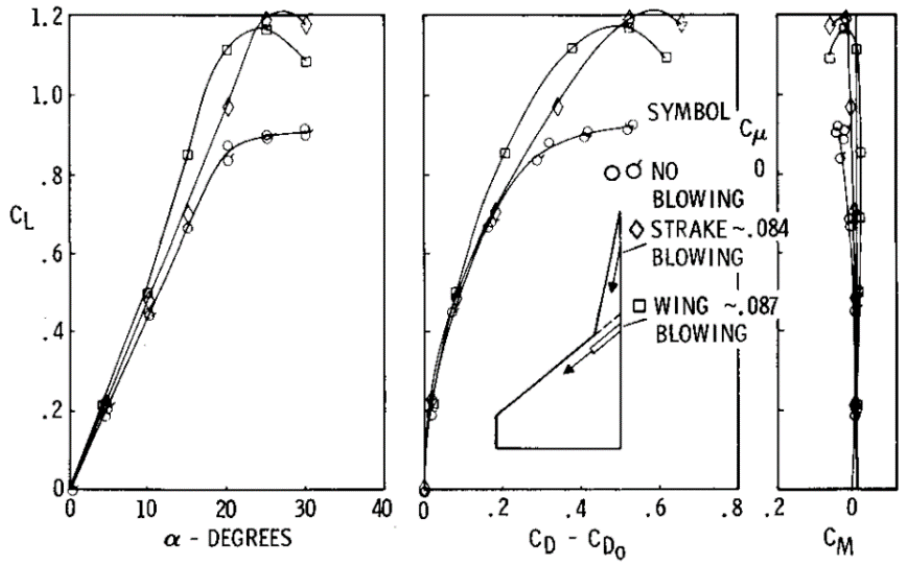


Figure 20. Force measurement results for leading-edge parallel blowing from Bradley et al [51]

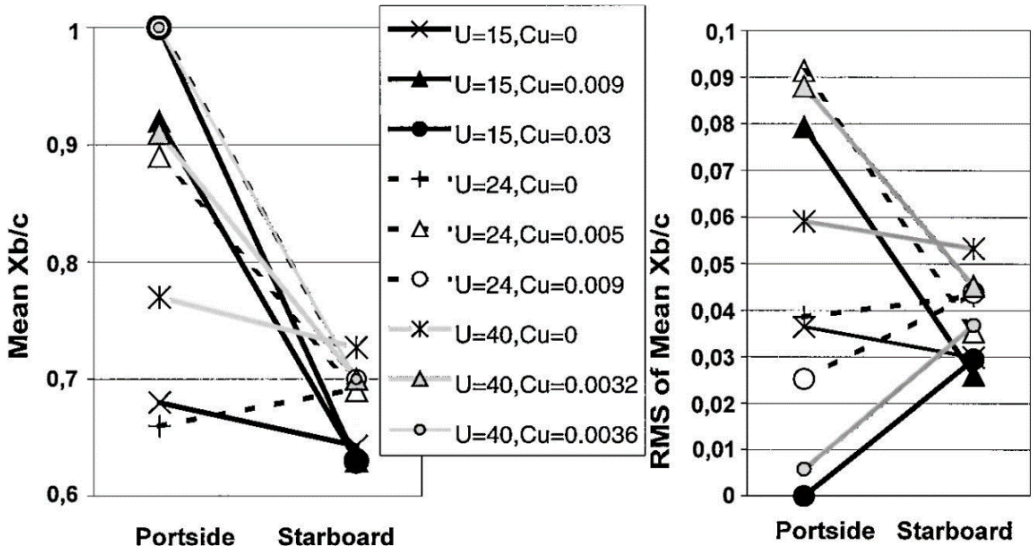


Figure 21. Time-averaged breakdown location and rms values with and without flow control at $\alpha = 27$ deg [52]

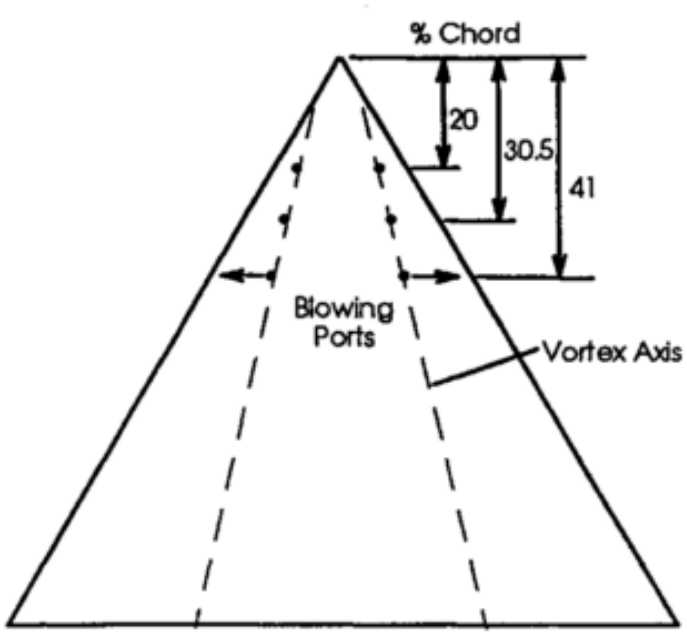


Figure 22. Recessed angled spanwise blowing model investigated by Johari et al [46]

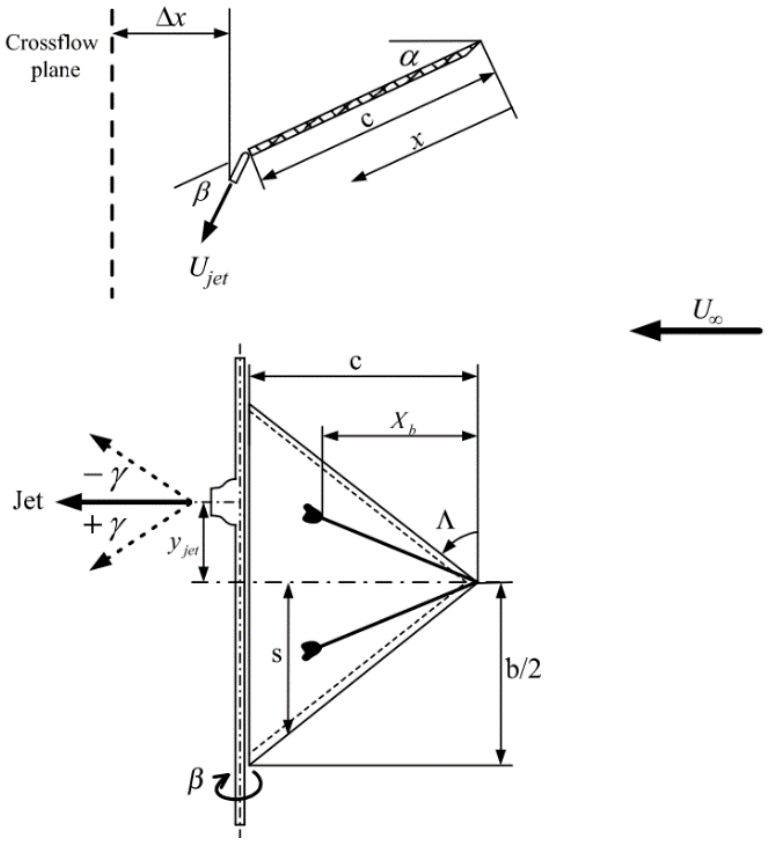


Figure 23. Trailing-edge blowing model investigated by Wang et al [53]

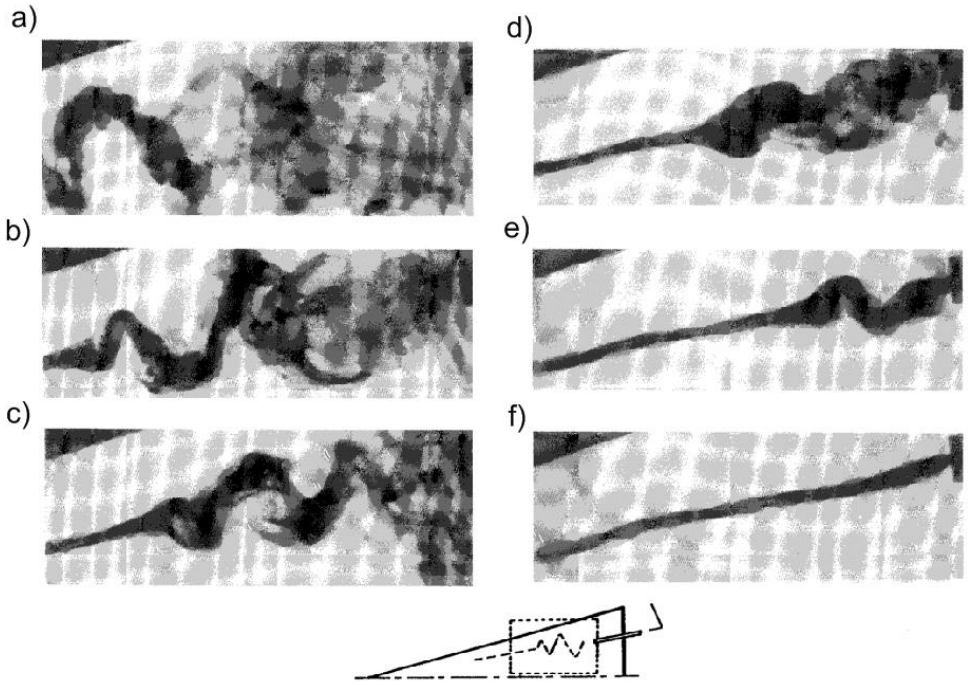


Figure 24. Progression through time of the stabilisation of the broken down vortex using transient suction, investigated by Parmenter and Rockwell [54]

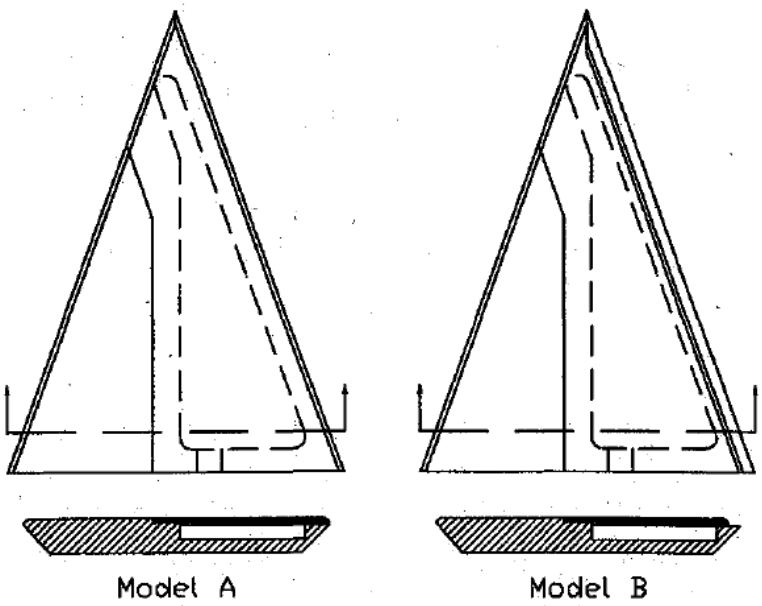


Figure 25. Suction models investigated by McCormick and Gursul [55]

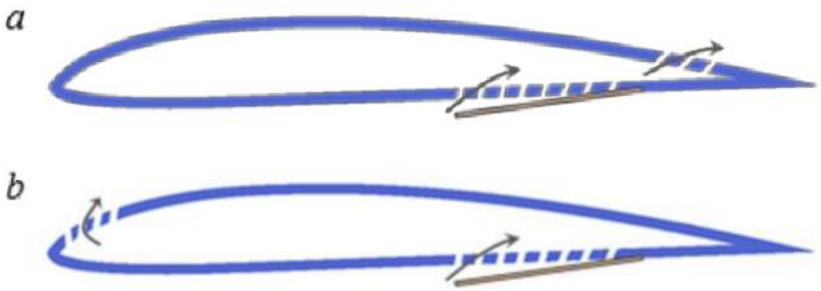


Figure 26. Aerofoil models used by Glezer and Leonard, investigating a) trailing-edge bleed and b) leading-edge bleed [58]

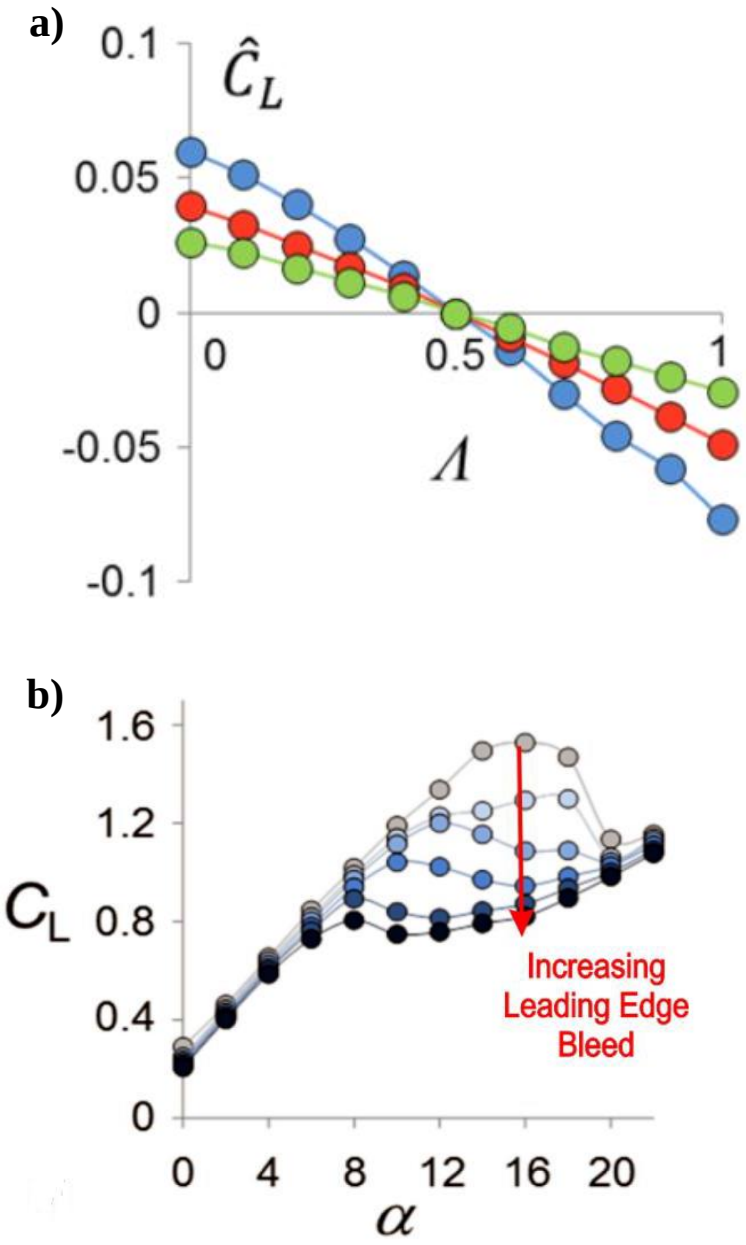


Figure 27. a) Variation of normalised lift with fractional opening of the trailing-edge louvers; α = 4˚ (blue), 8˚(red) and 12˚ (green); b) Variation of lift with angle of attack for different stationary leading-edge louver opening [58]

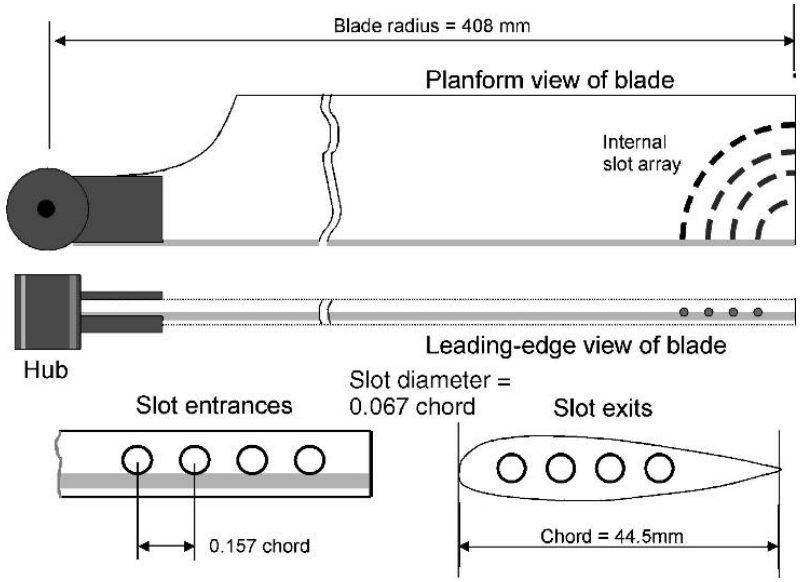


Figure 28. Rotor blade model used by Han and Leishman [59]

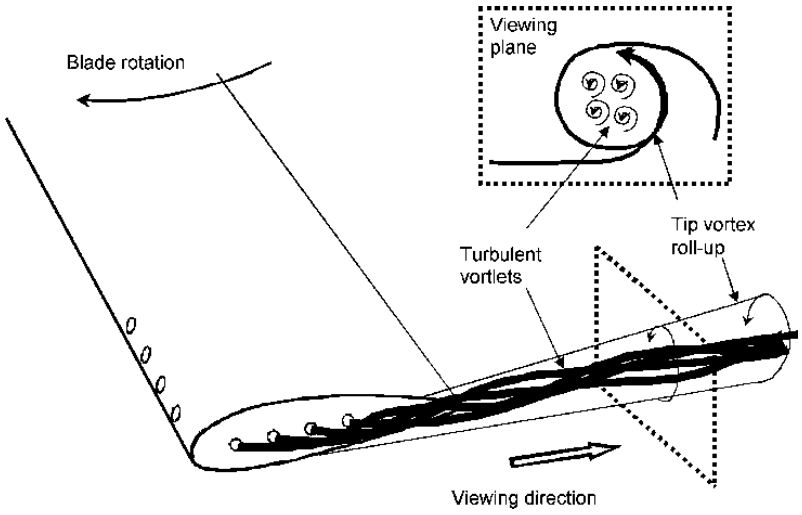


Figure 29. Schematic plot of the bleed flow interacting with the tip vortex [59]

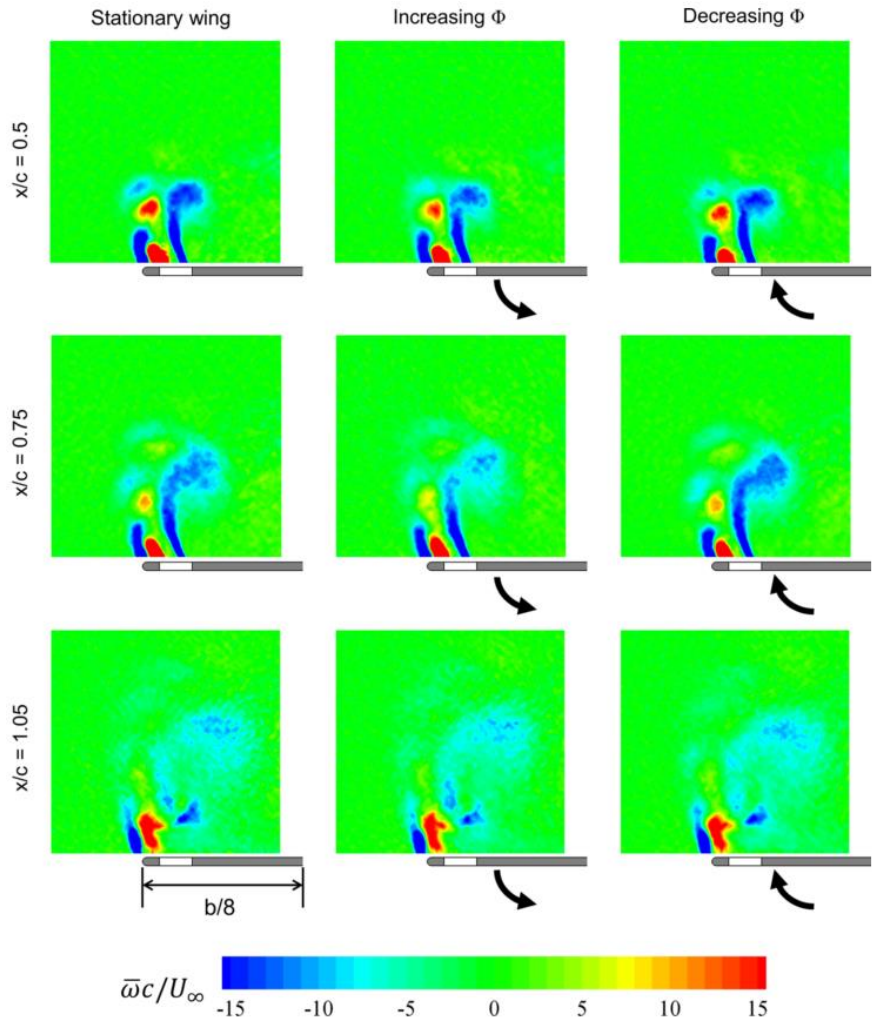


Figure 30. Time and phase averaged vorticity patterns at chordwise locations of x/c = 50%, 75% and 105% for stationary wing, increasing Φ, and decreasing Φ at Φ = 0˚ and α = 17˚ [60]

# CHAPTER 3.

# EXPERIMENTAL METHODOLOGY

## 3.1 Introduction

PIV experiments were carried out on various wing models in both a closed-loop water tunnel and a closed-loop wind tunnel, this section will cover the testing facility and wing models for both the wind tunnel and the water tunnel experiments, then the PIV setup will be described in detail, followed by the data processing method, and uncertainty analysis.

## 3.2 Wind Tunnel Setup and Models

The experiments for the wind tunnel investigation were conducted in a closed-loop wind tunnel facility with a test section of 2.13m × 1.52m × 2.70m, located in the Department of Mechanical Engineering at University of Bath, as shown in Figure 31. The tunnel has a maximum speed of 50 m/s and a freestream turbulence level of less than 0.1% of the freestream velocity. Figure 31 shows the experimental arrangement which includes the layout of the working section and the high-alpha rig. The wing models were attached to the high-alpha rig which allowed the angle of attack to be varied with an accuracy of ±0.25 degrees when the wind tunnel was running. Downstream of the wing model a PIV camera was mounted to the camera support, the mounting bar was connected to the ground and had no direct contact with the wind tunnel ceiling and floor to avoid unwanted vibrations. The blockage for the double delta wing model was approximately 2%. Underneath the model was the PIV laser which illuminated a laser sheet through the clear viewing window at the bottom. The temperature of the wind tunnel facility was measured daily through a thermometer before testing, the accuracy of the thermometer is ±0.25˚C and the drift of the air temperature during each individual testing set was less than 0.5˚C. This minor shift in

temperature resulted in insignificant changes of the viscosity, therefore had negligible impact on Reynolds number.

A double delta wing model with sweep angles of $\Lambda$ =70° and 50° (with the kink at mid-chord, as shown in Figure 32), and a simple slender delta wing model of $\Lambda$ =70° were tested. Both models had a chord length of $c$ = 353.75 mm and a thickness-to-chord ratio of $t/c$ = 2.8%. Both models were manufactured from Aluminium sheet and had a 45˚ bevel on leading edges, thus producing a sharp leading-edge, and a square trailing-edge. The wing models were mounted on the high alpha rig through a sting. The sting was mounted on the pressure surface of the wing models; the suction surface of the wing was flat. The models were painted matt black in order to reduce reflections created from the laser sheet during acquiring the PIV measurements. Experiments were conducted at a constant freestream velocity of $U_\infty$ = 10 m/s, giving a Reynolds number of $Re = 2.34\times10^5$ using the equation (1).

$$Re = \frac{U_\infty c}{\nu} \tag{1}$$

$U_\infty$ is the free-stream velocity and ν is the fluid kinematic viscosity

## 3.3 Water Tunnel Setup and Models

The water tunnel experiments were conducted in a free-surface closed-loop water tunnel (Eidetics Model 1520) located at the University of Bath (shown in Figure 33). The water tunnel has a maximum speed of 0.5 m/s through a closed circuit continuous flow system and has a working section of 0.38m × 0.51m × 0.15m. The turbulence intensity has been measured to be less than 0.5% of the freestream velocity. The tunnel working section has four optical glass viewing windows, three surrounding the working section and one downstream allowing axial viewing. The double delta wing models were mounted upside down in the tunnel using a hollow aerofoil-shaped sting projecting from the pressure surface of the model. The other end of the sting was attached to a mounting plate which was placed on top of the tunnel working section, as displayed in Figure 33. The angle of attack, $\alpha$, was varied by swinging the whole

assembly, including the wing and the mounting plate. The experiments were conducted at a constant freestream velocity of $U_\infty$ = 0.2 m/s, giving a constant Reynolds number of $Re = 2.8\times10^4$. Temperature of the water inside the tunnel was monitored constantly through a measuring device placed downstream of the main testing section and the value was updated real-time to an external display panel. The fluctuation in the water temperature was less than 0.5˚C during each test.

Three double delta wing models with sweep angles of $\Lambda$ =70° and 50° (with the kink at mid-chord, as shown in Figure 34) were used for active and passive flow control investigations. All models had a chord length of $c$ = 140 mm and a thickness-to-chord ratio of $t/c$ = 4.3%. They were manufactured from 6 mm thick Aluminium sheet and had a 45° bevel on leading-edges, thus producing a sharp leading-edge and a square trailing-edge. The maximum blockage was approximately 2%.

The model used for active flow control had four circular chambers machined on the wing upper (suction) surface along the trajectory of the strake vortex, as can be seen in Figure 34a. Circular plastic discs were manufactured to cover these circular chambers. Each plastic disc had a 1 mm diameter blowing hole at the center with a 20° inclined angle to the wing surface. The discs can be rotated to achieve different yaw angle $\beta$ measured from the spanwise axis (Figure 34a). The other side of the blowing chamber was connected to plastic tubes which were located inside the wing upper surface and extended out of the water tunnel through the hollow aerofoil-shaped sting (Figure 33). The tube was then connected to a flowmeter and a pressurized water tank, through which the volumetric flow rate (and hence jet velocity $V_j$) was adjusted. In the present study, the jet blowing momentum coefficient, calculated using equation (2), was kept equal or less than 2%.

$$C_\mu = \frac{\rho V_j^2 A_j}{\frac{1}{2}\rho U_\infty^2 S_w} \tag{2}$$

$A_j$ and $S_w$ denote the cross-sectional area of the jet blowing hole and surface area of the wing, respectively.

The first model used for passive flow control had a 2 mm diameter bleed hole drilled at various spanwise locations ($y_b$ = 2, 4, 6, 8 and 10 mm, or 0.10*s*, 0.21*s*, 0.31*s*, 0.42*s*, 0.52*s*, *'s'* is the local semi span of the wing) at *x/c* = 37.5%, as shown in Figure 34b, where $y_b$ is the distance between the wing centerline and the bleed hole center. The table below summaries all the bleed configurations.

| $y_b$/mm | 2 | 4 | 6 | 8 | 10 |
|---|---|---|---|---|---|
| $y_b$/'s' | 0.10s | 0.21s | 0.31s | 0.42s | 0.52s |
| Hole # | 1 | 2 | 3 | 4 | 5 |

Previous studies [8, 61, 62] suggested that, at low and moderate angles of attack, the maximum pressure difference between the lower and upper surfaces of the delta or double delta wings is around $\Delta C_P$ = 1. In this thesis, it was assumed that the velocity on the lower wing surface at bleed hole entrance is approximately the freestream velocity. Using the Bernoulli equation, the bleed velocity was estimated using equation (3),

$$\frac{U_B}{U_\infty} = \sqrt{1 + \Delta C_p} \tag{3}$$

The momentum coefficient of the bleed was therefore very roughly estimated to be on the order of $C_\mu$ = 0.1%. The second model used for passive flow control had a 10 mm bleed slot machined at x/c = 37.5%, as shown in Figure 34c.

## 3.4 Particle Image Velocimetry (PIV) Measurements

Particle Image Velocimetry (PIV) is an advanced technique for measuring the velocity of the flow fields using laser and high-speed camera. This experimental technique requires the flow to be seeded with micro-sized particles, then the interested plane will be illuminated using the laser which is synchronised with the high-speed camera. The instantaneous velocities of the flow field will be calculated by the displacements of the particles captured from two images that have very short time

interval Δt in between, furthermore, time-averaged analysis can also be performed using multiple pairs of images. Following the methods from Prasad [63], the equation below can be used to check if the particle size is suitable for the particular application by calculating the settling velocity of the particle:

$$u_s = \frac{g d_p^2 (\rho_p - \rho)}{18\mu} \tag{4}$$

Where $d_p$ is the particle diameter, g is the gravitational acceleration, μ is the dynamic viscosity, and $\rho_p$ and ρ are the particle and fluid density respectively.

For the wind tunnel test, velocity measurements at various crossflow planes (*x/c* = 25% - 1) over the double delta wing model and simple slender delta wing model were performed using a TSI 2D PIV system. The flow was seeded with olive oil droplets produced by a TSI model 9307-6 multi-jet atomizer. The mean size of the olive oil droplets was estimated to be 1 μm, which gives a settling velocity of 2.6 x $10^{-5}$ m/s, this is negligible when comparing with the free stream velocity. Illumination of the desired plane was achieved using dual 120 mJ Nd:YAG (Neodymium: Yttrium Aluminium Garnet) lasers. The laser sheets (with a thickness of 2 mm) were placed perpendicular to the freestream (see Figure 31). The images were captured using a TSI PowerView Plus 12bit CCD camera with a resolution of 2048×2048 pixels from a downstream location. The camera was mounted on a camera support that was independent of the working section of the tunnel, so there was minimum vibration during image capture. A TSI LaserPulse synchroniser unit was utilised to link the camera and the laser to enable accurate capture for the two frame cross-correlation analysis. The system was operated at a sampling frequency of 3.75 Hz in the cross-correlation mode. The commercial software package Insight 3G and a Hart cross-correlation algorithm were used to analyse the images. For the image processing, an interrogation window size of 24 x 24 pixels was used, thus producing velocity vectors for further processing. The effective grid size was around 1.0-1.5 mm. For each case, sequences of 2000 instantaneous frames were taken, and the time-averaged velocity and vorticity fields were calculated.

For the water tunnel test, velocity measurements were also taken using a TSI 2D PIV system. The water flow was seeded with hollow glass spheres with diameters in the range of 8 μm to 12μm, which give a settling velocity of $u_s$ = 1.5 x $10^{-6}$ m/s to 10.2 x $10^{-6}$ m/s, this is significantly smaller than the free stream velocity 0.2 m/s. The measurement plane was illuminated through the optical glass on the side of the water tunnel test section by a laser sheet (with a thickness of around 2 mm) generated from a dual 120 mJ Nd:YAG laser (Figure 33). The images were captured using a TSI PowerView Plus 12bit CCD camera with a resolution of 2048×2048 pixels through an optical viewing glass at a downstream location of the test section. A TSI LaserPulse synchroniser unit (TSI Model 610034) was used to synchronise the camera and the laser for the accurate capture of the crossflow images. The system was operated at a sampling frequency of 3.75 Hz in the cross-correlation mode. The commercial software package Insight 4G and a Hart cross-correlation algorithm were used to analyse the images. For the image processing, an interrogation window size of 24 x 24 pixels was used to produce velocity vectors for further processing. The effective grid size was between 1.0 – 1.5 mm (0.7%*c* – 1.1%*c*), depending on the chordwise location of the measurement plane. For each measurement, sequences of 700 instantaneous frames were taken, and the time averaged velocity and vorticity fields were calculated.

## 3.5 Data Processing

As mentioned earlier, the x and y component of the velocities are calculated by the displacement of the particles between two snapshots, as follow:

$$u = \frac{\Delta x}{\Delta t} \tag{5}$$

$$v = \frac{\Delta y}{\Delta t} \tag{6}$$

Where u and v are the velocity components in x and y directions, and Δx and Δy are the displacements in the x and y directions, Δt is the time interval between the image pairs of the PIV settings.

After obtaining the velocity data for each point on the 2-D plane, the next step is to calculate vorticity and circulation from the velocity data, vorticity and circulation are very closely related parameters and they are both important measures of rotational flow. On a three-dimensional space, the angular velocity of a fluid element can be described in Cartesian coordinates using equation (7) [11]:

$$\omega = \frac{1}{2}\left[\left(\frac{\partial w}{\partial y} - \frac{\partial v}{\partial z}\right)i + \left(\frac{\partial u}{\partial z} - \frac{\partial w}{\partial x}\right)j + \left(\frac{\partial v}{\partial x} - \frac{\partial u}{\partial y}\right)k\right] \quad (7)$$

In equation (7), u, v and w are the velocity components in the x, y and z directions. After angular velocities of the fluid element are obtained, vorticity is simply twice the angular velocity, as shown on equation (8):

$$\xi = 2\omega = \nabla \times V \quad (8)$$

The vorticity is then normalised using either chord length or local semi span and freestream velocity, as seen on equation (9) and (10). Please note, in this thesis '$\omega$' indicates vorticity instead of angular velocity.

$$\frac{\omega_x \cdot c}{U_\infty} \quad (9)$$

$$\frac{\omega_x \cdot s}{U_\infty} \quad (10)$$

Where c and s are chord length and local semi span respectively. Vorticity is a measure of the angular velocity or rotation of a fluid element, ie. at microscopic level. To describe the rotation of the flow in a macroscopic level, circulation is introduced. The circulation about a region is equal to the vorticity integrated over any open surface bounded by this region. For example, Figure 35 shows a three-dimensional surface area S bounded by the closed curve C. Assume that the surface is in a flow field and the velocity at point P is V, where P is any point on the surface (including any point on curve C), then:

$$\Gamma \equiv -\oint_C V \cdot ds = -\iint_S (\nabla \times V) \cdot dS \tag{11}$$

Therefore, the circulation of a region is vorticity integrated within the region. In this investigation, for each cross flow plane, circulation was calculated for the whole plane and then normalised by the chord length and freestream velocity, as shown on equation (12).

$$\frac{\Gamma}{U_\infty c} \tag{12}$$

The next important parameter to calculate in this investigation is the velocity magnitude. The velocity magnitude is calculated using equation (13):

$$U_{mag} = \sqrt{u^2 + v^2} \tag{13}$$

The standard deviation of the velocity fluctuation can also be obtained from the velocity magnitude:

$$U_{std} = \sqrt{\frac{\sum(U_{mag} - \overline{U_{mag}})^2}{N}} \tag{14}$$

In this investigation, both the velocity magnitude and standard deviation are normalised by the freestream velocity as follow:

$$\frac{U_{mag}}{U_\infty} \tag{15}$$

$$\frac{U_{std}}{U_\infty} \tag{16}$$

Other quantities such as vortex meandering amplitude, meandering probability and vortex centroid location are also calculated, their detailed derivation methods will be introduced in later chapters. However, all of them require the information of the

location of the vortex centre. In this study, vortex centre location in the cross flow plane is obtained using vortex detection methods [64, 65], by simply finding the maximum vorticity magnitude point within the vortex region.

## 3.6 Uncertainty Analysis

Although effort has been put into minimising the experimental uncertainties, certain level of uncertainty will always be present. The main source of uncertainty exists in the calculations associated with the momentum coefficient and the model measurement error. The method for evaluating uncertainties of relevant quantities were calculated based on the method from Moffat [66, 67]. It combines all the sources of uncertainty to obtain a value so that if the experiment were repeated, the confidence level would be 95%. From Moffat's study:

$$\delta R = \left\{\left(\frac{\partial R}{\partial x_1}\delta x_1\right)^2 + \left(\frac{\partial R}{\partial x_2}\delta x_2\right)^2 + \cdots \left(\frac{\partial R}{\partial x_n}\delta x_n\right)^2\right\}^{\frac{1}{2}} \tag{17}$$

When R, the desired quantity, is in the following form:

$$R = x_1^a x_2^b x_3^c \cdots, \tag{18}$$

The equation can be written as follow:

$$\frac{\delta R}{R} = \left\{\left(a\frac{\delta x_1}{x_1}\right)^2 + \left(b\frac{\delta x_2}{x_2}\right)^2 + \cdots \left(c\frac{\delta x_n}{x_n}\right)^2\right\}^{\frac{1}{2}} \tag{19}$$

### 3.6.1 Momentum Coefficient

Recall the equation (2) for calculating the momentum coefficient. As mentioned earlier, the blowing fluid is supplied from a pressurised water tank through a flowmeter to achieve desired flowrate. In this investigation, in order to match the PIV particle

seeding density, the water in the pressurised tank is drawn from the seeded freestream fluid, therefore $\rho_j$ and $\rho$ are equal. To estimate the uncertainty of the momentum coefficient, the uncertainties associated with $V_j$, $A_j$, $U_\infty$ and $S_w$ need to be targeted individually. However, since $V_j$ and $A_j$ are correlated as follow:

$$V_j = \frac{Q}{A_j} \tag{20}$$

Where Q is the volume flowrate, therefore the uncertainty of $V_j$ can be estimated using the uncertainty of volume flowrate Q and blowing hole area $A_j$.

The uncertainty of $A_j$, the cross-sectional area of the blowing hole, is induced from the measurement uncertainty when measuring the diameter of the blowing hole using a digital caliper. The blowing hole diameter, d, can be realistically measured to a resolution of 1 x $10^{-2}$ mm, which gives an uncertainty of $\delta d$ = 5 x $10^{-6}$ m.

Since

$$A_j = (\frac{d}{2})^2 \times \pi \tag{21}$$

$$\Rightarrow \frac{\delta A_j}{A_j} = 2 \times \frac{\delta d}{d} = 1\%$$

To estimate the uncertainty of $V_j$, the velocity of the blowing jet, it needs to be first written in terms of flowrate Q, and blowing hole cross sectional area $A_j$. The unit displayed on the flowmeter is CCM, which is cubic centimetre per minute; and the minimum increment on the flowmeter is 10ccm, hence it results in an uncertainty of 5ccm (or 8.33 x $10^{-8}$ $m^3$/s).

$$V_j = \frac{Q}{A_j} = Q \times (\frac{d}{2})^{-2} \times \pi^{-1}$$

Therefore

$$\frac{\delta V_j}{V_j} = 3.13\% \text{ for } C_\mu = 2\%;$$

and

$$\frac{\delta V_j}{V_j} = 5.23\% \text{ for } C_\mu = 0.5\%;$$

For the freestream velocity uncertainty, Cleaver [68] calibrated the freestream velocity to a water tunnel frequency setting, and calculated the associated uncertainty to be 1 x $10^{-3}$ m/s.

$$\text{Thus, } \frac{\delta U_\infty}{U_\infty} = 0.5\%$$

The uncertainty of the wing surface area is from the measurement uncertainty of the dimensions of the double delta wing model using a scientific ruler, which has an uncertainty of $\delta d$ = 5 x $10^{-3}$ m. After combining all the measurement uncertainties, the uncertainty of the wing surface area is estimated to be:

$$\frac{\delta S_w}{S_w} = 0.94\%$$

By combining all the uncertainties together, the uncertainty for the blowing momentum coefficient is estimated to be 5.50% ~ 10.00% depending on the value of momentum coefficient.

### 3.6.2 PIV Measurements

A PIV experiment requires the following components: PIV particle seeded flow, optically transparent test section, PIV laser, PIV camera and special purposed computer with analysing software [63]. Among them, the main sources of uncertainty arise in the PIV particle selection, PIV camera and analysing method.

With regards to the particle selection, the main varying parameters are particle size and seeding density. A suitable PIV particles must satisfy two requirements: 1) they should be able to follow the flow streamlines without excessive slip, and 2) they should

be efficient scatterers of the illuminating laser light [63]. As mentioned earlier in equation (4), the first requirement relates to the settling velocity of the particle, it needs to be significantly smaller than the freestream velocity in order to eliminate interference with the flow field, this sets the limit for the particle diameter. In this investigation, naturally buoyant TSI hollow glass spheres with 8μm mean diameter were selected for the water tunnel test. Whereas for the wind tunnel test, olive oil droplets are used as the seeding particle for the flow, due to the density difference between oil and the flow, the mean diameter of the droplets used were at 1μm. Apart from the particle size, another important parameter is the number of the particles per interrogation window (or PIV seeding density), it is crucial for capturing quality PIV data. Insufficient particles could increase the number of bad vectors and errors. Keane and Adrian [69] showed that the accuracy of the captured data increases as the number of particles increases, however, very high seeding density could result into over-exposed images and increased difficulties for the computer algorithm to identify each particle. Moreover, extremely high seeding density could also potentially alter the characteristics of the flow. In this study, in order to achieve the optimum seeding density and uniformly distributed flow, 1 $cm^3$ of hollow glass particles was mixed with 3 litres of water and then poured into the water tunnel. Before each test, the water tunnel was allowed to run 15 minutes without test rig, in order to achieve uniformly distributed seeding density. For the wind tunnel test, the oil droplets were released through a bended tube upstream of the test rig, it covers the whole span of the cross section and allows the particles to be uniformly distributed when reaching the testing area.

For the PIV camera setup, the user's experience will have significant impact on the level of errors induced. The consistent alignment of the camera with the crossflow plane throughout the test, the choice of lens and aperture stop are crucial for obtaining high quality data. To ensure that the camera axis is perpendicular to the laser sheet, sample PIV images were taken before the test in order to examine the out of focus particles. If the camera and the laser sheet are misaligned, part of the PIV image will display out of focus particles. The choice of lens varies between the water tunnel and wind tunnel tests, depends on the area of interest, appropriate lens was chosen for different tests which result in desired image size. The lens aperture affects the lighting condition and the depth of field of the image, the lower the f-stop (equivalent to wider

aperture), more light can reach the sensor and thinner depth of field can be achieved. Thinner depth of field can ensure that particles before and after the laser sheet will not be focused, however, it needs to be equal or slightly wider than the thickness of the laser sheet. Marles [70] pointed out that one of the contributors of the errors within PIV measurements is the out of plane motion of the seeding particles. For capturing the particles in a crossflow plane, the camera is placed at a downstream viewing window and centred around the crossflow plane centre. Therefore, as the particles travel through the laser sheet thickness and move out of the plane, the PIV system will capture a radial velocity which is zero in the middle of the PIV image, but increasing towards the edge of the field of view. Marles also carried out investigation to determine the PIV measurement error at the most extreme level of field of view, which resulted in 5% of the free stream velocity. Considering that in this investigation, the window size used to generate velocity vectors were mainly occupying about 40% of the field of view at the centre of the frame, the PIV error in this case is estimated to be 2% of the freestream velocity.

The last component within the PIV system is the computer and analysing software. After the correct setup of the PIV system, the output PIV images might still contain bad vectors. The so-called bad vectors (also referred to as false or spurious vectors) are readily identifiable when the vector field is replotted after subtracting the mean; bad vectors have magnitudes and/or directions which are substantially different from their neighbours [63]. In this investigation, the number of bad vectors were typically less than 0.3% of the total numbers of vectors.

## 3.7 Figures

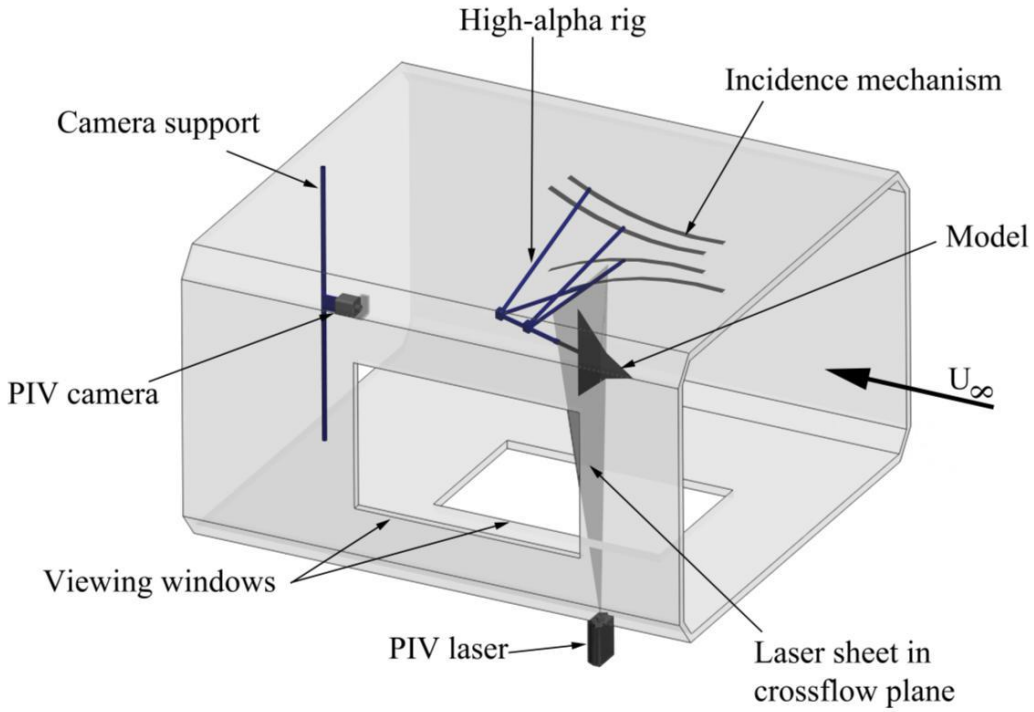


Figure 31. Wind tunnel experimental setup

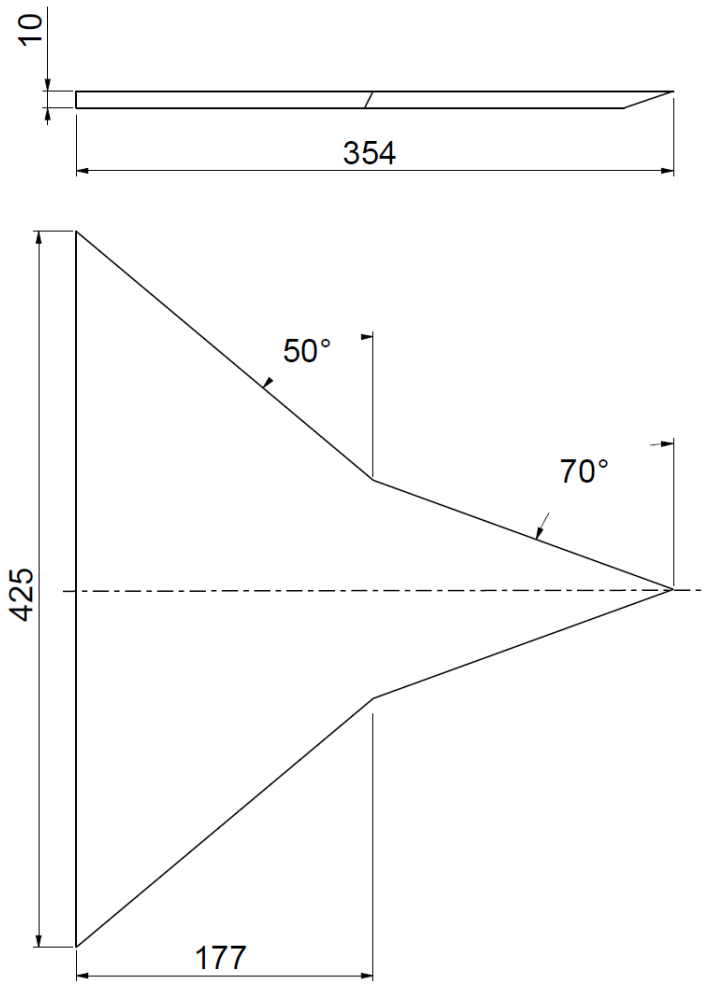


Figure 32. Drawing of the double delta wing

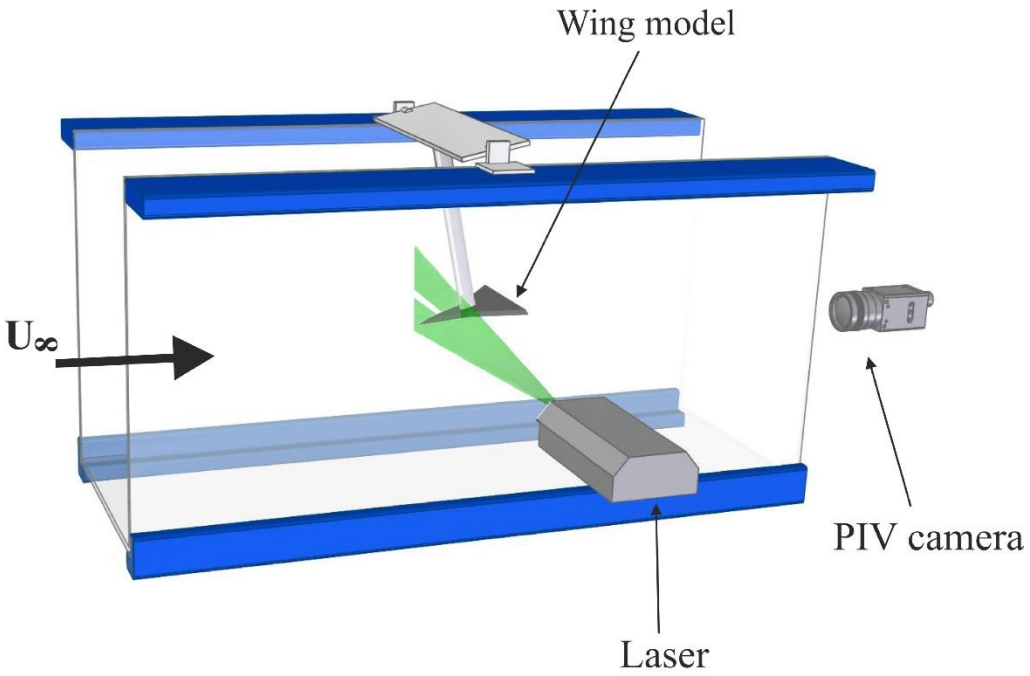


Figure 33. Water tunnel setup

a)

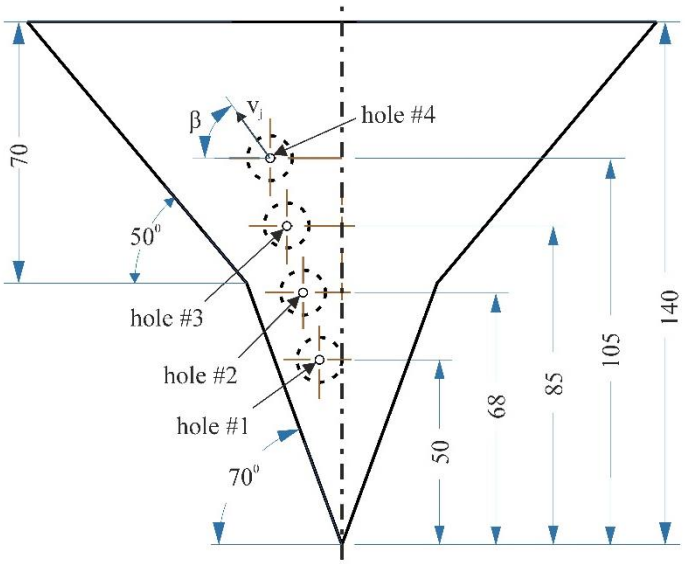


b)

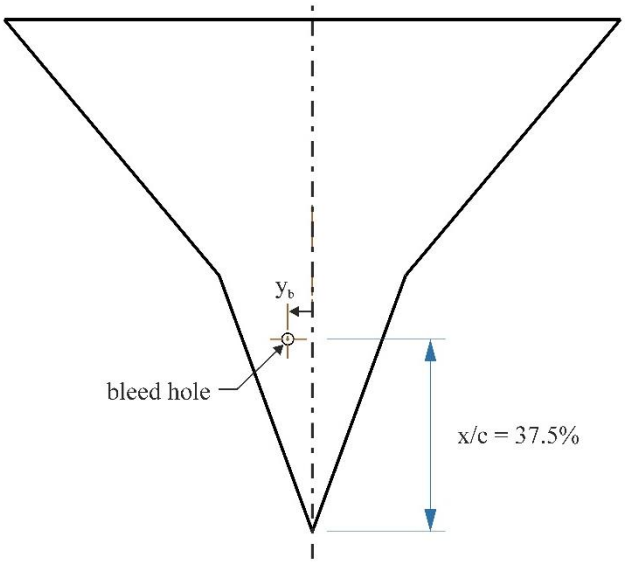


Figure 34. Drawing of a) blowing model; b) bleed model with bleed holes and c) bleed model with bleed slot.

c)

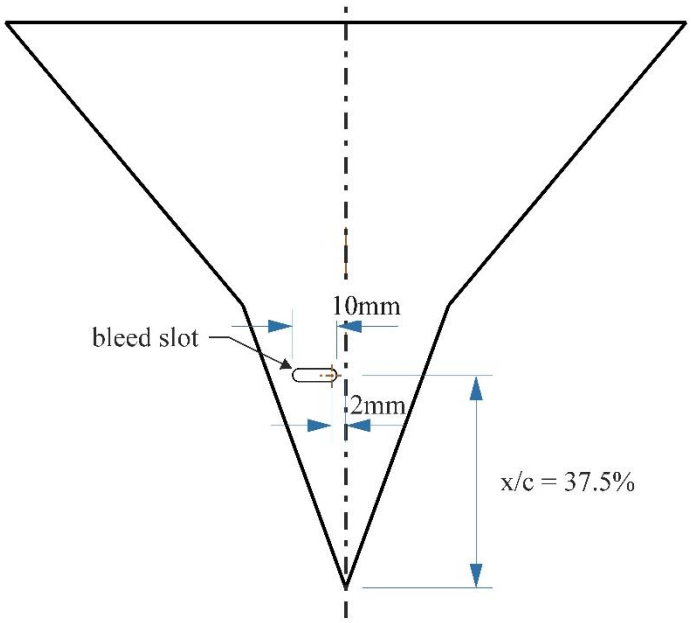


Figure 34. Continued

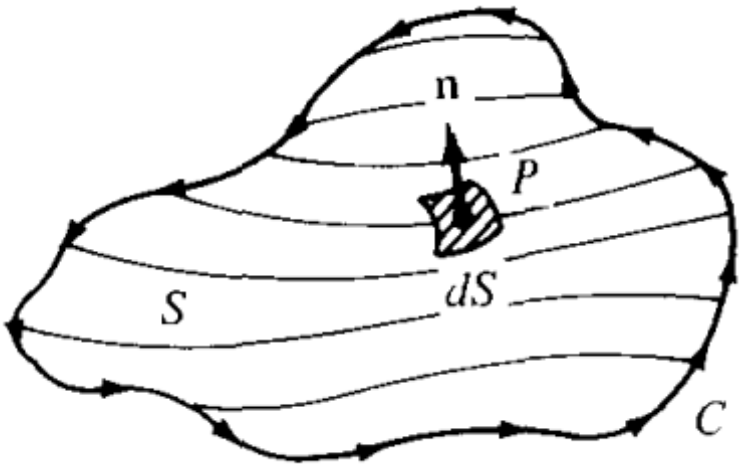


Figure 35. Three-dimensional surface area S bounded by the closed curve C [11]

# CHAPTER 4.

# EFFECT OF ANGLE OF ATTACK

## 4.1 Summary

Experiments were carried out in a closed-loop wind tunnel to investigate the effect of angle of attack on the vortical flow over a 70º/50º double delta wing, with kink at 50% chord. PIV measurements were taken at various chordwise locations for angles of attack from $4^0$ to $32^0$.

The time-averaged vorticity field displayed a very distinctive 'dual-vortex' structure at the double delta wing kink for the whole range of angles of attack tested, however such vortical structure was not observed over simple delta wing, which suggested that there was an upstream effect of the wing vortices on the formation of the strake vortices.

The rotational angle between the wing and strake vortices was small initially, but it became larger with downstream distance, at an increasing rate as angle of attack increases. The meandering properties of the vortices were also analysed from the instantaneous flow fields. The meandering probability results showed that prior to vortex breakdown, both wing and strake vortices were found meandering in relatively small regions. The normalised vortex meandering amplitude results also confirmed the findings from the probability plots. Coefficient of correlation showed generally low correlation between the displacements of the strake and wing vortices in both vertical and horizontal directions.

The proper orthogonal decomposition (POD) analysis of the instantaneous velocity fields suggested that, for both wing and strake vortices, the most energetic mode was the first helical mode, representing the displacement of the vortex core. The most energetic mode reveals out-of-phase displacements when the vortices are close to each other.

## 4.2 Results and Discussion

### 4.2.1 Time-averaged Flow

Time-averaged crossflow vorticity patterns over the double delta wing at various chordwise locations and wing incidences are present in Figure 36. In this figure, the vorticity is normalised by the local semi-span and the freestream velocity. The reason for this choice is that the vorticity magnitude varies substantially with the chordwise distance. (For example, for a conical vortex, it varies with the inverse of chordwise distance from the apex). Therefore, if a fixed length scale such as chord length is used to nondimensionalise, it becomes difficult to display variations near the trailing-edge. At $\alpha = 4^{o}$, both strake and wing vortices form near the wing surface. With increasing angle of attack, the strake and wing vortices move away from the wing surface and become stronger. Vortex breakdown of both strake vortex and wing vortex are observed at the trailing-edge of the double delta wing at $\alpha = 12^{o}$ (Figure 36c). The onset of vortex breakdown moves upstream as the angle of attack is increased (Figures 36d-h). It is noted that the strake vortex breaks down first. This observation is different from the case reported in [8] for a $76^{o}/40^{o}$ double delta wing, where the wing vortex breaks down first. This may be due to the lower sweep angle of the wing and larger difference between the wing and strake sweep angles in [8]. It is clear from Figure 36 that the strake and wing vortices interact and coil-up. When the vortices merge, there is also breakdown (this is best illustrated for $\alpha = 12^{o}$ and $\alpha = 16^{o}$ near the trailing-edge).

It is observed that, at x/c = 50% (kink location of the double delta wing), the vorticity pattern exhibits a 'dual-vortex' structure. This is somewhat surprising, given that the wing vortex has not yet developed at this chordwise location. In order to understand the flow physics behind the dual-vortex structure observed over the double delta wing model and also for comparison, PIV measurements over the simple slender delta wing were conducted at x/c = 50%. Figure 37 presents the time-averaged crossflow vorticity patterns over the double delta wing and the simple delta wing at various angles of attack at the fixed station of x/c = 50%. In this figure and in the rest of the chapter, the vorticity is nondimensionalised by the chord length as the comparisons were made for the same cross-flow planes. It can be seen that, up to $\alpha = 28^{o}$, as wing incidence is increased, the vortices over double delta wing and the

leading-edge vortex over simple delta wing move away from the wing surface and gain strength (Figures 37a-f). However, at $\alpha = 28^{o}$ and $32^{o}$ (Figures 37g & 37h), vortex breakdown of the strake vortex over double delta wing is observed, which results in a dramatic decrease of the vorticity magnitude and the loss of coherent vortical structure. Vortex breakdown is however not observed over the simple delta wing model. For all angles of attack tested, the vortex over the simple delta wing is closer to the wing surface. Even at $\alpha = 4^{o}$ for the double delta wing, the 'dual-vortex' structure is visible. With increasing angle of attack up to $\alpha = 24^{o}$, the two vortices move away from the surface while rotating about each other. However, it appears that the two vortices merge immediately as there is only one vortex at x/c = 62.5% (see Figure 36). The two vortices observed at x/c =50% for up to $\alpha = 24^{o}$ eventually merge at higher wing incidences (Figures 37g & 37h), and exhibit breakdown. The dual-vortex structure is absent for all incidences for the simple delta wing. The dual-vortex structure as well as the major difference in the location of the vortices between the double delta wing and simple delta wing suggest that the wing vortices over the double delta wing have upstream effect on the formation of the strake vortices.

Returning to the time-averaged flow shown in Figure 36, the early stages of the interaction of the strake and wing vortices (between x/c = 62.5% and 75%) reveal a relatively small increase in the rotation angle between the two vortices. This is shown more clearly in Figure 38, where the crossflow streamline patterns over the double delta wing at x/c = 62.5% and x/c = 75% are presented. The definition of the rotation angle is sketched in this figure. It is noted that the rotation angle does not appear to be sensitive to angle of attack at early stages. Although both vortices move away from the wing surface with increasing angle of attack, the relative positions of the vortices do not vary much with angle of attack. This is different than the co-rotating trailing vortices for which the rotation rate is expected to increase linearly with the strength of the vortices [71]. It is observed that, for all angles of attack tested, the wing vortex is slightly closer to the wing surface at x/c = 62.5%. At x/c = 75%, however, the wing vortex moves away from the wing surface and also becomes closer to the strake vortex. Note that, at $\alpha = 28^{o}$ and x/c = 75% (Figure 38f), both vortices have broken down, as evidenced by the vorticity patterns (Figure 36g), and this is also reflected in the streamlines spiralling out from the vortex axis.

With increasing chordwise distance, it appears that the rotation angle increases faster (see Figure 36). Also, the interaction at x/c = 87.5% is more sensitive to angle of attack (see Figure 36). This is best seen by comparing the time-averaged vorticity fields at $\alpha$ = 8, 12º, 16º, 20º, 24º, and 28º in Figure 39. The wing vortex and strake vortex rapidly rotate around each other with increasing angle of attack. This faster increase of rotation angle with distance and vortex strength (due to incidence) is similar to the 'convective stage' described for the co rotating trailing vortices [71]. However, a direct comparison is not possible due to the varying strength and separation between the vortices with the chordwise distance as well as the orientation of the vortex filaments over the double delta wing.

### 4.2.2 Unsteady Aspects

Figure 40 presents the standard deviation of crossflow velocity fluctuations over the double delta wing at various chordwise locations and wing incidences. It is observed that, for all the angles of attack tested, the peak standard deviation for both strake vortex and wing vortex were located near the vortex centres, suggesting large vortex meandering amplitudes. After the vortex breakdown, velocity fluctuations spread over a larger area, however the maximum standard deviation decreases substantially. With increasing angle of attack, velocity fluctuations occupy a larger area over the wing.

In order to quantify the characteristics of the aforementioned vortex meandering, the instantaneous locations of the wing and strake vortices at various chordwise locations and wing incidences were obtained from the instantaneous PIV images. In this chapter, the vortex centre was defined as the location of maximum vorticity magnitude in the PIV measurement plane and rounded to the nearest grid point, giving an accuracy of half of the effective grid size, which varies from 0.5 to 0.75 mm. Figure 41 presents an example of the time-averaged crossflow vorticity field, instantaneous vorticity field, and the instantaneous locations of the wing vortex and strake vortex in a crossflow plane (x/c = 75%) over the double delta wing at $\alpha$ = 12º. (Spacing of the triangle symbols indicates the spatial resolution of the measurements). Colours represent the probability of the wing or strake vortex at each grid point. It can be seen

that both the wing vortex and strake vortex meander in an area with the highest probability located near the centres of the time-averaged vortices (Figure 41a).

Figure 42 presents contours of the probability of instantaneous vortex location over the double delta wing at various chordwise locations. It is observed that, for all the wing incidences tested, prior to vortex breakdown, both strake vortex and wing vortex meander in relatively small regions with high probability concentrations near the time-averaged vortex centres. For example, for $\alpha = 12^{o}$ (Figure 42c) and $\alpha = 16^{o}$ (Figure 42d), the area in which the vortices meander is small with a large maximum probability of 20%. As the vortices develop downstream and vortex breakdown occurs, the meandering is spread over a larger area with smaller maximum probability. Note that Figure 42 also reveals the dual-vortex structure at x/c = 50% and the corresponding contours of the probability of instantaneous vortex locations.

In order to quantify the magnitude of vortex meandering, vortex meandering amplitudes were calculated from the PIV measurements conducted over both the double delta wing and the simple delta wing, using equation (22)

$$a_M = \sqrt{\frac{\sum (z_i - z_c)^2 + (y_i - y_c)^2}{N}} \qquad (22)$$

Here N is the number of PIV snapshots in the crossflow plane, $z_i$ and $z_c$ are the coordinates of instantaneous and time averaged vortex locations in the normal direction, $y_i$ and $y_c$ are the coordinates of instantaneous and time averaged vortex locations in the spanwise direction. Figure 43 shows the variation of vortex meandering amplitude, $a_M$ /c, as a function of streamwise distance x/c for all wing incidences tested. It is seen that, generally, the meandering amplitudes of both wing vortex and strake vortex increase as they develop downstream, but at a faster rate after vortex breakdown. A sharp increase in meandering amplitudes is first observed near the wing trailing edge for $\alpha = 12^{o}$ due to the onset of vortex breakdown, and then propagates upstream with increasing incidence. Note that the meandering amplitude for the leading-edge vortex over the simple delta wing at x/c = 50% was also included

in Figure 43, which exhibits comparable meandering amplitude to that of the strake vortex over the double delta wing.

In order to further study the possible interactions between wing vortex and strake vortex, the correlation coefficients between instantaneous vortex locations were calculated for all cases where multiple vortices exist. The correlation coefficients were calculated between $r_A$ and $r_B$, $r_A$ and $r_B$ are instantaneous distances of vortex A and B to the wing centreline in crossflow plane, defined as in equation (23) and (24).

$$r_A = \sqrt{z_A^2 + y_A^2} \tag{23}$$

$$r_B = \sqrt{z_B^2 + y_B^2} \tag{24}$$

The correlation coefficient is then defined using equation (25) as shown below:

$$\frac{\sum_1^N (r_{Ai} - \bar{r}_A)(r_{Bi} - \bar{r}_B)}{\sqrt{\sum_i^N (r_{Ai} - \bar{r}_A)^2}\sqrt{\sum_i^N (r_{Bi} - \bar{r}_B)^2}} \tag{25}$$

Here N is the number of PIV snapshots in the crossflow plane, $r_{Ai}$ and $\overline{r_A}$ are the instantaneous and mean values of $r_A$ , $r_{Bi}$ and $\overline{r_B}$ are the instantaneous and mean values of $r_B$. Figure 44 shows the results at x/c = 50%, 62.5%, 75% and 87.5%. Note that, in Figure 44, the correlation coefficient at x/c = 50% was between the vortices of the dual-vortex structure that originated from the strake, whereas the correlation coefficients at other streamwise locations were calculated between the strake vortex and the wing vortex. Figure 44a indicates that the correlation coefficient between the vortices of the dual-vortex structure reached -0.4 at α = 12º, then it gradually dropped to near zero at α = 24º and 28º. It is interesting that, at α = 12º, the two vortices are aligned vertically (see Figure 37). It is also clear that the correlation becomes weaker as vortex breakdown develops. Further downstream at x/c = 62.5% the strake and wing vortices are weakly correlated. Surprisingly, with increasing streamwise distance, there is an increase in the correlation coefficient at intermediate incidences α = 12º and

16º (Figures 44b-d). Figure 36 suggests that this is due to the decreasing distance between the vortices before merging.

### 4.2.3 Proper Orthogonal Decomposition

The proper orthogonal decomposition (POD) analysis expands a random function as a series of deterministic functions with random coefficients so that it is possible to separate the deterministic part from the random one [72, 73]. The energy of stochastic signal is given by the sum of the eigenvalues such that each eigenvalue taken individually represents the energy contribution of the corresponding deterministic function [74]. In the past, the application of POD has been limited by the lack of sufficient data to perform the decomposition. However, the instantaneous velocity fields attainable with PIV have become a natural complement to POD. When the decomposition involves a sequence of instantaneous velocity fields (as captured from PIV), the method is termed snapshot POD, which was introduced by Sirovich [75]. Lumley [72] decomposed the velocity fields of turbulent flows as a spatial vectorial function and extracted the most energetic (spatial) eigenfunction representing the eddies of the flow. As far as the applications related to the streamwise vortices are concerned, this analysis technique was used to capture the dynamic flow structure of the leading-edge vortices as well as the vortex-tail interaction by extracting its most energetic eigenmodes [76, 77]. The POD analysis was also used recently to study the trailing vortices by Roy and Leweke [78] and del Pino et al. [79]. In the present investigation, POD analysis was performed on the captured PIV data in crossflow planes over the simple and double delta wings. The analysis was performed using commercial software TSI GRAD POD TOOLBOX, which employs the spatio-temporal data analysis technique proposed by Heiland [80]. For each case, the first four most energetic modes were extracted.

Figure 45 presents the cumulative energy distribution, time-averaged vorticity field and the flow structures of the four most energetic modes in a crossflow plane over the simple delta wing at x/c = 50% and $\alpha = 12^{\circ}$. It can be observed that the 1$^{st}$ (most energetic) mode exhibited one vortex pair which was centred on the time-averaged leading-edge vortex, representing displacement of the vortex. A similar

vortex pair was also observed in the 2nd mode (2nd most energetic) along with visible decompositions of the shear layer. A linear combination of these eigenmodes provides displacements of the vortex cores, which can be characterized as an azimuthal wavenumber of m = 1. The same first helical mode was identified in the meandering of the trailing vortices [78, 79] and inlet (ground) vortices [81]. Higher modes with decreasing energy are also shown in Figure 45, which reveal the displacements of the vortex core in various directions as well as the shear layer vortical structures.

Time-averaged vorticity fields and flow structures of the first (most energetic) mode in a crossflow plane over the double delta wing at x/c = 50% for various wing incidences are shown in Figure 46. Note that these are the 'dual-vortex' structures of the apex vortex at this plane. It is seen that two pairs of counter rotating vortices were present in the 1st mode, corresponding to the two time-averaged vortices. At $\alpha = 12^{o}$, both vortex pairs in the 1st mode had dominant movement vertically but in the opposite directions, suggesting out-phase meandering of the two vortices. It is noted that this angle of attack corresponds to the most negative correlation coefficient shown in Figure 44. As the wing incidence is increased to $\alpha = 16^{o}$ and $\alpha = 20^{o}$, the meandering direction of the two vortices starts to deviate from the vertical direction. It is interesting that the corresponding correlation coefficient decreases (see Figure 44).

Figure 47 shows the time-averaged vorticity fields and flow structures of the first (most energetic) mode in various downstream crossflow planes over the double delta wing at $\alpha = 12^{o}$. At all the chordwise locations, both wing vortex and strake vortex exhibit a pair of counter rotating vortices in the 1st mode, although the one for the strake vortex at x/c = 87.5% is less clear due to the vortex breakdown (Figure 47c). Note that, at x/c = 62.5% (Figure 47a), the two vortex pairs have relatively large separation, which may explain very small correlation coefficients (Figure 44). At the most downstream location x/c = 87.5% (Figure 47c), the two vortices are much closer, resulting in increased negative correlation.

## 4.3 Conclusions

An experimental investigation of the interaction of multiple vortices over a 70˚/50˚ double delta wing has been performed in a wind tunnel. Particle image velocimetry

measurements in crossflow planes at various chordwise locations and wing incidences were conducted. The results were compared with those obtained over a simple slender delta wing with a sweep angle of 70˚. The following conclusions can be drawn:

a) At x/c = 50% (kink location of the double delta wing) before the wing vortex developed, a dual-vortex structure of the strake vortex was identified. The two vortical structures rotated around each other with increasing angle of attack. The upstream effect of the wing vortex also caused the formation of the vortical structure to move further away from the wing surface when compared to the simple delta wing.

b) Strake and wing vortices moved closer to each other as angle of attack increased, resulting in intensified interaction, merging, and earlier onset of vortex breakdown. Rotation of the vortices around each other with increasing distance and angle of attack was initially slow, but accelerated towards the trailing-edge.

c) Prior to breakdown, both wing and strake vortices were found meandering in relatively small regions with high probability concentrations at the time-averaged vortex centres. The amplitude of vortex meandering exhibited a sharp increase after the onset of vortex breakdown. The correlation between the displacements of the vortex cores increased as the time-averaged vortices became closer to each other. The proper orthogonal decomposition (POD) analysis of the captured PIV velocity data indicated that, for all vortices, the most energetic mode was the first helical mode. When the vortices were closer to each other, their displacement became out-of-phase.

## 4.4 Figures

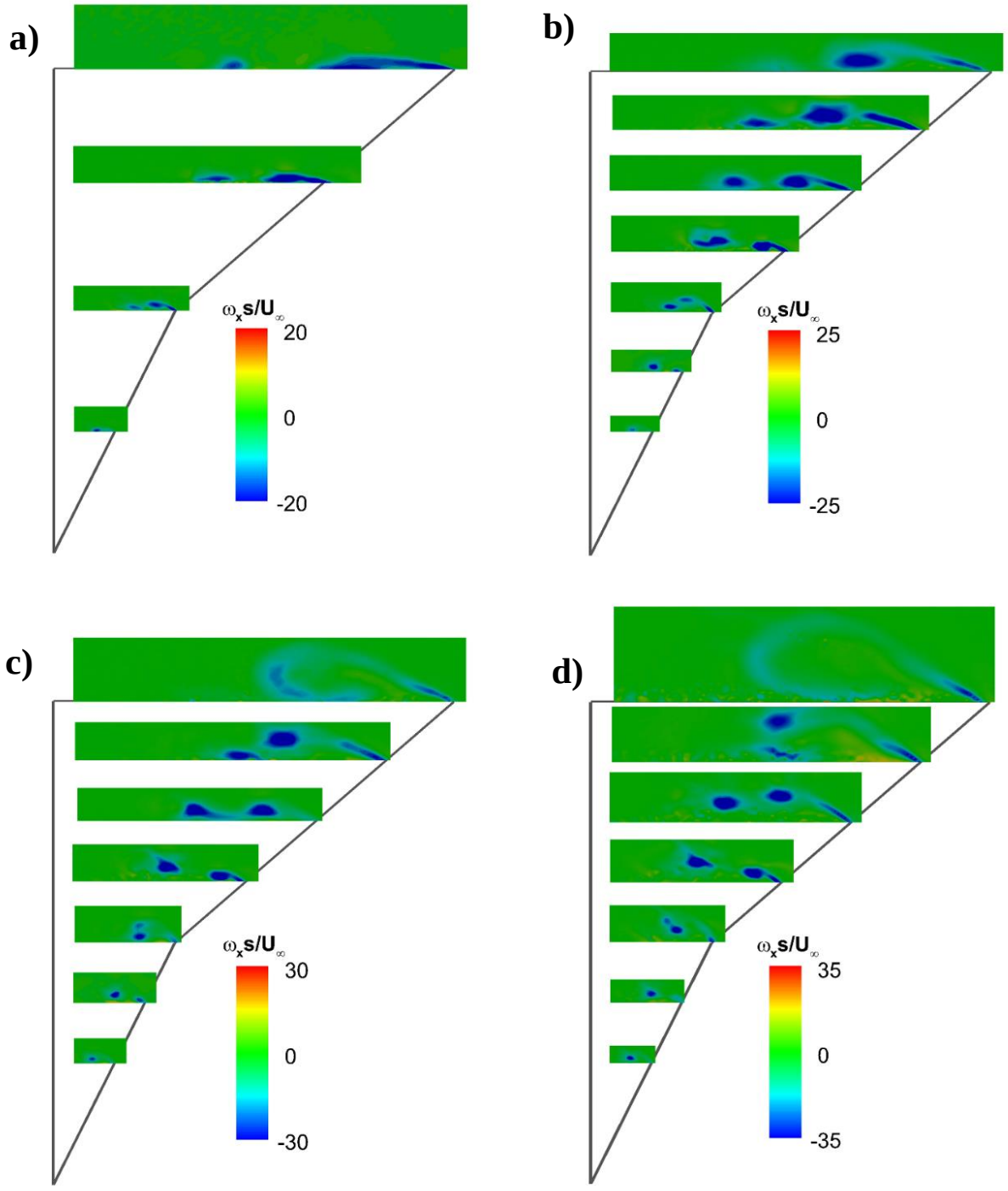


Figure 36. Time-averaged vorticity plots for a) α = 4˚; b) α = 8˚; c) α = 12˚; d) α = 16˚; e) α = 20˚; f) α = 24˚; g) α = 28˚; h) α = 32˚

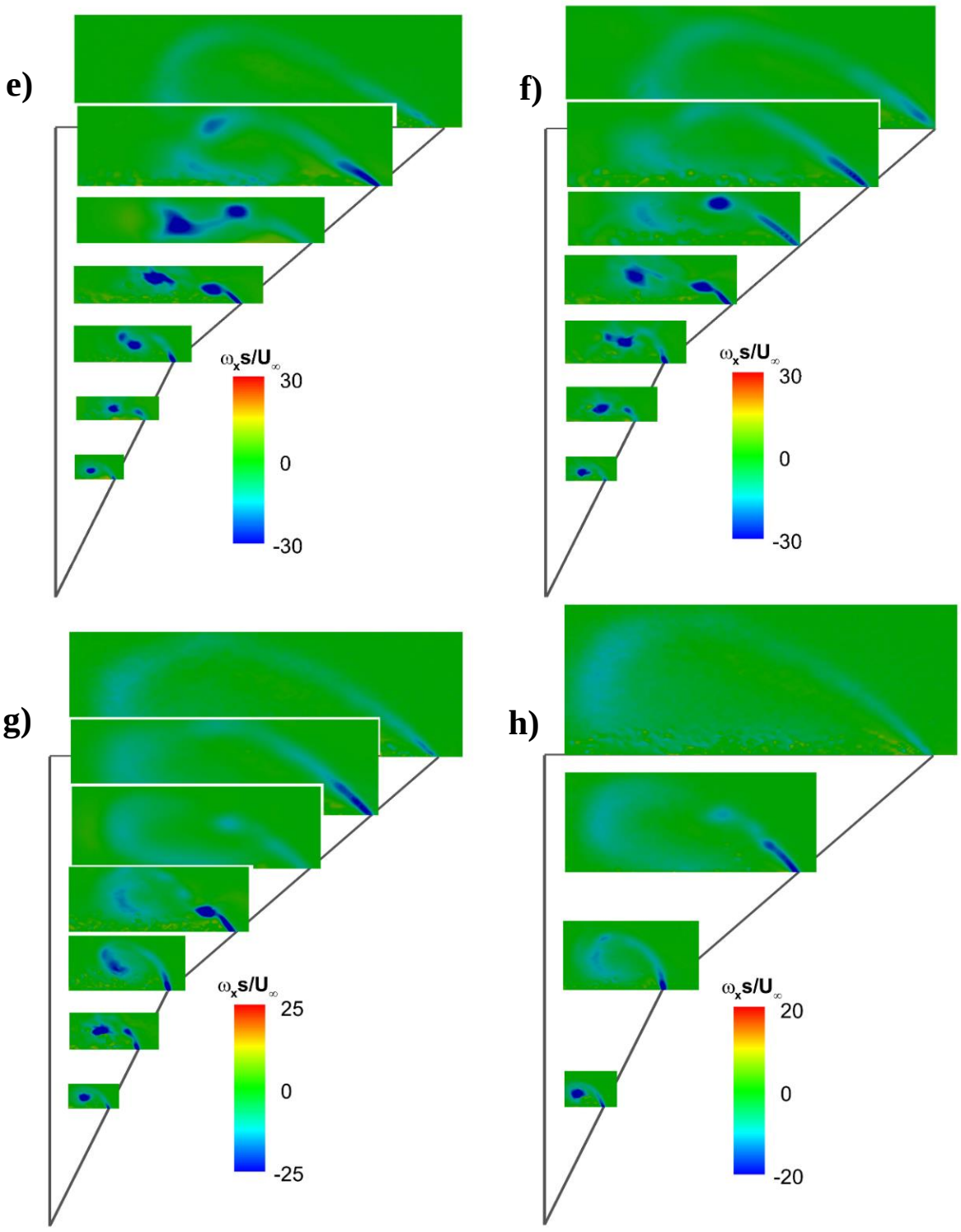


Figure 36. Continued

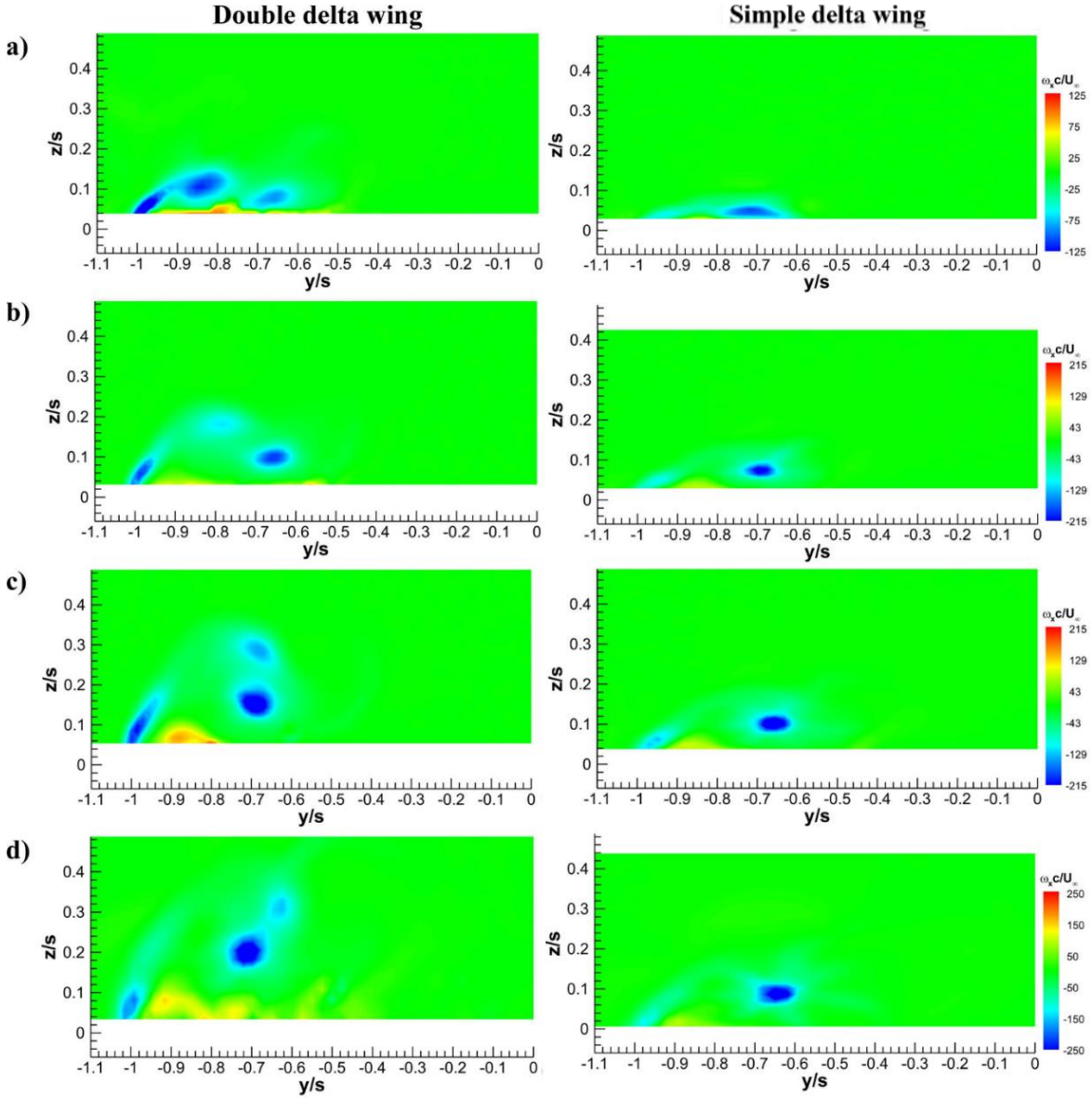


Figure 37. Time-averaged vorticity plots at x/c = 50% for a) α = 4˚; b) α = 8˚; c) α = 12˚; d) α = 16˚; e) α = 20˚; f) α = 24˚; g) α = 28˚; h) α = 32˚

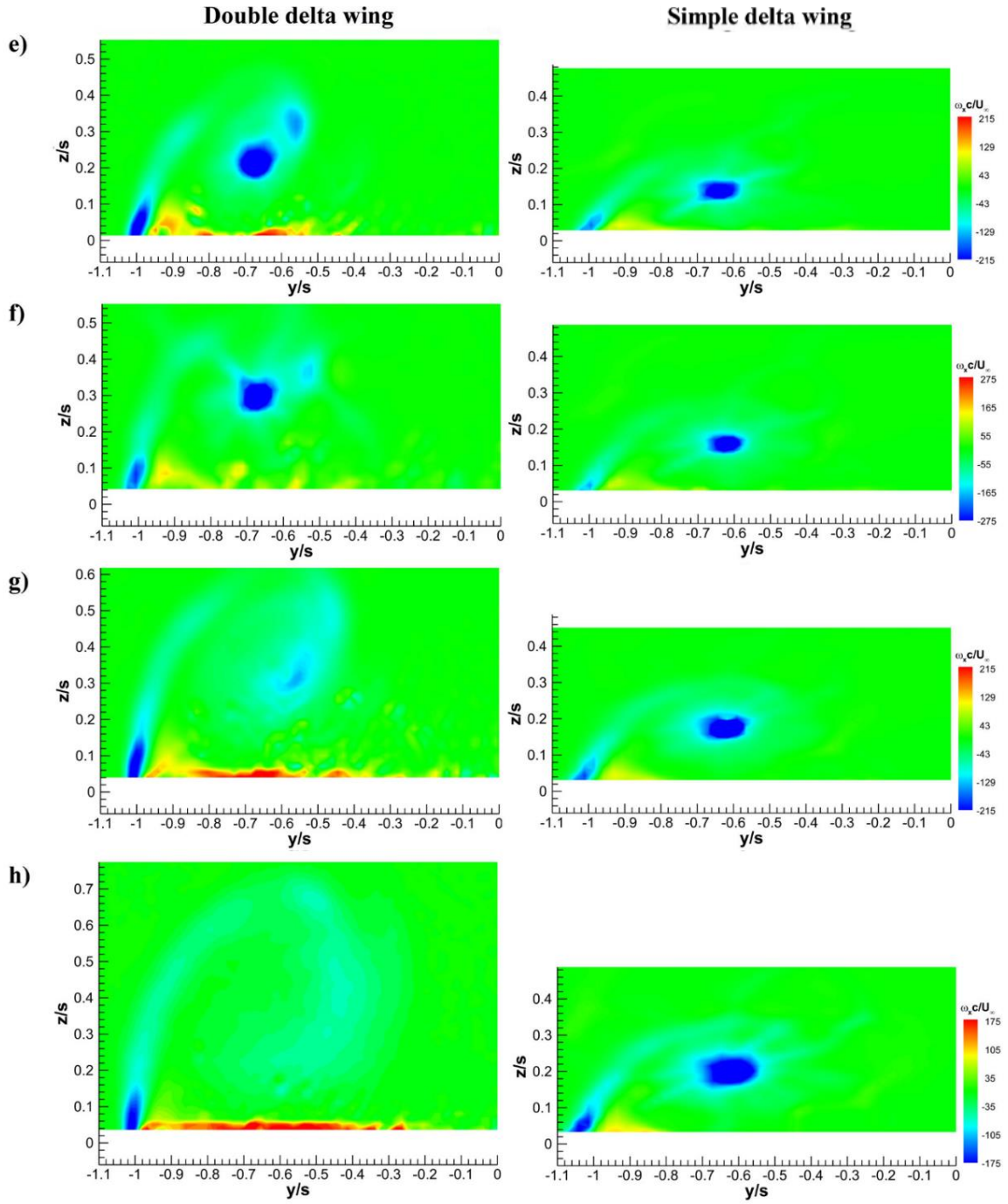


Figure 37. Continued.

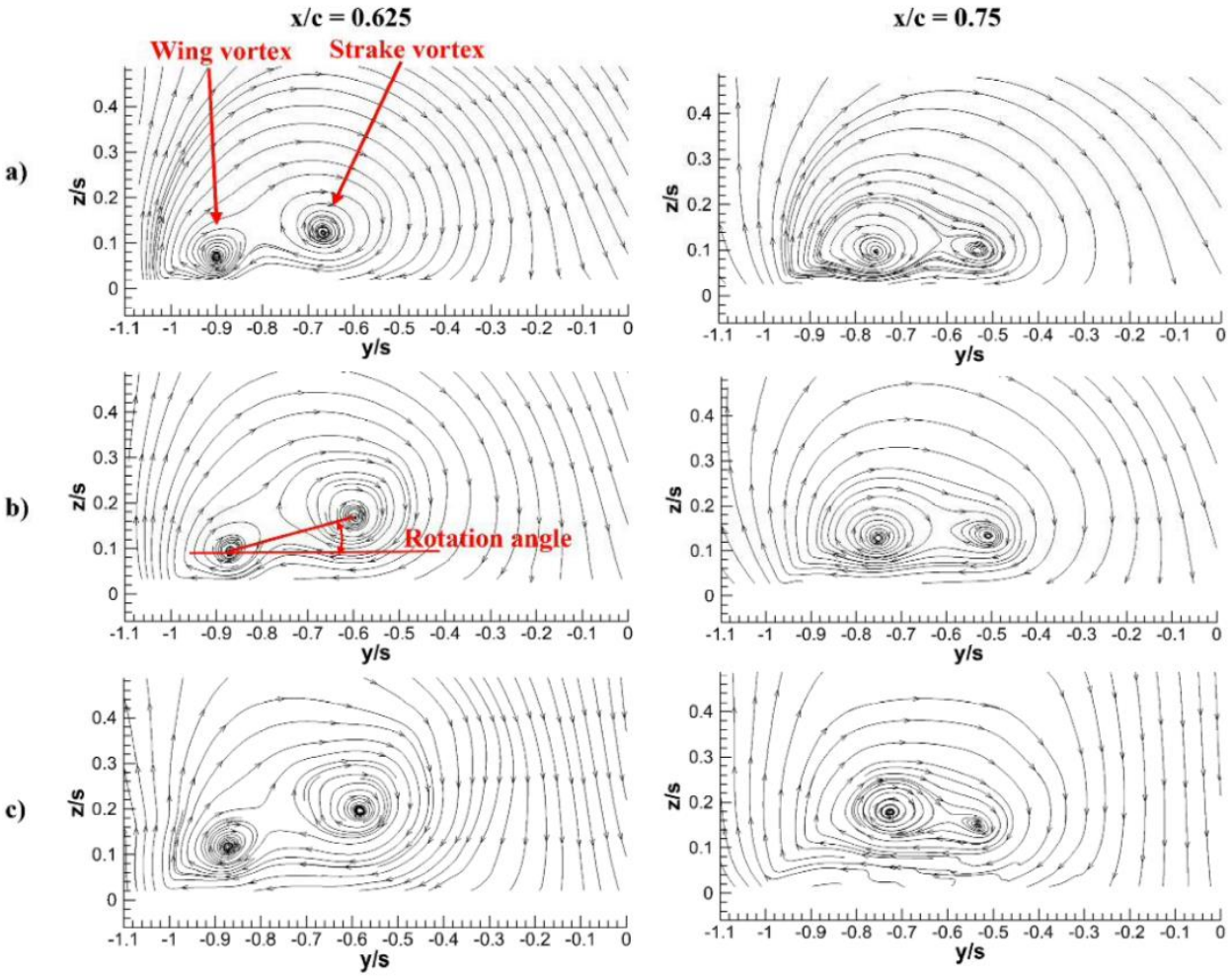


Figure 38. Streamline plot at x/c = 62.5% and x/c = 75% for a) α = 8˚; b) α = 12˚; c) α = 16˚; d) α = 20˚; e) α = 24˚; f) α = 28˚

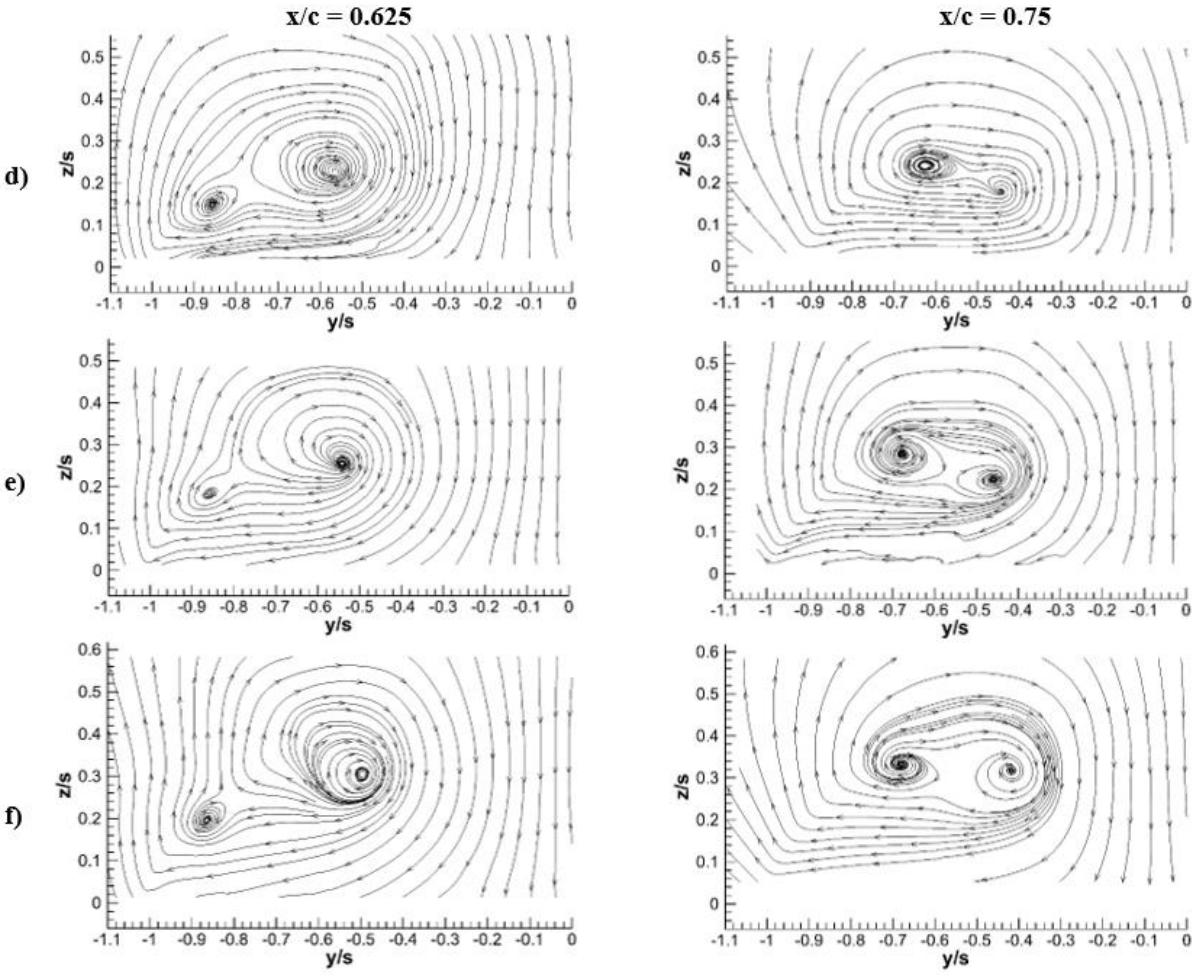


Figure 38. Continued.

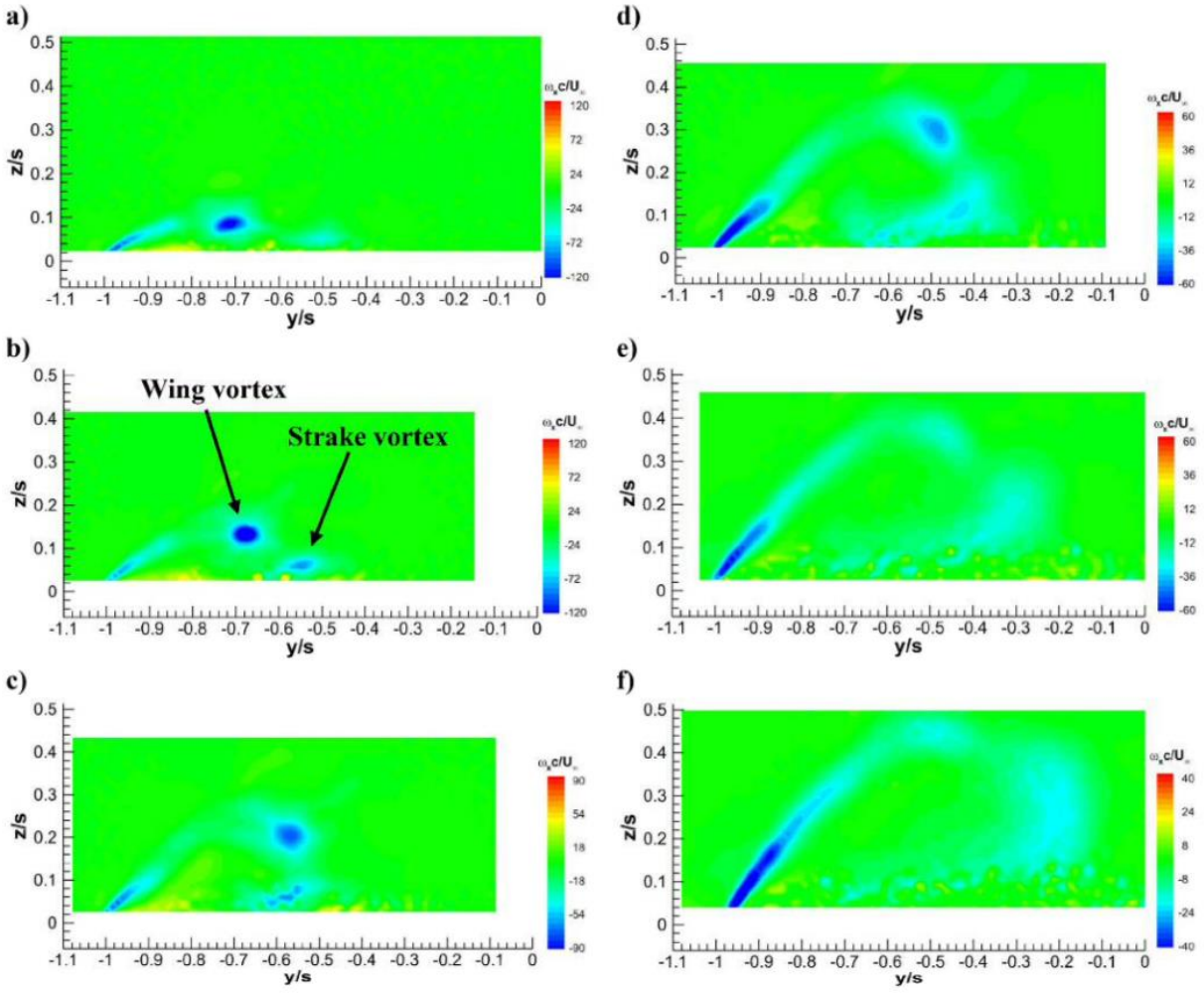


Figure 39. Time-averaged crossflow vorticity patterns over the double delta wing at x/c = 87.5% for a) α = 8˚; b) α = 12˚; c) α = 16˚; d) α = 20˚; e) α = 24˚; f) α = 28˚

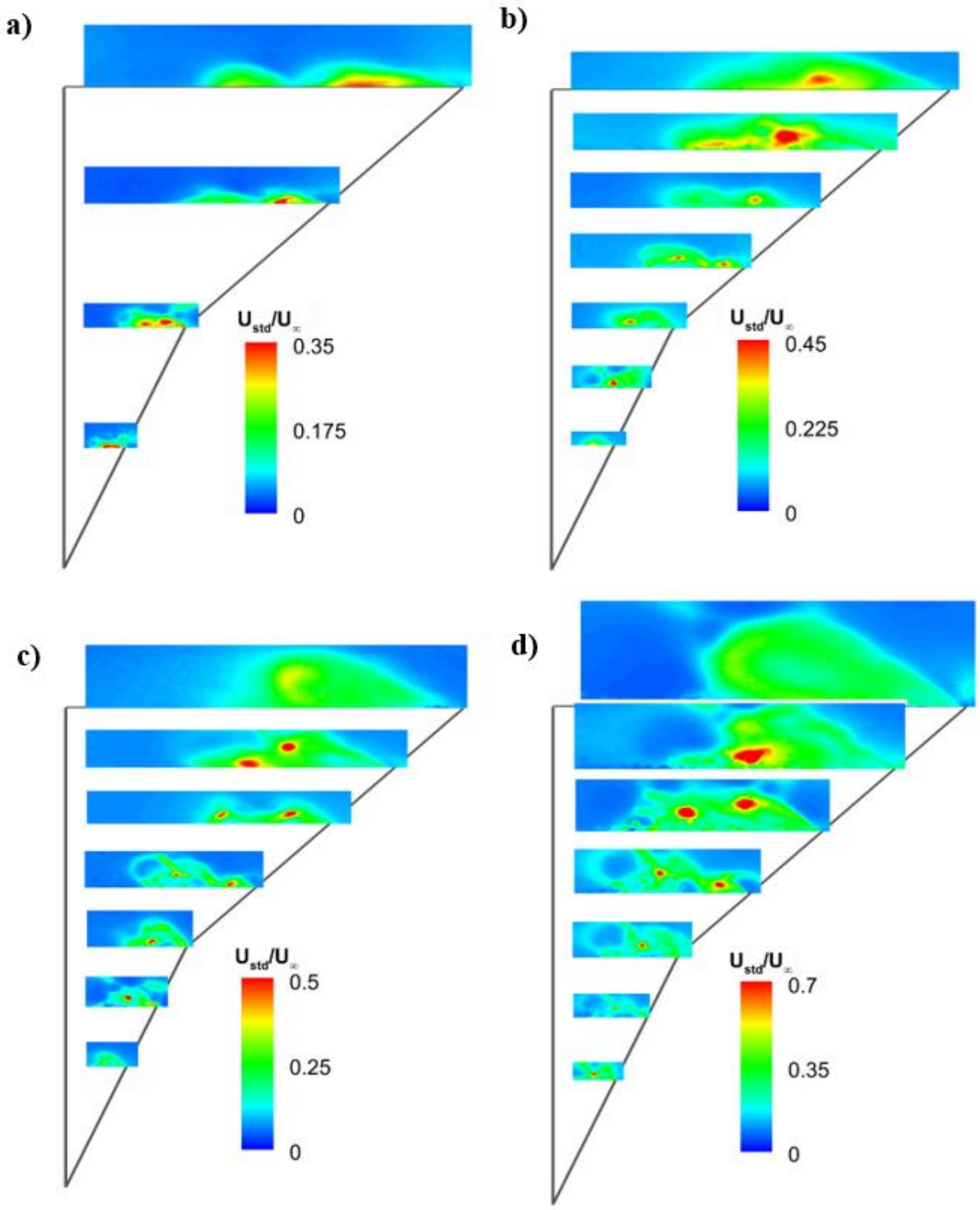


Figure 40. 3-D Standard deviation plots for a) α = 4˚; b) α = 8˚; c) α = 12˚; d) α = 16˚; e) α = 20˚; f) α = 24˚; g) α = 28˚; h) α = 32˚.

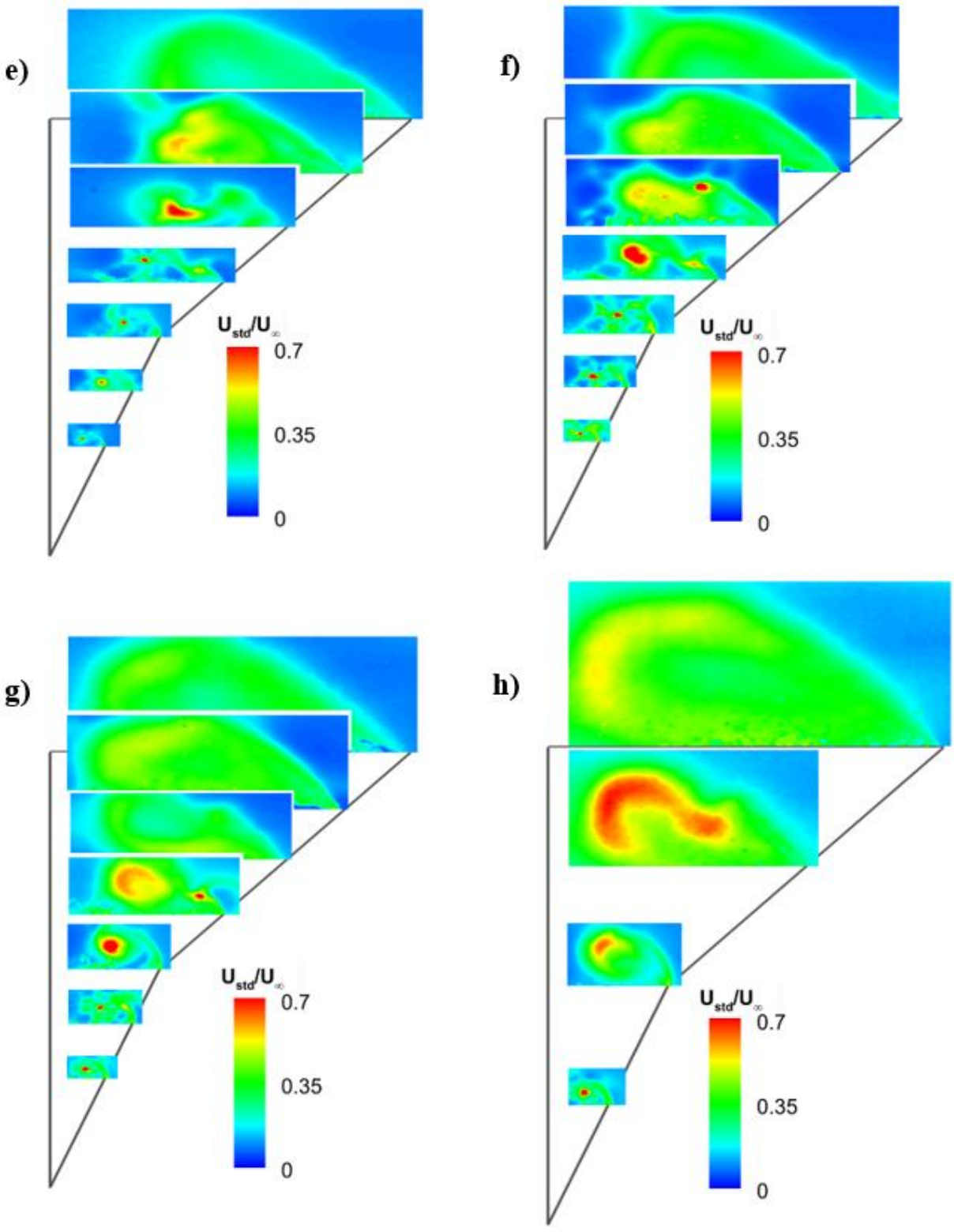


Figure 39. Continued

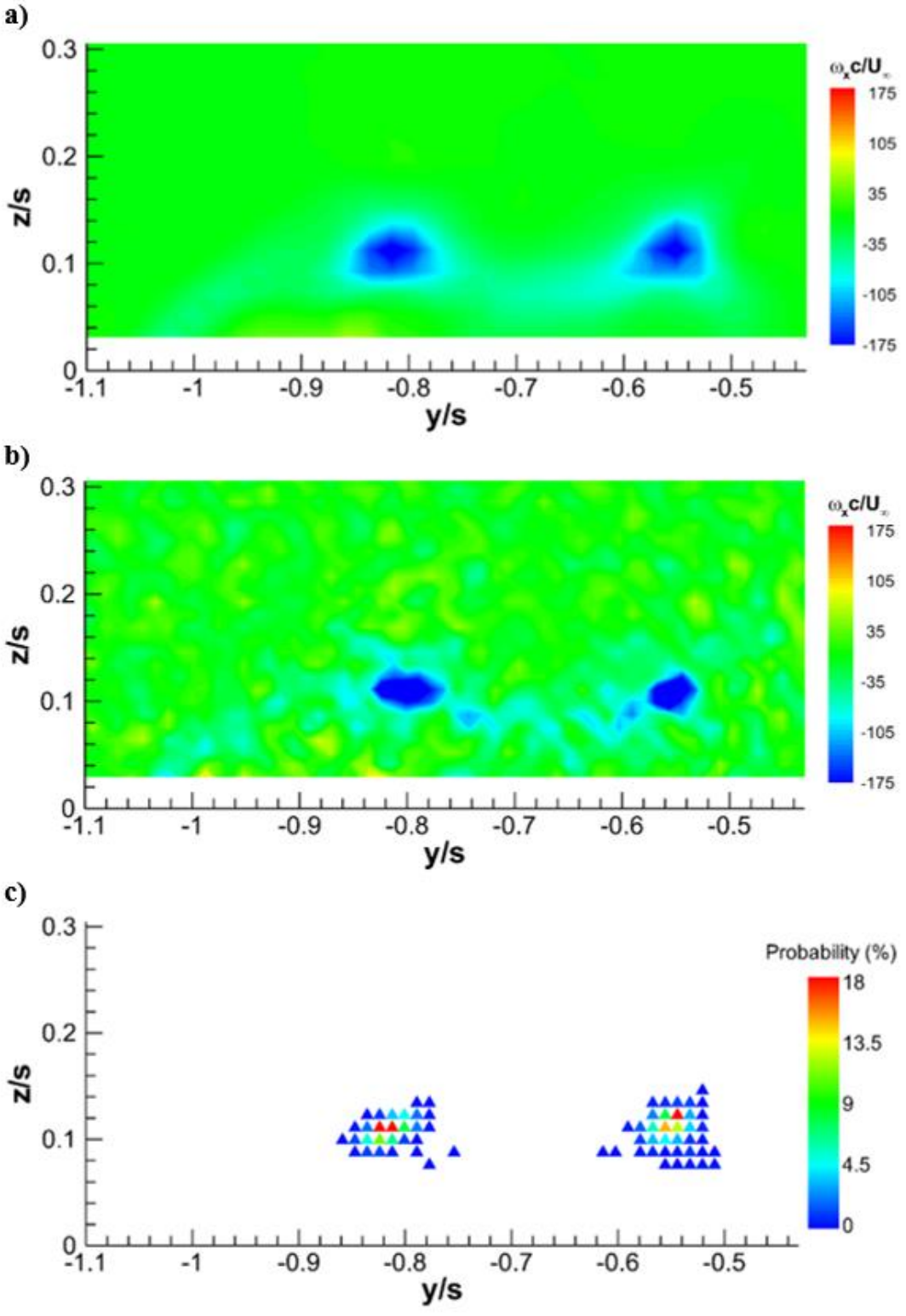


Figure 41. Vorticity and vortex meandering probability plots at α = 12˚, x/c = 75%. a) Time-averaged vorticity plot; b) Instantaneous vorticity plot; c) Vortex meandering probability plot

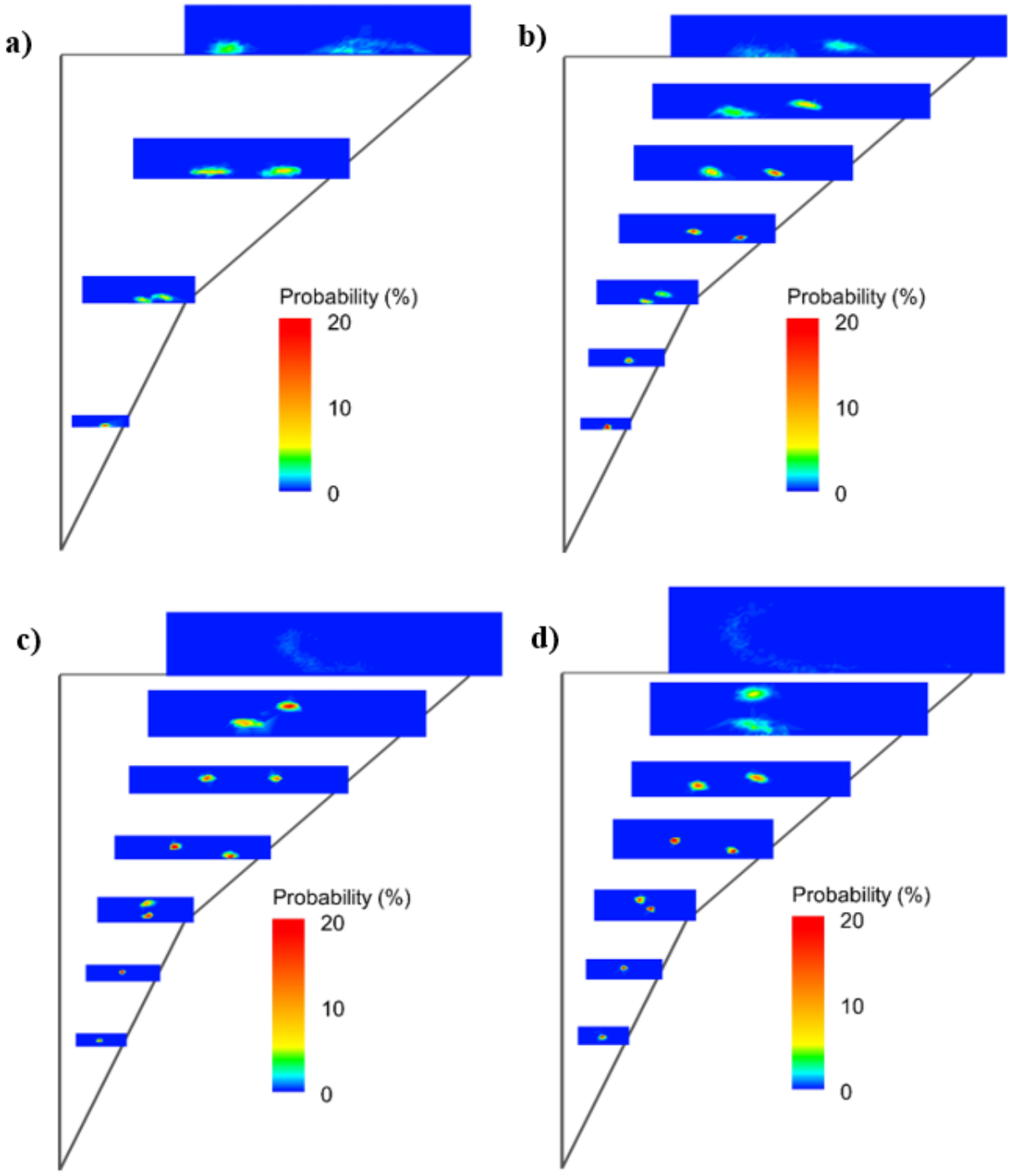


Figure 42. 3-D vortex meandering probability plots for a) α = 4˚; b) α = 8˚; c) α = 12˚; d) α = 16˚; e) α = 20˚; f) α = 24˚; g) α = 28˚; h) α = 32˚.

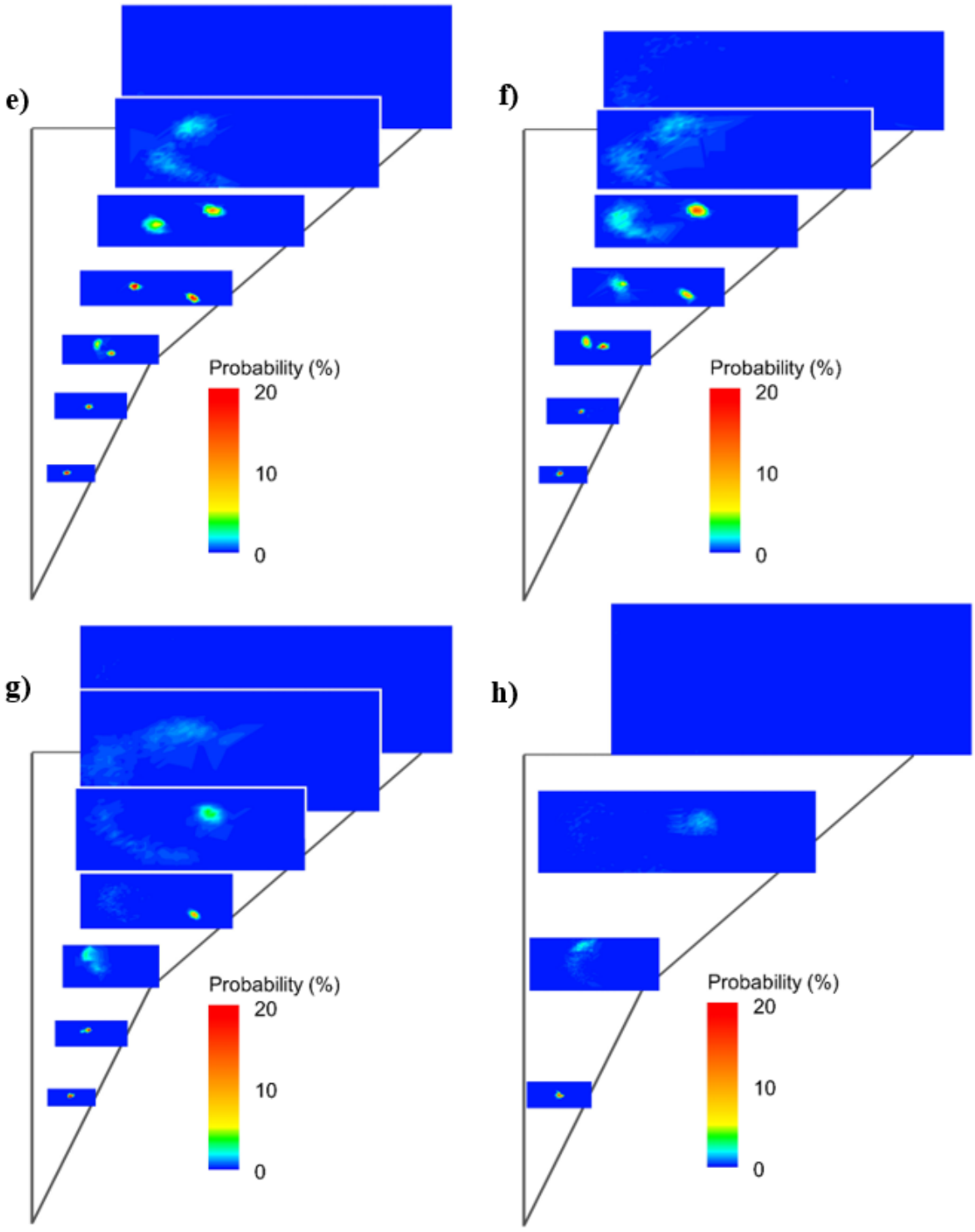


Figure 41. Continued.

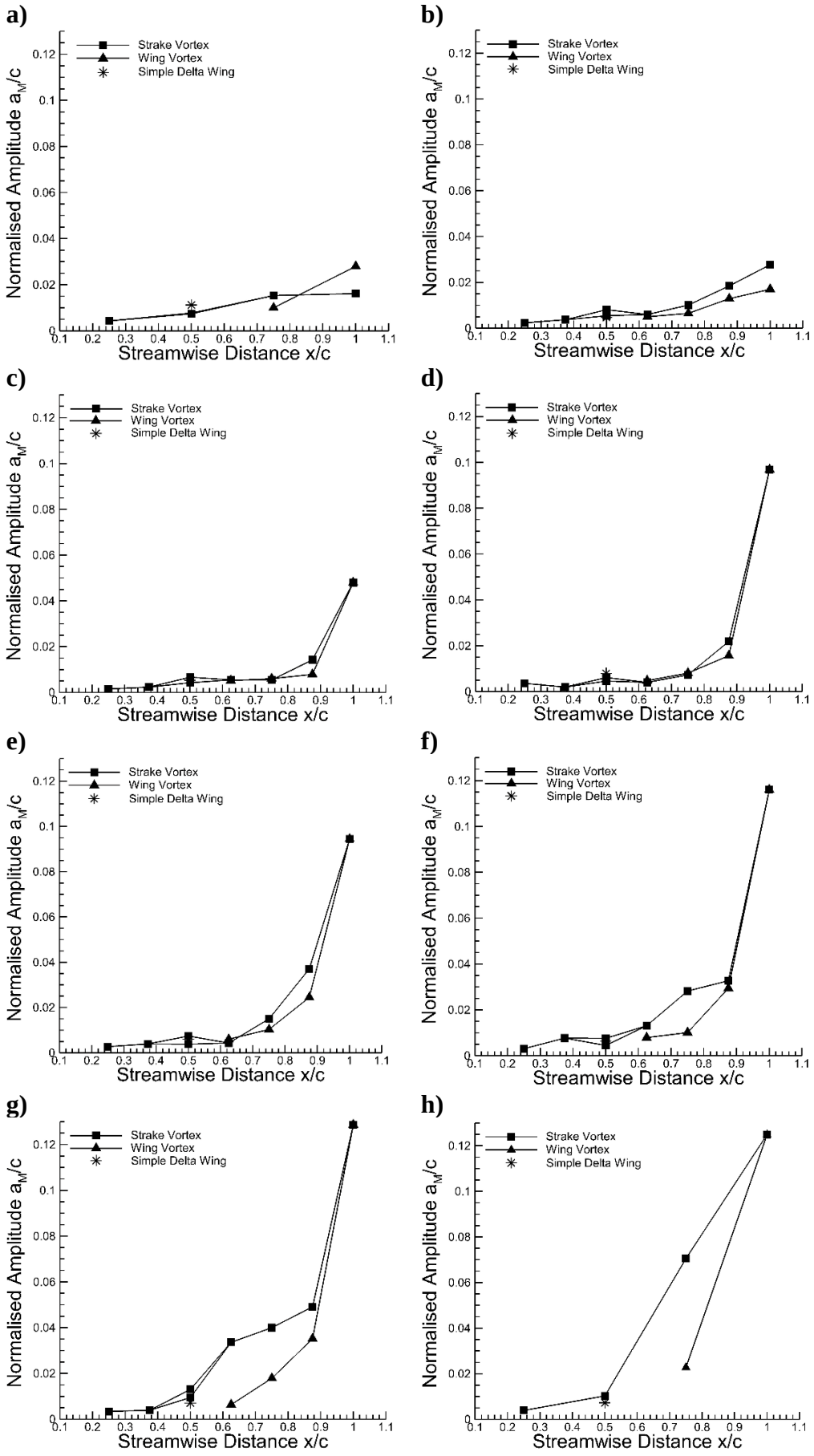


Figure 43. Normalized vortex meandering amplitude for a) α = 4˚; b) α = 8˚; c) α = 12˚; d) α = 16˚; e) α = 20˚; f) α = 24˚; g) α = 28˚; h) α = 32˚.

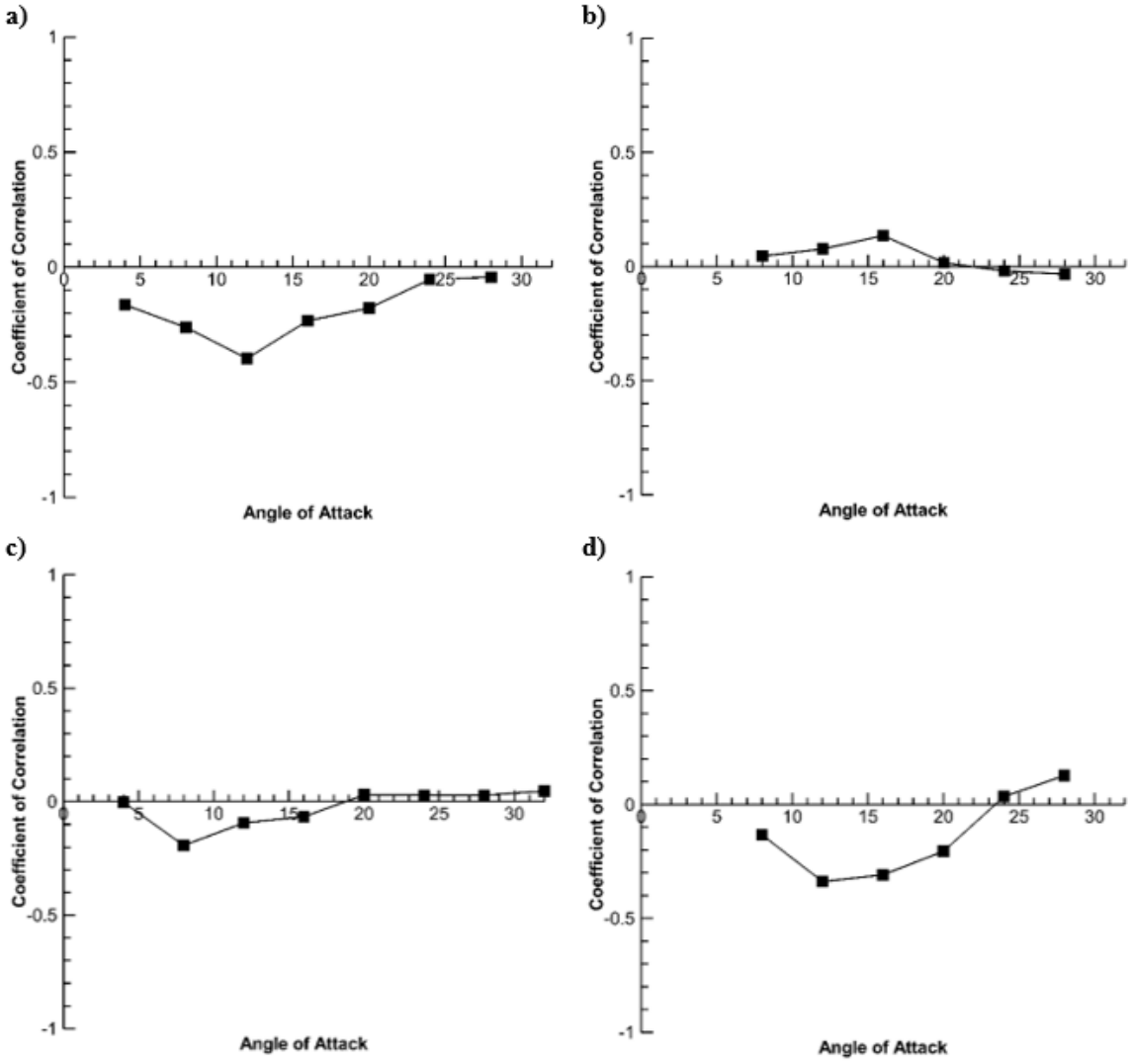


Figure 44. Coefficient of correlation at a) x/c = 50%; b) x/c = 62.5%; c) x/c = 75%; d) x/c = 87.5%.

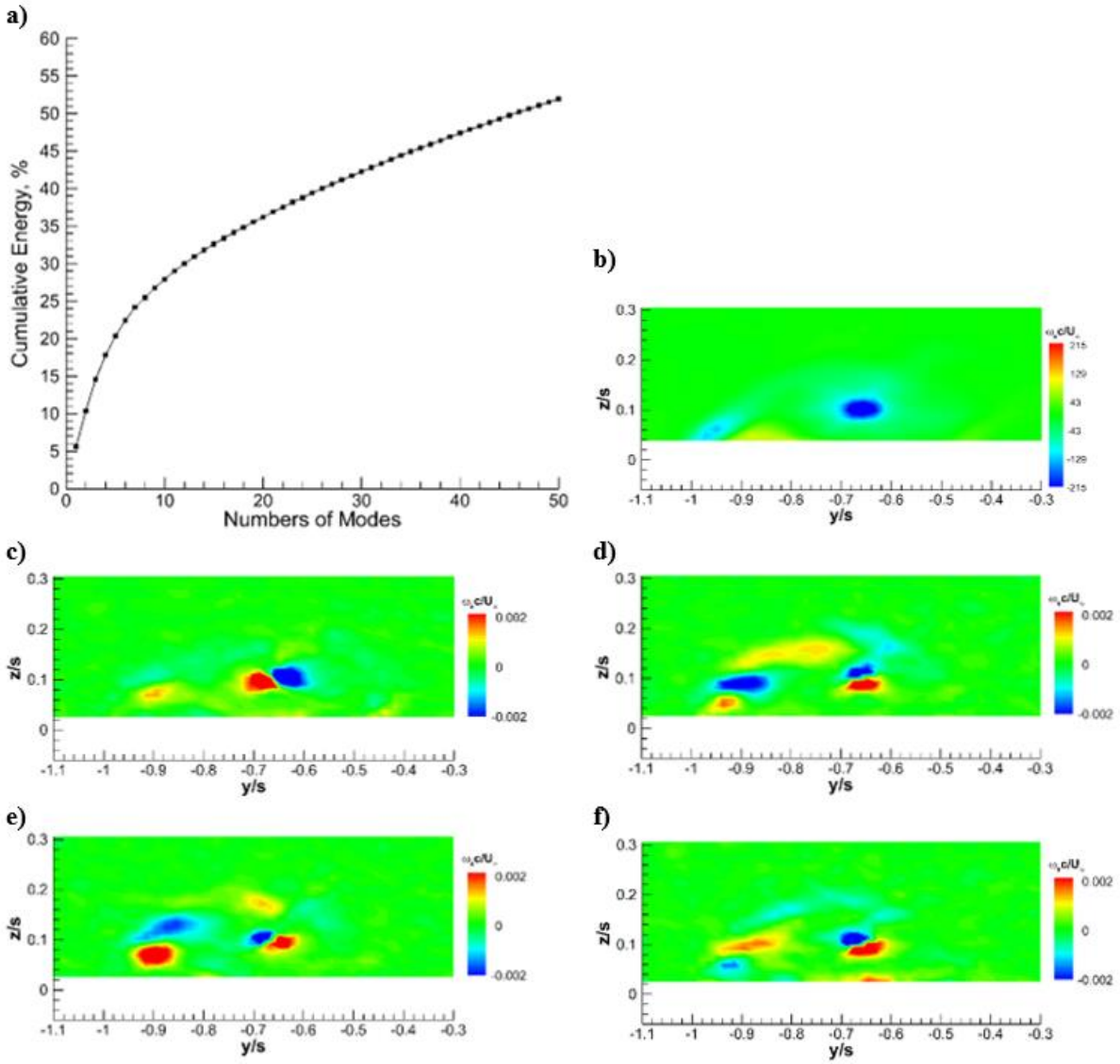


Figure 45. POD analysis for α = 12º, x/c = 50% over simple delta wing. a) Cumulative energy; b) Time-averaged vorticity; c) 1st mode; d) 2nd mode; e) 3rd mode; f) 4th mode.

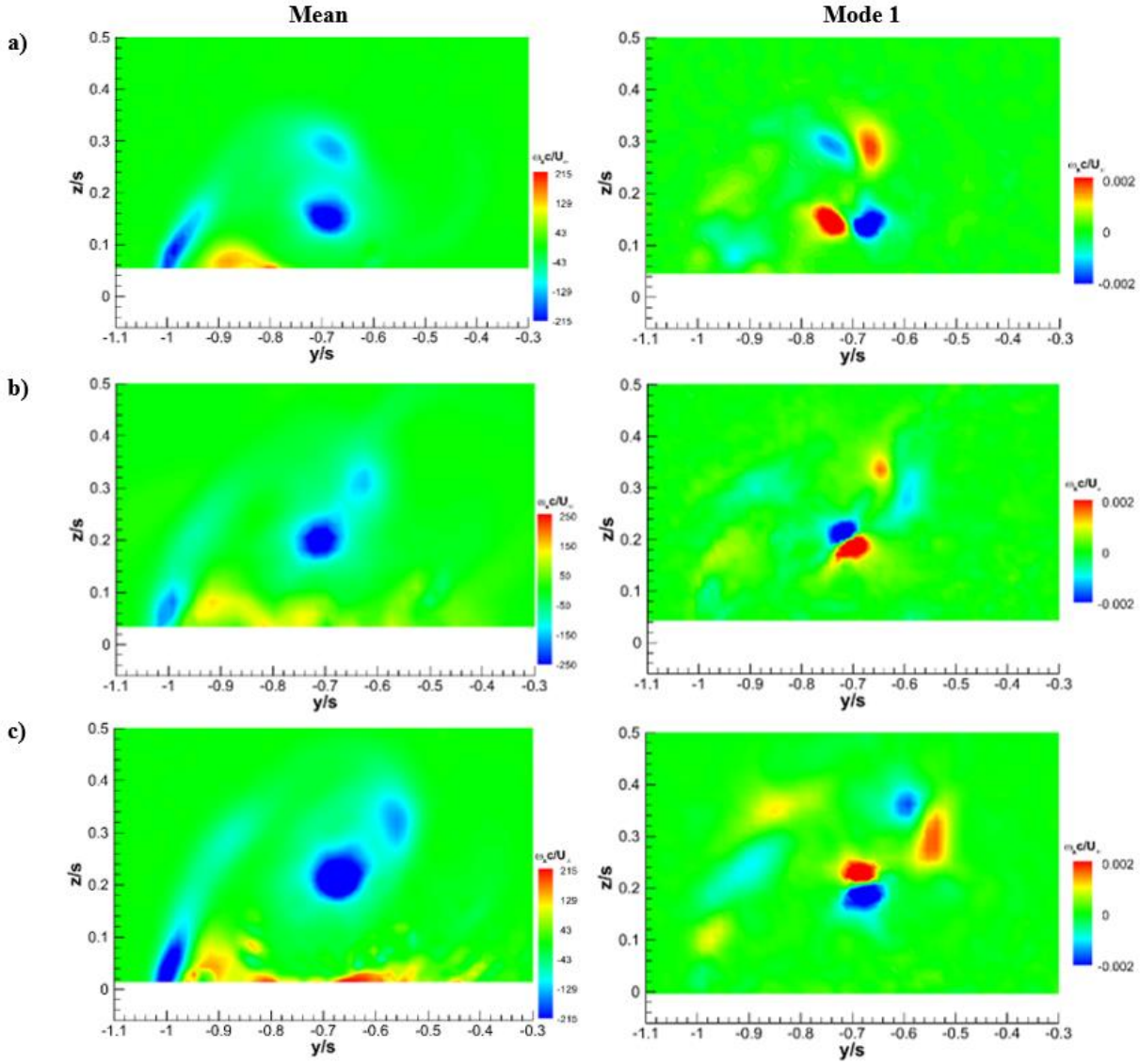


Figure 46. POD results comparison at x/c = 50% over double delta wing for a) α = 12˚; b) α = 16˚; c) α = 20˚.

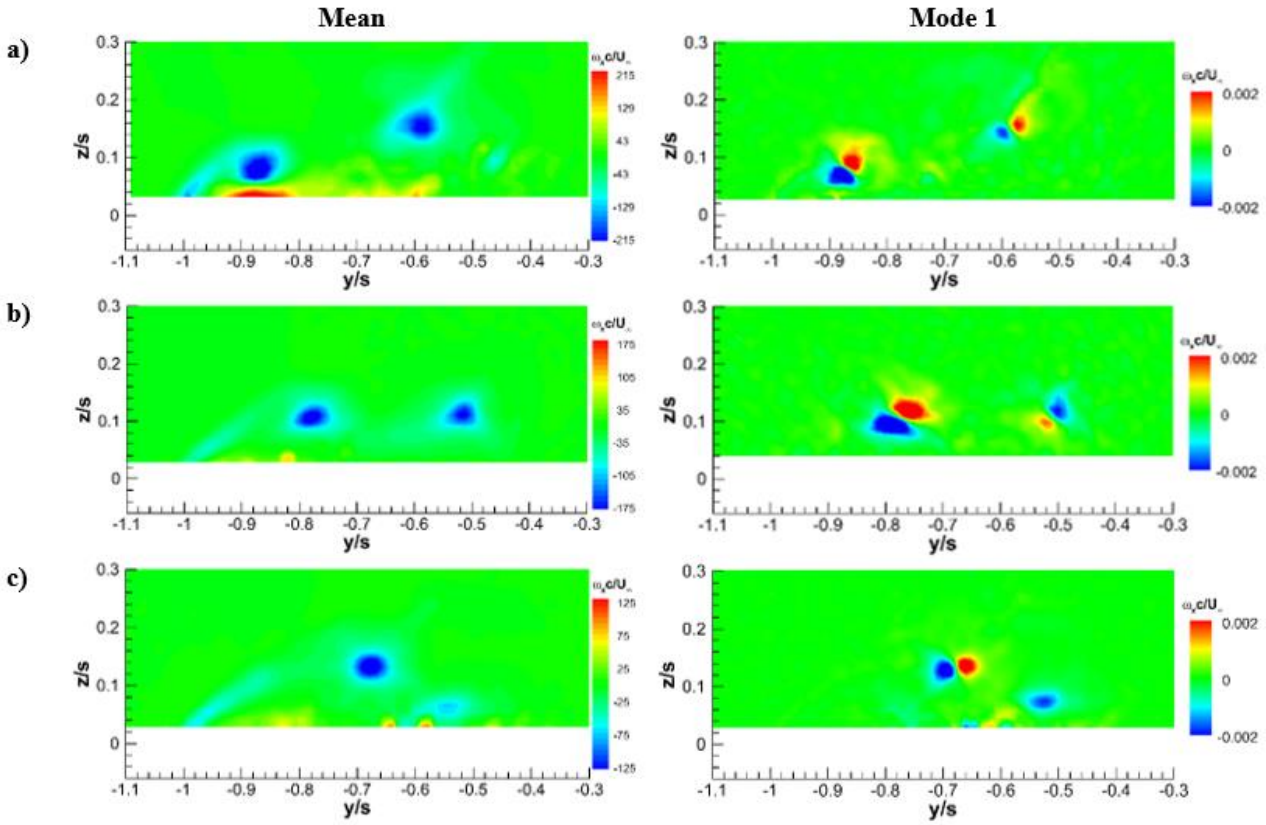


Figure 47. POD results comparison at α = 12˚ over double delta wing for a) x/c = 62.5%; b) x/c = 75%; c) x/c = 87.5%.

# CHAPTER 5.

# EFFECT OF JET BLOWING

## 5.1 Summary

This chapter documents the following investigations: 1) a comparison of vortical flow over double delta wings for two different Reynolds numbers; 2) the effect of active blowing on double delta wing vortical flow, this includes the effect of blowing hole location and blowing yaw angle; 3) for selected cases, the effect of blowing momentum coefficient.

A dual vortex structure is present at x/c = 50% on the data obtained from the wind tunnel test at Re = 2.34 x $10^5$, however, this structure is not visible in the water tunnel test at Re = 2.80 x $10^4$. At Re = 2.80 x $10^4$, the wing vortex tends to break down first, whereas at Re = 2.34 x $10^5$ the strake vortex breaks down first. A higher Reynolds number also results in higher peak standard deviation and higher vortex meandering amplitude. With the active blowing, depending on the blowing jet angle and location, the interaction between the two vortices can be intensified or reduced. In particular, blowing at hole #1 and $\beta = 30^0$ results in strengthened wing and strake vortices with widened distance between them. Whereas blowing at hole #1 and $\beta = 75^\circ$ results in only one merged vortex. The first mode of the POD analysis illustrates a pair of counter rotating vortices at the strake and wing time-averaged vortex locations. Two cases are selected for investigating the effect of momentum coefficient, it was found that the strength, interactions and the relative spatial positions of the wing and strake vortices can be effectively controlled by changing the jet blowing momentum coefficient.

## 5.2 Results and Discussion

### 5.2.1 Effect of Reynolds Number

Figure 48 illustrates the time-averaged vorticity comparison between the two different Reynolds numbers, Re = 2.8 x $10^4$ and Re = 2.34 x $10^5$, which were taken in the water tunnel and wind tunnel respectively. At first glance, it is apparent that the dual-vortex structure found in the kink location at Re = 2.34 x $10^5$ is no longer present at Re = 2.8 x $10^4$. At $\alpha = 8^0$ (Figure 48a), the strake vortex for Re = 2.34 x $10^5$ breaks down after x/c = 87.5%, while the wing vortex displays a much higher vorticity value with a larger core diameter. However, for Re = 2.8 x $10^4$, both vortices maintain their vortical structures without breaking down throughout the whole wing chord length. When increasing the angle of attack to $12^0$ (Figure 48b), stronger interactions between the strake and wing vortices can be observed for both Reynolds numbers. For the Re = 2.8 x $10^4$ case, comparing with $\alpha = 8^0$, both vortices have gained strength and the wing vortex moves closer towards the strake vortex at the trailing-edge. For Re = 2.34 x $10^5$, however, the strake vortex moves underneath the wing vortex at x/c = 87.5%, then they merge and break down at the trailing-edge. At $\alpha = 16^0$ (Figure 48c), the strake and wing vortices merge at x/c = 87.5% with no signs of breakdown even at the trailing-edge for Re = 2.8 x $10^4$. For Re = 2.34 x $10^5$, the two vortices rotate around each other and gradually move closer as the measurement plane moves from x/c = 62.5% to 87.5%; a total breakdown then occurs at the trailing-edge. Increasing the angle of attack to $24^0$ (Figure 48d) causes both vortices to break down at the trailing-edge for Re = 2.8 x $10^4$ case. Prior to breakdown, the strake vortex retains vorticity strength until x/c = 87.5%, while the wing vortex is not easy to be identified at this angle of attack. For Re = 2.34 x $10^5$, the previously identified rotational motion between the strake and wing vortices can still be recognised between x/c = 62.5% and x/c = 87.5%. At x/c = 87.5%, the wing vortex becomes much weaker while still maintaining its vortical structure; however the strake vortex has already broken down at x/c = 87.5%. At $\alpha = 28^0$, the onset of breakdown for the strake vortex occurs at x/c = 75% for the Re = 2.8 x $10^4$ case, with no distinguishable vortical structure for the wing vortex throughout whole chord length. On the contrary, for Re = 2.34 x $10^5$, the strake vortex breaks down before the wing vortex, as can be observed at x/c = 75%. After x/c = 75%, both vortices exhibit a broken-down structure.

The streamline results illustrated in Figure 49 show agreement with the findings in the vorticity plots. It can be seen that for Re = 2.34 x $10^5$, at $\alpha = 8^0$ (Figure 49a) the wing vortex has a larger high crossflow velocity region than the strake vortex at x/c = 75%. Downstream of x/c = 75%, the strake vortex can no longer be identified while the wing vortex still displays a well-defined vortical structure. At $\alpha = 12^0$ (Figure 49b), very different streamline profiles can be observed between Re = 2.34 x $10^5$ and Re = 2.8 x $10^4$ cases. For the Re = 2.8 x $10^4$ case (Figure 49b), both the streamline profiles for strake and wing vortices can be recognised all the way to the trailing-edge, although the strake vortex reduces significantly in the high crossflow velocity area and the wing vortex moves closer to the strake vortex. However, for Re = 2.34 x $10^5$, the streamline profile for the strake vortex can only be distinguished from x/c =50% to 75%, after which only the streamline profile of one circulating region can be seen. When increasing the angle of attack to $16^0$ (Figure 49c), vortex breakdown can be noticed from the streamline profile for Re = 2.34 x $10^5$ at the trailing-edge, however no breakdown is indicated on Re = 2.8 x $10^4$ case. For $\alpha = 20^0$ and $24^0$ (Figure 49d & 49e), it can be observed that the high crossflow velocity region for Re = 2.34 x $10^5$ cases have a lower streamline density than Re = 2.8 x $10^4$ cases. Moreover, the decrease in streamline density post vortex breakdown is greater at Re = 2.34 x $10^5$ for both angles of attack.

Figure 50 illustrates the standard deviation of the crossflow velocity fluctuations for both Reynolds numbers at various angles of attack. It can be seen that a higher Reynolds number results in higher peak standard deviation around the vortex cores for all angles of attack. At $\alpha = 8^0$ for Re = 2.34 x $10^5$ (Figure 50a), it can be observed that the wing vortex has peak standard deviation area around the vortex core location throughout the entire chord length, and it expands in area after x/c = 87.5%. On the other hand, the peak standard deviation for the strake vortex diffuses and disappears after x/c = 75%. At $\alpha = 12^0$ (Figure 50b), the standard deviation results for Re = 2.34 x $10^5$ illustrate the same rotational movement between the strake and wing vortices from x/c = 62.5% to 87.5%, followed by the breakdown of the merged vortex at the trailing-edge. However, for the Re = 2.8 x $10^4$ case, the peak standard deviation is much lower compared with Re = 2.34 x $10^5$. For $\alpha = 16^0$ and Re = 2.34 x $10^5$ (Figure

50c), it can be seen that at x/c = 62.5% and 75%, the strake and wing vortices display rotational movement around each other, meanwhile the high standard deviation areas for both vortices have expanded at x/c = 75%. At x/c = 87.5%, only the standard deviation of a single merged vortex can be observed. At the trailing-edge, the standard deviation concentration of the merged vortex has disappeared due to the vortex breakdown. At higher angles of attack (Figure 50d and 50e), both Reynolds numbers show very diffused standard deviation, however the peak standard deviation around the vortex core is still present for upstream locations at $Re = 2.34 \times 10^5$.

Figure 51 shows the vortex meandering probability plot for the two Reynolds numbers. At $\alpha = 8^0$ (Figure 51a), the distance between the strake and wing vortex is greater at $Re = 2.34 \times 10^5$, and the peak probability values for the $Re = 2.34 \times 10^5$ case is generally less compared with $Re = 2.8 \times 10^4$ for all the chordwise locations. It can be observed that at x/c = 87.5% and $Re = 2.34 \times 10^5$, the strake vortex meandering probability starts expanding in area while dropping in peak probability, it then shows a broken-down profile downstream at the trailing-edge. For $\alpha = 12^0$ and $16^0$ (Figure 51b & 51c), it is quite distinctive that $Re = 2.34 \times 10^5$ has a much greater level of vortex interaction than $Re = 2.8 \times 10^4$. For both angles of attack, $Re = 2.34 \times 10^5$ cases show higher peak probability values for both vortices until x/c = 75%. At x/c = 87.5%, the strake and wing vortices for $Re = 2.34 \times 10^5$ cases undertake merging process while they spiral around each other and break down at the trailing-edge, as indicated by the decrease in meandering probability. However, for both angles of attack, the strake vortex for the $Re = 2.8 \times 10^4$ case displays a well defined probability distribution throughout the chord length with minimum interactions with the wing vortex; while the wing vortex starts showing signs of breakdown (dropping in peak probability and expanding in area) at x/c = 87.5% for $\alpha = 12^0$, and it is no longer distinguishable at x/c = 87.5% for $\alpha = 16^0$. As the angle of attack keeps increasing (Figure 51d & 51e), both Reynolds numbers show earlier onset of vortex breakdown, however the breakdown of the strake vortex for $Re = 2.8 \times 10^4$ occurs later than for $Re = 2.34 \times 10^5$. This indicates that a more stable strake vortex is achieved at a lower Reynolds number, while a more stable wing vortex is achieved at a higher Reynolds number.

To quantify the difference in the vortex meandering between the two cases further, vortex meandering amplitude is calculated, as seen in Figure 52. For $\alpha = 8^0$ (Figure 52a), it can be noticed that the meandering amplitude of the strake vortex for Re = 2.34 x $10^5$ is greater than the wing vortex, however in the Re = 2.8 x $10^4$ case both strake and wing vortex meandering amplitudes are similar. At $\alpha = 12^0$ (Figure 52b), for Re = 2.8 x $10^4$ the strake vortex is more stable throughout the chord length, the meandering amplitude for the wing vortex gradually increases after x/c = 75% and exceeds strake vortex meandering amplitude at x/c = 87.5%. For Re = 2.34 x $10^5$, the meandering amplitudes for both vortices keep relatively constant until x/c = 87.5%, after which a dramatic increase in meandering amplitude for both vortices can be observed. At $\alpha = 16^0$ (Figure 52c), the strake vortex for Re = 2.8 x $10^4$ is very stable with a small increase in the meandering amplitude between x/c = 50% and the trailing-edge, while the wing vortex is not distinguishable after x/c = 75%. On the other hand, both vortices for the Re = 2.34 x $10^5$ case start increasing in meandering amplitude after x/c = 75%, followed by a sharp increase between x/c = 87.5% and the trailing-edge, this indicates the onset of vortex breakdown. At $\alpha = 20^0$ and $24^0$ (Figure 52d & 52e), the same large scale increase in meandering amplitude (vortex breakdown) can also be found for the strake vortex at Re = 2.8 x $10^4$, which is consistent with previous results. However, since the wing vortex is not distinguishable for both angles of attack, it is not shown on the figure. For Re = 2.34 x $10^5$, both vortices also experience vortex breakdown as indicated by the sharp increase in meandering amplitude. At $\alpha = 20^0$ (Figure 52d), the Re = 2.34 x $10^5$ case shows higher strake vortex meandering amplitude than Re = 2.8 x $10^4$ for the same chordwise planes. At $\alpha = 24^0$ (Figure 52e), the strake vortex for Re = 2.8 x $10^4$ is very stable at x/c = 50% and 62.5%, however a sharp increase in the meandering amplitude can be seen after x/c = 62.5%. For Re = 2.34 x $10^5$, the wing vortex displays higher stability than the strake vortex before x/c = 87.5%, after which they both break down.

Figure 53 shows the time-averaged vorticity and the most energetic mode ($1^{st}$ mode) of the POD results for $\alpha = 8^0$ and $12^0$ at x/c = 75%. It can be seen for both Reynolds numbers that the most energetic mode displays a pair of counter rotating vortices at the locations of the time-averaged strake and wing vortices. The first POD mode for

Re = 2.8 x $10^4$ illustrates a more coherent structure, in addition the first POD modes of both Reynolds numbers show a similar level of vorticity magnitude.

### 5.2.2 Effect of Blowing Jet Location and Blowing Angle (β)

#### 5.2.2.1 Time-averaged Analysis

To examine the effect of a circular jet blowing as an active control method, various jet locations and blowing angles were tested at a fixed jet-momentum coefficient of Cμ = 2%. Time-averaged vorticity patterns in the crossflow plane at x/c = 87.5% with and without jet blowing of Cμ = 2% through hole #1 at various wing incidences and jet blowing yaw angles are illustrated in Figure 54. When there is no jet blowing, a strake vortex and a wing vortex can be observed over the wing model at α = 8°, 12° and 16° though their spanwise locations are slightly different (Figure 54a). At α = 8°, for β = 30° (Figure 54b), while the wing vortex remains at the same location, the strake vortex moves further inboard and away from the wing surface. The increased separation suggests weak interactions between the wing vortex and the strake vortex. However, this effect can be used to generate rolling moment for flight control. Increasing the wing incidence to α = 12°, the separation distance between the vortices decreases and resembles that of without jet blowing case, and both vortices move inboard closer to the wing centerline. Further increasing the wing incidence to α = 16°, the wing vortex appears moving away from the wing surface and closer to the strake vortex, suggesting intensified interaction and likely merging. Note that, for β = 30°, the rotation angle between the two vortices appears to increase with wing incidence as vortices get closer to each other. These phenomena have also been observed over a similar double delta wing model at a much higher Reynolds number of Re = 2.3 × $10^5$ by Zhang et al [82]. For all the wing incidences shown in Figure 54, with jet blowing through hole 1 and β = 60°, 75° and 90° (Figure 54c-e), only one coherent vortex is observed over the double delta wing except for one case. Note that, at α = 8° and β = 90°, a small vortex is observed close to the wing surface at y/s = -0.57 alongside the main vortex.

Figure 55 displays the effect of different blowing positions for three chosen blowing angles (β = $30^0$, $60^0$ and $90^0$) at α = $8^0$ and x/c= 87.5%. It can be observed that for β =

$30^0$ (Figure 55a), moving the blowing hole location downstream results in shortening the distance between the strake and wing vortices. Furthermore, at $\beta = 30^0$, blowing hole #1 displays the most effect; blowing hole #2 results in much diffused wing and strake vortices; blowing hole #3 shows similar effects as blowing hole #1 but with smaller distance between the two vortices and a more strengthened strake vortex; blowing hole #4 displays an interfered vortical field by the blowing jet. At $\beta = 60^0$, blowing hole #1 and #2 show similar vortical fields, in which only one diffused vortex alongside a small area of vorticity concentration can be observed. However, more complicated vortical fields are present for blowing hole #3 and #4 with the introduction of additional vortices originating from the blowing jet. At $\beta = 90^0$, similar vortical fields can be observed across all the blowing hole locations, which include the presence of a pair of distinctive strake and wing vortices. As the blowing hole location moves downstream, the distance between the two vortices widens slightly.

To uncover the vortical characteristics in crossflow planes, measurement data covering x/c = 50% to the trailing-edge for various selected blowing configurations are illustrated, Figure 56 displays the results for $\alpha = 8^0$. Without blowing, well defined strake and wing vortices are formed near the wing surface (Figure 56a). No vortex breakdown is observed over the double delta wing for this incidence. With jet blowing through hole #1 at $\beta = 30°$ (Figure 56b), both the wing vortex and the strake vortex become stronger. The strake vortex shifts inboard towards the wing centreline and moves away from the wing surface. It appears that the jet blowing feeds additional vorticity into both vortices, jet blowing also encourages the separation distance between the two vortices to increase. This becomes more profound as the vortices develop downstream and there is no sign of any interaction between the two vortices. On the contrary, only one coherent vortex can be observed over the double delta wing when increasing the jet yaw angle further to $\beta = 75°$ (Figure 56c). When increasing the incidence to $\alpha = 12°$, well defined wing and strake vortices can be found at the baseline case between x/c = 50% and 75% (Figure 57a), the wing vortex then becomes diffused and moves closer to the strake vortex at the trailing-edge. Similar effects are found at $\alpha = 8°$ and $\alpha = 12°$ for blowing hole #1 and $\beta = 30°$ (Figure 57b), both vortices have gained vorticity strength and moved inboard while the separating distance between them widens. At blowing hole #1 and $\beta = 75°$ (Figure 57c), a single strong coherent

vortex is displayed in the time-averaged vorticity patterns, which is the result of the merging of the vortices. In addition, very low vorticity concentration can be seen along the trajectory of the blowing jet. At blowing hole #3 and $\beta = 30°$ (Figure 57d), the wing and strake vortices merge into a well defined large vortex over the rear part of the wing after x/c = 75%. However, this merging process cannot be seen when increasing the jet yaw angle to $\beta = 60°$ (Figure 57e). Instead, an additional vortex inboard of the strake vortex is observed at x/c = 75%, which subsequently merges with the strake vortex at x/c = 87.5%.

Time-averaged vorticity patterns in crossflow planes over the double delta wing with and without jet blowing of various configurations at $\alpha = 16°$, 20° and 24° are displayed in Figures 58, 59 and 60, respectively. At $\alpha = 16°$, without jet blowing, well defined strake and wing vortices can be observed up to x/c = 75%, after which the two vortices start merging into one large coherent vortex at the trailing-edge. Figure 58a shows that the strake vortex appears much stronger than the wing vortex. The jet blowing through hole #2 at $\beta = 60°$ (Figure 58b) promotes early merging of the wing and strake vortices; the vortices merge into one coherent vortex at x/c = 87.5%. A similar merging process can also be observed at x/c = 87.5% with jet blowing through hole #3 at $\beta = 30°$ (Figure 58c), however this vortex undergoes breakdown at the wing trailing-edge. Increasing the wing incidence to $\alpha = 20°$, without jet blowing, Figure 59a shows only one merged coherent vortex and the vortex breakdown is observed at the trailing-edge. The vortex breakdown is delayed and the merged coherent vortex can be seen over the double delta wing with jet blowing through hole #2 at $\beta = 60°$ (Figure 59b). when increasing the jet blowing yaw angle to $\beta = 90°$ (Figure 59c), the flow patterns over the double delta wing resemble those of without jet blowing case, e.g. one merged vortex undergoes breakdown at the trailing-edge. At $\alpha = 24^0$ blowing hole #2 and $\beta = 75^0$ (Figure 60b), the delay of the vortex breakdown is more profound. At x/c = 62.5%, both the strake vortex and wing vortex are well present whereas the baseline case (Figure 60a) only displays a single strake vortex. Between x/c = 62.5% and 87.5%, the two vortices undertake a merging process; at the trailing-edge, a single merged vortex is present as opposite to the broken-down vortex shown in the baseline case. Blowing at hole #3 with $\beta = 90^0$ (Figure 60c) also delays the breakdown of vortices but less effective than blowing at hole #2 with $\beta = 75^0$ (Figure 60b).

Figure 61 shows the streamline plots for the blowing configurations at $\alpha = 8^0$. The baseline case (Figure 61a) indicates that the distance between the two vortices is small with many shared streamlines at the upstream planes. For the blowing hole #1 and $\beta = 30^0$ configuration (Figure 61b), it can be observed that the two vortices move apart with fewer shared streamlines between them, indicating weakened interactions of the two vortices compared to the baseline case. For blowing hole #1 and $\beta = 75^0$ (Figure 61c), only the circulation pattern of one single vortex is displayed until x/c = 87.5%. Between x/c = 87.5% and the trailing-edge, an extra circulation area can be found next to the main vortex. By comparing this with the vorticity plot (Figure 56c), the extra circulation is shown to be caused by the vorticity concentrations formed in the shear layer. The streamlines for blowing configurations at $\alpha = 12^0$ are shown in Figure 62. By comparing the blowing case at hole #1, $\beta = 30^0$ and the baseline case (Figure 62b and 62a), it can be seen that this blowing configuration enhances the wing vortex while weakens the strake vortex. The high crossflow velocity region (dense streamline area) of the strake vortex at x/c = 87.5% and at the trailing-edge has reduced significantly from the baseline case. At blowing hole #1 and $\beta = 75^0$ (Figure 62c), only the streamline pattern of one circulating region can be recognised. In addition, bending of the streamlines due to the blowing jet can be seen along the blowing jet direction, this jet interference is also present in the vorticity plot as indicated by the small additional vorticity concentration (Figure 57c). For blowing hole #3 and $\beta = 30^0$ (Figure 62d), the strake vortex streamlines become diffused at x/c = 62.5% compared with the baseline case due to the blowing jet being at a downstream location (x/c = 62.5%) with an outward blowing angle. At planes further downstream of x/c = 62.5%, the wing vortex moves much closer to the leading-edge, while the strake vortex remains in the same position as the baseline case. At blowing hole #3 and $\beta = 60^0$ (Figure 62e), the wing vortex moves slightly inboard towards the wing centreline. However, the strake vortex streamline is only recognisable up to x/c = 75%.

Figure 63 illustrates the streamline plots for configurations at $\alpha = 16^0$. At blowing hole #2 and $\beta = 60^0$ (Figure 63b), it can be observed that the overall streamline patterns are similar to those found in the baseline case. However, at x/c = 75%, the streamline structure has elongated in the spanwise direction and only one large circulation area

can be observed. Between x/c = 87.5% and the trailing-edge, the streamline profile also displays the circulating region caused by the vorticity concentration near the wing leading-edge found on the time-averaged vorticity result. At blowing hole #3 and $\beta = 30^0$ (Figure 63c), the streamline plot is rather different compared to the baseline case. It can be observed that at x/c = 75%, only the profile of one large circulating area is present, which is consistent with the single vortex found in the vorticity plot (Figure 58c). Downstream of x/c = 75%, the streamline profile consists of two circulating regions, one represents the merged vortex and one represents the vorticity concentration formed within the shear layer near the wing leading-edge. Figure 64 illustrates the streamline profile for blowing cases at $\alpha = 20^0$. Blowing at hole #2 and $\beta = 60^0$ (Figure 64b) shows little effect to the streamline profile, on the other hand, blowing at hole #2 and $\beta = 90^0$ (Figure 64c) displays mainly one circulating region for all the chordwise locations. The streamline plots for $\alpha = 24^0$ are displayed in Figure 65, blowing at hole #2 and $\beta = 75^0$ (Figure 65b) results in a very different streamline profile compared to the baseline case. At downstream planes (x/c = 87.5% and trailing-edge), only one large circulating region and a small counter rotating circulating region can be recognised. By comparing with the vorticity result (figure 60b), it shows that the large circulating region is due to the merged vortex, whereas the small counter rotating circulating region is caused by the secondary flow. Blowing at hole #3 and $\beta = 90^0$ (Figure 65c) displays the streamline profile of mainly two circulating regions, comparing with the vorticity results (Figure 60c), it indicates that one represents the merged vortex and the other represents the vorticity concentration found in the shear layer of the time-averaged vorticity plot.

#### 5.2.2.2 Unsteady Aspects

In order to understand the vortical flow patterns, the standard deviation results of the crossflow velocity fluctuations for the same configurations are illustrated in Figure 66 – Figure 70, baseline and blowing cases for $\alpha = 8^0$ are shown in Figure 66. It can be seen that without blowing, only one region of high standard deviation is observed in all crossflow planes; which suggests strong interaction between the wing and strake vortices. The region of the high standard deviation is smallest at x/c = 50% (the kink point) and appears to increase towards the trailing-edge (Figure 66a), thus suggesting

increased meandering amplitudes in the streamwise direction for both wing and strake vortices [83]. The jet blowing through hole #1 at $\beta = 30°$ adds unsteadiness to the vortex system over the double delta wing, in particular to the strake vortex. Figure 66b shows that, in all crossflow planes, the peak standard deviation for both strake and wing vortices are located near the vortex centres, suggesting large vortex meandering amplitudes and weak interactions. Note that the magnitude of peak standard deviation decreases in the streamwise direction and velocity fluctuations spread over a larger area, in addition a 'kidney' shaped high standard deviation area is observed near the strake vortex core. Figure 65c shows that jet turbulence can be identified when the jet yaw angle is increased further to $\beta = 75°$; it is likely that some of the initial jet turbulence is ingested into the vortex system, which may explain the merging of the vortex system into one vortex. This is similar to the observations of Marles and Gursul for vortex merging of co-rotating vortices in the freestream [70].

At the $\alpha = 12^0$ baseline case, both vortices appear meandering over the wing surface when evolving downstream as evidenced by the peak standard deviation regions centered on both the time-averaged wing vortex and strake vortex (Figure 67a). At $\alpha = 12^0$, blowing at hole #1 and $\beta = 30^0$ (Figure 67b), the strake vortex shows higher peak standard deviation of velocity fluctuations, suggesting higher meandering amplitude. In addition, the same 'kidney' shaped high standard deviation area is displayed near the strake vortex. Figure 67c shows the jet turbulence and how it interacts with the vortex system at a jet blowing yaw angle to $\beta = 75°$, it is suggested that turbulence ingestion aids the vortex merging. Figure 67d exhibits a strip of high standard deviation of velocity fluctuations wrapping around both the wing and strake vortices, suggesting intensified lateral movement of the vortices. This may further suggest intensified interactions between the two vortices and, at last, merging with each other. Figure 67e exhibits a small region of high peak standard deviation in the path of the jet blowing at x/c = 75% and inboard of the strake vortex. This peak standard deviation is centred on the aforementioned additional vortex, suggesting that the vortex is induced by the blowing jet.

Figure 68 shows the standard deviation plots at $\alpha = 16^0$, the result for the baseline case (Figure 68a) shows a much greater level of noise and lower overall standard

deviation magnitude than the blowing cases. Both blowing cases at this incidence restore the high standard deviation concentration of the strake vortex up to x/c = 87.5%, beyond which the peak standard deviation decreases significantly due to vortex breakdown. Moving to the cases at $\alpha = 20^0$, the standard deviation results can be found in Figure 69. Blowing at hole #2 and $\beta = 90^0$ (Figure 69c) shows very little effect on the overall standard deviation result compared with the baseline case. However, blowing at hole #2 and $\beta = 60^0$ (Figure 69b) restores the high standard deviation concentration of the strake vortex across all the chordwise planes. Blowing cases at $\alpha = 24^\circ$ are shown in Figure 70. Overall, blowing at this incidence shows the effect of restoring the high standard deviation concentration around the vortex core, it is more noticeable at blowing hole #2, $\beta = 75^0$ (Figure 70b). This finding can also be confirmed from the vorticity result (Figure 60), which indicates that blowing at this incidence delays the vortex breakdown.

Figure 71 displays the normalised meandering amplitude results for all the blowing and non-blowing configurations. At $\alpha = 8^\circ$ (Figure 71a), it can be seen that the baseline case shows a very low level of meandering amplitude compared with the other configurations. The meandering amplitudes for both wing and strake vortices in the baseline case are similar throughout the chord length. Blowing at hole #1 and $\beta = 30^0$ increases the overall meandering amplitude from x/c = 50% to 87.5%, but decreases the meandering amplitude at the trailing-edge when compared with the baseline case. For both the blowing and baseline cases, the wing vortex has larger meandering amplitude than the strake vortex after x/c = 75%. At blowing hole #1 and $\beta = 75^0$, the wing vortex is no longer recognisable but the strake vortex shows an increase in meandering amplitude for all the chordwise planes when compared with the baseline case. Figure 71b illustrates the meandering amplitude for cases at $\alpha = 12^\circ$. At the baseline case, the strake vortex meandering amplitude has a very similar level to the wing vortex at upstream locations (x/c = 50% to 75%); the wing vortex meandering amplitude then increases dramatically near the trailing-edge. All the blowing configurations at $\alpha = 12^\circ$ result in an increase in the meandering amplitude of the strake vortex, among them, blowing at hole #1 and $\beta = 75^0$ displays the largest increases. However, for the meandering amplitude of the wing vortex, blowing decreases its meandering amplitude at downstream planes compared with the baseline case.

At $\alpha = 16^{\circ}$ (Figure 71c), it can be seen that blowing increases the meandering amplitude of the strake vortex dramatically, especially for downstream locations between x/c = 75% and the trailing-edge. Whereas for the baseline case at $\alpha = 16^{\circ}$, both the strake and wing vortices meander at relatively low level. Blowing at hole #2 and $\beta = 60^{0}$ increases the meandering amplitudes of both vortices by more than double the magnitude. Blowing at hole #3 and $\beta = 30^{0}$ shows the biggest increase in meandering amplitude at this angle of attack, especially at downstream planes. At $\alpha = 20^{\circ}$ (Figure 71d), the wing vortex is not recognisable for most of the cases, in addition, a sharp increase in the strake vortex meandering amplitude can be seen for the baseline case and blowing hole #2, $\beta = 90^{0}$. Comparing with the corresponding vorticity result (Figure 59), it can be noticed that the sharp increase in meandering amplitude is related to the vortex breakdown at the trailing-edge for these two configurations. At blowing hole #2 and $\beta = 60^{0}$, however, this sharp increase in strake vortex meandering amplitude at the trailing-edge location is reduced by around 60%. This is also reflected in the vorticity results (Figure 59b), which illustrate the restoring of the broken-down vortex at the trailing-edge. At $\alpha = 24^{\circ}$ (Figure 71e), a dramatic increase in strake vortex meandering amplitude can be observed between x/c = 62.5% and 75% for the baseline case, indicating the onset of vortex breakdown. Blowing at hole #3 and $\beta = 90^{0}$ delays this sharp increase in meandering amplitude to x/c =87.5%. At blowing hole #2 and $\beta = 75^{0}$, the sharp increase in strake vortex meandering amplitude can no longer be observed, which suggests that the strake vortex breakdown at this configuration is delayed.

Figure 72 shows the total circulation for all the blowing configurations and angles of attack. At $\alpha = 8^{\circ}$ (Figure 72a), it can be observed that blowing from hole #1 with $\beta = 30^{0}$ increases the total circulation due to additional vortices being fed into both vortices by the jet blowing, whereas blowing from hole #1 with $\beta = 75^{0}$ displays similar levels of circulation as the baseline case. Differing from $\alpha = 8^{\circ}$, the normalized total circulations over the double delta wing $\alpha = 12^{\circ}$ with jet blowing are comparable to those of the without blowing case for $x/c \leq 75\%$ (Figure 72b). At $\alpha = 16^{\circ}$ (Figure 72c), the normalized total circulations over the double delta wing with jet blowing are comparable, though increased slightly, to that of the no blowing case. Blowing at hole

#3 with $\beta = 30^0$ causes deviation from the linear trend of the total circulation at x/c = 75%, which is just downstream of the blowing hole (at x/c = 62.5%). When increasing the angle of attack to $\alpha = 20^{\circ}$ and $24^{\circ}$ (Figure 72d & 72e), the total circulation exhibits only minor differences between the without and with jet blowing cases.

The effects of jet blowing on the vortical flow structures over the double delta wing can be illuminated further by comparing vortex centroids of various jet blowing configurations. In this thesis, for each configuration, the vortex centroid for each crossflow plane is calculated using equation (26),

$$(\bar{y}, \bar{z}) = \frac{1}{\Gamma} \int (y, z) \omega_x dA \tag{26}$$

Where

$$\Gamma = \int \omega_x dA \tag{27}$$

$\Gamma$ is the total circulation in the crossflow plane. The global vortex centroid, involving all the measurement planes overt the double delta wing, of each configuration is then calculated as follow,

$$(\bar{Y}, \bar{Z}) = M_v / \sum \Gamma \tag{28}$$

Where

$$M_v = \sum [(\bar{y}, \bar{z}) / (\frac{b}{2})] \cdot \Gamma \tag{29}$$

The results are present in Figure 73. It can be observed that, at $\alpha = 8°$ with jet blowing through hole #1 and depending on the jet blowing yaw angle $\beta$, the global vortex centroid moves inboard and away from or closer to the wing surface. As wing incidence increases, for the baseline cases, the global vortex centroid moves inboard towards the wing centerline and further away from the wing surface. With various jet blowing configurations, however, the global vortex centroid tends to move outboard

and closer to the wing surface. This may be an advantage for flight control with increasing angle of attack.

### 5.2.2.3 Proper Orthogonal Decomposition

The first POD mode (most energetic mode) of all the blowing and non-blowing configurations are illustrated from Figure 74 to Figure 78. For $\alpha = 8^{\circ}$ baseline case (Figure 74a), a pair of counter rotating vortices can be recognised at the wing and strake vortex locations, however they are not very distinctive due to the small distance between the two vortices. At blowing hole #1, $\beta = 60^{0}$ (Figure 74b) and blowing hole #1, $\beta = 75^{0}$ (Figure 74c), the vortex pair is more distinctive with better defined vortical structures, the jet-generated vorticity concentration for $\beta = 75^{0}$ also results in a pair of counter rotating vortices along the jet trajectory in the first POD mode. At $\alpha = 12^{\circ}$ baseline case (Figure 75a), a pair of counter rotating vortices can be observed at the strake and wing vortex locations from x/c = 62.5% to the trailing-edge, however the first POD mode also displays the decomposition of the vorticity concentration within the shear layer. At blowing hole #1 $\beta = 30^{0}$ (Figure 75b), very distinctive counter rotating vortex pairs can be observed for both the wing and strake vortices between x/c = 75% and the trailing-edge. At blowing hole #1, $\beta = 75^{0}$ (Figure 75c), the jet-generated vortex found on the vorticity plot displays a counter rotating vortex pair in the first POD mode, which follows the trajectory of the blowing jet. In addition, at the location of the merged vortex, a counter rotating vortex pair can also be observed. For blowing at hole #3 with $\beta = 30^{0}$ (Figure 75d), planes between x/c = 50% and 75% illustrate counter rotating vortex pairs at the strake and wing vortices. However, from x/c = 87.5% to the trailing-edge, the vortex pair can only be found at the strake vortex location. At blowing hole #3 with $\beta = 60^{0}$ (Figure 75e), the counter rotating vortex pair can be observed at both the strake and wing vortex locations between x/c = 62.5% and the trailing-edge. As the angle of attack increases to $\alpha = 16^{\circ}$ (Figure 76), the first POD mode for the baseline case starts losing the coherent vortex pair structure and has a higher noise level due to the increase in vortex unsteadiness at higher angles of attack. However, blowing at hole #2 with $\beta = 60^{0}$ (Figure 76b) results in well defined counter rotating vortex pairs for both the strake and wing vortices, whereas blowing at hole #3,

$\beta = 30^0$ (Figure 76c) introduces even more noise into the POD results. This can be confirmed by the time-averaged vorticity result (Figure 58), as blowing at hole #2 and $\beta = 60^0$ enhances the strake vortex, and blowing at hole #3 and $\beta = 30^0$ accelerates the onset of vortex breakdown. For higher angles of attack at $\alpha = 20^\circ$ and $24^\circ$ (Figure 77 and 78), due to the earlier onset of vortex breakdown, the first POD mode displays very noisy vortical patterns with many additional vortices.

### 5.2.3 Effect of Jet Momentum Coefficient (Cμ)

Figure 79 illustrates the effect of changing the blowing momentum coefficient on the vortical flow at $\alpha = 8^\circ$, hole #1 and $\beta = 30^\circ$. It can be found that as the momentum coefficient increases, the distance between the strake and wing vortices also increases. For the baseline case (Figure 79a), the two vortices are very close to each other, their positions are also close to the wing surface and near the leading-edge. As blowing is added at $C\mu = 0.5\%$ (Figure 79b), the strake vortex moves inboard towards the wing centreline and away from the wing surface. On the other hand, the wing vortex is slowly attracted to the strake vortex from x/c = 62.5% to 75%, then it merges with the strake vortex at x/c = 87.5%. At $C\mu = 1\%$ (Figure 79c), the merging of the two vortices seen at $C\mu = 0.5\%$ is no longer visible, the two vortices show great separating distance between them. In addition, both vortices have gained more strength and display better defined vortical structures. Moving to $C\mu = 2\%$ (Figure 79d), the distance between the two vortices has been widened further, with the strake vortex moving closer to the wing centreline and the wing vortex moving closer to the wing leading-edge. Both vortices also show higher vorticity strength as a result of blowing. Figure 80 displays the effect of changing the momentum coefficient to $\alpha = 12^\circ$, hole #1 and $\beta = 75^\circ$. Compared with $\alpha = 8^\circ$, hole #1 and $\beta = 30^\circ$, it can be observed that in this case increasing the jet momentum coefficient encourages the merging process of the two vortices. Blowing at $C\mu = 0.5\%$ (Figure 80b) causes the merging of the two vortices at the trailing-edge and results in a more diffused strake vortex. At $C\mu = 1\%$ (Figure 80c), only one single vortex is observed from x/c = 62.5% to the trailing-edge. In addition, this single vortex moves closer to the wing leading-edge than the strake vortex position at $C\mu = 0.5\%$. Blowing at $C\mu = 2\%$ also results in only one single vortex throughout the wing section, the vortex appears to be enhanced and its position

moves even closer to the wing leading-edge. Also, a jet-generated vortex can be observed along the trajectory of the blowing jet.

Figures 81 and 82 show the first mode of the POD results for the two changing momentum coefficient cases. At $\alpha = 8^{\circ}$, hole #1 and $\beta = 30^{\circ}$ (Figure 81), as the momentum coefficient increases and the two vortices interact less, better defined counter rotating vortex pairs can be observed on the strake and wing time-averaged vortex locations in the first POD mode. At $\alpha = 12^{\circ}$ baseline case (Figure 82a), the first POD mode shows increased noise level, in addition, the vortex pairs at the strake and wing vortex locations are not as distinctive as the baseline cases at $\alpha = 8^{\circ}$ (figure 81a). As blowing is introduced at $\alpha = 12^{\circ}$, hole #1 and $\beta = 75^{\circ}$ for $C\mu = 0.5\%$ and 1%, multiple vortical structures in the POD results are present, their positions appear to be around the secondary vortex location seen in the time-averaged vorticity results (Figure 80b & 80c). At $C\mu = 2\%$, a counter rotating vortex pair can be observed along the location of the jet-generated vortex, this jet-generated vortex can also be seen in the time-averaged vorticity result, such a vortex pair is not present at $C\mu = 0.5\%$ and 1%.

Vortex meandering amplitude results for the two changing momentum coefficient cases are displayed in Figure 83. For $\alpha = 8^{\circ}$, blowing hole #1 and $\beta = 30^{\circ}$ (Figure 83a), it is observed that the baseline case displays very low meandering amplitude from x/c = 50% to 87.5%, then a great increase occurs at the trailing-edge. As $C\mu$ increases to 0.5%, both the strake and wing vortices illustrate very high meandering amplitude throughout the wing section, across all the momentum coefficients it is the highest between x/c = 75% and the trailing-edge. As the momentum coefficient increases from 0.5%, the meandering amplitudes for both the strake and wing vortices decrease from the level shown at $C\mu = 0.5\%$, overall the meandering amplitude for the wing vortex is greater than the strake vortex. At a momentum coefficient equal to 2%, the meandering amplitudes for both vortices decrease further between x/c = 75% and the trailing-edge. However, at this momentum coefficient, the meandering amplitude for the strake vortex increases greatly at x/c = 50% and 62.5% when compared with the baseline case.

Blowing and non-blowing cases for $\alpha = 12^{\circ}$ at hole #1 and $\beta = 75^{\circ}$ are shown in Figure 83b. For the baseline case, the strake vortex shows a very steady and low meandering amplitude throughout the wing section, but the wing vortex meandering shows a sharp increase after x/c = 75%, which corresponds to the expansion and diffusion of the wing vortex seen on the vorticity result (Figure 80a). The $C\mu = 0.5\%$ case experiences the sharpest increase in meandering amplitude for both vortices at x/c = 87.5%, which can relate to the vortex merging and the onset of vortex breakdown seen in Figure 80b. At upstream locations, blowing at $C\mu = 0.5\%$ results in a much higher meandering amplitude for the wing vortex. As momentum coefficient increases from 0.5%, the vortex meandering amplitude decreases for downstream locations. For higher momentum coefficients, the wing vortex is no longer recognisable and only the meandering amplitude of the strake vortex is shown. At $C\mu = 1\%$, the meandering amplitude of the strake vortex increases slightly from the baseline case between x/c = 50% and 87.5%, followed by a sharp increase at the trailing-edge. At $C\mu = 2\%$, the meandering amplitude of the strake vortex is very steady throughout the wing section. It is increased greatly from the baseline level at upstream locations (x/c = 50% to 75%), but a similar level is then maintained up to the trailing-edge.

Figure 84 illustrates the normalised circulation results for the two changing Cμ cases and the baseline cases. For the baseline case at $\alpha = 8^{\circ}$, it is observed that both the strake and wing vortices show lower levels of circulation than the blowing cases; between them, the wing vortex displays a slightly lower circulation level than the strake vortex. For the blowing cases, as the momentum coefficient increases, the overall circulation level of the strake vortex tends to decrease. At $\alpha = 8^{\circ}$ and $C\mu = 0.5\%$ (Figure 84a), the strake vortex circulation is at a similar level to the other blowing cases between x/c = 50% and 75%, it then shows a sharp increase after x/c = 75%, such a sharp increase in circulation is not observed for the higher momentum coefficient. On the other hand, for the wing vortex, blowing at $C\mu = 1\%$ shows the highest circulation throughout the wing section. As the angle of attack increases to $12^{\circ}$ (Figure 84b), the circulation of the strake vortex increases while the circulation of the wing vortex decreases when compared with $\alpha = 8^{\circ}$ (Figure 84a). For the strake vortex, at upstream locations (x/c = 50% and 62.5%), blowing at $C\mu = 2\%$ results in the lowest circulation, followed by the baseline case. Moving downstream (between x/c = 75% and the trailing-edge), for the strake vortex, the baseline case displays the lowest

circulation and the Cμ = 1% case has the highest circulation. For the wing vortex, the baseline case displays the biggest increase in circulation as the measurement plane moves from x/c = 50% to the trailing-edge. Blowing at Cμ = 1% and 2% shows the most consistent wing vortex circulation levels throughout the wing section.

## 5.3 Conclusion

Studies have been carried out investigating the effects of Reynolds number, blowing yaw angle, blowing location and momentum coefficient on the vortical flow over a double delta wing. A dual-vortex structure is observed at the mid-chord location for the higher Reynolds number case tested in the wind tunnel; however, the same dual vortex structure is not present for the lower Reynolds number tested in the water tunnel. As the angle of attack increases, both wing and strake vortices start experiencing earlier onset of vortex breakdown for both Reynolds numbers. At the higher Reynolds number, the strake vortex breaks down first; however, at the lower Reynolds number, the wing vortex breaks down first. Greater interactions between the two vortices can be observed at the higher Reynolds number. The higher Reynolds number also results in a higher and more concentrated peak standard deviation around the vortex core, in addition, greater meandering amplitude is also observed. With the jet blowing, depending on the blowing configuration, the interaction between the two vortices can be intensified as well as reduced. In particular, blowing at hole #1 with $\beta = 30^{o}$ results in increased distance between the two vortices and strengthened vortices. On the other hand, blowing at hole #1 and $\beta = 75^{o}$ results in only one merged vortex, together with the presence of small vorticity concentration along the blowing jet trajectory. A 'kidney' shaped high standard deviation area is present for blowing hole #1 and $\beta = 30^{o}$, the total circulation at this configuration also increases from the baseline level. The POD analysis displays a pair of counter rotating vortices at the strake and wing vortex locations on the 1$^{st}$ mode. As the angle of attack increases the vortex pair starts losing its structure due to the earlier onset of vortex breakdown. To investigate the effect of momentum coefficient, the following two cases were selected, which were: 1) $\alpha = 8^{o}$, blowing hole #1 and $\beta = 30^{o}$, and 2) $\alpha = 12^{o}$, blowing hole #1 and $\beta = 75^{o}$. It can be observed that as the momentum coefficient increases, the distance between the two vortices widens and the interaction weakens for $\alpha = 8^{o}$ case. However,

increasing the momentum coefficient at $\alpha = 12^0$ case encourages the merging process of the two vortices.

## 5.4 Figures

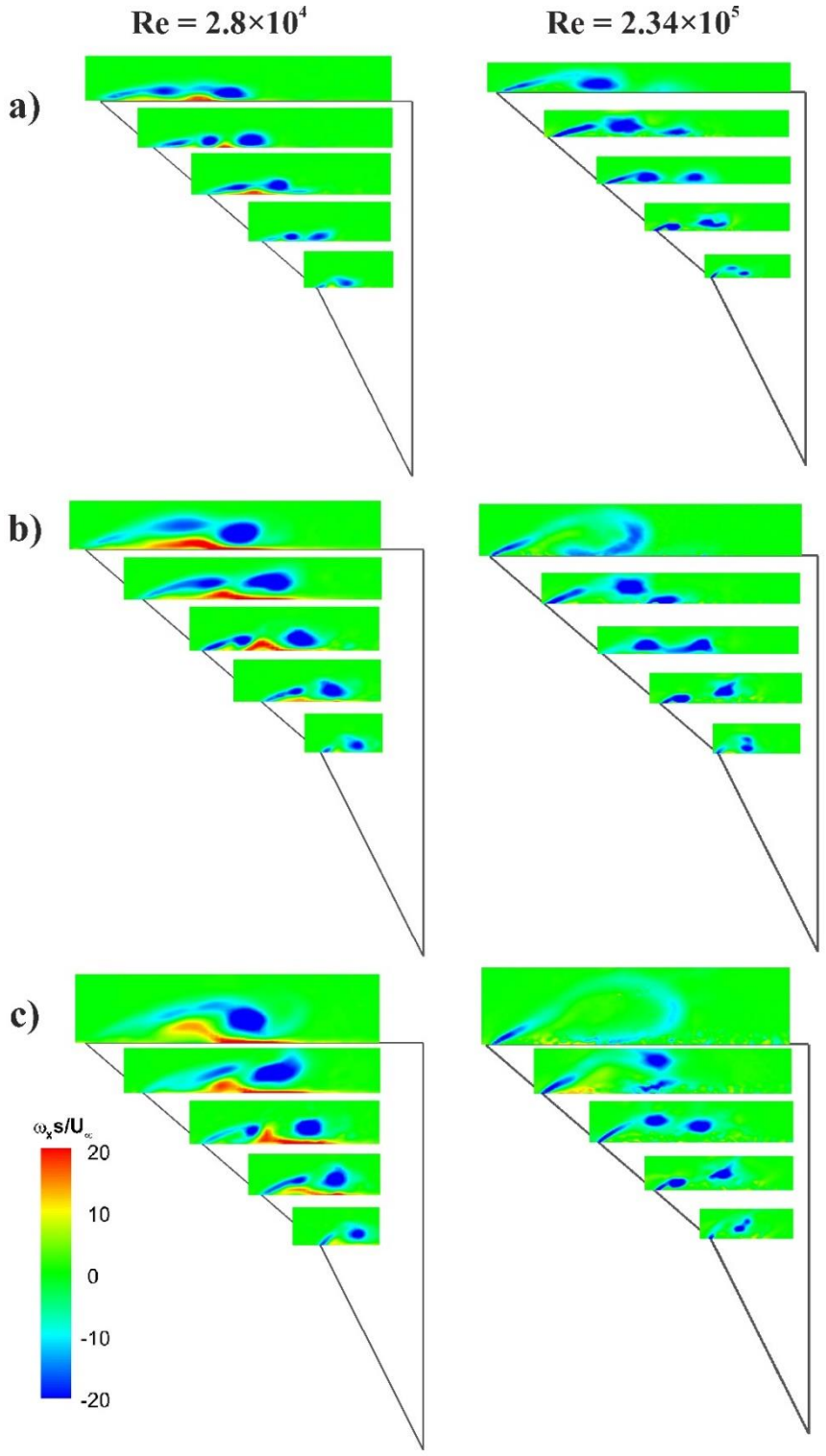


Figure 48. Time-averaged vorticity for a) α = 8º; b) α = 12º; c) α = 16º; d) α = 20º and e) α = 24º

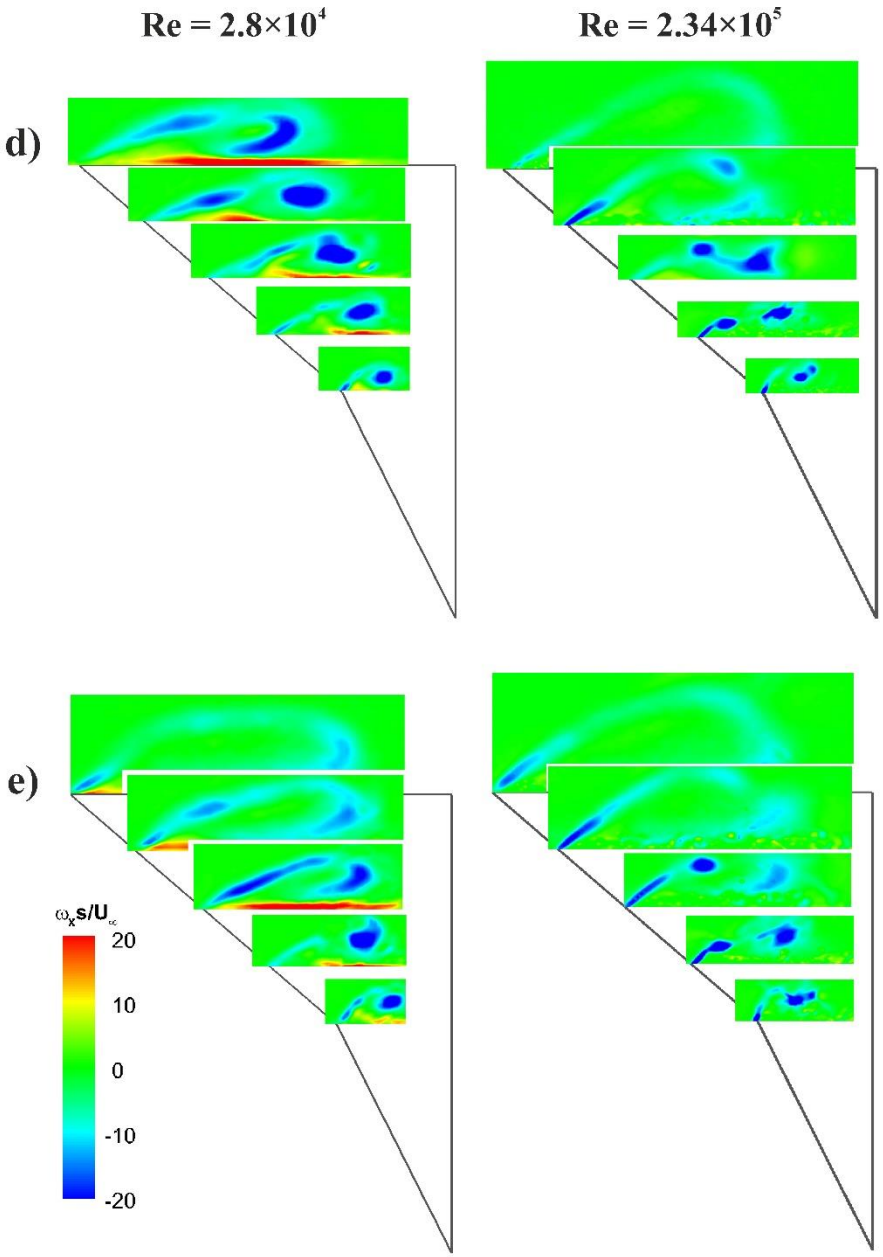


Figure 48. Continued.

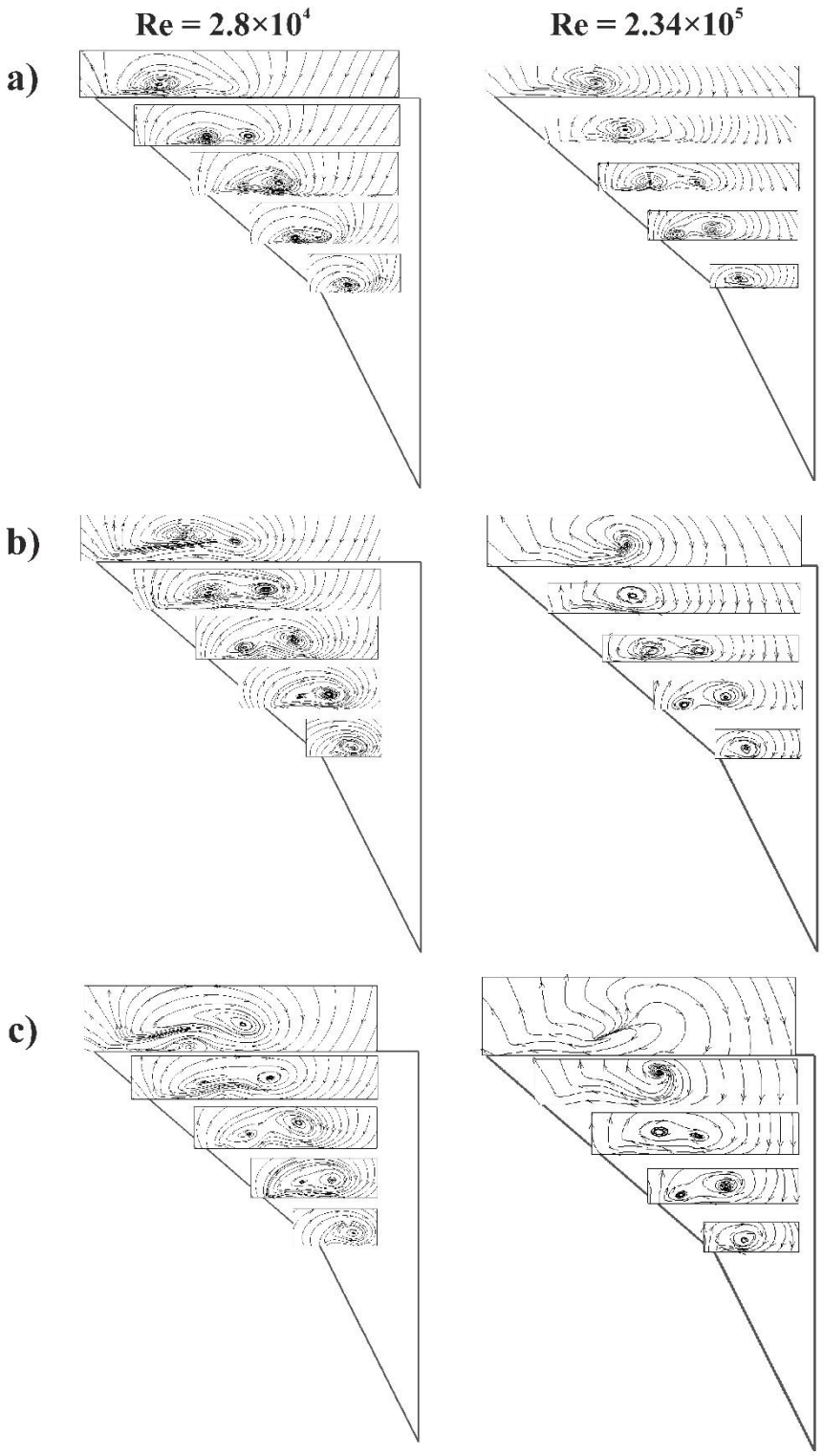


Figure 49. Streamline for a) α = 8º; b) α = 12º; c) α = 16º; d) α = 20º and e) α = 24º;

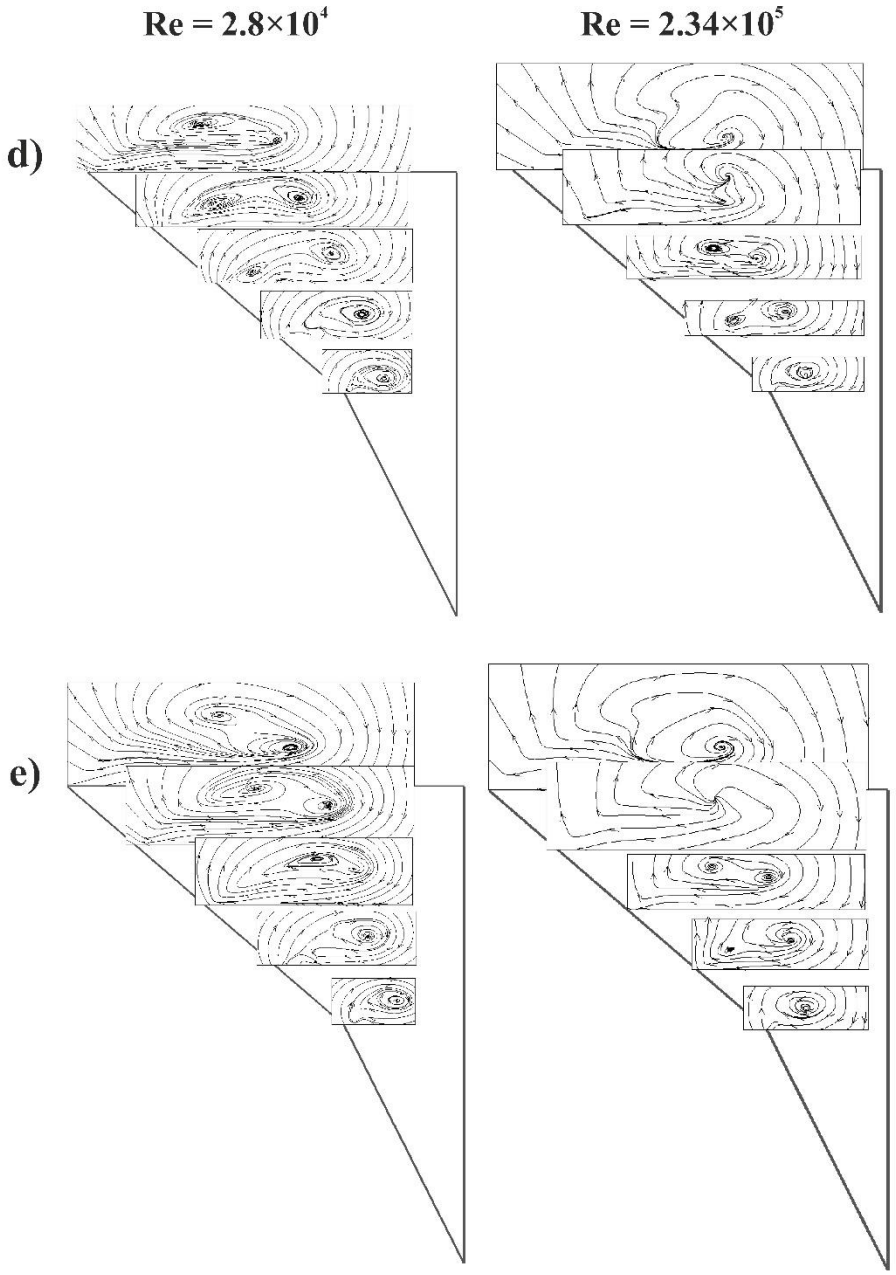


Figure 49. Continued.

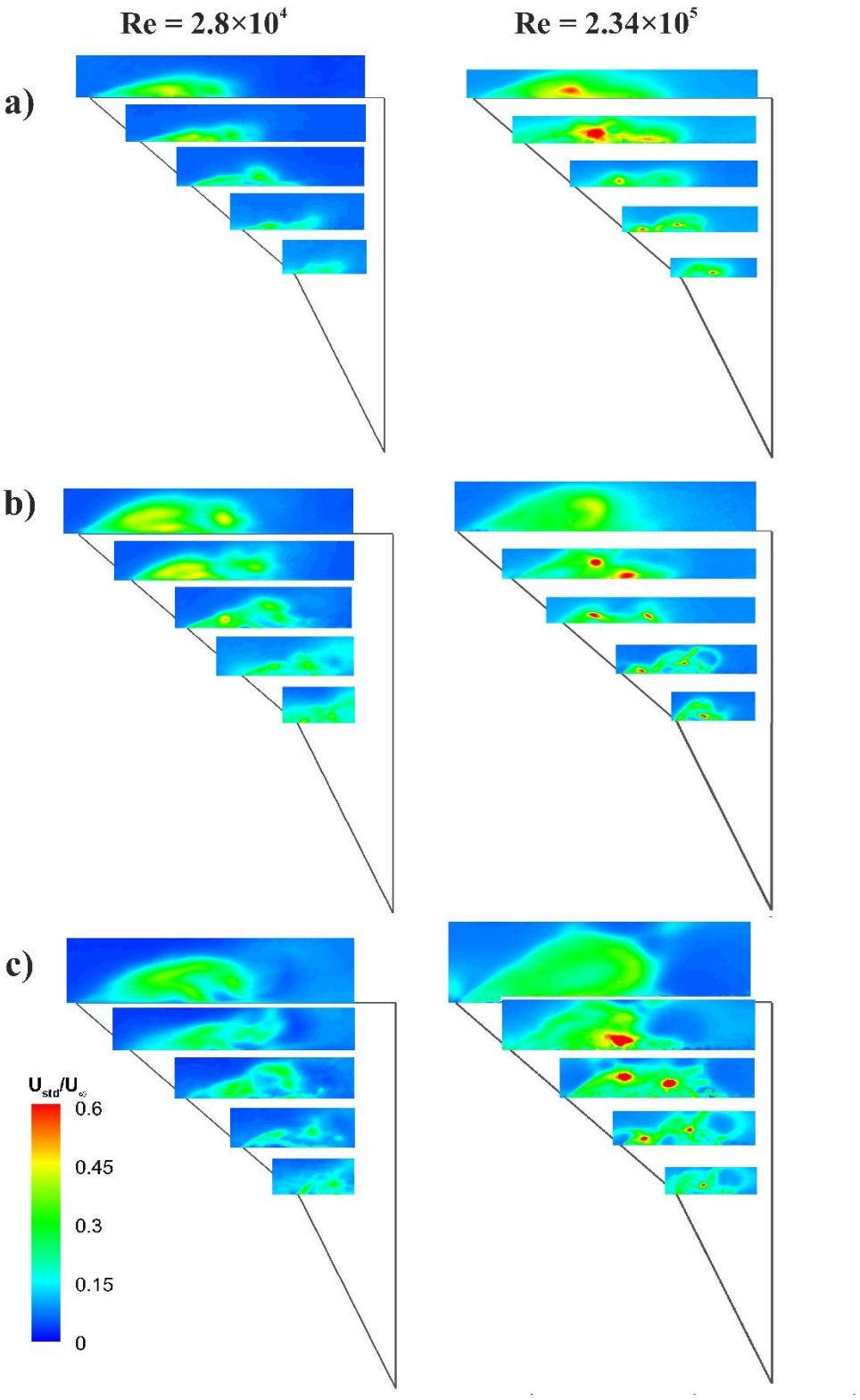


Figure 50. Standard deviation for a) α = 8º; b) α = 12º; c) α = 16º; d) α = 20º and e) α = 24º;

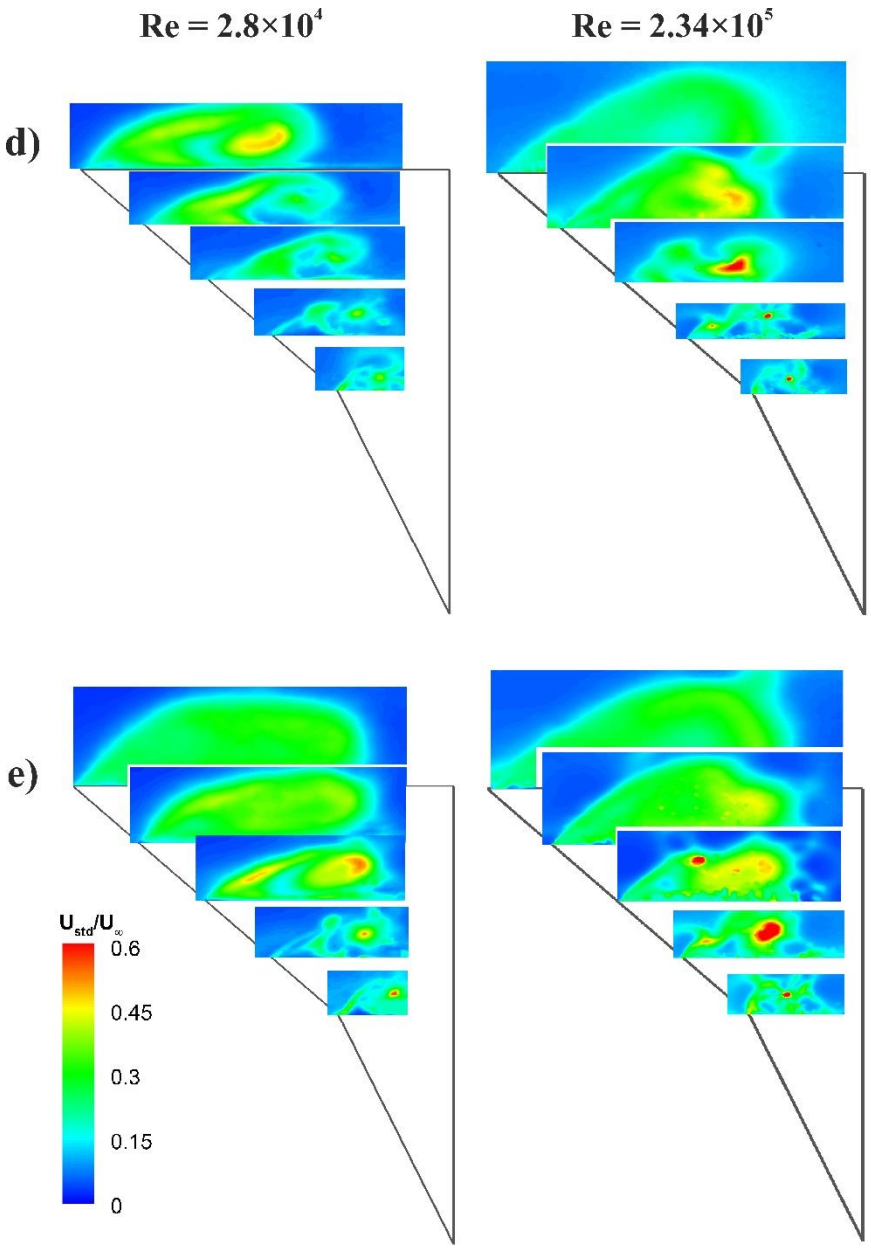


Figure 50. Continued.

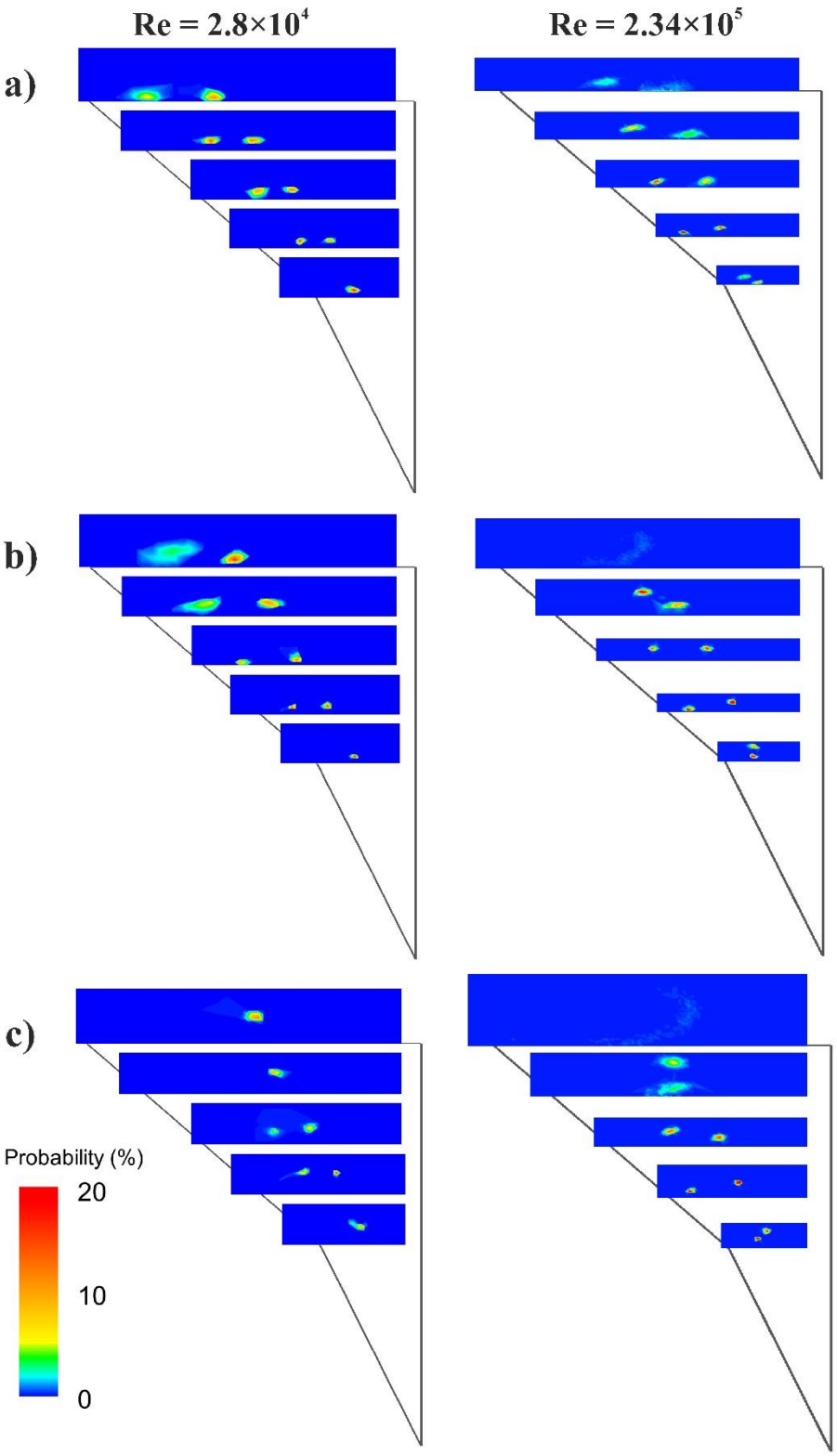


Figure 51. Meandering probability for a) α = 8º; b) α = 12º; c) α = 16º; d) α = 20º and e) α = 24º;

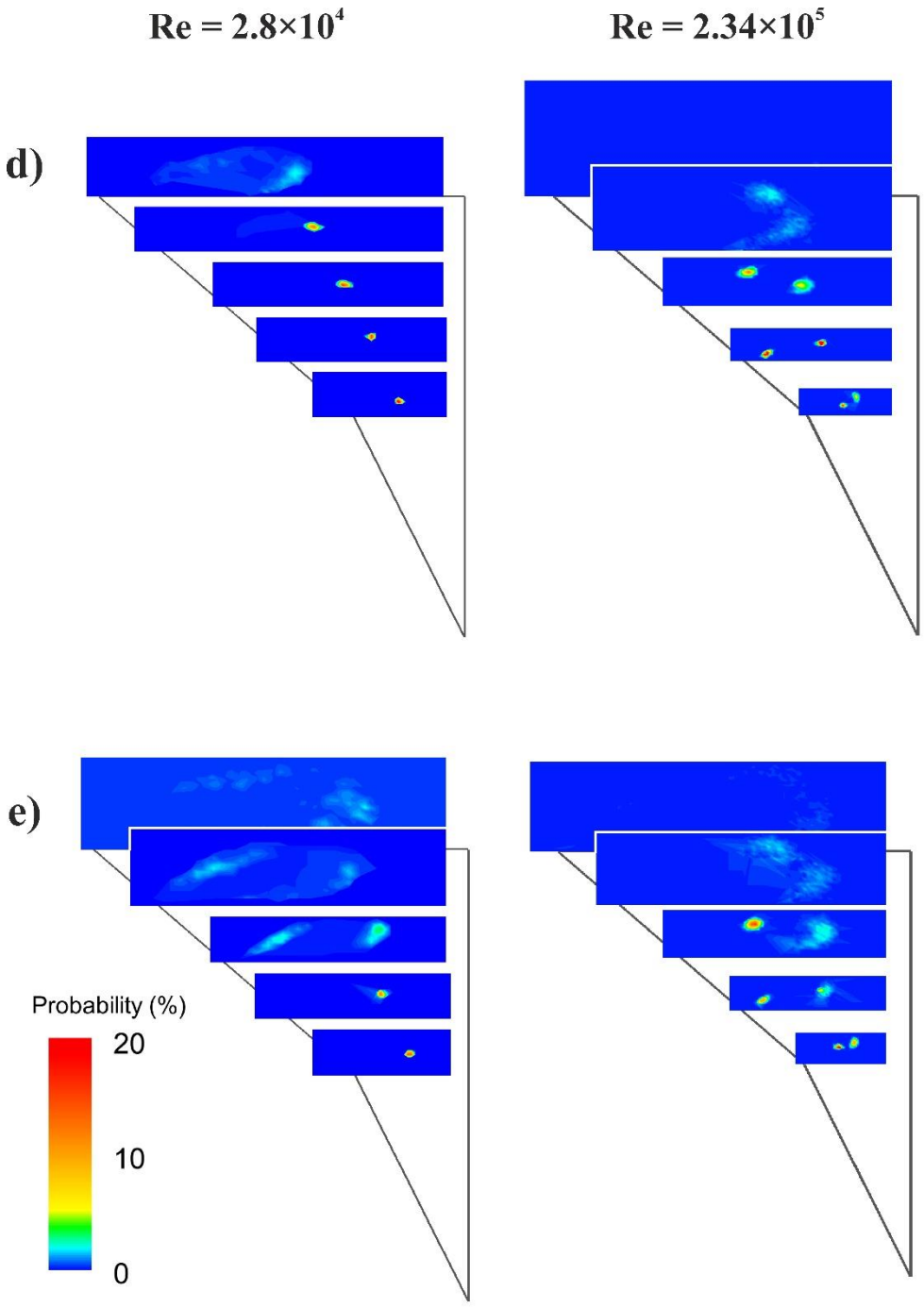


Figure 51. Continued.

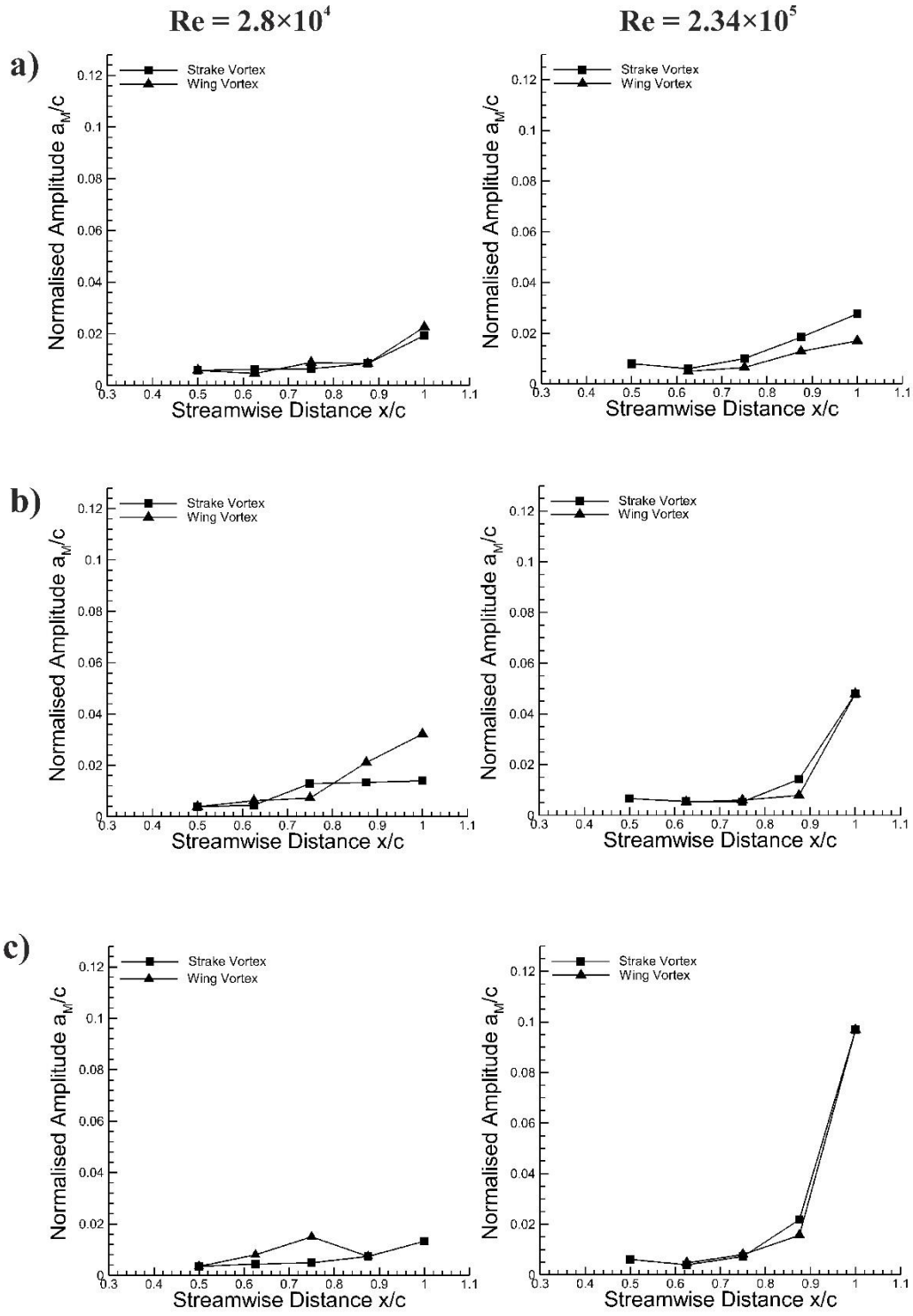


Figure 52. Normalised meandering amplitude for a) α = 8º; b) α = 12º; c) α = 16º; d) α = 20º and e) α = 24º;

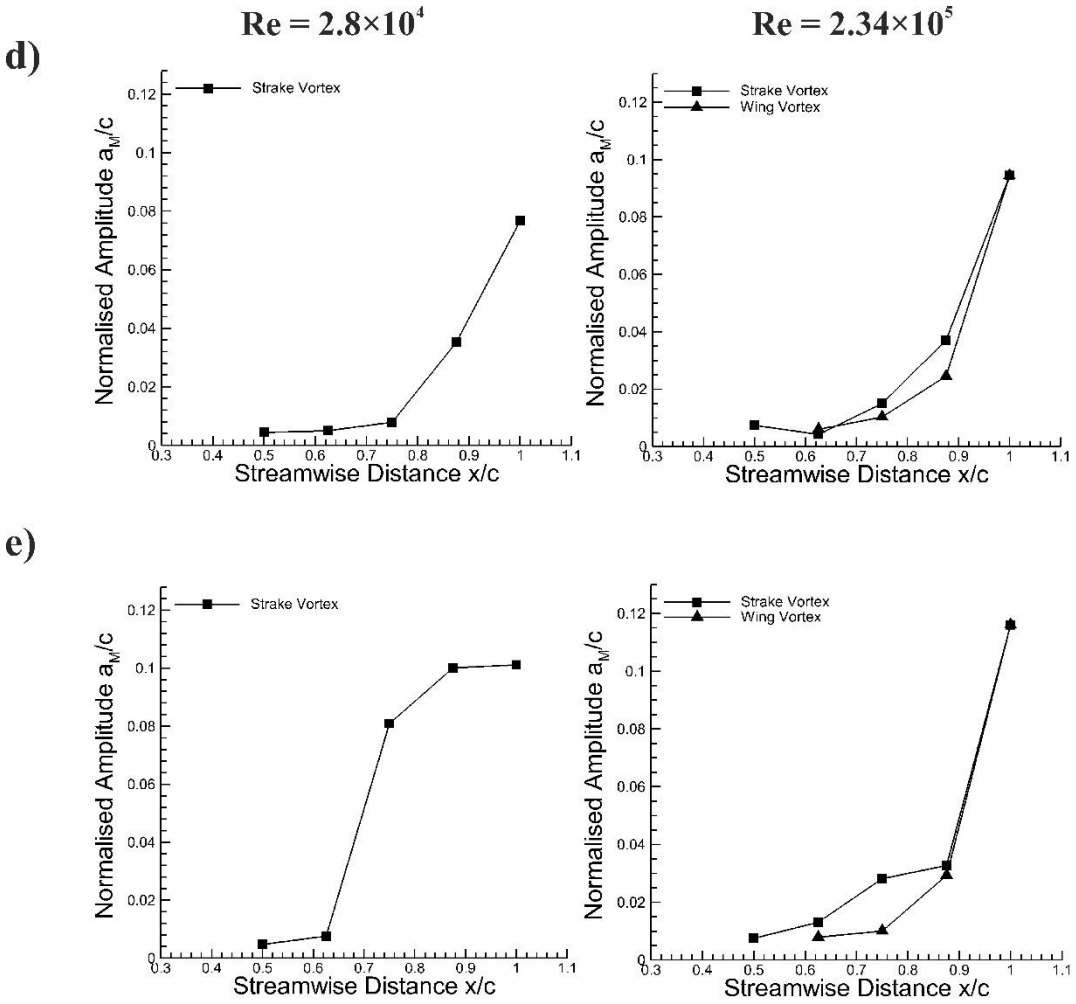


Figure 52. Continued.

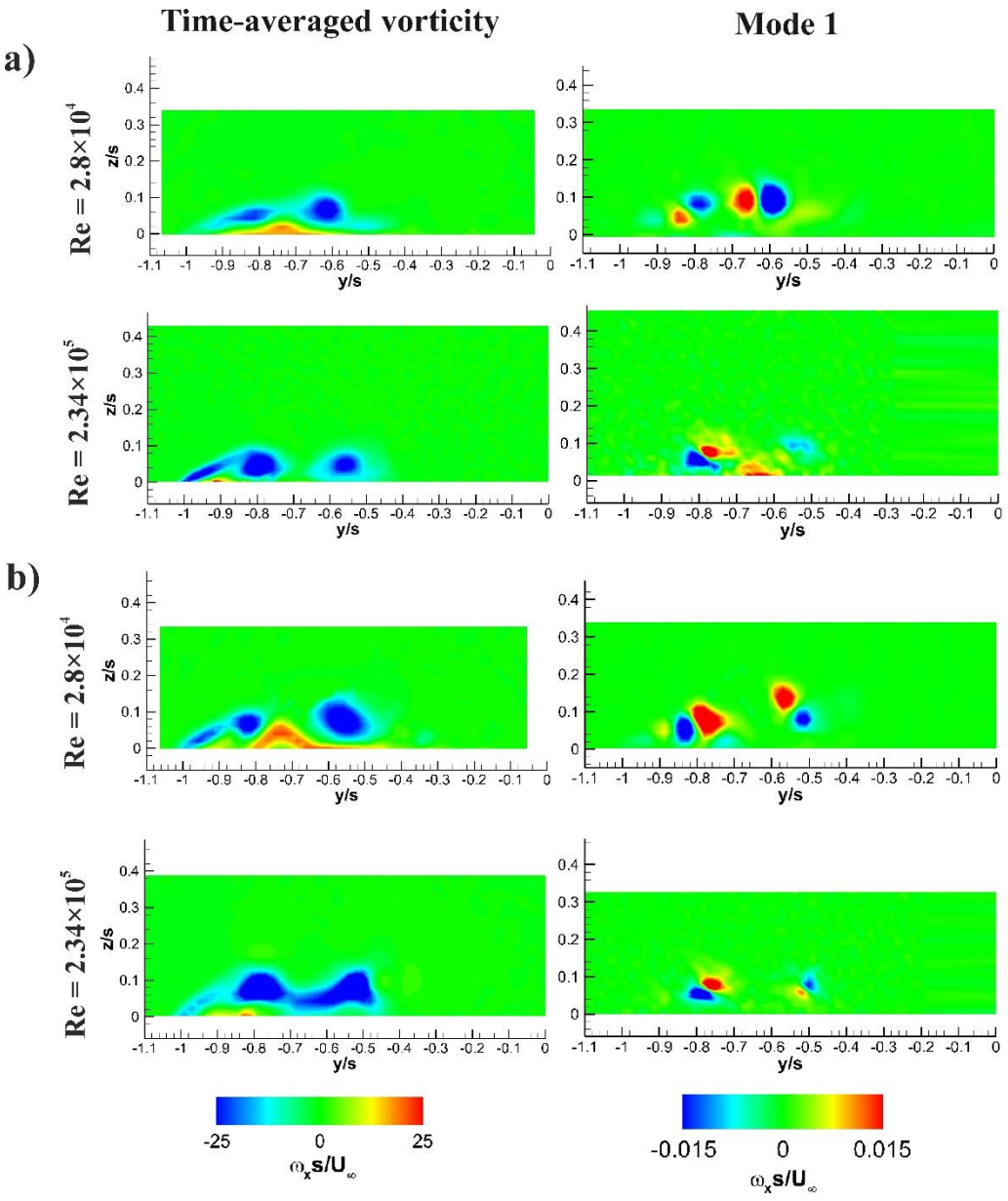


Figure 53. Time-averaged vorticity and first POD mode for a) $\alpha = 8^{o}$ and b) $\alpha = 12^{o}$.

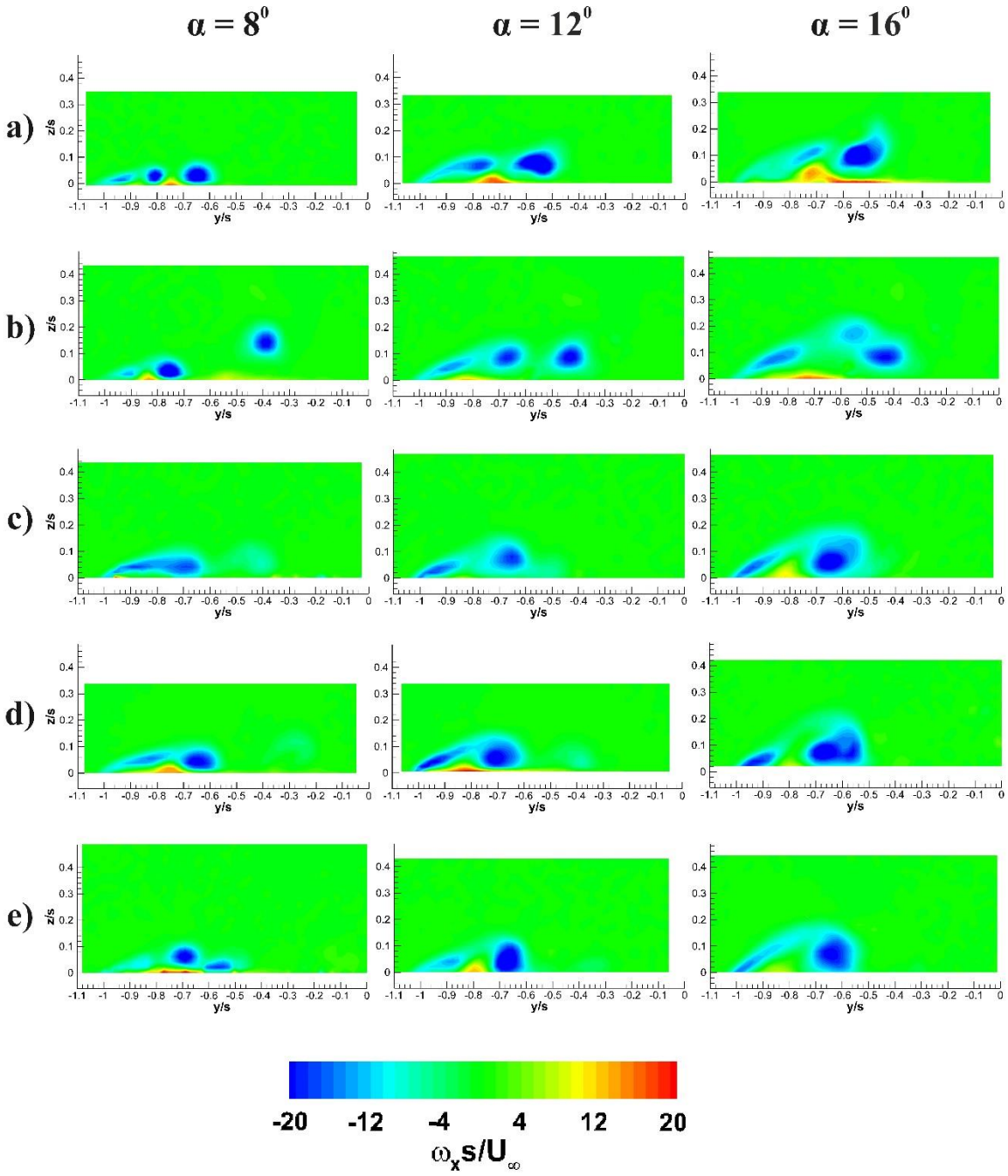


Figure 54. Time-averaged vorticity patterns in the crossflow planes at and x/c = 87.5% over double delta wing with and without blowing through hole #1 at various wing incidences for a) without blowing; b) β = 30º; c) β = 60º; d) β = 75º and e) β = 90º;

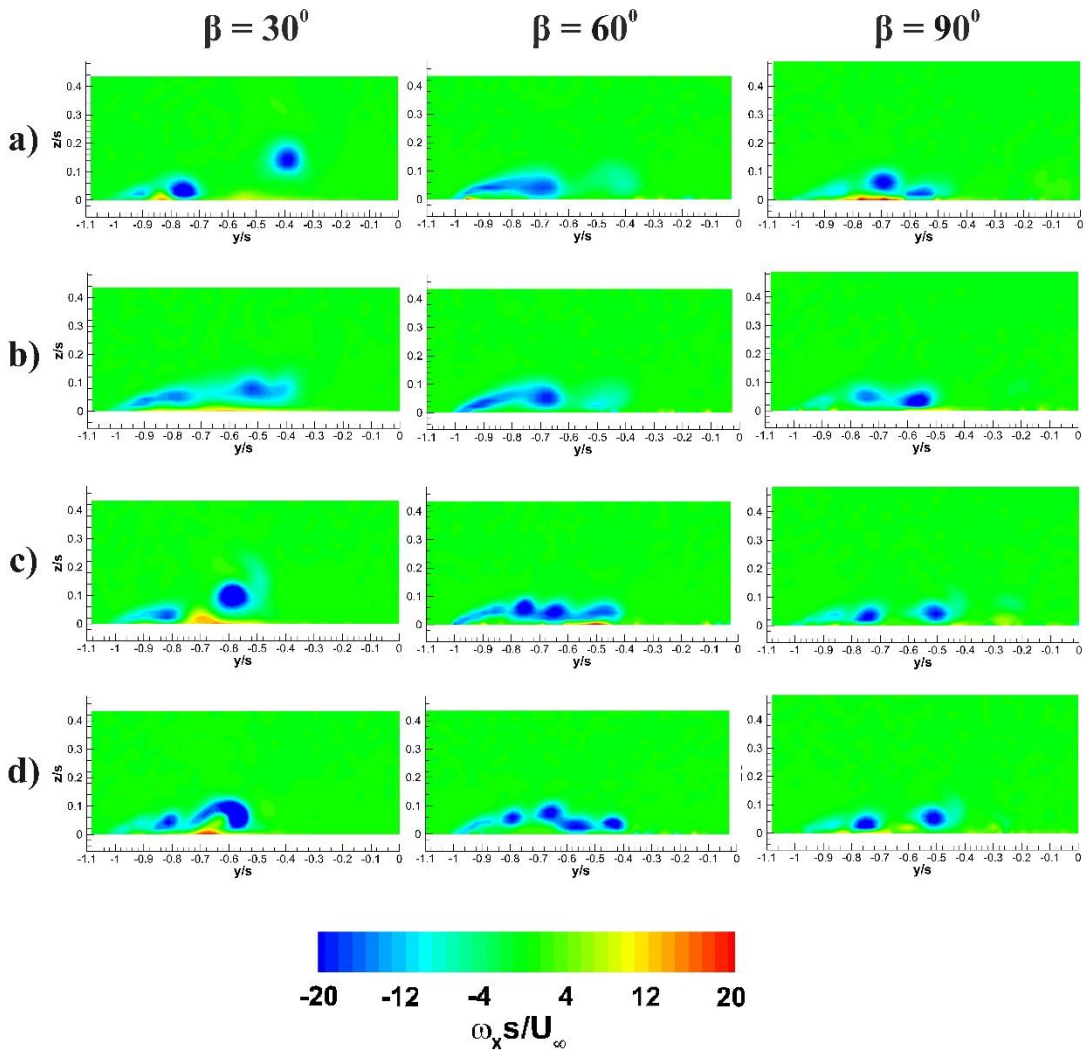


Figure 55. Time-averaged vorticity at α = 8º and x/c = 87.5% for a) blowing hole #1; b) blowing hole #2; c) blowing hole #3 and d) blowing hole #4.

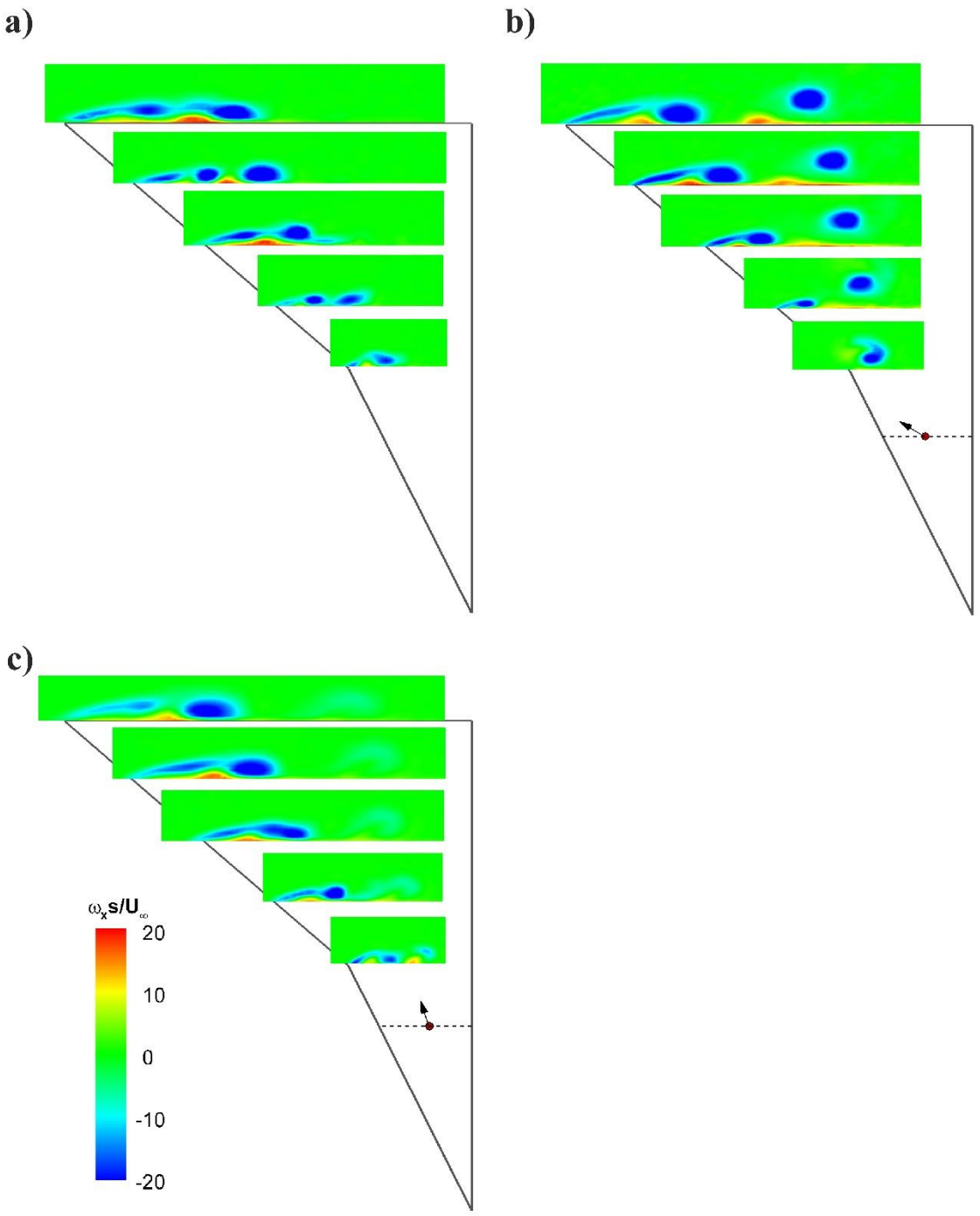


Figure 56. Time-averaged vorticity for α = 8º at a) baseline case; b) blowing hole #1, β = 30º and c) blowing hole #1, β = 75º.

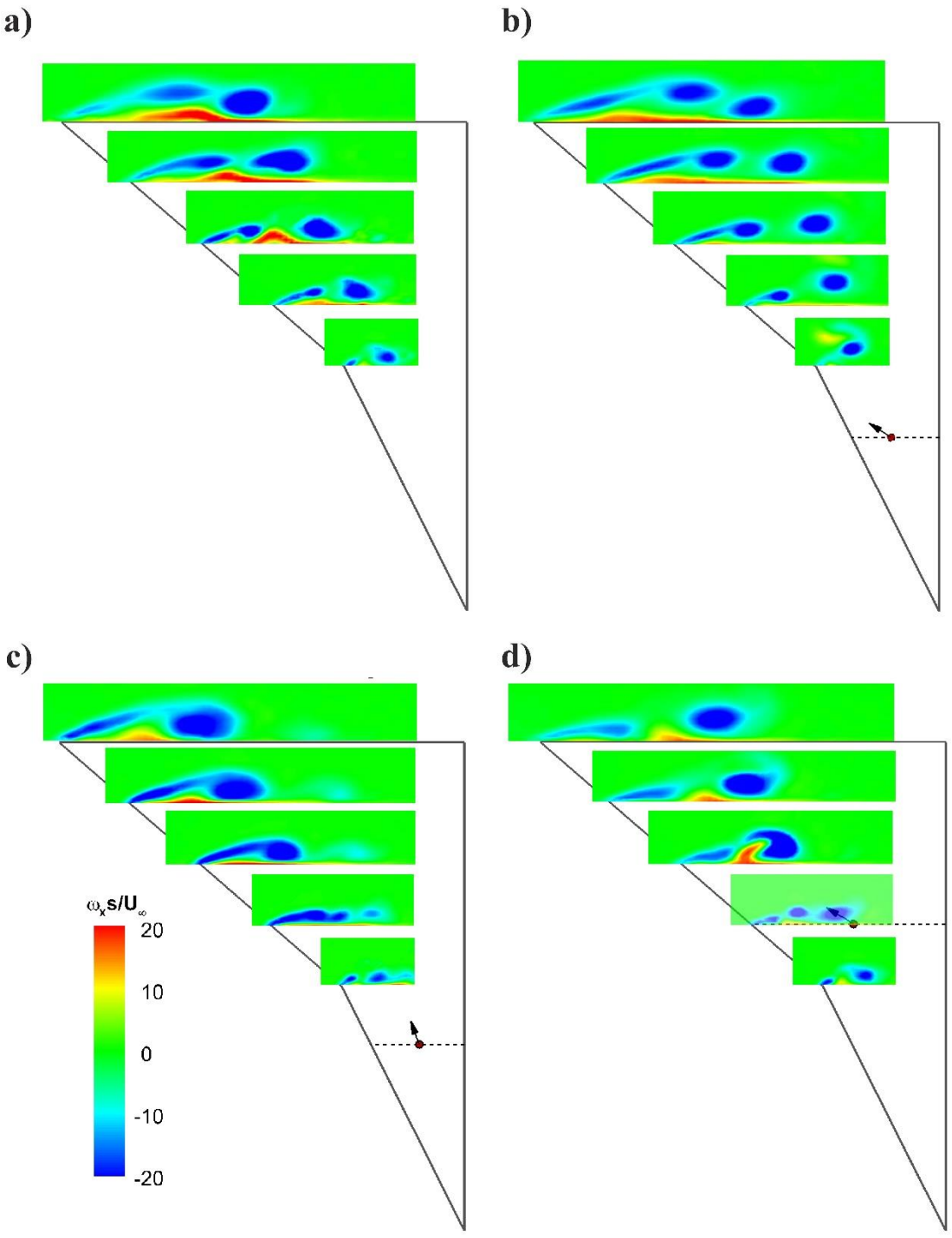


Figure 57. Time-averaged vorticity for α = 12º at a) baseline case; b) blowing hole #1, β = 30º; c) blowing hole #1, β = 75º; d) blowing hole #3, β = 30º and e) blowing hole #3, β = 60º.

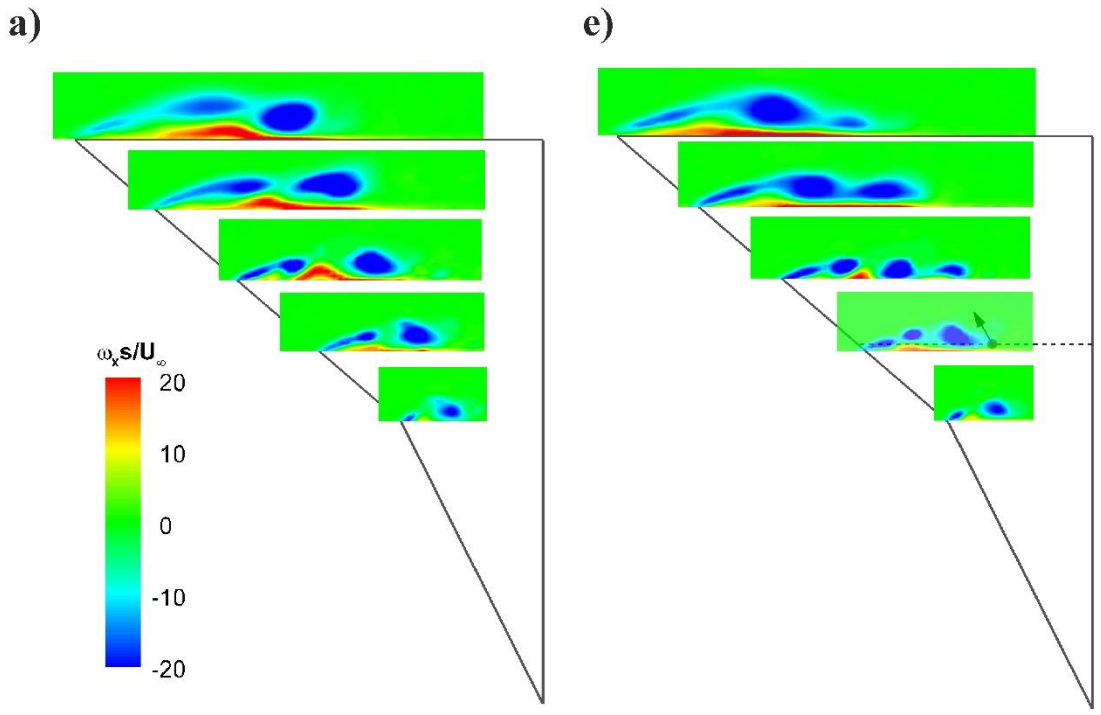


Figure 57. Continued.

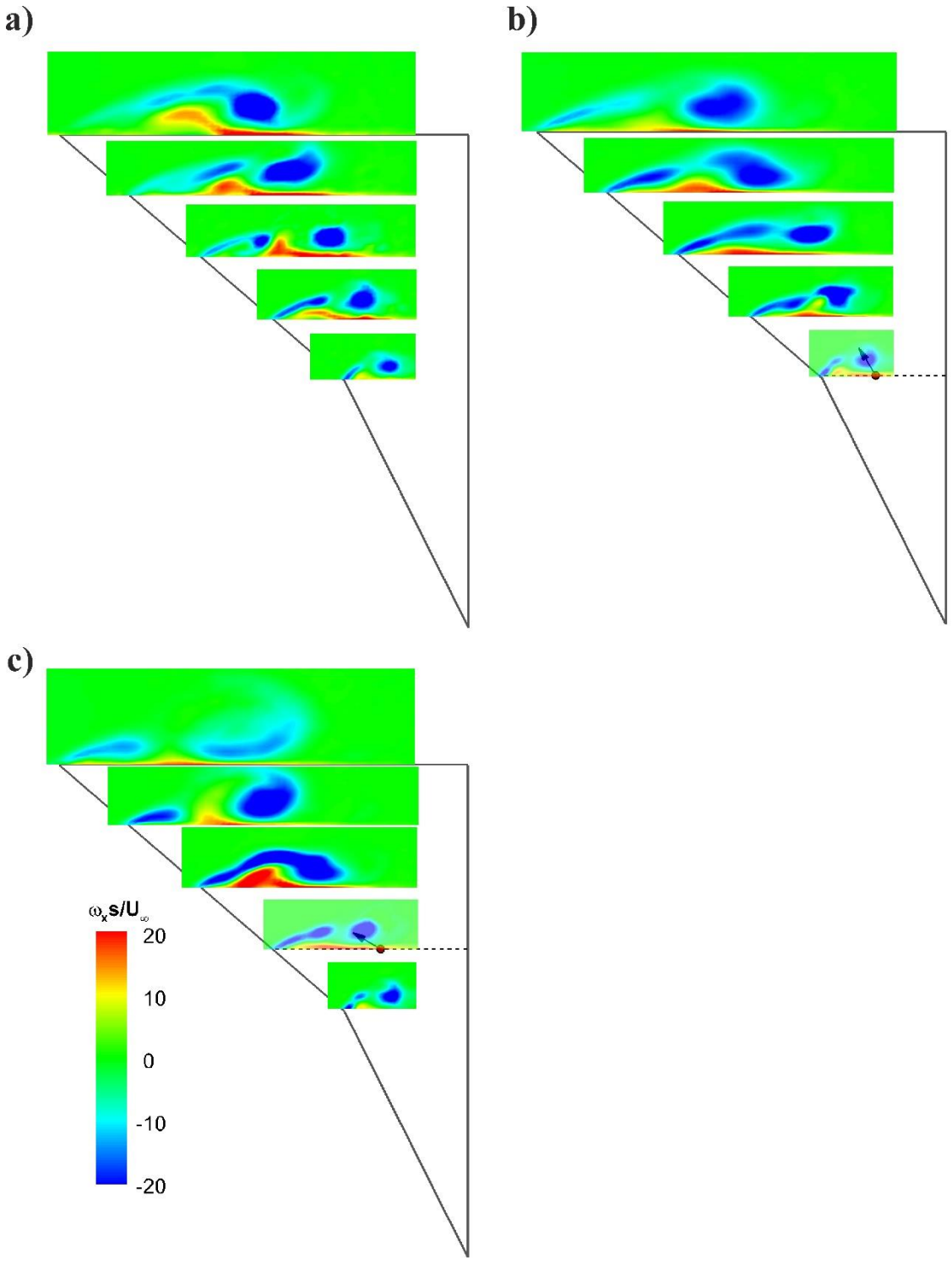


Figure 58. Time-averaged vorticity for α = 16º at a) baseline case; b) blowing hole #2, β = 60º and c) blowing hole #3, β = 30º.

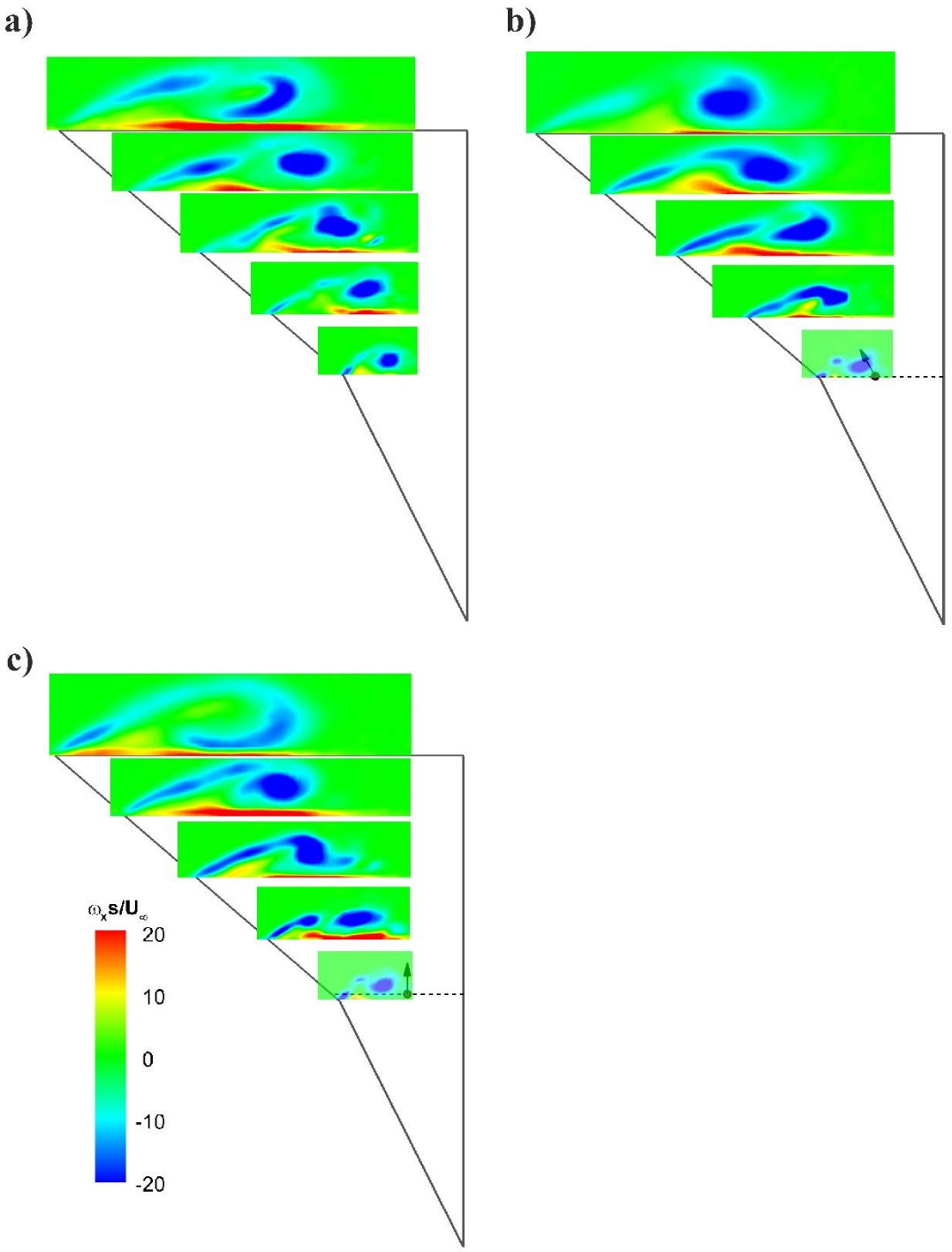


Figure 59. Time-averaged vorticity for α = 20º at a) baseline case; b) blowing hole #2, β = 60º and c) blowing hole #2, β = 90º.

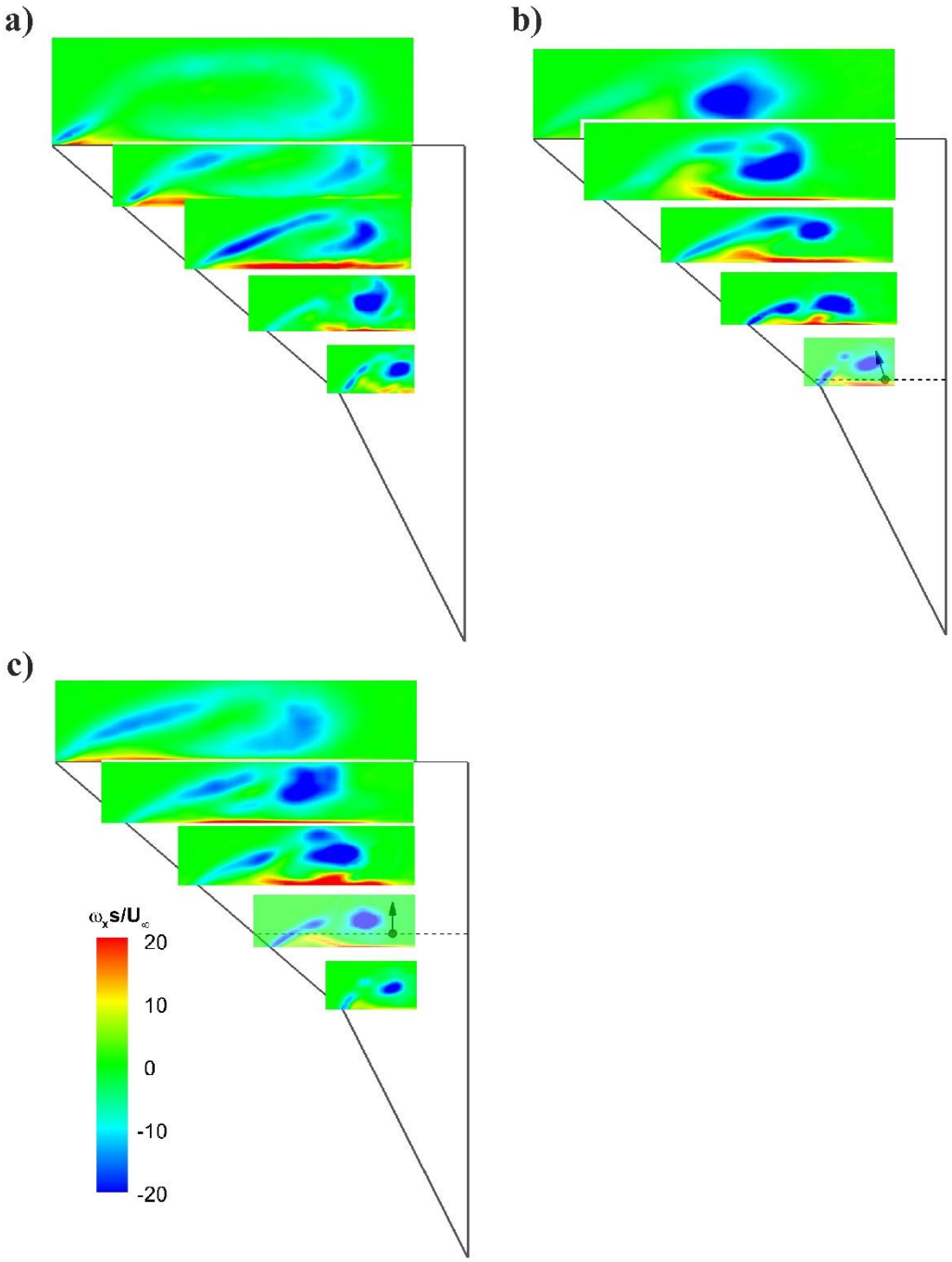


Figure 60. Time-averaged vorticity for α = 24º at a) baseline case; b) blowing hole #2, β = 75º and c) blowing hole #3, β = 90º.

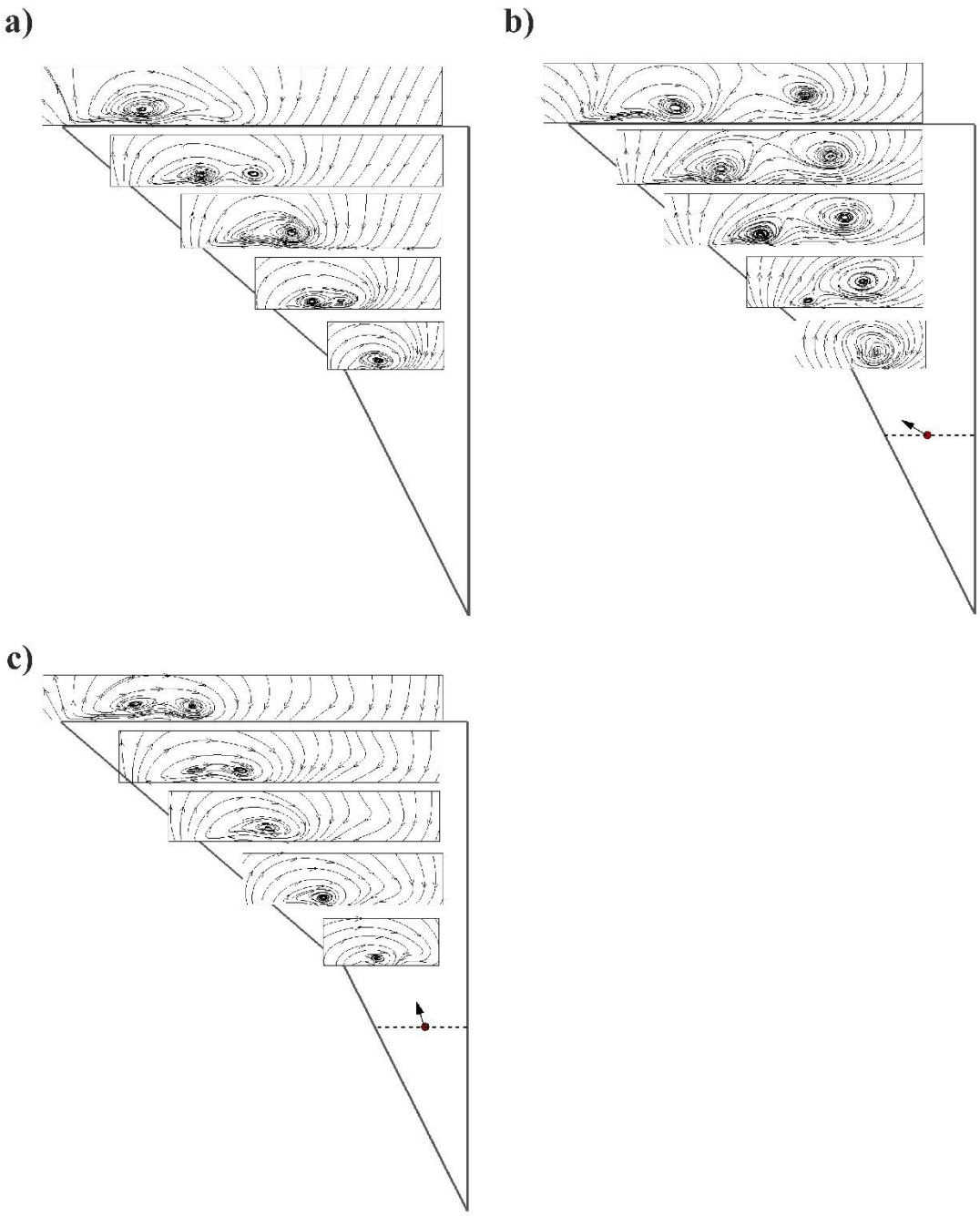


Figure 61. Streamline for α = 8º at a) baseline case; b) blowing hole #1, β = 30º and c) blowing hole #1, β = 75º.

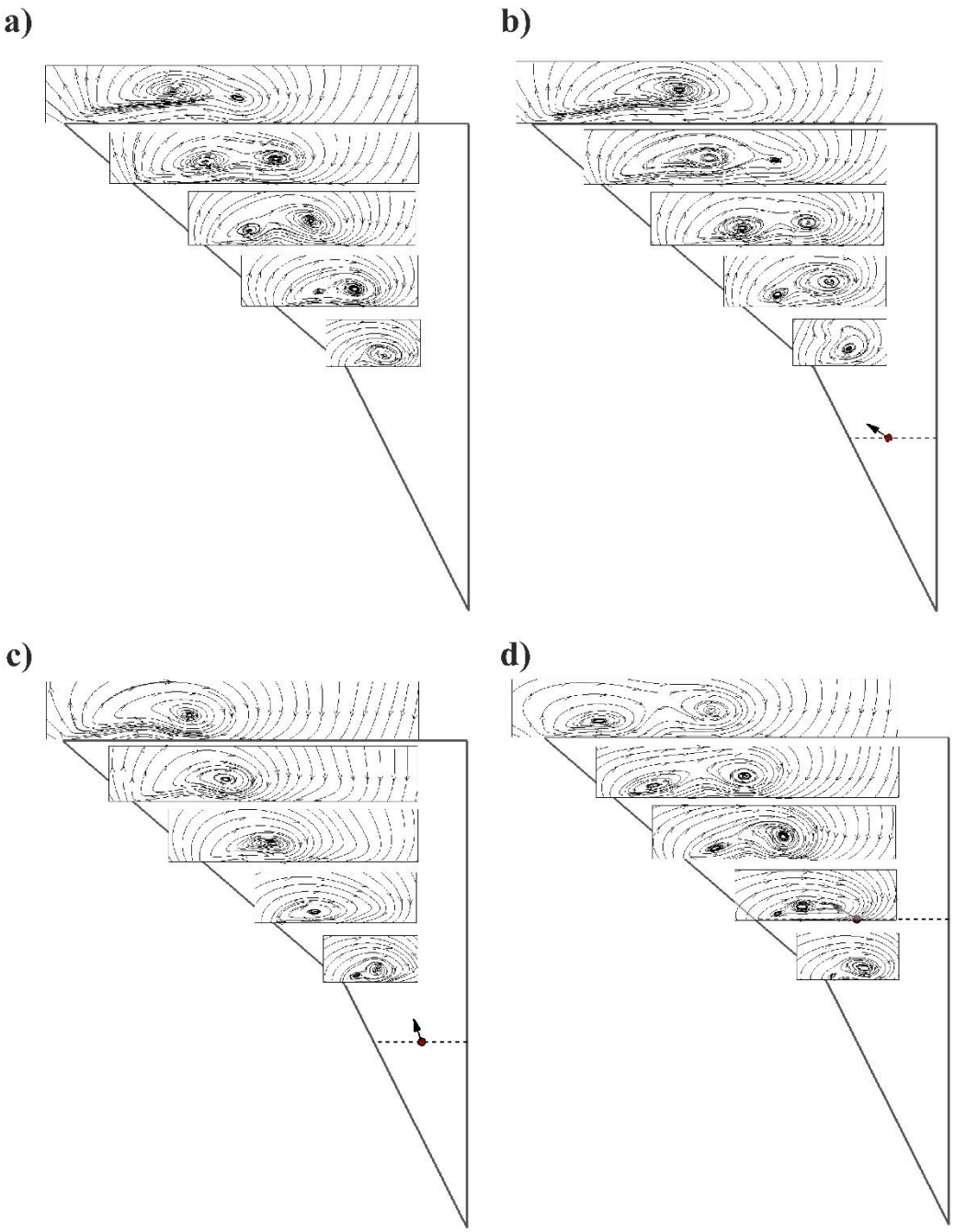


Figure 62. Streamline for α = 12º at a) baseline case; b) blowing hole #1, β = 30º; c) blowing hole #1, β = 75º; d) blowing hole #3, β = 30º and e) blowing hole #3, β = 60º.

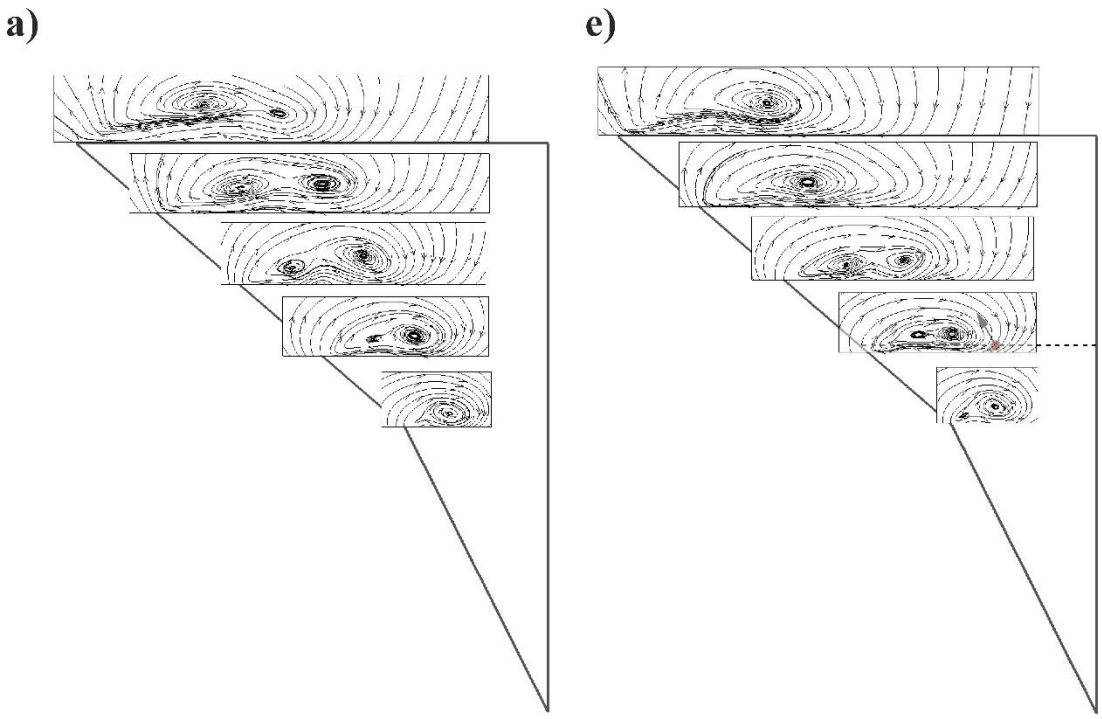


Figure 62. Continued.

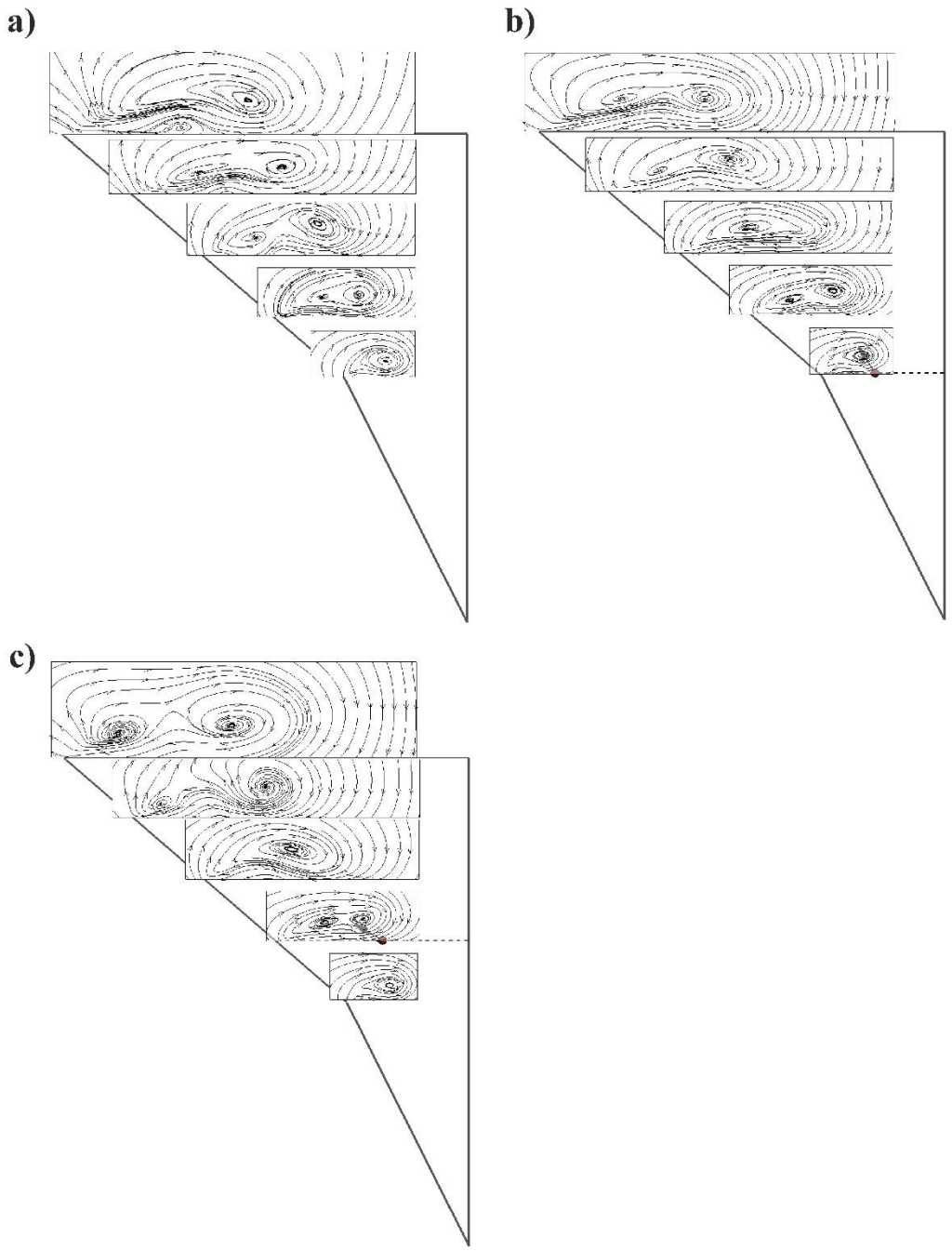


Figure 63. Streamline for α = 16º at a) baseline case; b) blowing hole #2, β = 60º and c) blowing hole #3, β = 30º.

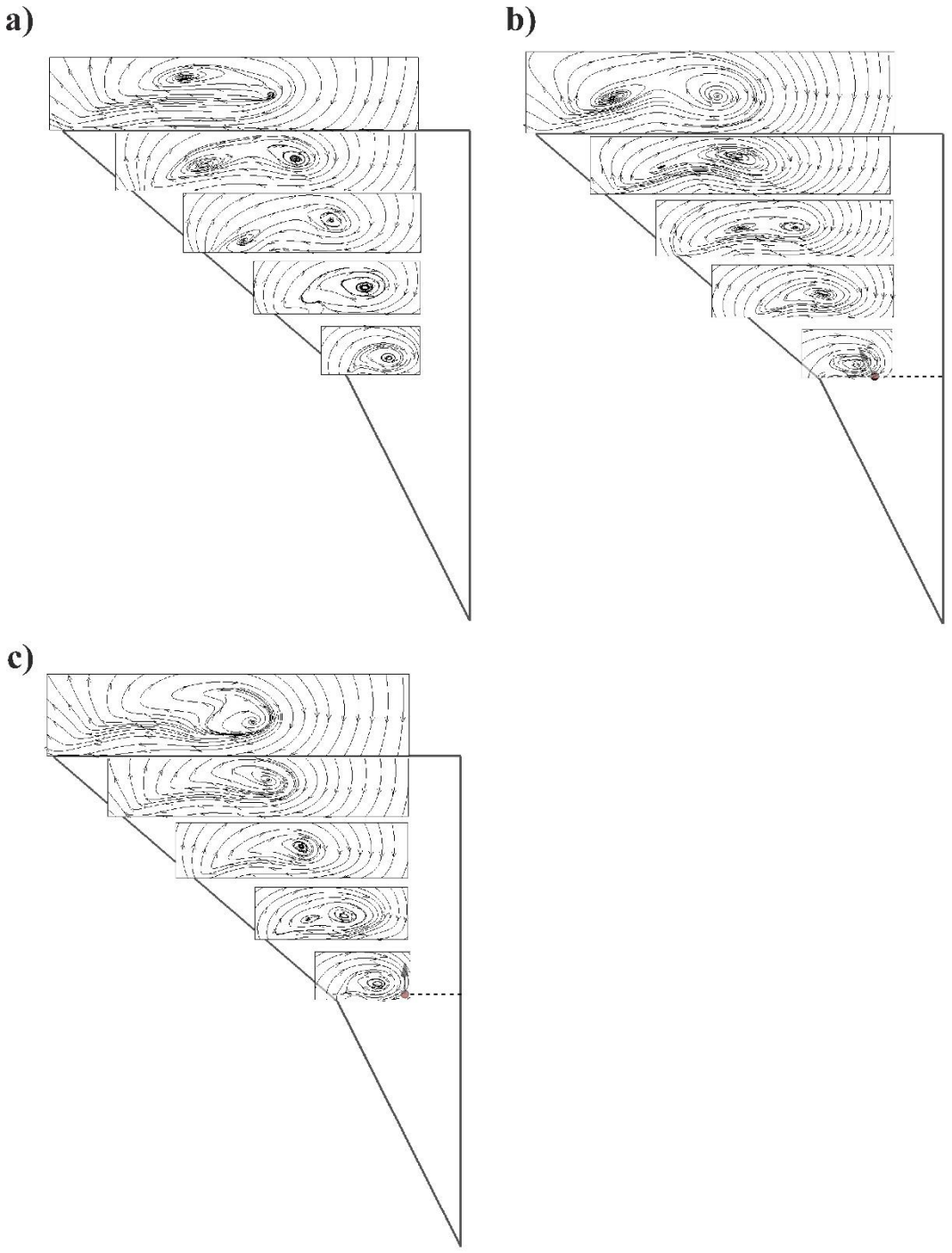


Figure 64. Streamline for α = 20º at a) baseline case; b) blowing hole #2, β = 60º and c) blowing hole #2, β = 90º.

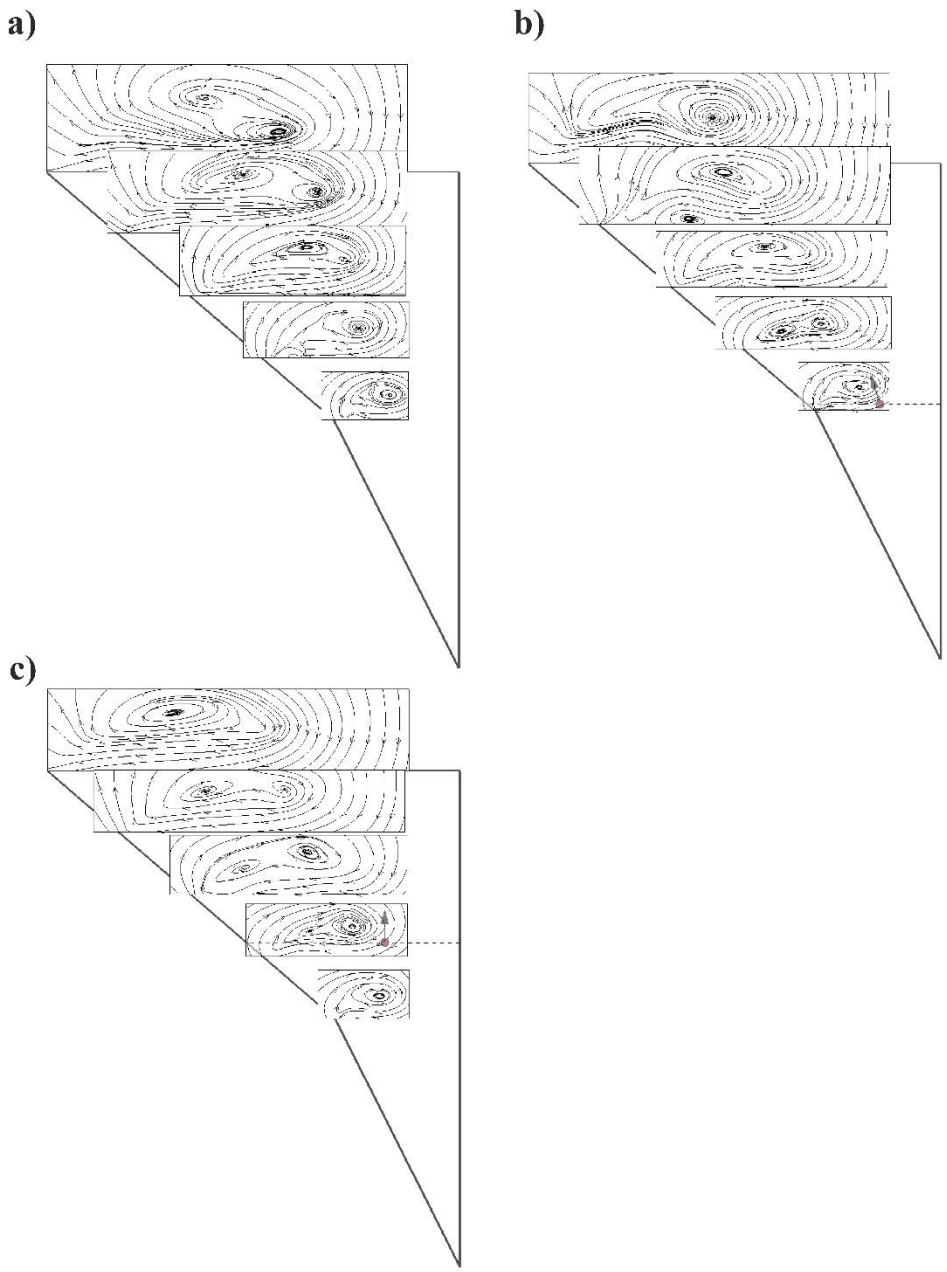


Figure 65. Streamline for α = 24º at a) baseline case; b) blowing hole #2, β = 75º and c) blowing hole #3, β = 90º.

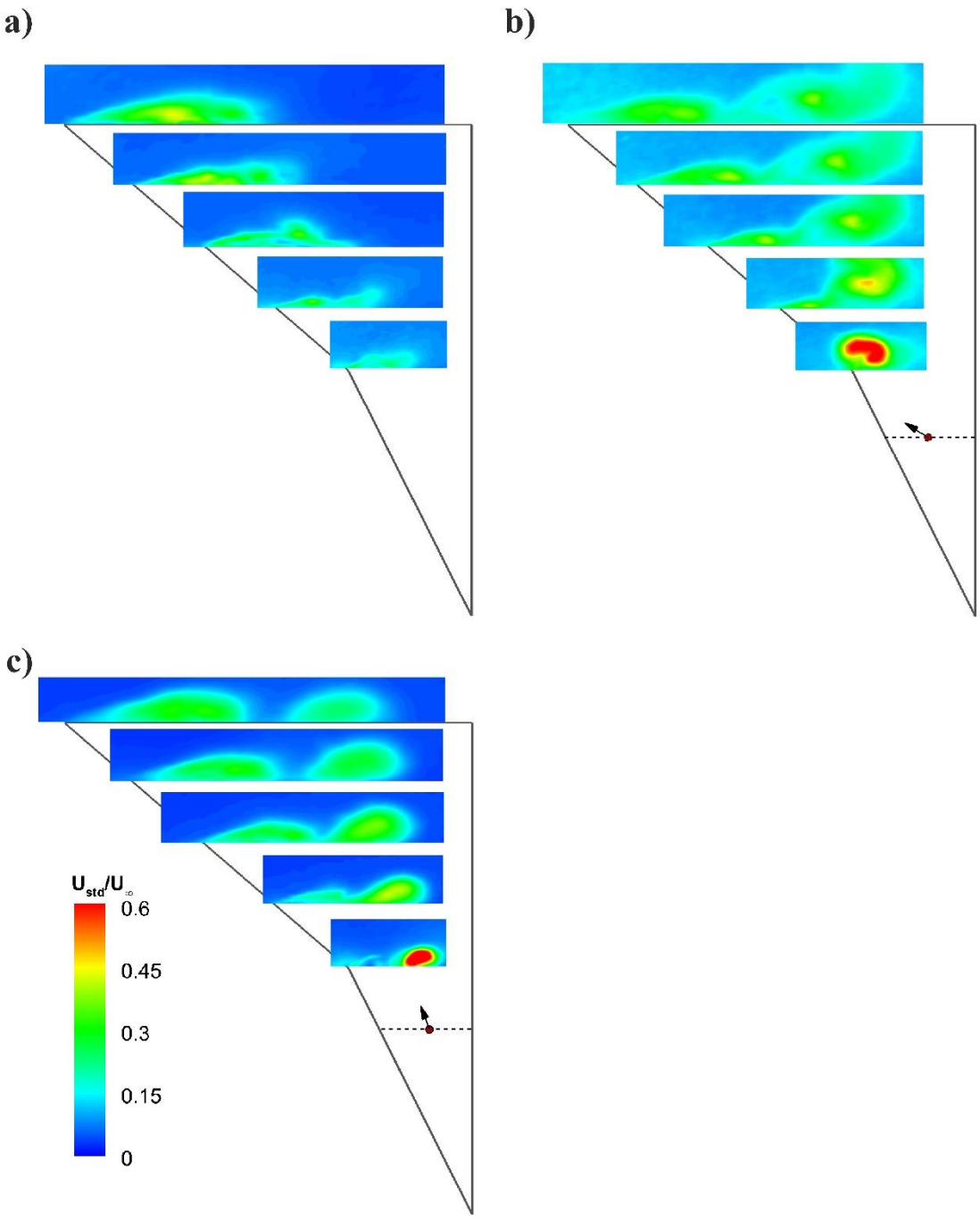


Figure 66. Standard deviation for α = 8º at a) baseline case; b) blowing hole #1, β = 30º and c) blowing hole #1, β = 75º.

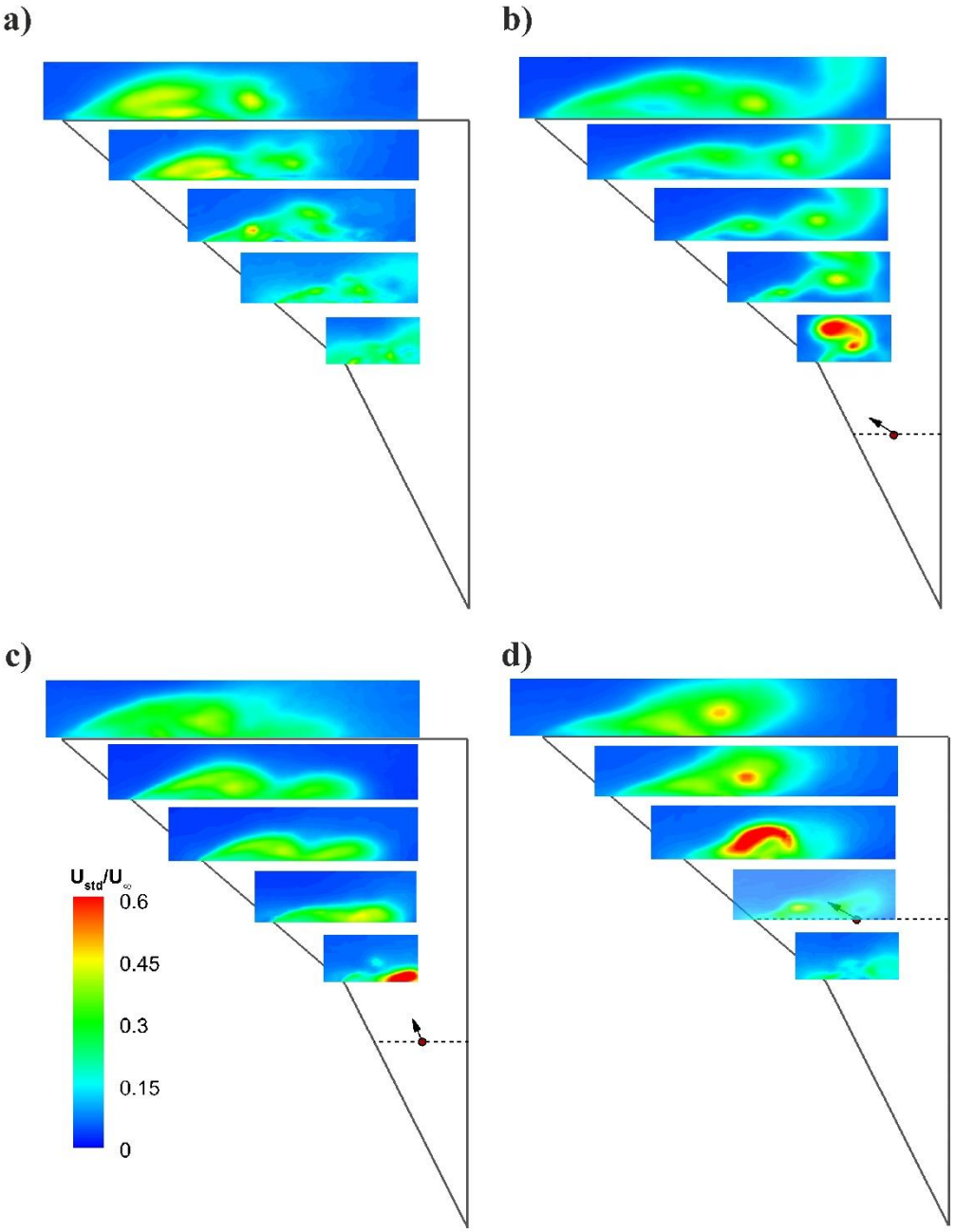


Figure 67. Standard deviation for α = 12º at a) baseline case; b) blowing hole #1, β = 30º; c) blowing hole #1, β = 75º; d) blowing hole #3, β = 30º and e) blowing hole #3, β = 60º.

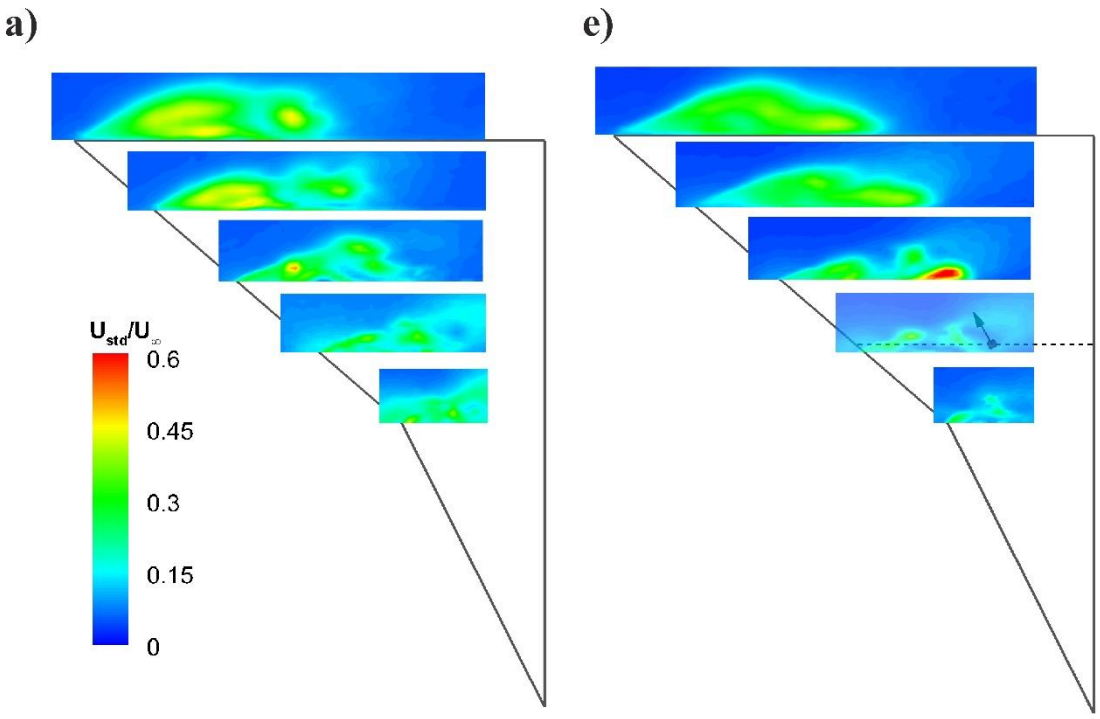


Figure 67. Continued.

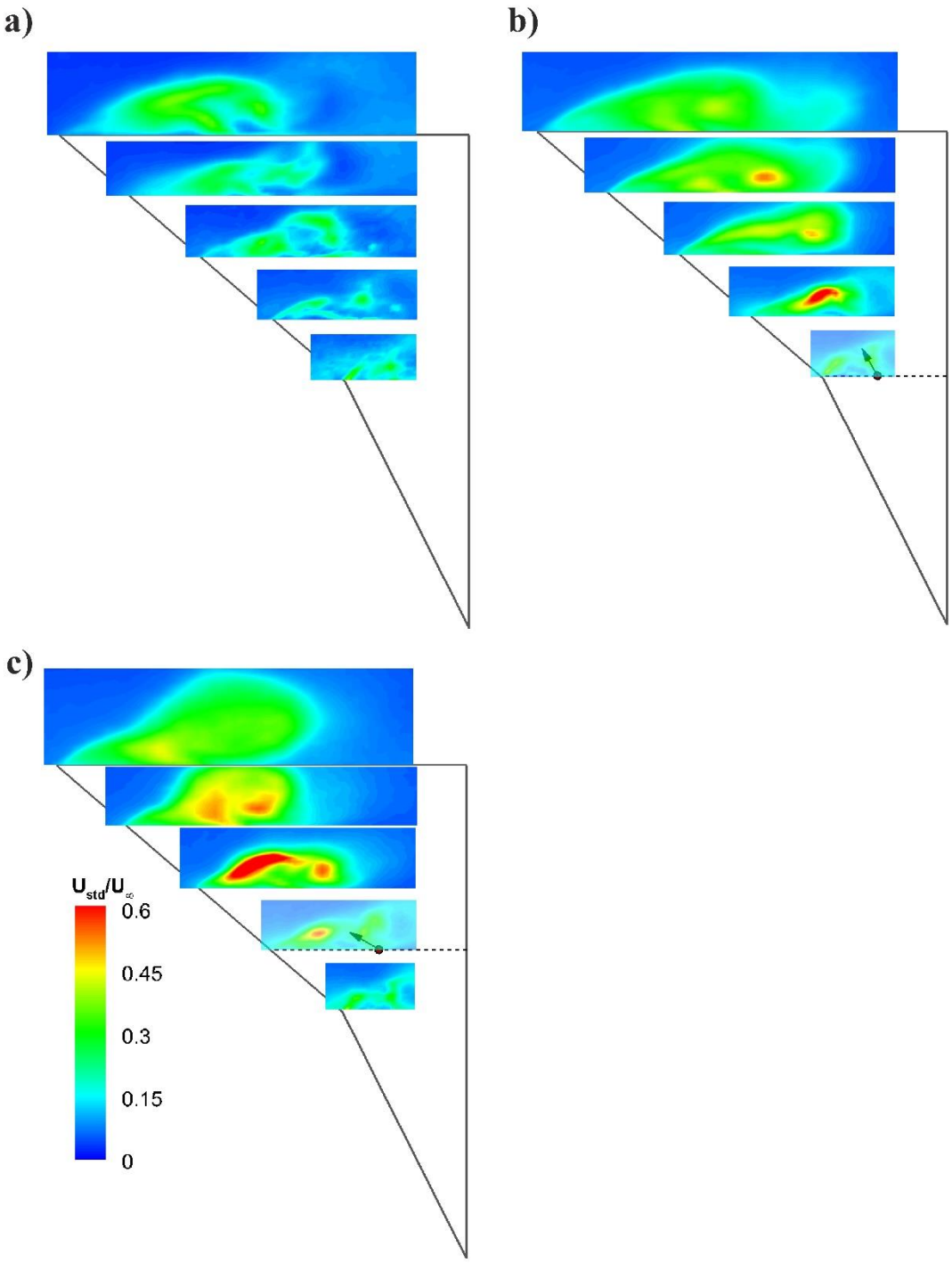


Figure 68. Standard deviation for α = 16º at a) baseline case; b) blowing hole #2, β = 60º and c) blowing hole #3, β = 30º.

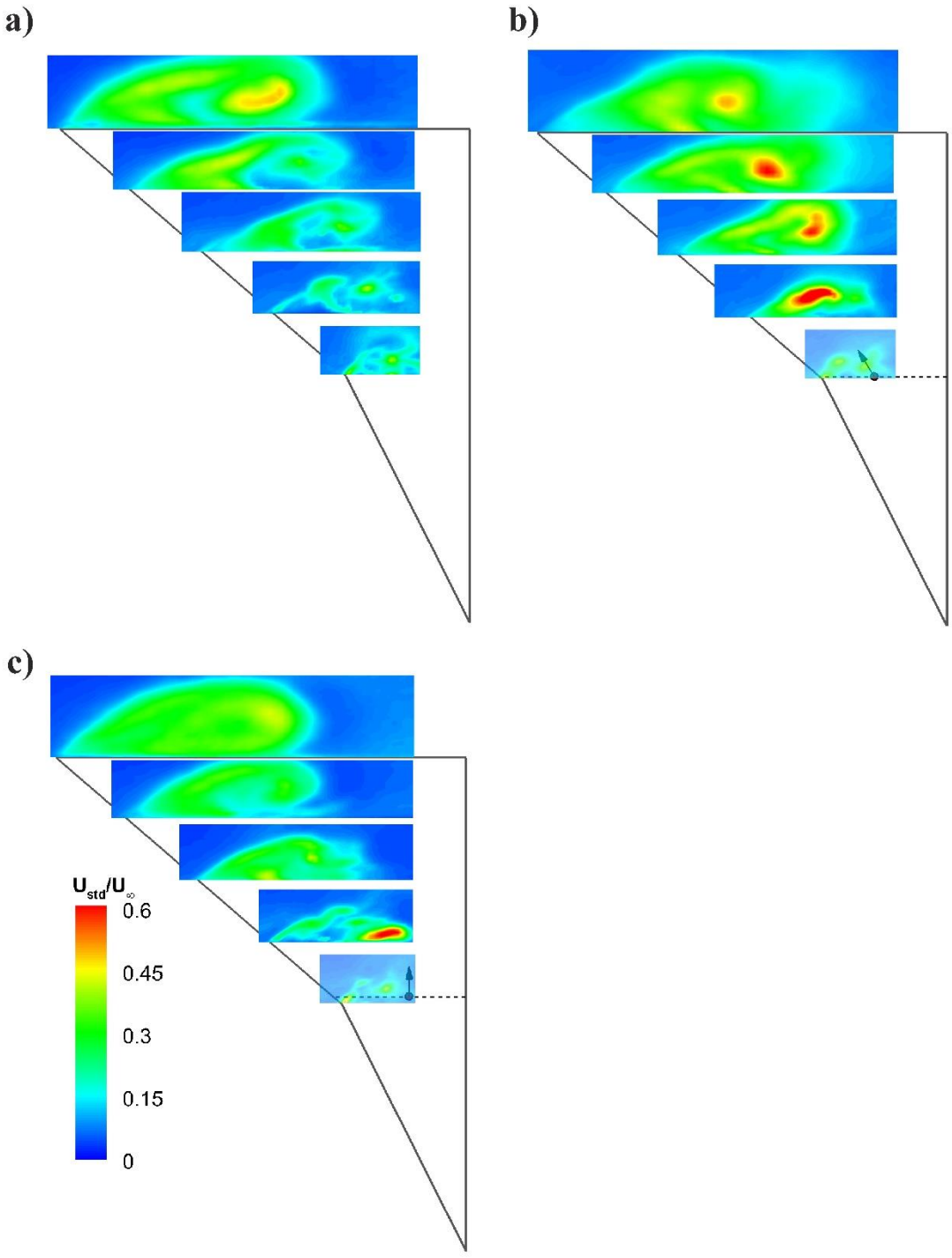


Figure 69. Standard deviation for α = 20º at a) baseline case; b) blowing hole #2, β = 60º and c) blowing hole #2, β = 90º.

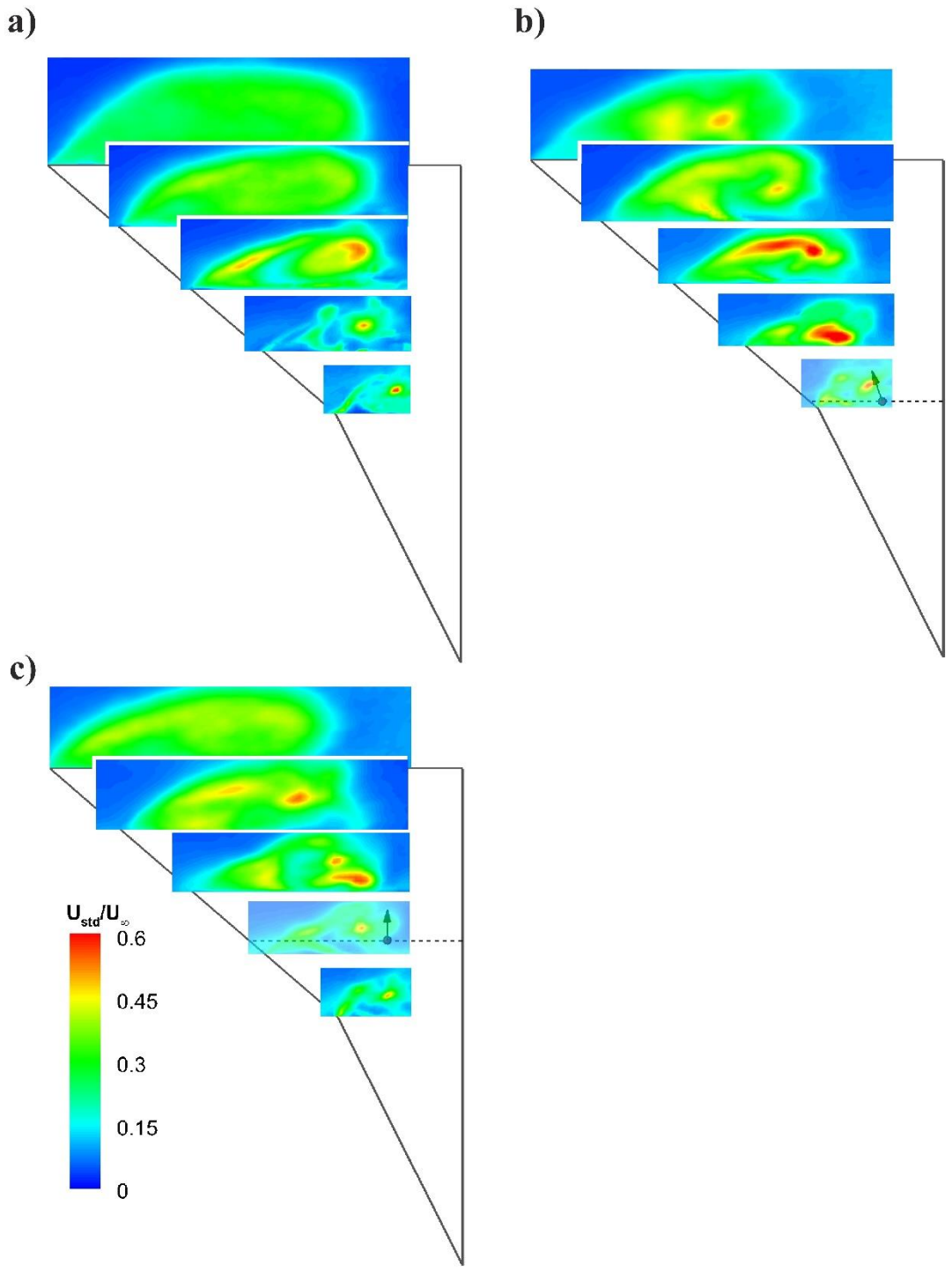


Figure 70. Standard deviation for α = 24º at a) baseline case; b) blowing hole #2, β = 75º and c) blowing hole #3, β = 90º.

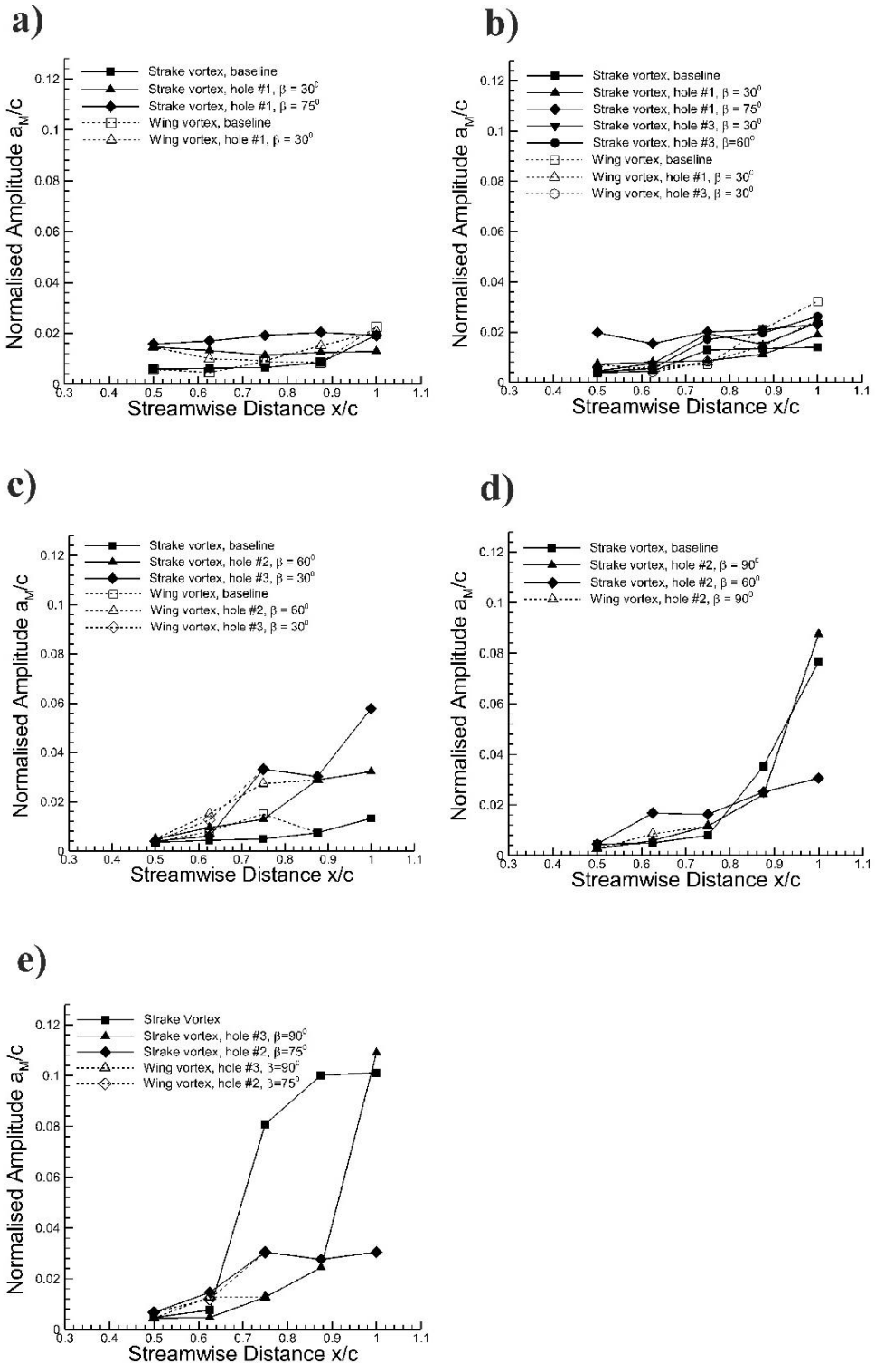


Figure 71. Normalised meandering amplitude for a) α = 8º; b) α = 12º; c) α = 16º; d) α = 20º and e) α = 24º.

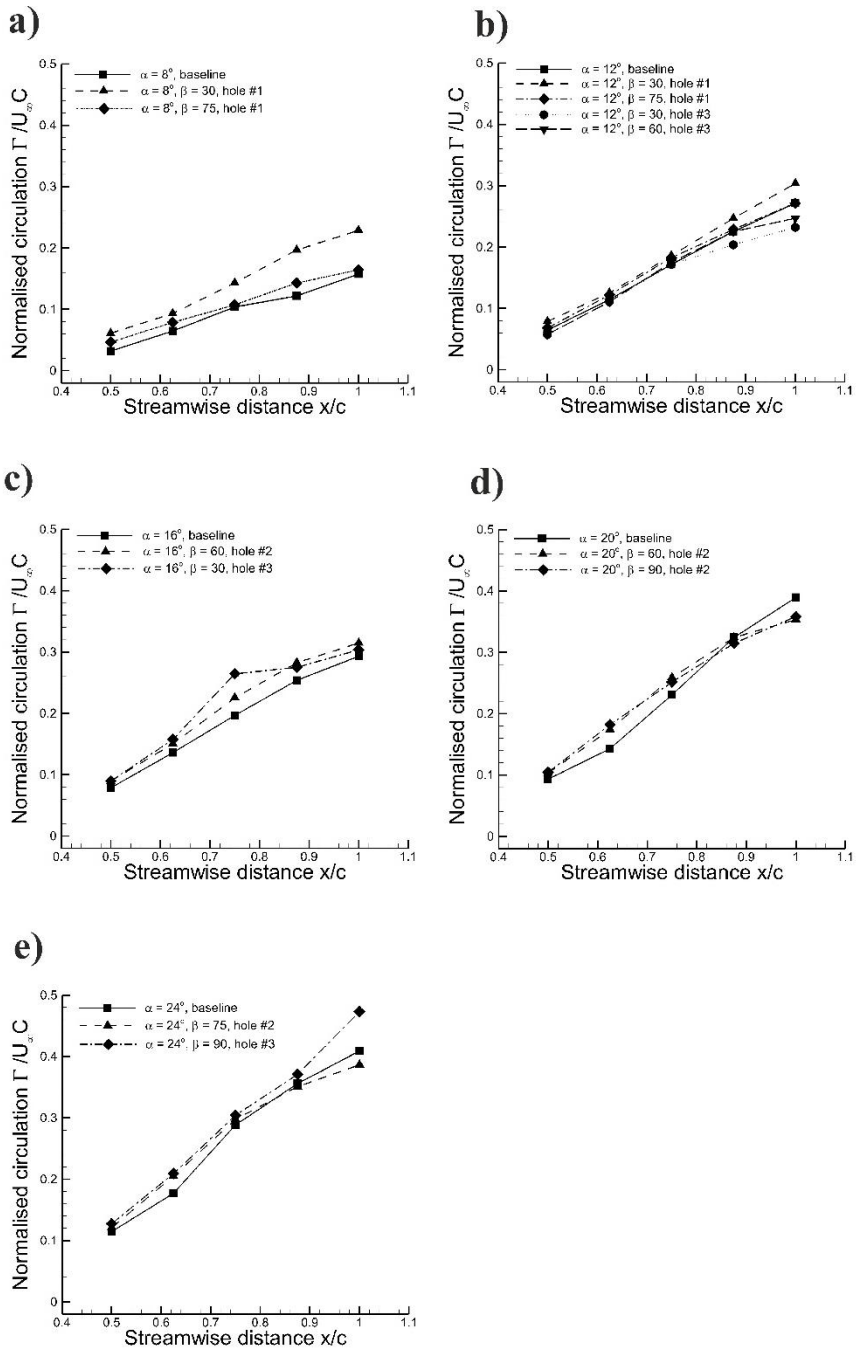


Figure 72. Normalised total circulation for a) α = 8º; b) α = 12º; c) α = 16º; d) α = 20º and e) α = 24º.

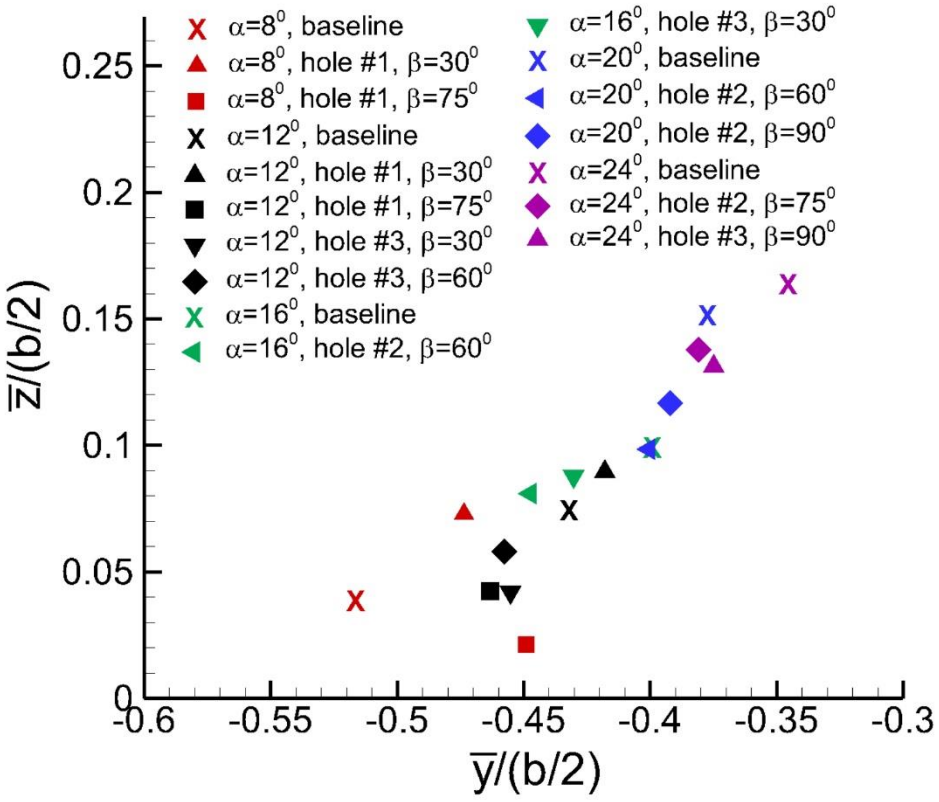


Figure 73. Vortex centroid locations for different blowing configurations

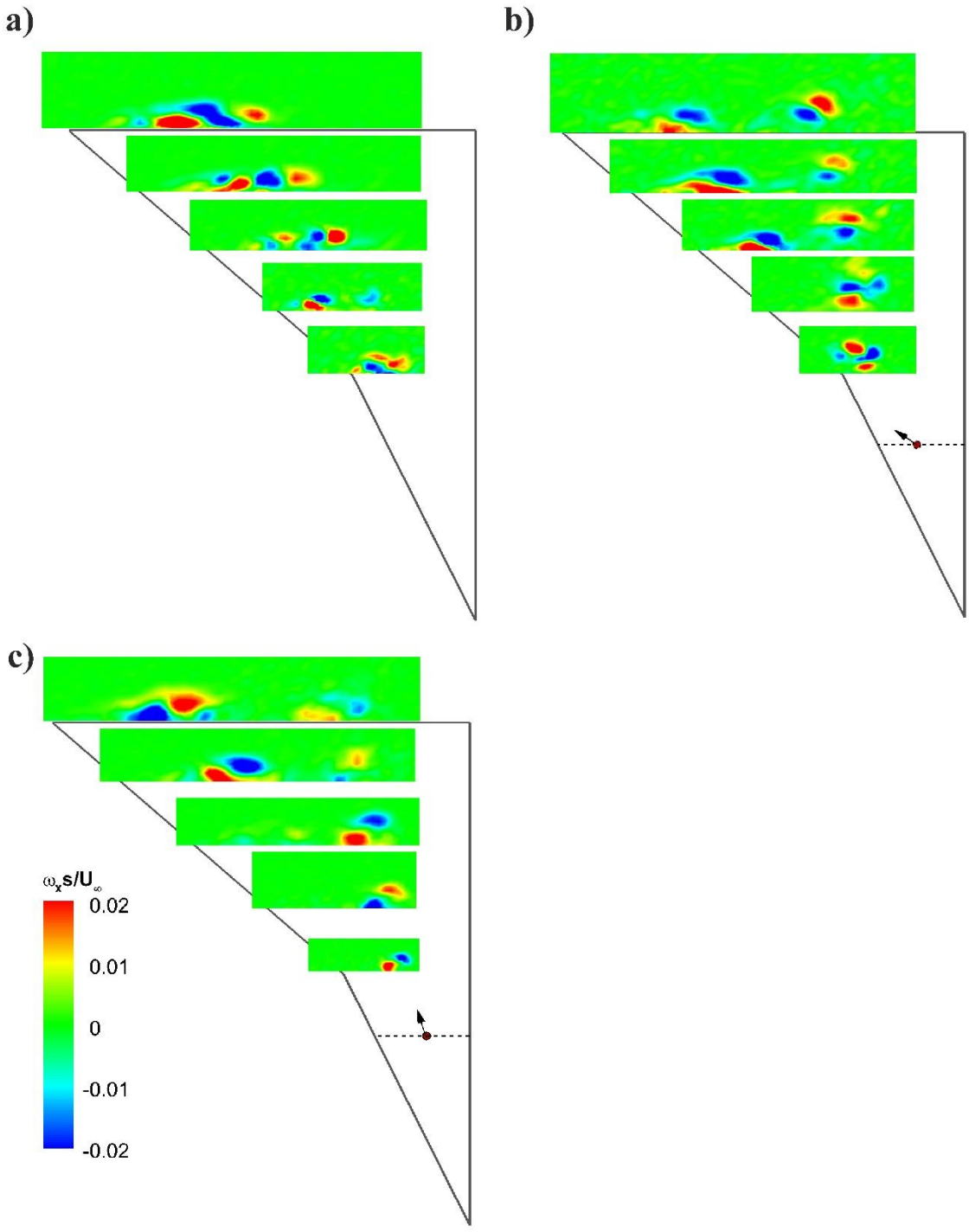


Figure 74. 1st POD mode for α = 8º at a) baseline case; b) blowing hole #1, β = 30º and c) blowing hole #1, β = 75º.

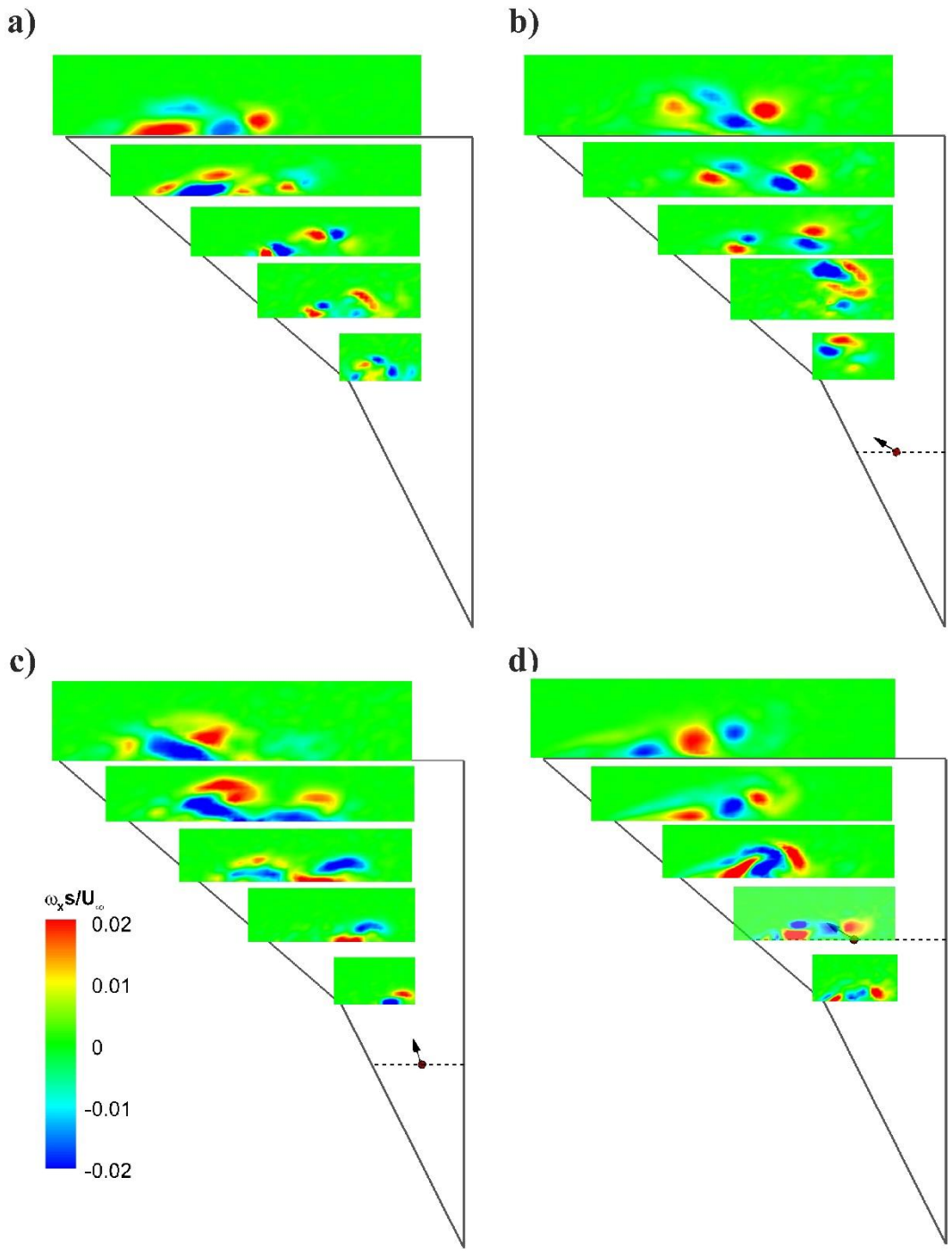


Figure 75. 1st POD mode for α = 12º at a) baseline case; b) blowing hole #1, β = 30º; c) blowing hole #1, β = 75º; d) blowing hole #3, β = 30º and e) blowing hole #3, β = 60º.

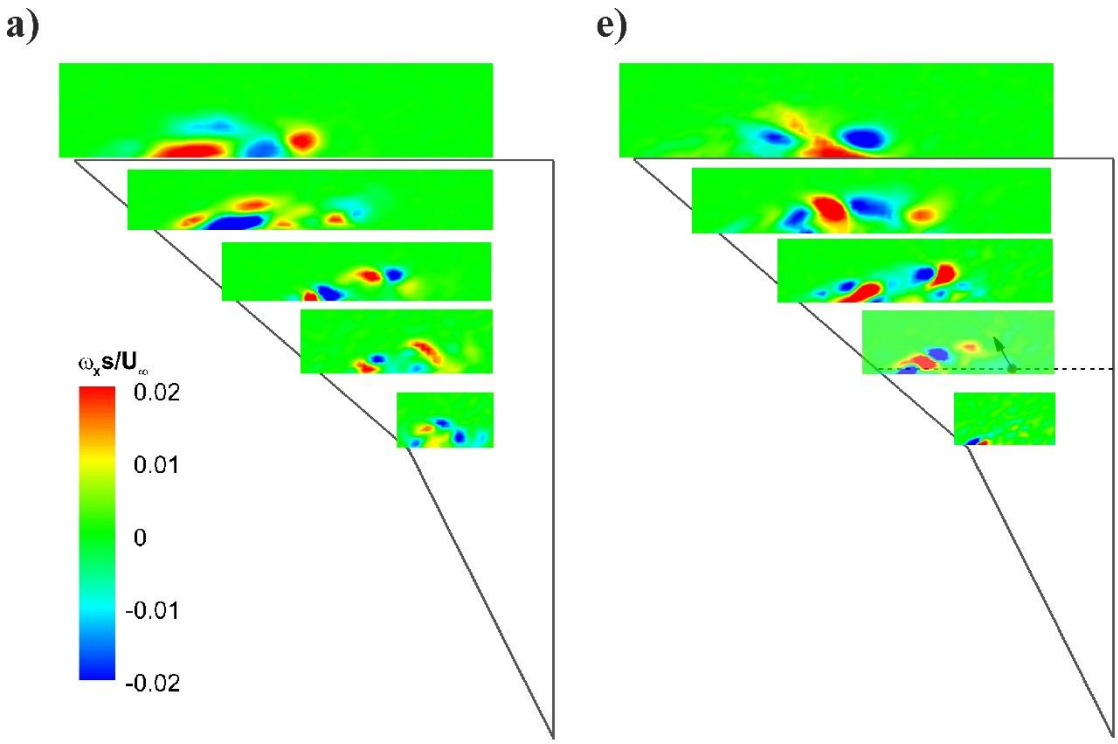


Figure 75. Continued

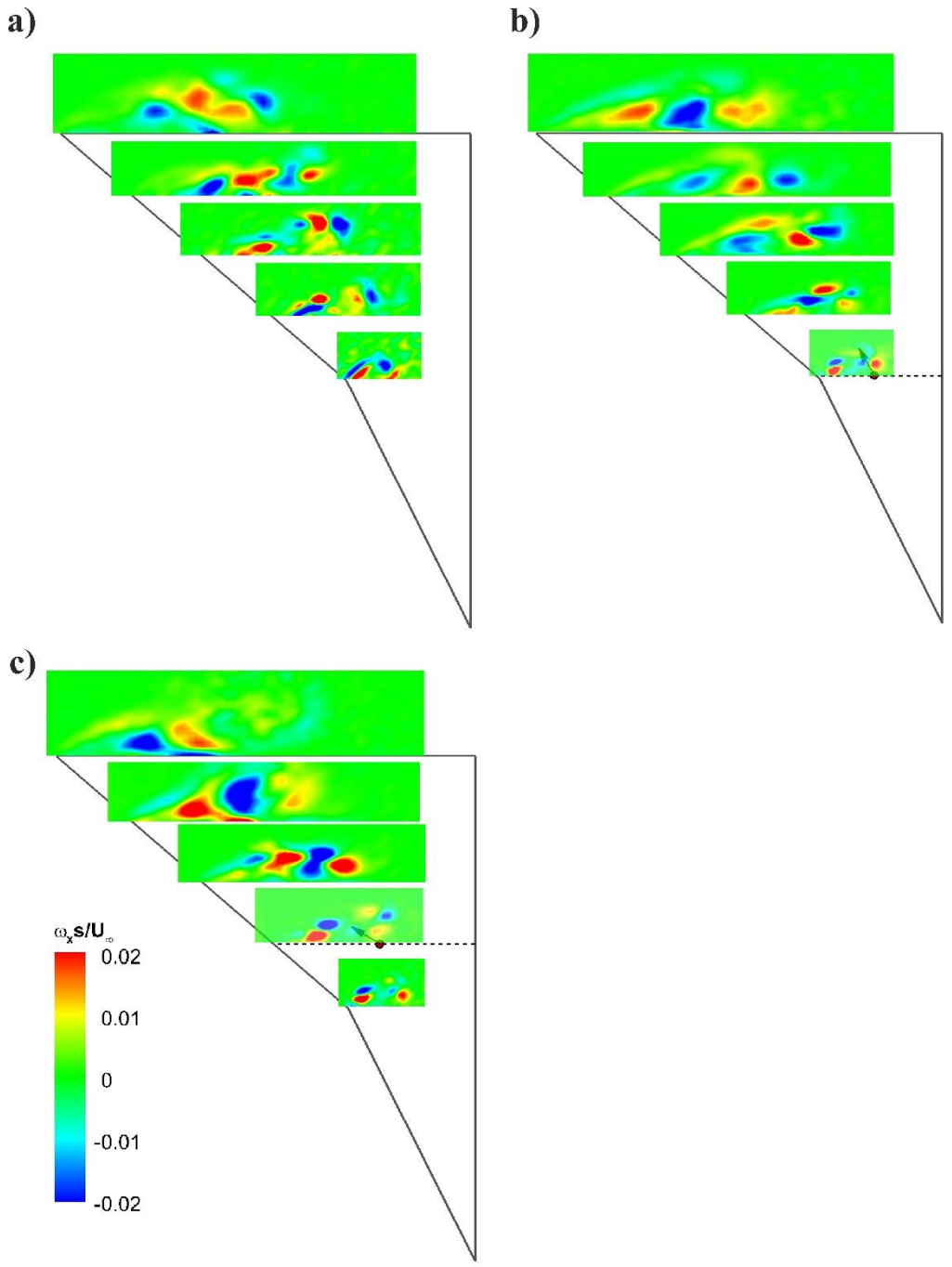


Figure 76. 1st POD mode for α = 16º at a) baseline case; b) blowing hole #2, β = 60º and c) blowing hole #3, β = 30º.

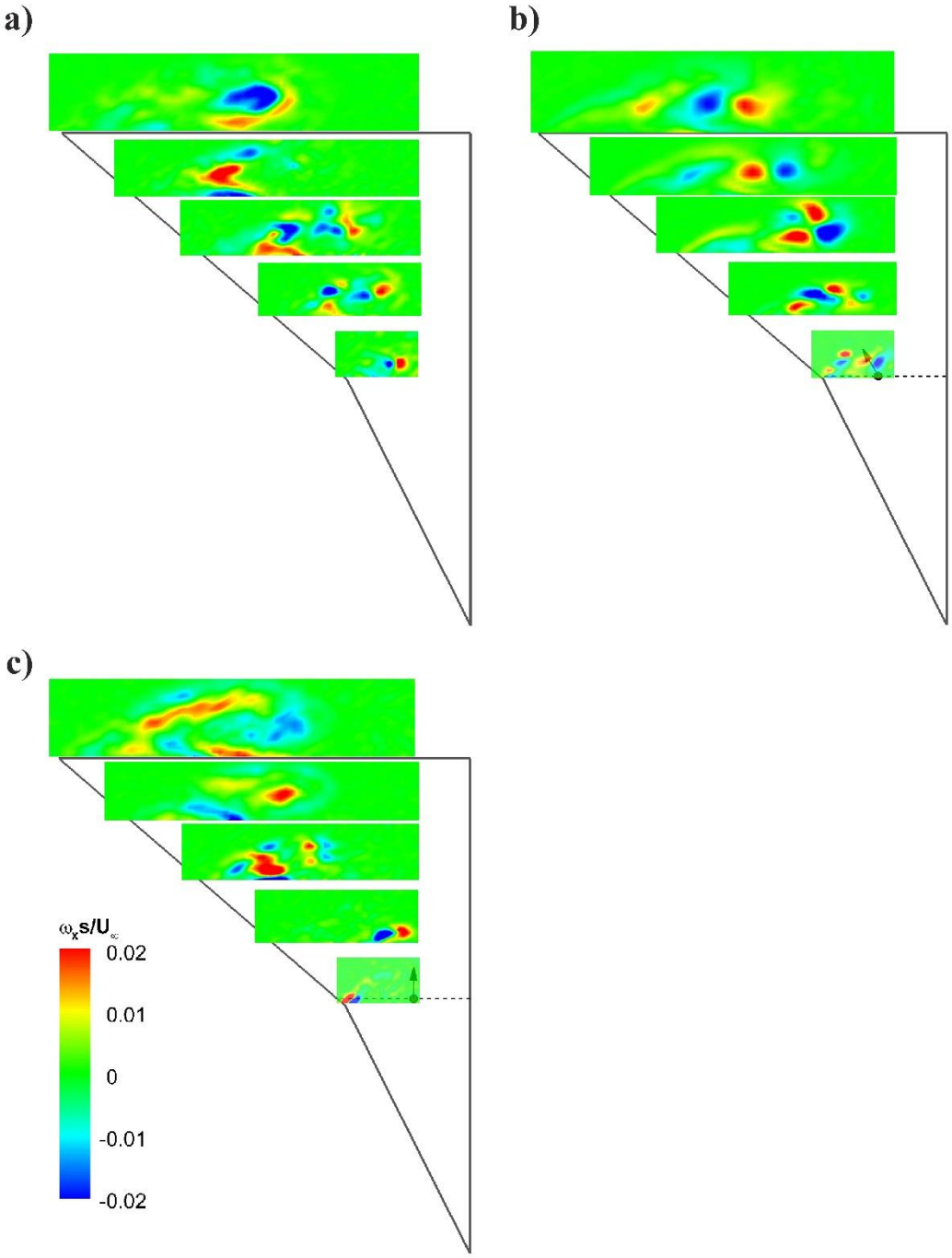


Figure 77. 1st POD mode for α = 20º at a) baseline case; b) blowing hole #2, β = 60º and c) blowing hole #2, β = 90º.

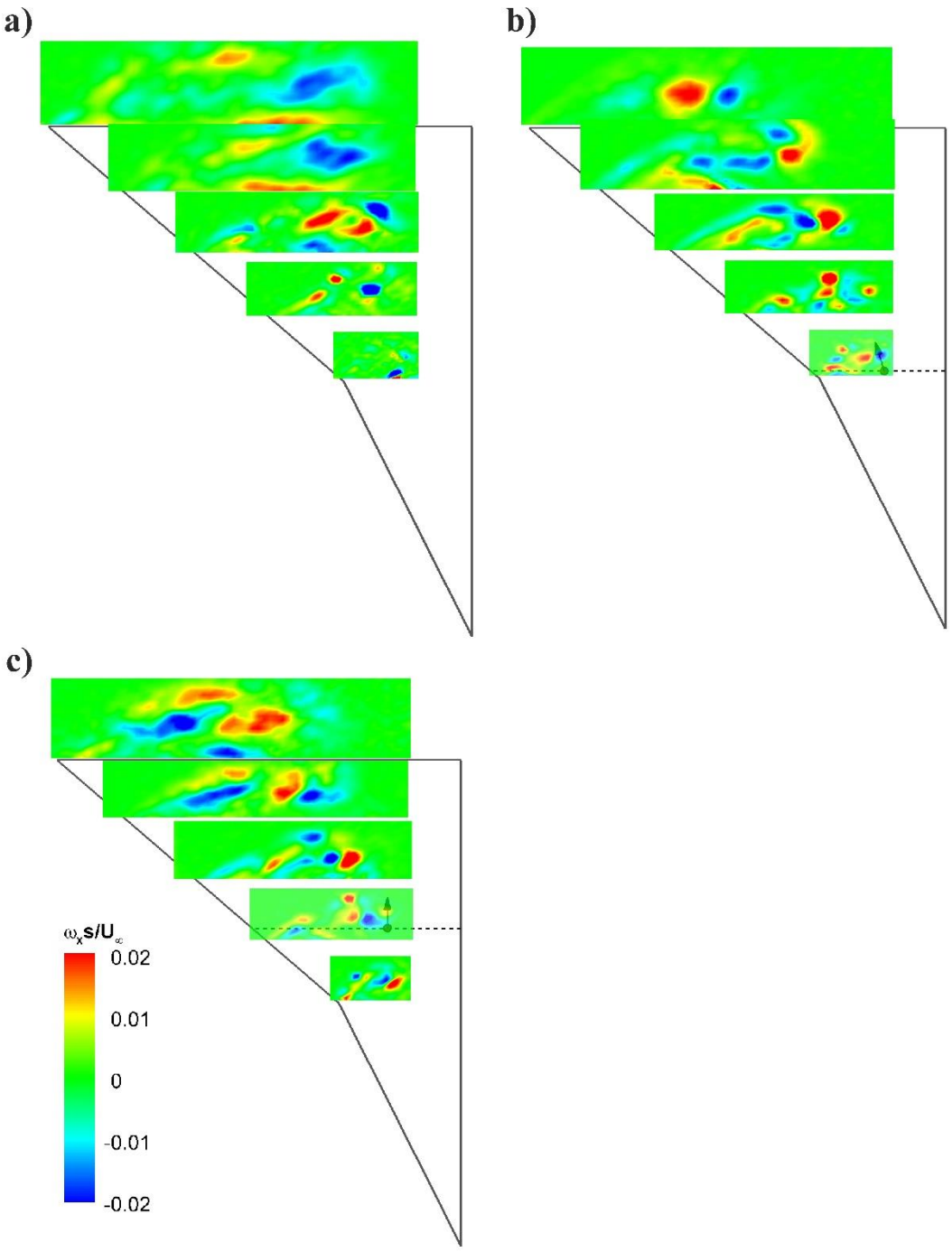


Figure 78. 1st POD mode for α = 24º at a) baseline case; b) blowing hole #2, β = 75º and c) blowing hole #3, β = 90º.

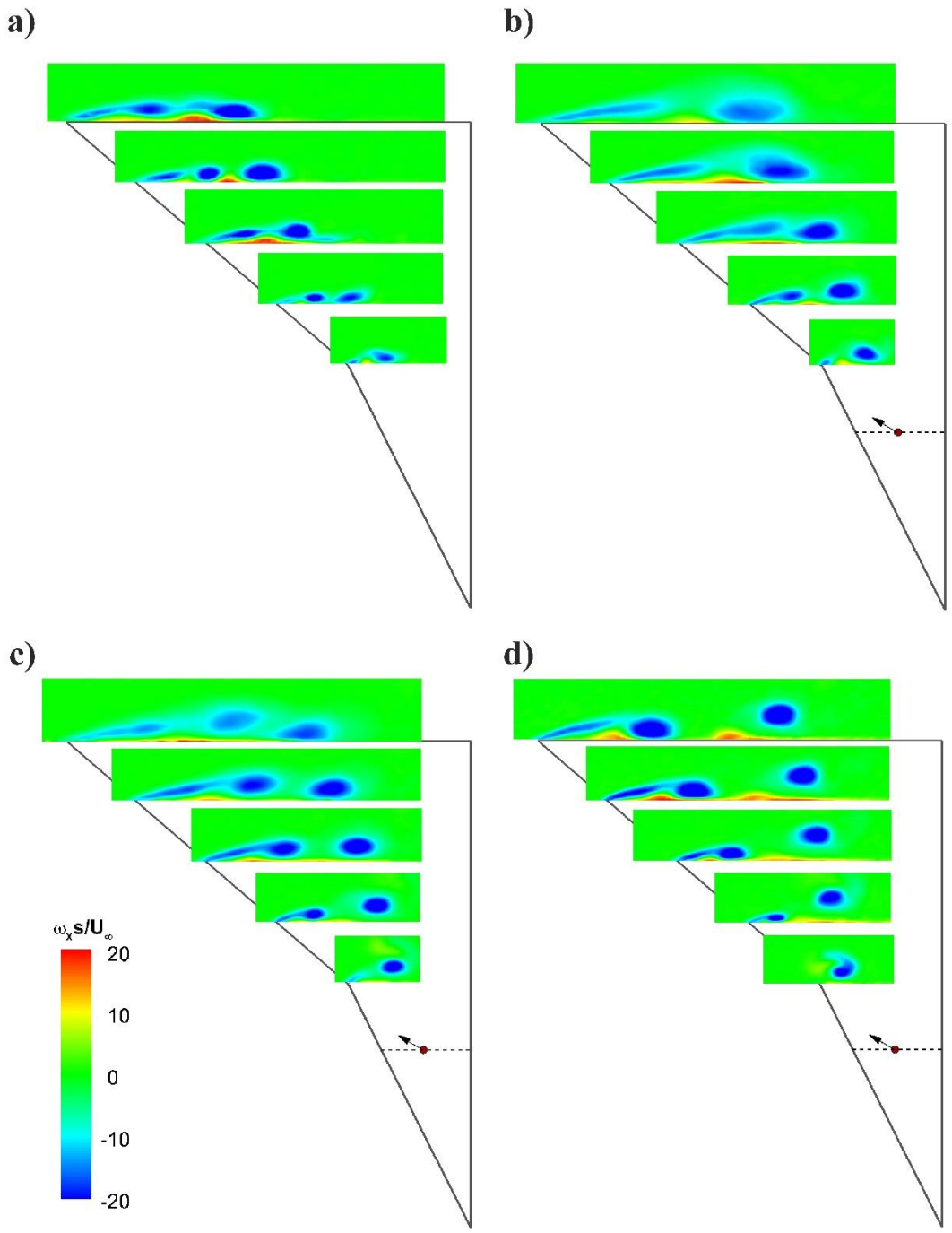


Figure 79. Time-averaged vorticity for blowing hole #1, α = 8º, β = 30º at a) Cμ = 0; b) Cμ = 0.5%; c) Cμ = 1% and d) Cμ = 2%.

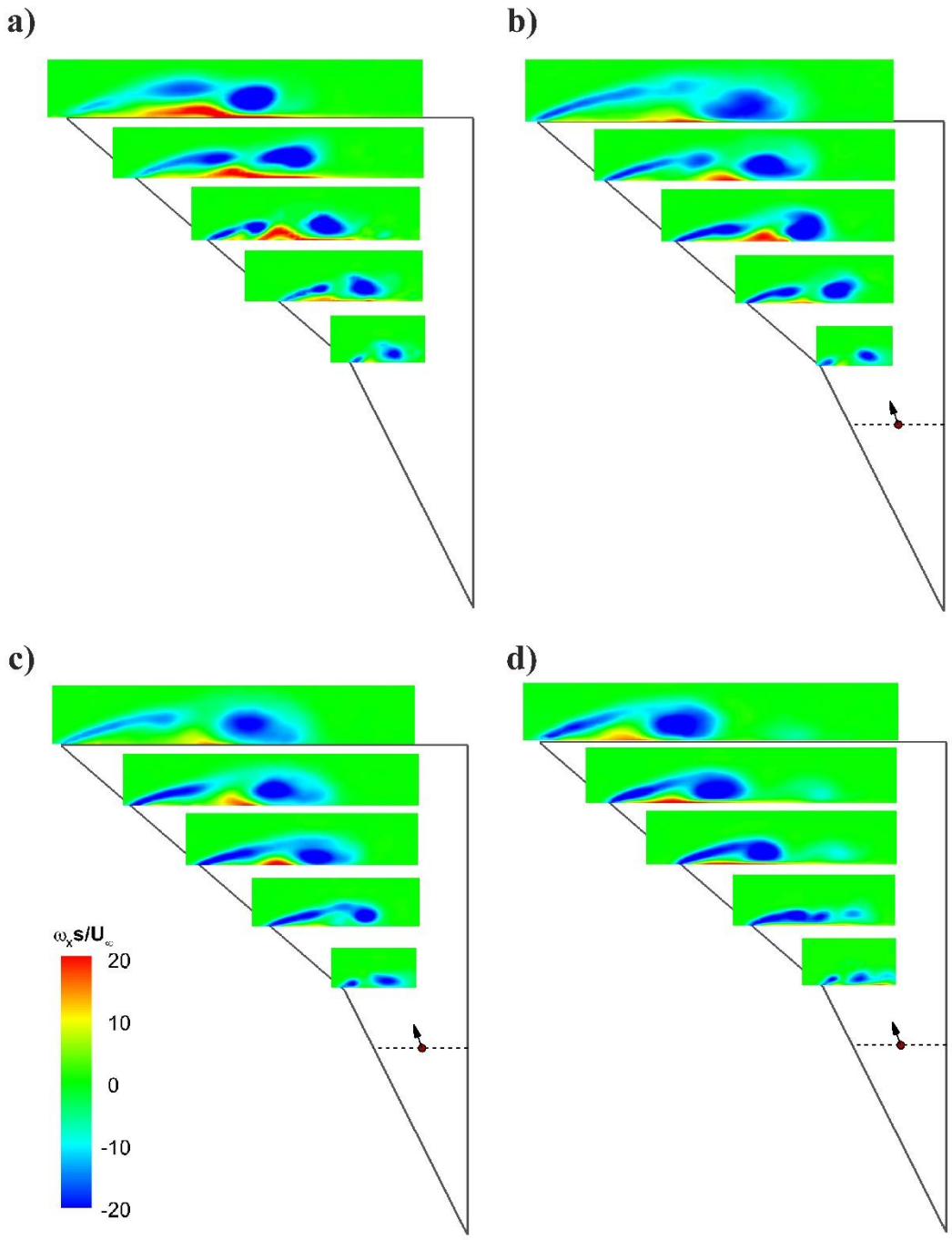


Figure 80. Time-averaged vorticity for blowing hole #1, α = 12º, β = 75º at a) Cμ = 0; b) Cμ = 0.5%; c) Cμ = 1% and d) Cμ = 2%.

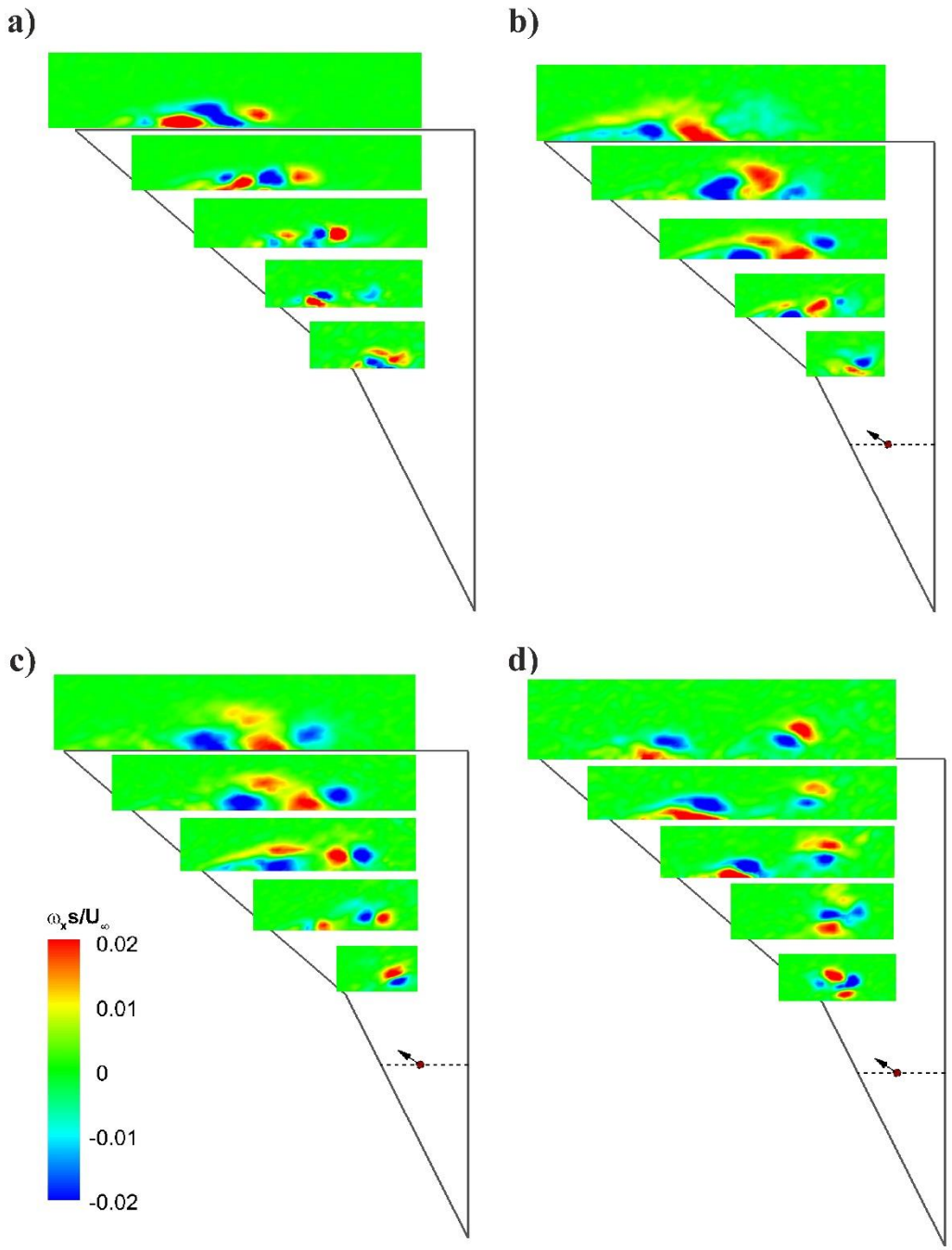


Figure 81. POD 1st mode for blowing hole #1, α = 8º, β = 30º at a) Cμ = 0; b) Cμ = 0.5%; c) Cμ = 1% and d) Cμ = 2%.

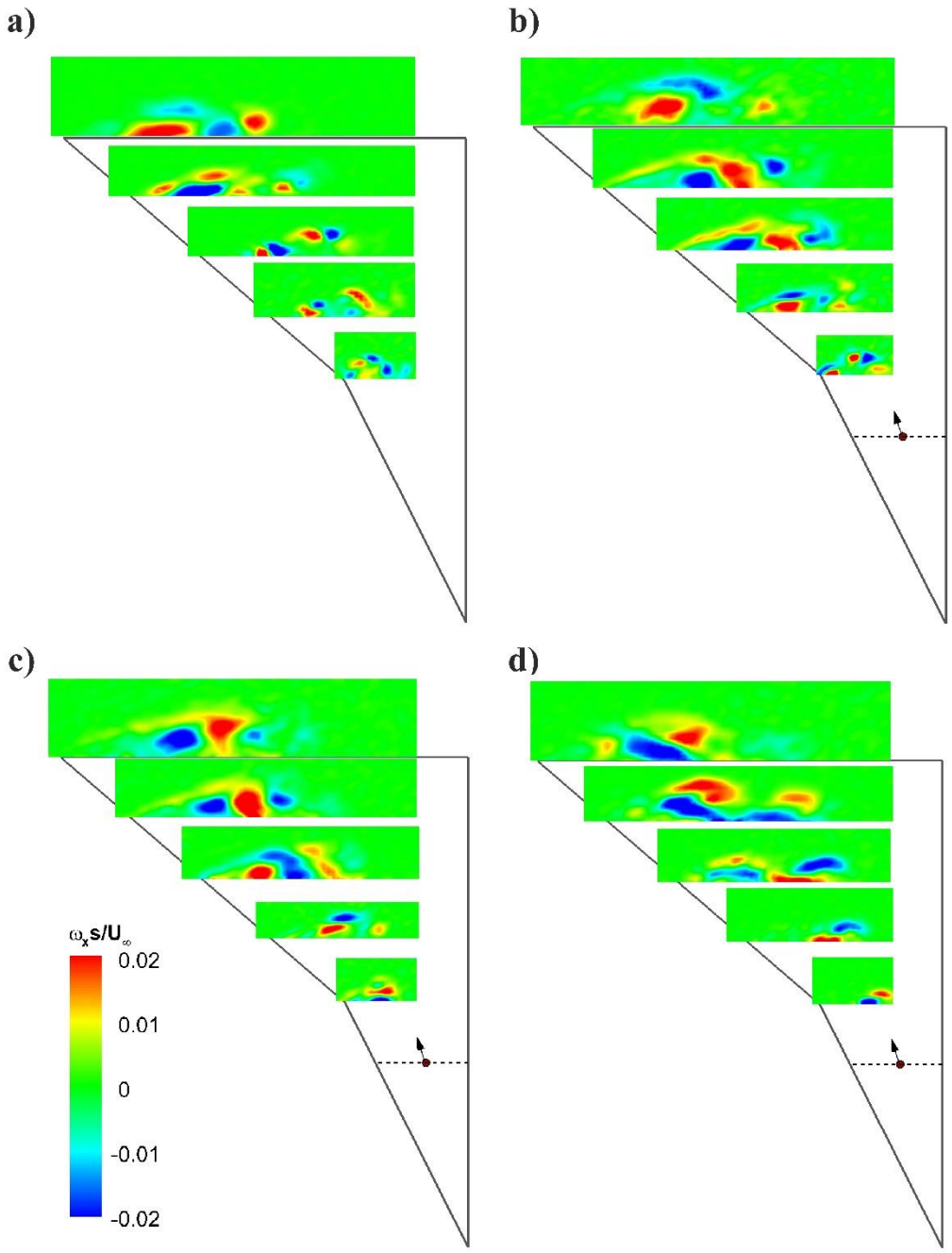


Figure 82. POD 1st mode for blowing hole #1, α = 12º, β = 75º at a) Cμ = 0; b) Cμ = 0.5%; c) Cμ = 1% and d) Cμ = 2%.

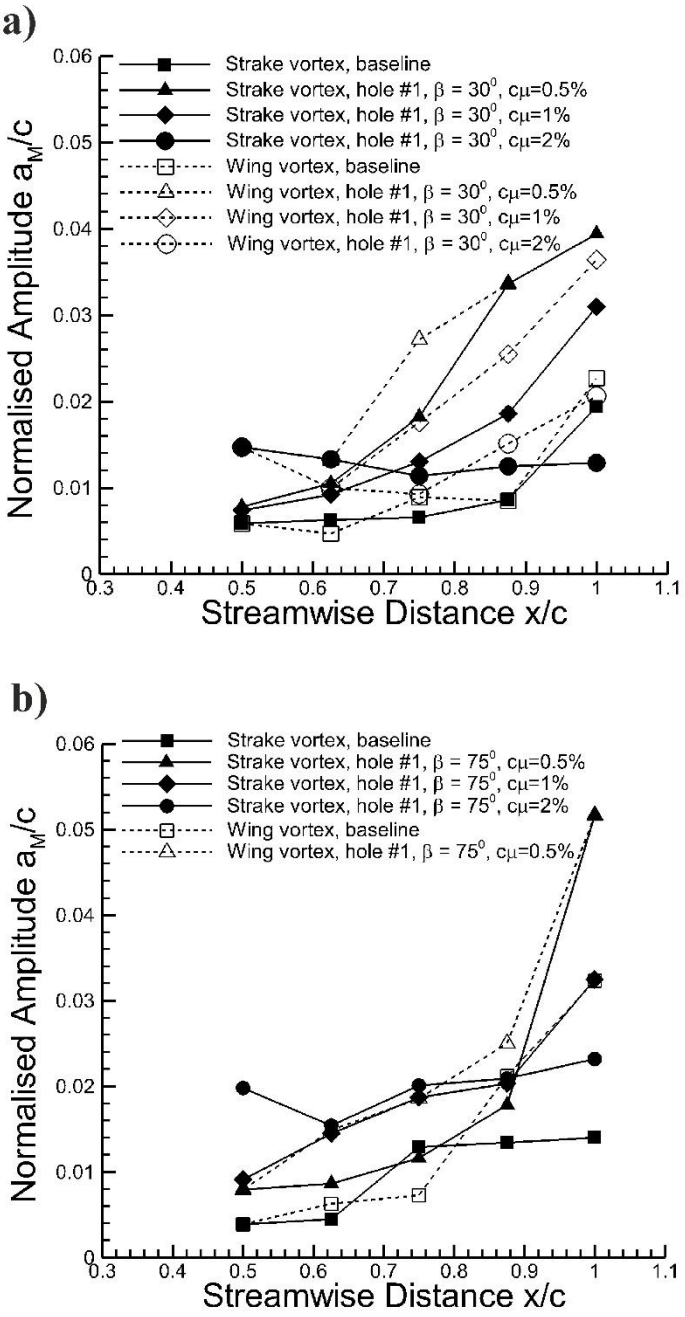


Figure 83. Normalised meandering amplitude for a) α = 8º blowing hole #1, β = 30º and b) α = 12º blowing hole #1, β = 75º.

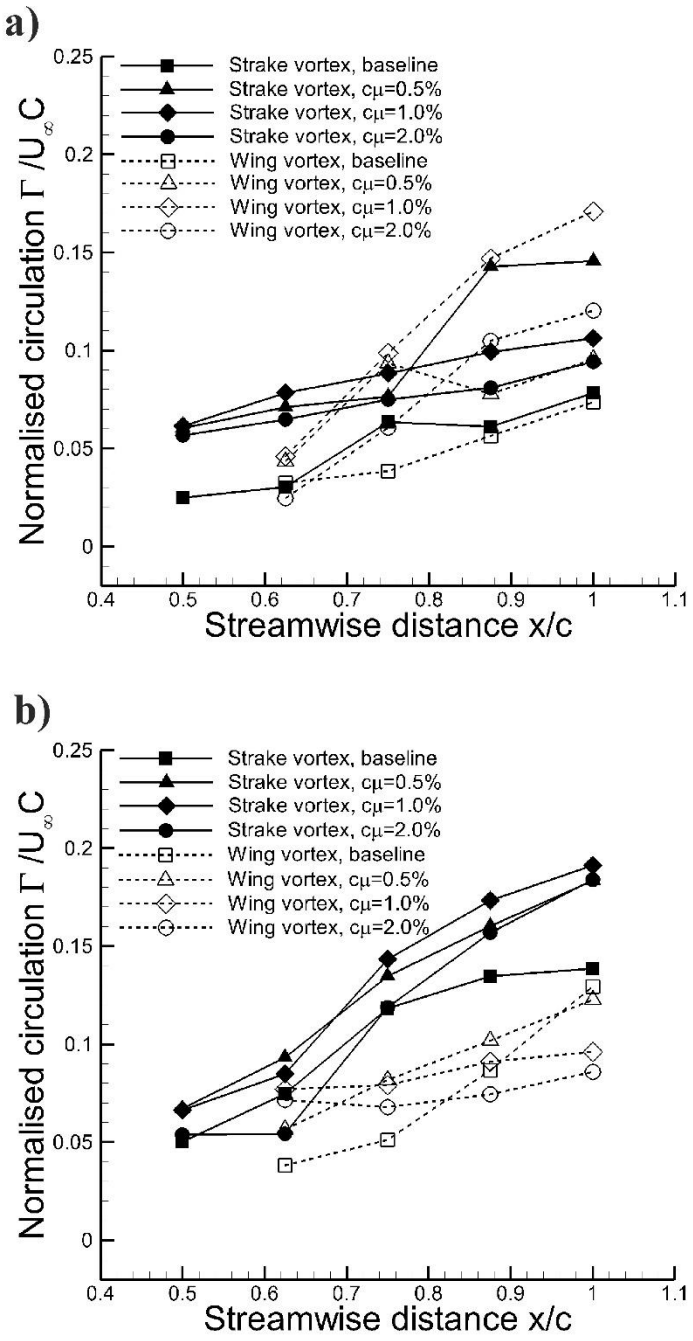


Figure 84. Normalised circulation for a) α = 8º blowing hole #1, β = 30º and b) α = 12º blowing hole #1, β = 75º.

# CHAPTER 6.

# EFFECT OF PASSIVE BLEED

## 6.1 Summary

Experiments have been carried out investigating the effect of passive bleed on double delta wing vortical flow. Different bleed configurations, including both bleed hole and bleed slot, were tested at various angles of attack. Depending on the bleed hole location, passive bleed can result in different effects on the vortical flow. It can be observed that as bleed is introduced, it enhances the counter rotating secondary vortex, this secondary vortex could then interfere with the shear layer or the main wing vortex and alter the vortical flow structure. Bleed also increases the overall standard deviation of the crossflow velocity fluctuation and the vortex meandering amplitude. With bleed, the global vortex centroid moves inboard towards the wing centreline. More specifically, moving the bleed hole location towards the wing leading-edge results in the global vortex centroid moving inboard towards the wing centreline. It was found that bleed is more effective at lower angles of attack.

## 6.2 Results and Discussion

Figure 85 presents time-averaged vorticity patterns in the crossflow plane at x/c = 87.5% over the double delta wing at $\alpha = 8^{\circ}$ without and with bleed at various spanwise locations. As aforementioned, without bleed, well defined wing and strake vortices are formed near the wing surface (Figure 85a) and a small counter-rotating secondary vortex is observed over the wing surface between the two main vortices at around y/s = -0.7. With bleed at hole #1 (Figure 85b), both wing and strake vortices move inboard slightly, the wing vortex is stretched inboard and tends to merge with the strake vortex. Also, it appears that the counter-rotating secondary vortex is strengthened by the bleed and moves away from the wing surface. When the bleed hole is located outboard at bleed hole #2 (Figure 85c) and hole #3 (Figure 85d), the strengthened secondary vortex moves further away from the wing surface and is positioned between the wing and strake vortices. Both wing and strake vortices appear to be strengthened. Note that at

bleed hole #3 another small counter-rotating secondary vortex is visible near the leading-edge at y/s = -0.9, and this is strengthened further when the bleed hole is located even closer to the wing leading-edge at bleed hole #4 (Figure 85e) and hole #5 (Figure 85f), while the secondary vortex located between the two main vortices is weakened. As a result, both wing and strake vortices are displaced inboard towards the wing centerline. For the bleed slot case (Figure 85g), however, both vortices show lower vorticity magnitude. The counter rotating secondary vortices are not present at this configuration.

In order to further investigate the effects of bleed on the wing and strake vortices in the streamwise direction, crossflow PIV measurements were taken at various chordwise locations. Figure 86 presents time-averaged vorticity patterns over the double delta wing at $\alpha = 8^{\circ}$ without and with bleed at various spanwise locations. For the baseline case (Figure 86a), well-established strake and wing vortices can be observed throughout the tested chordwise planes. In addition, a small counter rotating secondary vortex very close to the wing surface can also be noticed from x/c = 75%. With bleed at hole #1 (Figure 86b), the secondary vortex can be seen from x/c = 62.5% onward. Meanwhile, the wing vortex is displaced and stretched inboard and tends to merge with the strake vortex at x/c = 87.5%, the merging process is completed at the wing trailing-edge. Note that, induced by the counter-rotating secondary vortex, another wing vortex is being developed from the shear layer that separates from the leading-edge. Similar flow patterns can also be observed with the bleed at an outboard location of bleed hole #3 (Figure 86c). For example, the bleed strengthens the counter rotating secondary vortex further and, as a result, the merging process of the wing and strake vortices starts at x/c = 75%. The wing and strake vortices merge into a large coherent vortex at x/c = 87.5%. Concurrently, from x/c = 75%, another wing vortex is being developed from the separated shear layer from the wing leading-edge.

Figure 87 illustrates the streamline patterns at $\alpha = 8^{\circ}$ for the same configurations mentioned in Figure 86. For the baseline case (Figure 87a), both the strake and wing vortices display high crossflow velocity regions up to x/c = 87.5%, after which only the streamline profile of the wing vortex can be observed at the trailing-edge. In addition, as the measurement plane moves downstream from x/c = 75%, the density of the streamline profile of the strake vortex decreases. On the contrary, the streamline

density and size of the wing vortex maintain relatively consistent at downstream planes. At bleed hole #1 (Figure 87b), dense and well-defined streamline profile can be observed for the wing vortex from x/c = 62.5% to the trailing-edge. The streamline profile for the strake vortex gradually loses its density as the measurement plane moves downstream, it becomes unrecognisable at x/c = 75%. Meanwhile, the streamline profile of the previously discussed additional wing vortex which induced by the secondary vortex is present at the trailing-edge. For bleed hole #3, well-defined streamline profiles for both the strake and wing vortices can be observed at x/c = 62.5%. After x/c = 62.5%, the strake vortex starts losing its structure and being ingested into the streamline profile of the wing vortex at x/c = 87.5%. This observation is consistent with the time-averaged vorticity result seen in Figure 83c, in which merging process of the strake and wing vortices occurs at x/c = 87.5%. In addition, the streamline profile of the additional vortex induced by the counter rotating secondary vortex can be seen near the wing leading-edge.

The standard deviation results of the crossflow velocity fluctuation for the above-mentioned cases are illustrated in Figure 88. It can be seen that the baseline case (Figure 88a) has concentrated high standard deviation regions around the strake and wing vortices, the area underneath the shear layer separated from the wing leading-edge is displaying much higher standard deviation than other areas. As bleed is introduced hole #1 and #3 (Figure 88b & 88c), the standard deviation concentration spreads over the wing surface in the spanwise direction, meanwhile the rest of the area (region outside the shear layer) displays higher overall standard deviation than the baseline case, this could indicate increased level of meandering. To investigate the vortex meandering properties, the meandering probability plot is shown in Figure 89. For the baseline case (Figure 89a), it can be observed that very small meandering area with high meandering probability is shown for both strake and wing vortices for all the measurement planes, although the wing vortex meandering area at the trailing-edge starts to expand and diffuse. At bleed hole #1 (Figure 89b), both the strake and wing vortices show slightly expanded meandering area with diffused peak probability compared with the baseline case. In addition, the merging process of the strake and wing vortices can be observed from x/c = 75% to the trailing-edge. At x/c = 87.5%, the wing vortex moves towards the strake vortex, they then merge into one big coherent vortex with decreased peak meandering probability at the trailing-edge. At

the trailing-edge, the meandering probability of the additional vortex that formed within the shear layer is also shown. The meandering area of the additional vortex displays the same elliptical shape as the primary vortices, which elongates in the spanwise direction, its peak meandering probability is much lower than the wing vortex in the baselines case at the trailing-edge. Bleed hole #3 is shown in Figure 89c, where the presence of three vortices can be observed at x/c = 75%, which are the wing and strake vortices, and the additional wing vortex induced by the secondary vortex. Prior to x/c = 75%, both strake and wing vortices show slightly expanded meandering area than the baseline case, however, they maintain high peak meandering probabilities. At x/c = 75%, the strake and wing vortices move closer to each other and merge into one vortex at x/c = 87.5%, the merged vortex shows high peak meandering probability and moves further away from the wing surface. At the trailing-edge, the meandering characteristics of the additional vortex show much diffused area with very low peak probability, while the meandering characteristics of the merged vortex still display well defined vortical shape but with much lower peak probability.

Figure 90 examines the meandering amplitude and total circulation for the bleed and non-bleed cases at $\alpha = 8^{\circ}$. From Figure 90a, it can be observed that both the strake and wing vortices at the baseline case display relatively low meandering amplitudes. As bleed is introduced, the meandering amplitudes of both vortices increase. In particular, bleed at hole #3 increases the meandering amplitude of the wing vortex most significantly and bleed at hole #1 increases the meandering amplitude of the strake vortex the most. In the normalised total circulation result (Figure 90b), the baseline case illustrates the lowest level of circulation, adding the passive bleed increases the circulation level. Between the two bleed cases, bleed at hole #3 results in a slightly higher circulation before x/c = 75%, and bleed at hole #1 results in higher circulation after x/c = 75%. The first POD modes for these three cases are shown in Figure 91, it can be observed that a counter rotating vortex pair is present in the wing and strake vortex locations for the two bleed cases. In addition, the baseline case POD result shows several additional vortices alongside the main vortex pair.

Figure 92 illustrates the time-averaged vorticity patterns at x/c = 87.5% and $\alpha = 12^{\circ}$ for the baseline case and the bleed cases for different spanwise bleed hole locations. When bleed at hole #1 (Figure 92b), a strengthened secondary vortex can be observed

between the strake and wing vortices. In addition, the strake vortex stretches in the vertical direction while the wing vortex moves closer to the wing surface, both vortices show strengthened vorticity as a result of the bleed. On the other hand, at bleed hole #2 and #3 (Figure 92c&d), only the strake vortex is strengthened while the wing vortex appears to be weakened due to the bleed yet they both move inboard towards the wing centreline. As the bleed hole location moves closer to the wing leading-edge at bleed hole #4 (Figure 92e), the counter rotating secondary vortex spreads outboard over the wing surface. Meanwhile, wing vortex moves significantly inboard and closer to the strake vortex and the strake vortex moves towards the wing surface and underneath the wing vortex, the two vortices tend to merge in this bleed configuration. At bleed hole #5 (Figure 92f), the strake and wing vortices are in the process of merging, meanwhile an additional vortex forms within the shear layer separated from the wing leading-edge. For the bleed slot configuration (Figure 92g), the vortical shapes for both the strake and wing vortices are similar to that of the baseline cases, however, both vortices and the counter rotating secondary vortex appear to be strengthened by the bleed.

Figure 93 illustrates the crossflow vorticity patterns at $\alpha = 12^{\circ}$ for the baseline case and bleed cases at bleed hole #4 and #5. At bleed hole #4 (Figure 93b), it can be observed that the wing vortex starts moving closer towards the strake vortex at x/c = 75%, they then undergo a merging process to form one big coherent vortex at the trailing-edge. Bleed at hole #5 (Figure 93c) shows a notably strengthened counter rotating secondary vortex at x/c = 75%, which induces an additional vortex near the wing leading-edge. Meanwhile, the wing vortex moves closer inboard towards the strake vortex and initiates the merging process. At x/c = 87.5%, the merging process between the strake and wing vortices are complete while the additional vortex formed near the wing leading-edge starts to expand and lose its vortical structure. At the trailing-edge, both the additional vortex and the merged vortex expand and diffuse further, which indicates vortex breakdown.

The streamline profiles of the baseline case and the bleed cases at $\alpha = 12^{\circ}$ are shown in Figure 94. It can be observed that for the baseline case (Figure 94a), the streamline profiles for both the strake and wing vortices display well defined vortical structures with high streamline density for all the streamwise planes. At bleed hole #4 (Figure

94b), the wing vortex moves further inboard towards the wing centreline and appears to be the more dominant vortex between the two vortices. At x/c = 62.5%, the streamline profiles for both strake and wing vortices display a well defined structure and high crossflow velocity areas around the vortex locations. At x/c = 75%, the high velocity region of the strake vortex shrinks significantly and it is slowly being ingested into the wing vortex streamline structure. At x/c = 87.5%, also indicated in Figure 93b, the strake and wing vortices undergo a merging process, the streamline profile of the strake vortex is no longer recognisable and only the streamline of one big coherent vortex is observed. At the trailing-edge, together with the merged vortex, the streamline profile of the additional vortex is also present. For bleed hole #5 (Figure 94c), well defined strake and wing vortex streamline profiles can be observed at x/c = 62.5%. At x/c = 75%, the strake vortex has lost its streamline structure and being inscribed into the streamline profile of the wing vortex; meanwhile, the streamline profile of the additional vortex can be seen near the wing leading-edge. Moving downstream to x/c = 87.5%, the strake and wing vortices have completed the merging process and only one vortical structure can be observed that follows the trajectory of the wing vortex. In addition, the streamline profile of the additional vortex can also be found near the wing leading-edge. At the trailing-edge, both the merged vortex and the additional vortex expand in size and display slightly less dense streamlines, this is consistent with the time-averaged vorticity result shown in Figure 93c.

Figure 95 displays the standard deviation of the crossflow velocity for baseline case and bleed cases at $\alpha = 12^{\circ}$. It can be seen that in the baseline case (Figure 95a), similar to $\alpha = 8^{\circ}$, a high standard deviation area can be observed around the strake and wing vortices which occupies the area underneath the separated shear layer. These distinctive standard deviation peaks can be recognised at downstream planes around the vortex core locations of the strake and wing vortices. Very low standard deviation is observed for the rest of the area. On the contrary, for the bleed cases, the high standard deviation region spreads over the wing surface in the spanwise direction with reduced peak values, while the rest of the area increases in overall standard deviation magnitude. This may indicate that bleed increases vortex meandering level. The meandering probability results for the same cases at $\alpha = 12^{\circ}$ are illustrated in Figure 96. For the baseline case (Figure 96a), it can be observed that both the strake and wing vortices show very concentrated meandering area with high peak probability before

x/c = 87.5%. At x/c = 87.5%, the peak probabilities for both vortices decrease and the meandering area for the wing vortex expands greatly. At the trailing-edge, the meandering area of the wing vortex continues to expand and a much lower peak meandering probability is present, this indicates that the wing vortex is entering the breakdown process. On the other hand, the strake vortex maintains certain level of peak probability value and meandering area. At bleed location #4 (Figure 96b), both the strake and wing vortices display slightly larger meandering area with reduced peak meandering probability than the baseline case. During the merging process at x/c = 87.5%, the peak probability for both vortices decrease slightly, and the two vortices move much closer to each other but maintain individual vortex meandering region. At the trailing-edge, however, the merged vortex shows very low meandering probability with a more diffused meandering area. At bleed hole #5 (Figure 96c), both vortices show a very concentrated meandering area and high peak probability at x/c = 62.5%. At x/c = 75%, the meandering probability of the additional vortex is also present together with the strake and wing vortices, all of them show relatively high meandering probabilities with small meandering areas. At x/c = 87.5%, the meandering area of the additional vortex appears to be elongated in the spanwise direction with a greatly reduced peak probability, and the merged strake and wing vortex displays high probability with a small meandering area. At the trailing-edge, however, both vortices lose the probability concentration and illustrate very diffuse meandering regions.

To quantify this vortex meandering, meandering amplitude results are illustrated in Figure 97, together with circulation results. It can be observed that for the strake vortex, the baseline case shows significantly lower meandering level than the bleed cases throughout the tested crossflow planes, apart from x/c = 75% where the baseline case illustrates similar level as the bleed cases. Comparing the two bleed cases, they display similar meandering level before x/c = 75% while after x/c = 75%, bleed at hole #4 shows much higher strake vortex meandering amplitude than the other. For the meandering amplitude of the wing vortex, bleed at hole #5 shows very similar meandering level as the baseline case, however, bleed at hole #4 results in much higher wing vortex meandering amplitude. The normalised circulation result (Figure 97b) indicates that very similar levels of circulation are seen between the baseline case and bleed hole #4 case, while bleed at hole #5 shows a slightly higher circulation level than the other two cases. Figure 98 illustrates the 1$^{st}$ mode (most energetic) of the POD

results for the three cases at $\alpha = 12^{\circ}$. For the baseline case, it can be observed that both the strake and wing vortices present a pair of counter rotating vortices, there are also additional vortices along the separated shear layer shown in the result at downstream planes (x/c = 87.5% & trailing-edge). At bleed hole #4 (Figure 98b) upstream planes (x/c = 50% & 62.5%), the first POD mode shows counter rotating vortex pair at the strake vortex location. At downstream planes between x/c = 75% and trailing-edge, the 1st mode displays the vortex pair at the wing vortex location. Bleed at hole #5 (Figure 98c) results in much cleaner POD vorticity field, however, for downstream planes (x/c = 75% to trailing-edge), the vortex pair is now at the location of the counter rotating secondary vortex that was found in the time-averaged vorticity result. At x/c = 50% and 62.5%, a much weakened vortex pair can be observed at the strake vortex location.

For higher angles of attack, Figure 99 illustrates the time-averaged vorticity patterns for baseline case and four different bleed configurations at x/c = 87.5% and various angles of attack. It can be observed that at $\alpha = 16^{\circ}$, all the bleed cases share very similar vorticity patterns as the baseline case, although a slightly enhanced counter rotating secondary vortex is present on all the bleed cases. At $\alpha = 20^{\circ}$, the baseline case displays a strong and well defined vortical structure for the strake vortex. When bleed is introduced, both strake and wing vortices tend to break down on all the bleed configurations. In particular, bleed slot configuration experiences complete breakdown of the two vortices, and lower overall vorticity magnitude is observed. At $\alpha = 24^{\circ}$ all the bleed and non-bleed cases display complete breakdown of both strake and wing vortices.

For the higher angles of attack, bleed slot configuration at $\alpha = 20^{\circ}$ was investigated further since it caused the complete breakdown of both vortices when compared with the baseline case. Figure 100 shows the time-averaged vorticity patterns for baseline case and bleed slot case at $\alpha = 20^{\circ}$. For the baseline case (Figure 100a), it can be observed that a strong and well defined strake vortex is present from x/c = 50% to 87.5%. The wing vortex, however, is not recognisable. At the trailing-edge, the strake vortex is undergoing the breakdown process. For the bleed slot configuration (Figure 100b), the well established vortical structure of strake vortex can be seen at x/c = 50% and 62.5%. After x/c = 62.5% the strake vortex undergoes the vortex breakdown

process and completely breaks down by x/c = 87.5%. In addition, a much weaker counter rotating secondary vortex can be observed for the bleed slot configuration when compare with the baseline case. Figure 101 contains the streamline results for the baseline and bleed slot configurations at $\alpha = 20^{\circ}$. For the baseline case (Figure 101a), a well defined vortical streamline profile can be observed for the strake vortex from x/c = 50% to 87.5%. Although the strake vortex has broken down at the trailing-edge in the time-averaged vorticity result (Figure 100a), a circulating area can be found at the trailing-edge in the streamline results. For the bleed slot case (Figure 101b), the streamline result also displays a weak level of circulation post vortex breakdown at x/c = 75%. The centre of this circulating region lies within the centre of the broken down vortical flow.

Figure 102 illustrates the standard deviation of crossflow velocity fluctuation for the baseline case and the bleed slot case at $\alpha = 20^{\circ}$. It can be noticed that after adding the bleed slot, the high standard deviation area expands greatly compared with the baseline case. Meanwhile, there is no distinctive standard deviation peaks in the bleed slot case. The vortex meandering probability plot is shown in Figure 103 where it can be observed that the baseline case (Figure 103a) displays very concentrated meandering probability for the strake vortex from x/c = 50% to 87.5%. It then shows a broken down vortex meandering profile at the trailing-edge. On the other hand, for the bleed slot configuration (Figure 103b), a well established vortex meandering shape with slightly lower peak probability can be observed only at x/c = 50% and 62.5%, after x/c = 62.5% it displays a broken down meandering shape. To quantify the magnitude of the vortex meandering, the normalised vortex meandering amplitude is shown in Figure 104 together with normalised total circulation. For the meandering amplitude (Figure 104a), the strake vortex on the baseline case shows a very low meandering amplitude from x/c = 50% to 75%, before increasing dramatically after x/c = 75%. On the other hand, for the bleed slot case, the meandering amplitude starts increasing dramatically as early as at x/c = 62.5%. This dramatic increase in meandering amplitude can be associated with the onset of vortex breakdown, the observation in the meandering amplitude results match previous results. For the total circulation result, it can be seen that the bleed slot configuration shows slight increase in the circulation between x/c = 62.5% and 75% compare with the baseline case, on other streamwise locations the two cases share very similar levels of strake vortex

circulation level. The vorticity patterns on the first POD mode for the two cases are shown in Figure 105. For the baseline case (Figure 105a), a pair of counter rotating vortices can be seen at the strake vortex location from x/c = 50% to 75%. After x/c = 75% the POD result shows the decomposition of the broken down vortical flow. However, due to the early onset of vortex breakdown for the bleed slot case, the POD result only displays the decomposition of the broken down vortical flow. Figure 106 shows that for both $\alpha$ = 8° and $\alpha$ = 12° the global vortex centroid moves inboard towards the wing centreline when bleed is deployed. Furthermore, when the bleed location is moved outboard towards the wing leading-edge, the global vortex centroid moves further inboard. This effect is particularly strong at the lower wing incidence.

## 6.3 Conclusion

A study has been carried out investigating the effect of passive bleed on double delta wing vortical flow at various angles of attack and bleed locations. As bleed is introduced, it can enhance the strength of the counter rotating secondary vortex so that the secondary vortex can effectively interfere with the main wing vortex and the shear layer, which results in the presence of additional vortices. This phenomenon was observed at α = 8˚, bleed hole #3 and α = 12˚, bleed hole #5. For optimised bleed locations the strake and wing vortices merged into one coherent vortex, this was facilitated by the ingestion of turbulence from the bleed. Due to this ingestion of turbulence, the overall standard deviation of the crossflow velocity and the vortex meandering amplitude are also increased when bleed is introduced. With bleed, the global vortex centroid location moves inboard towards the wing centreline; in particular, as the bleed hole location moves outboard towards the wing leading-edge, the vortex centroid location moves inboard. However, as angle of attack increases, the effect of bleed decreases, bleed at α = 8˚ has much stronger effect in changing the vortex centroid than α = 12˚.

## 6.4 Figures

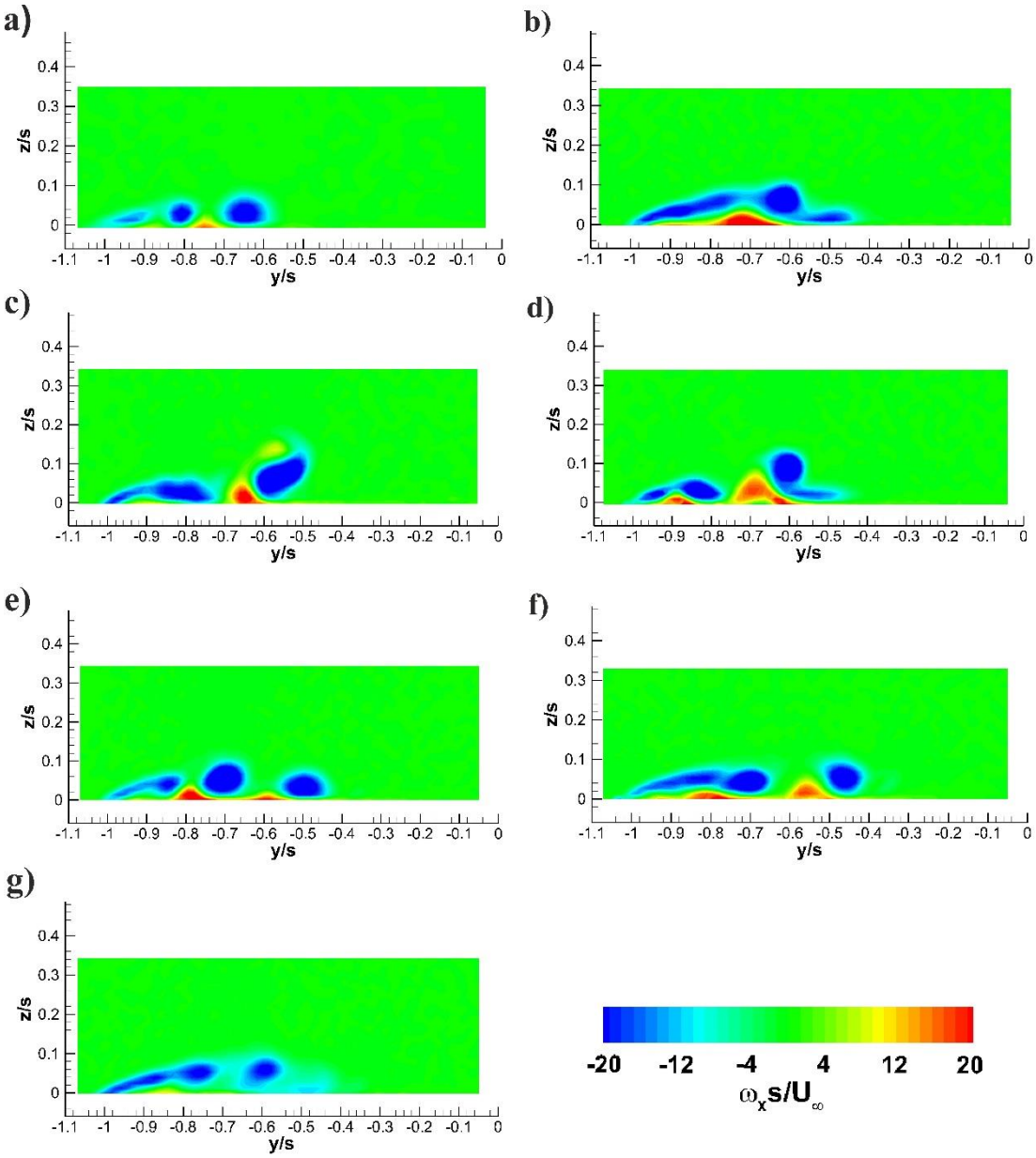


Figure 85. Time-averaged vorticity at x/c = 87.5% and α = 8º for a) baseline case, b) bleed hole #1, c) bleed hole #2, d) bleed hole #3, e) bleed hole #4, f) bleed hole #5 and g) bleed slot.

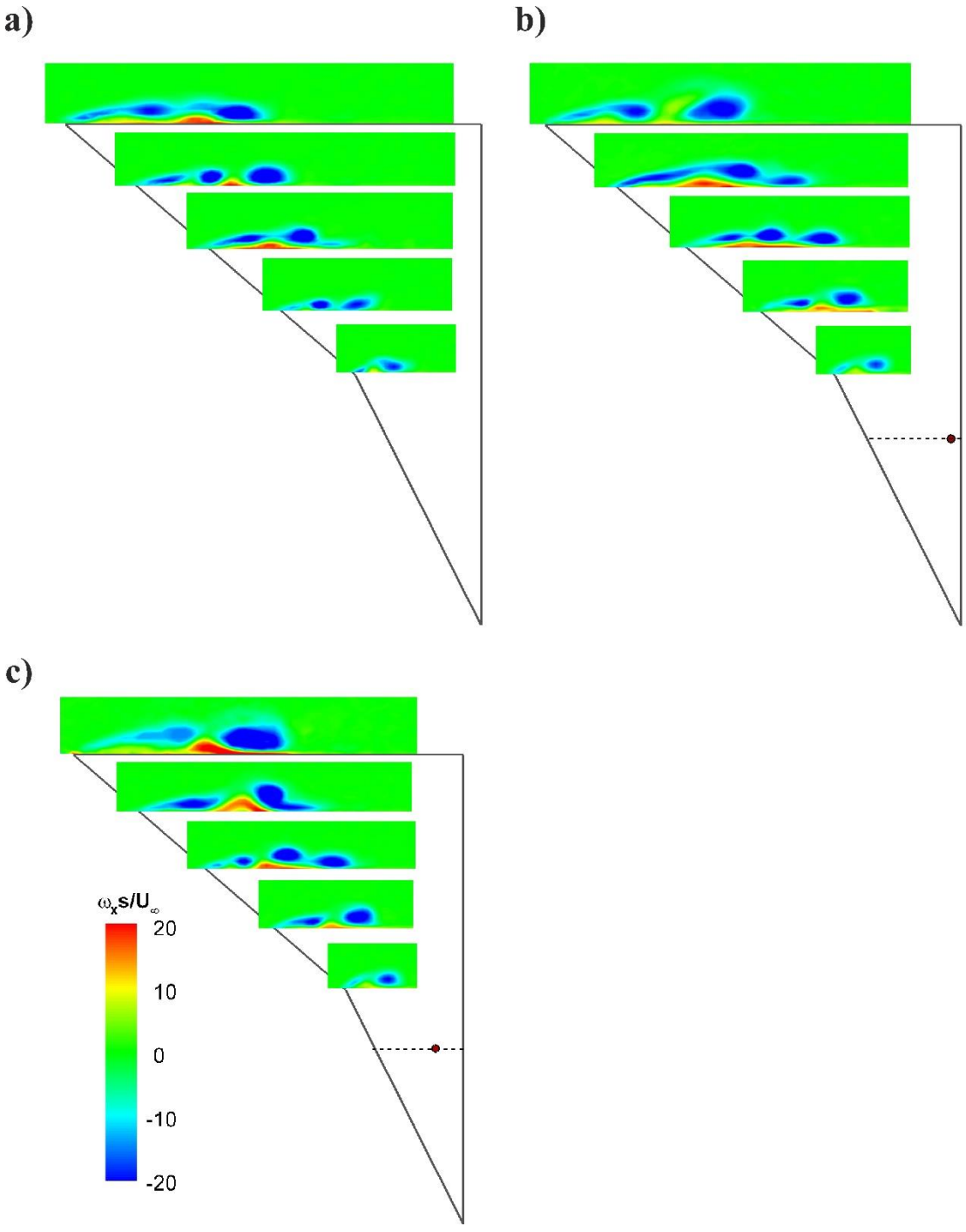


Figure 86. Time-averaged vorticity for α = 8º at a) baseline case, b) bleed hole #1 and c) bleed hole #3.

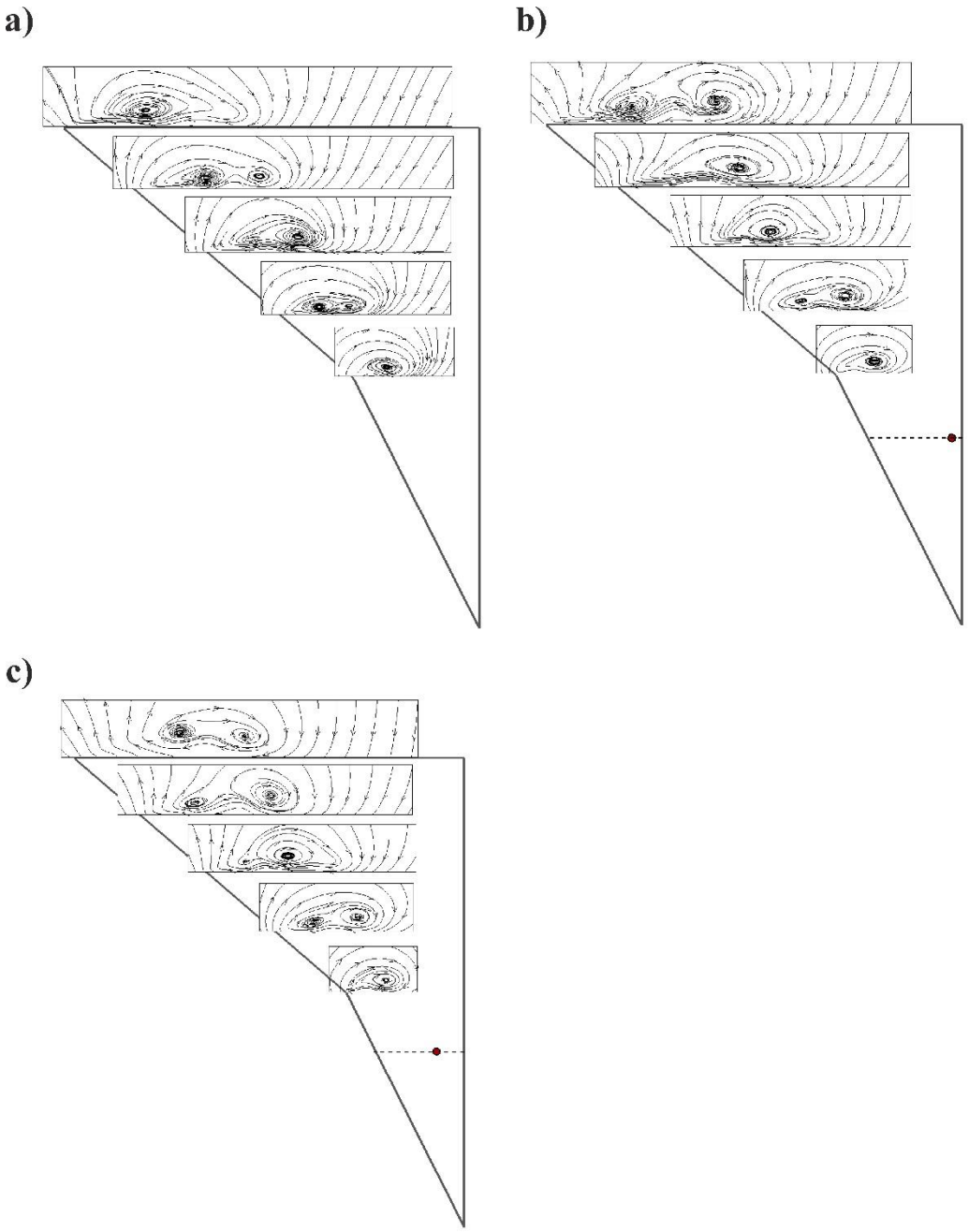


Figure 87. Time-averaged vorticity for α = 8º at a) baseline case, b) bleed hole #1 and c) bleed hole #3.

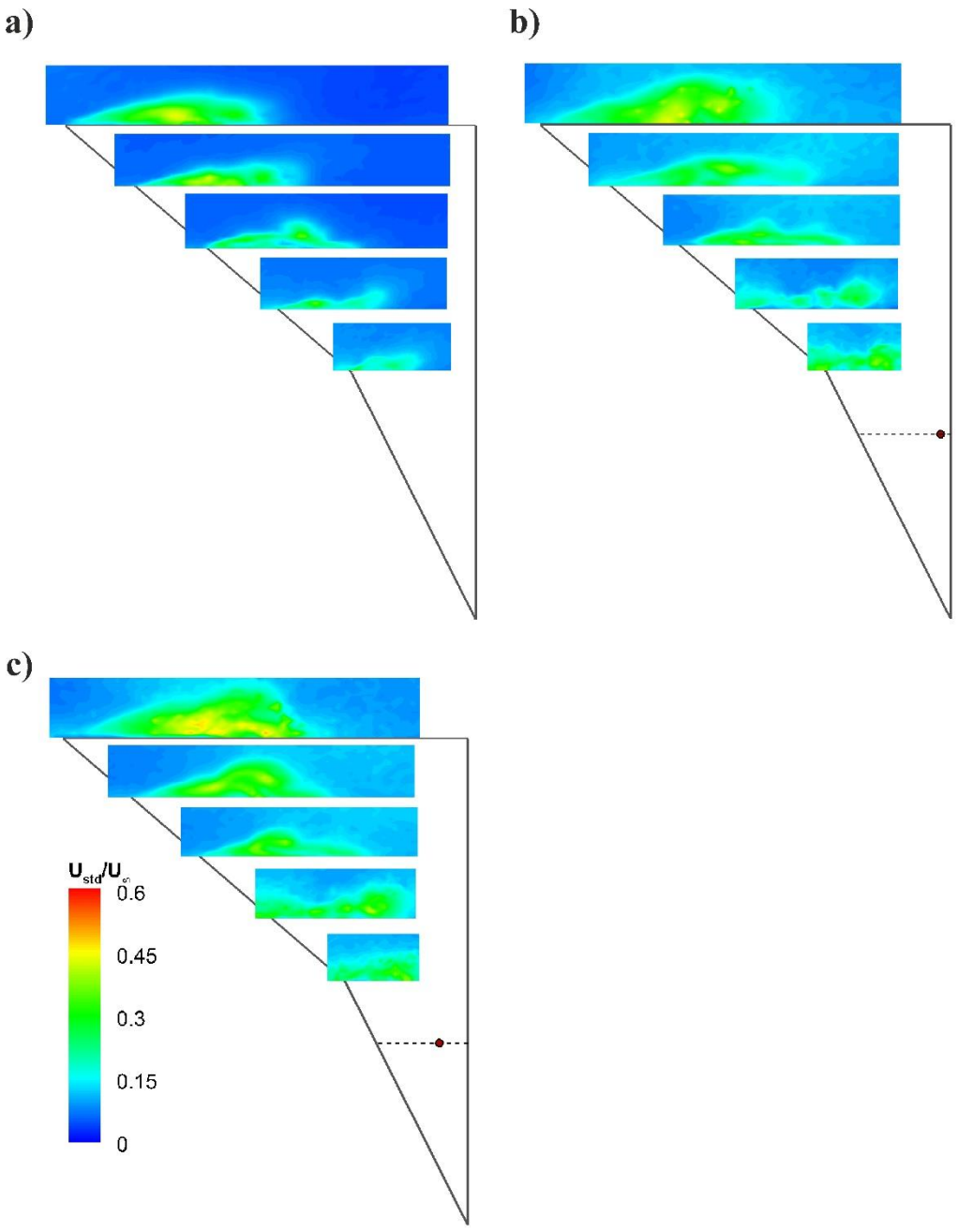


Figure 88. Standard deviation for α = 8º at a) baseline case, b) bleed hole #1 and c) bleed hole #3.

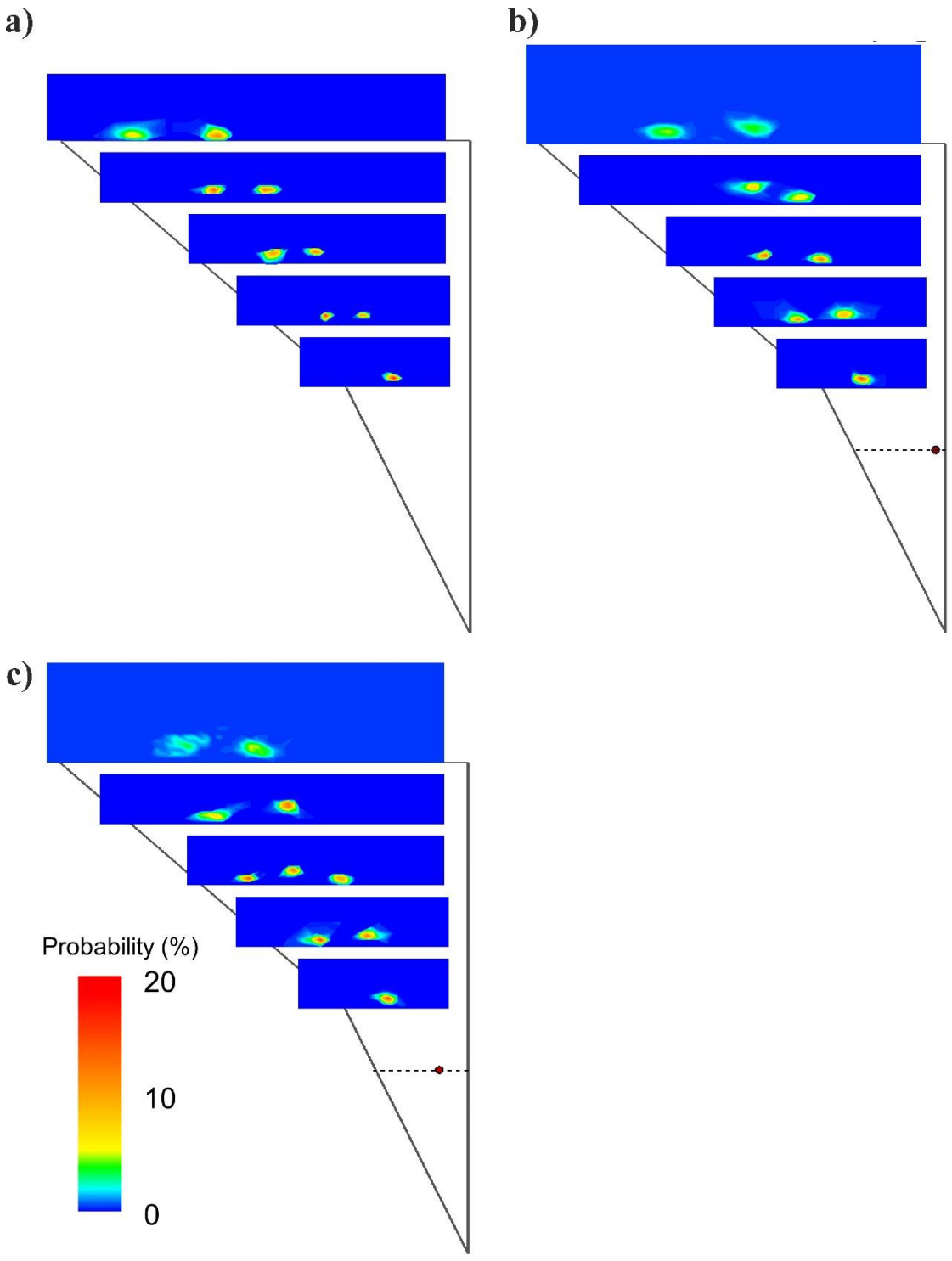


Figure 89. Meandering probability for α = 8º at a) baseline case, b) bleed hole #1 and c) bleed hole #3.

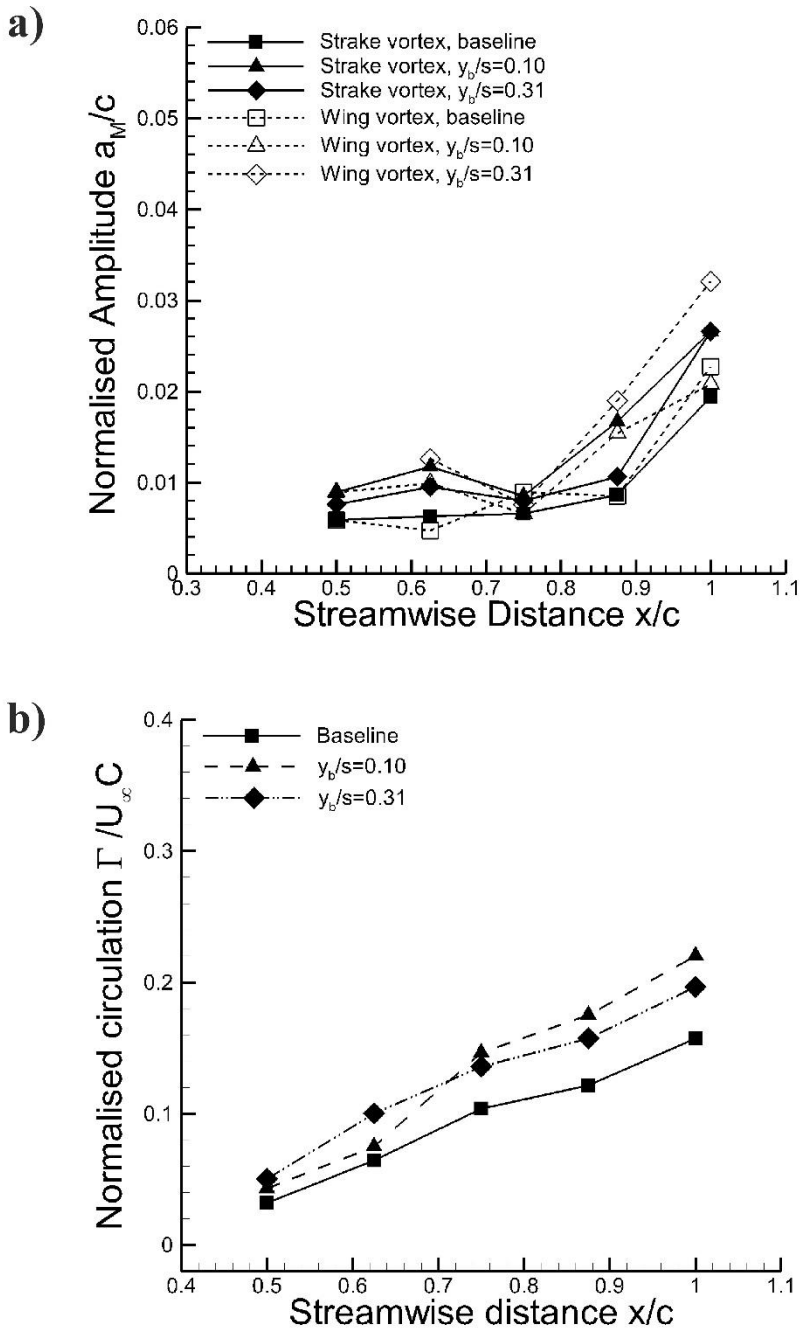


Figure 90. a) Normalised meandering amplitude at α = 8º and b) normalised total circulation.

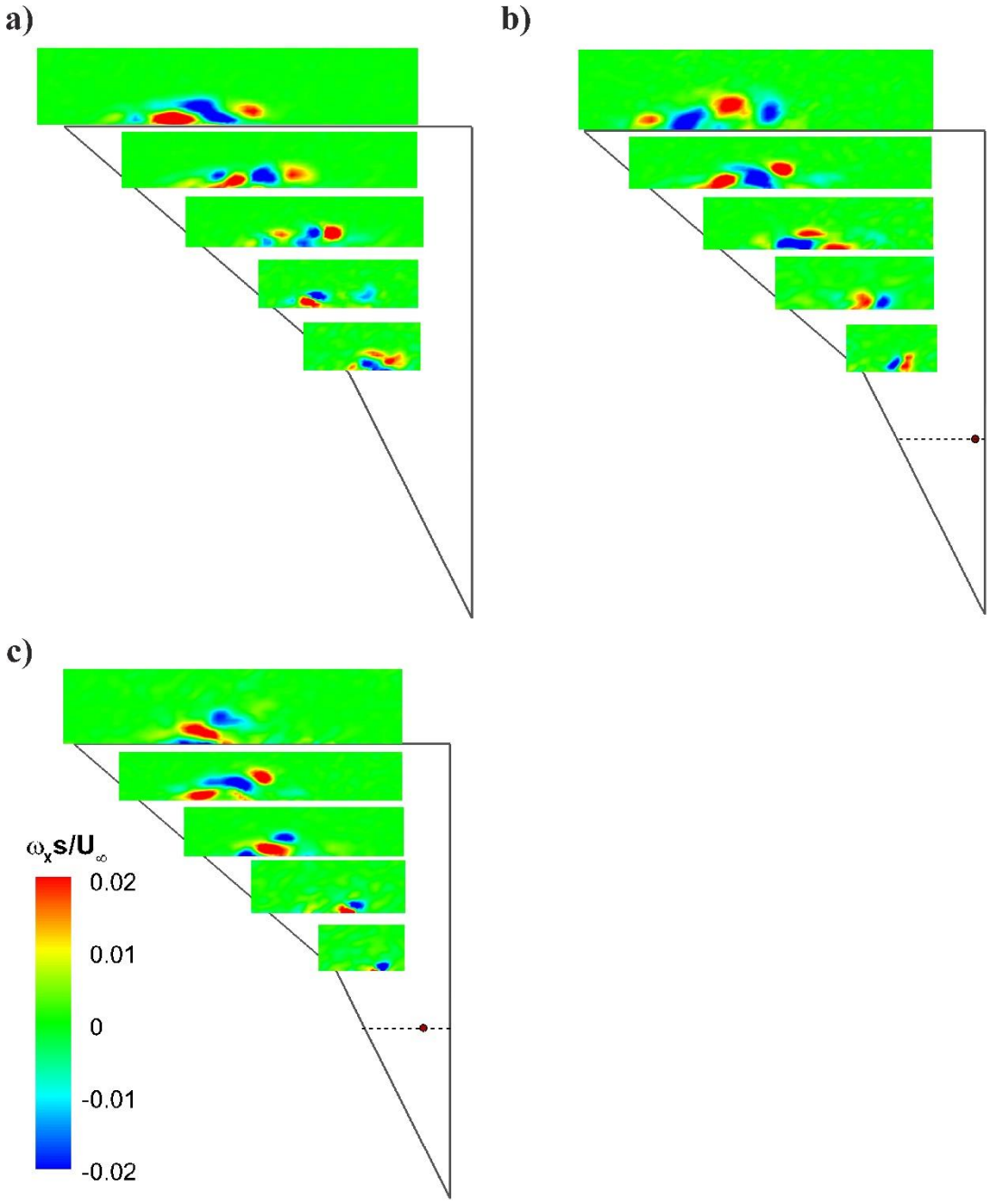


Figure 91. POD mode 1 for α = 8º at a) baseline case, b) bleed hole #1 and c) bleed hole #3.

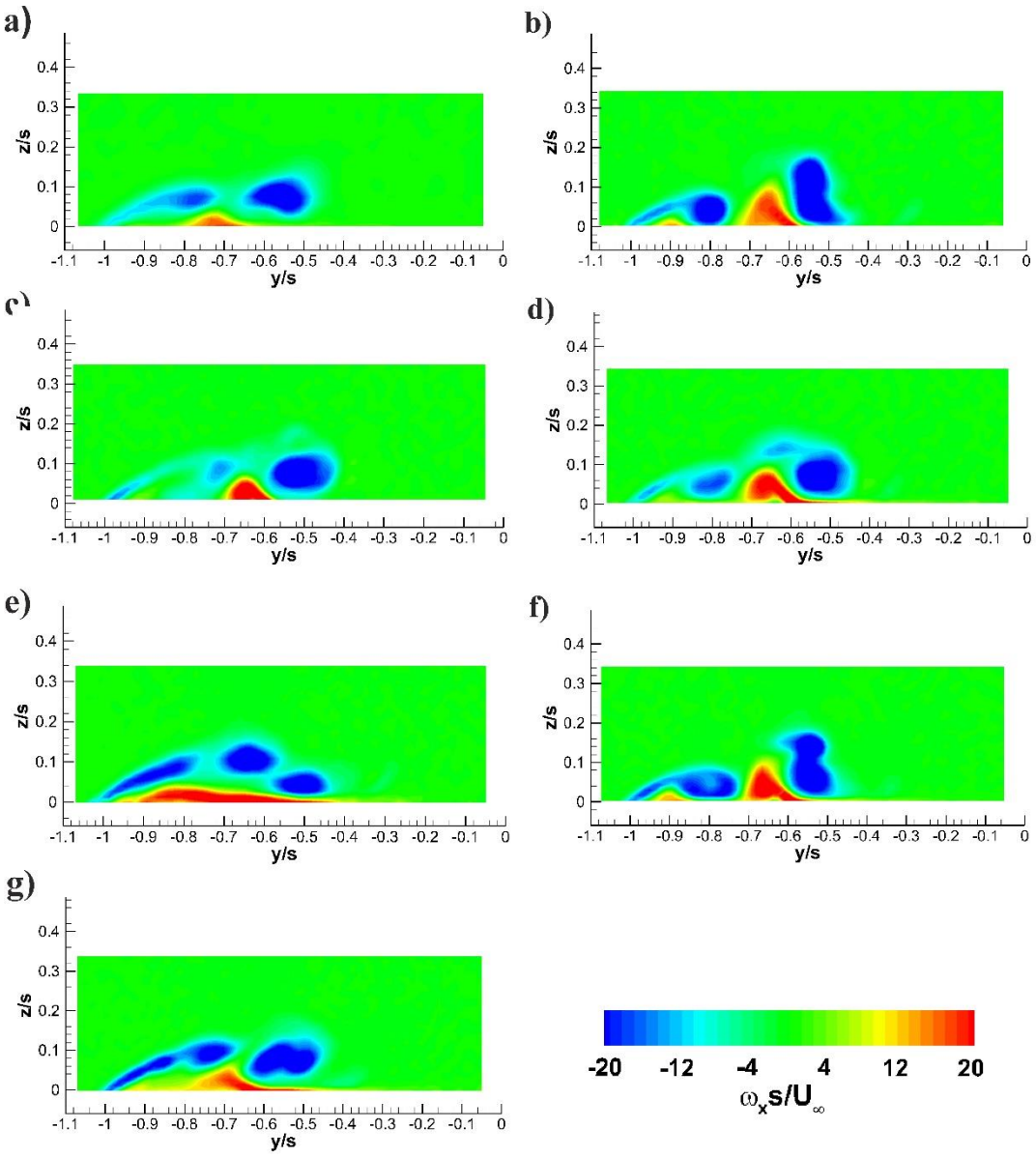


Figure 92. Time-averaged vorticity at x/c = 87.5% and α = 12º for a) baseline case, b) bleed hole #1, c) bleed hole #2, d) bleed hole #3, e) bleed hole #4, f) bleed hole #5 and g) bleed slot.

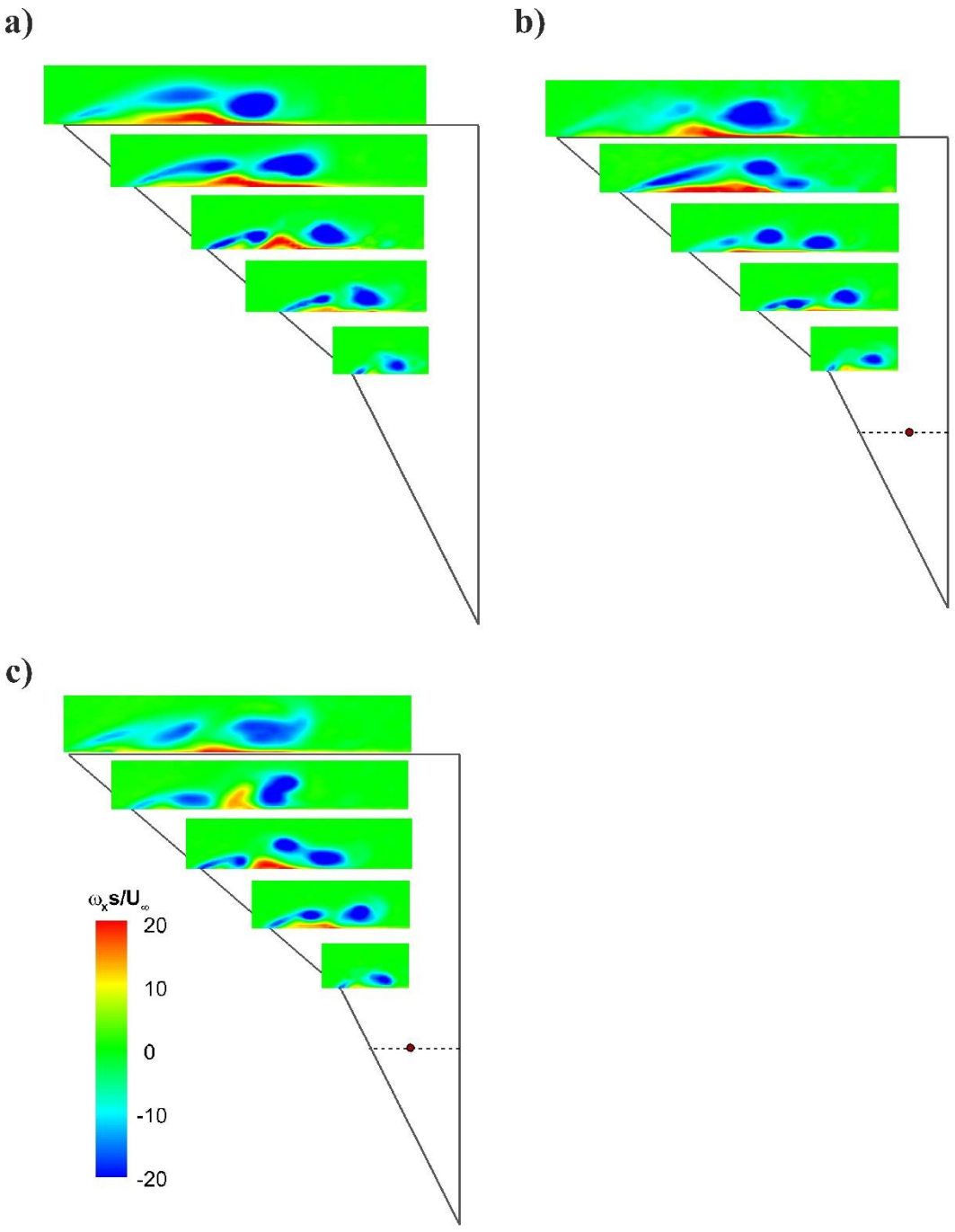


Figure 93. Time-averaged vorticity for α = 12º at a) baseline case, b) bleed hole #4 and c) bleed hole #5.

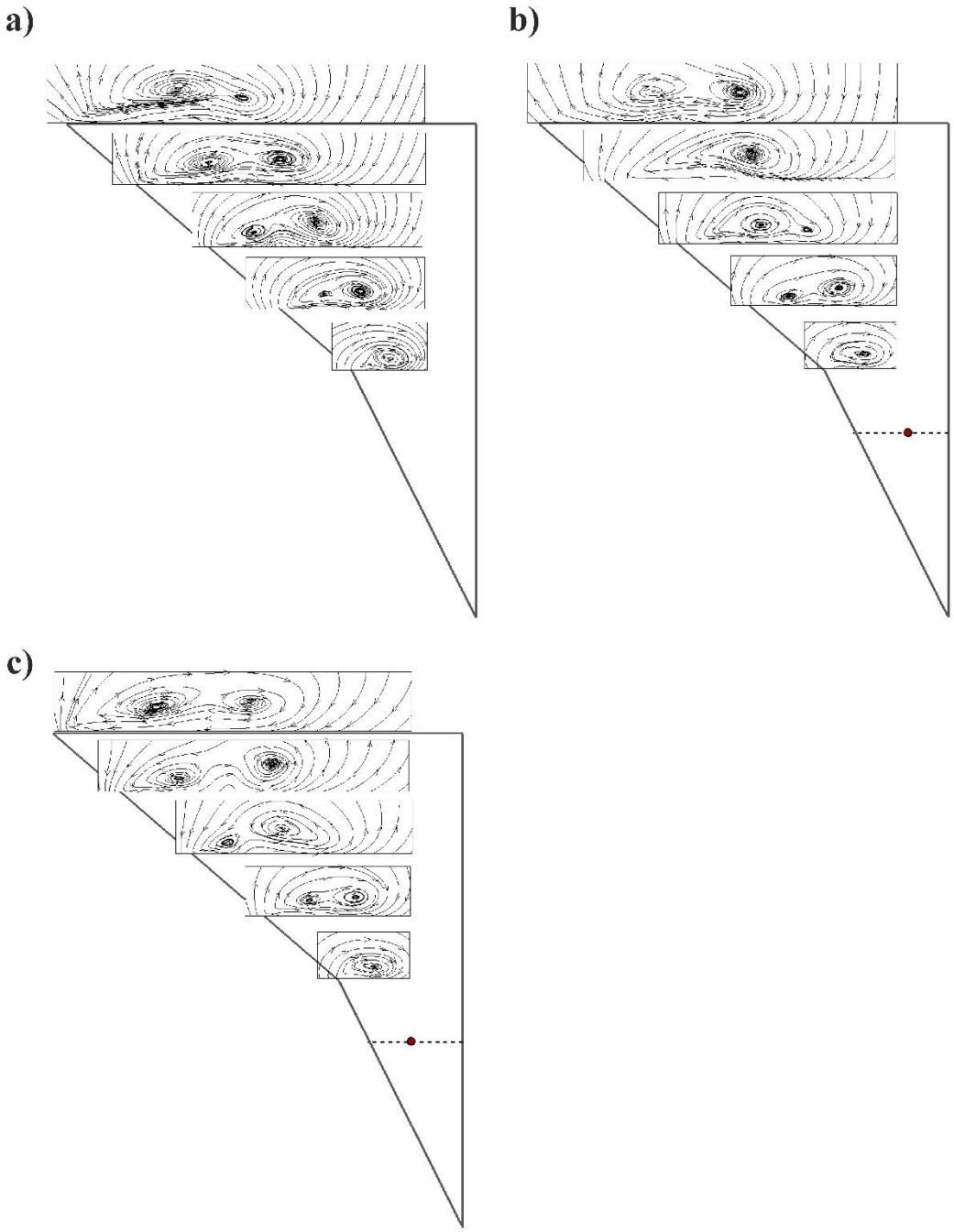


Figure 94. Streamline for α = 12º at a) baseline case, b) bleed hole #4 and c) bleed hole #5.

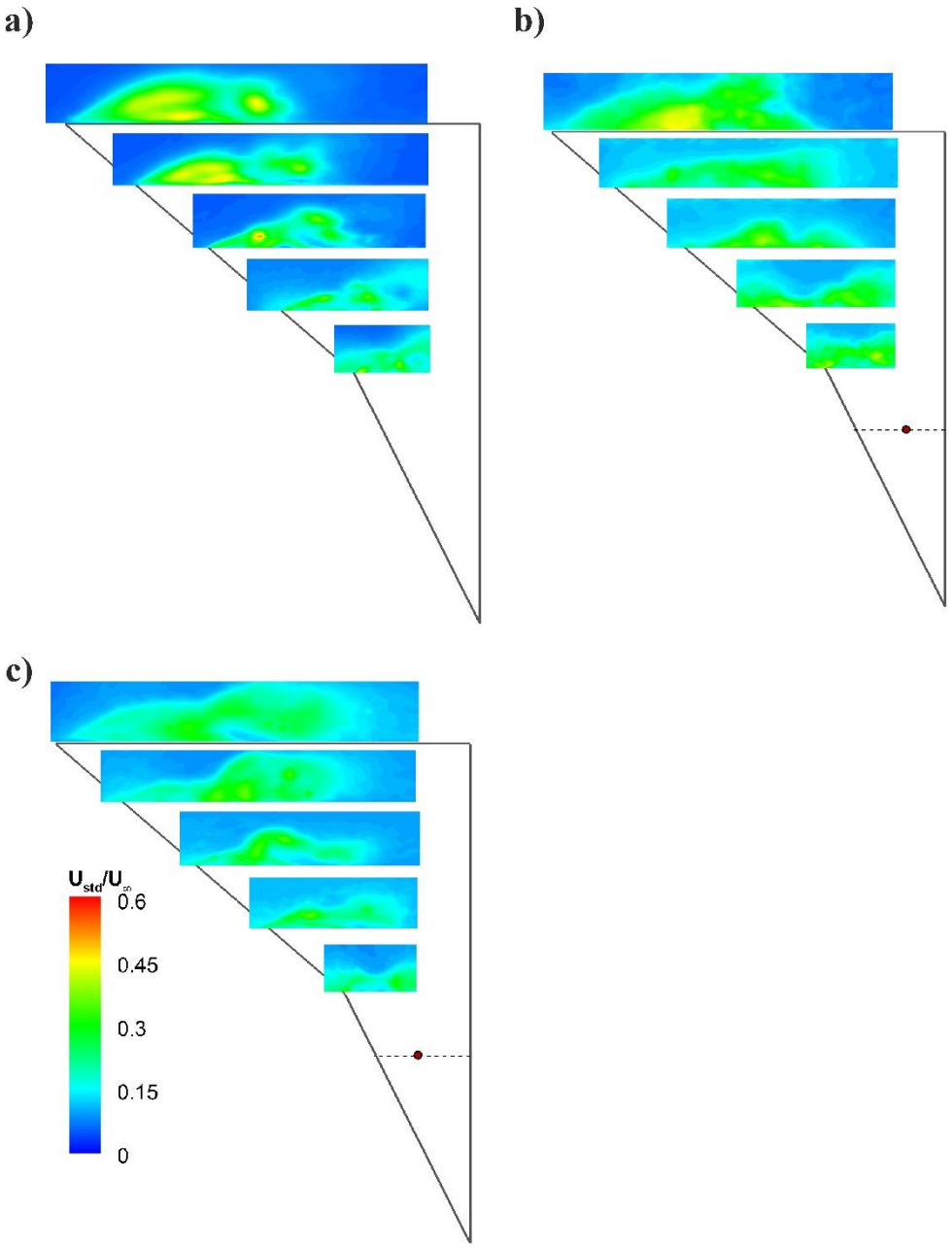


Figure 95. Standard deviation for α = 12º at a) baseline case, b) bleed hole #4 and c) bleed hole #5.

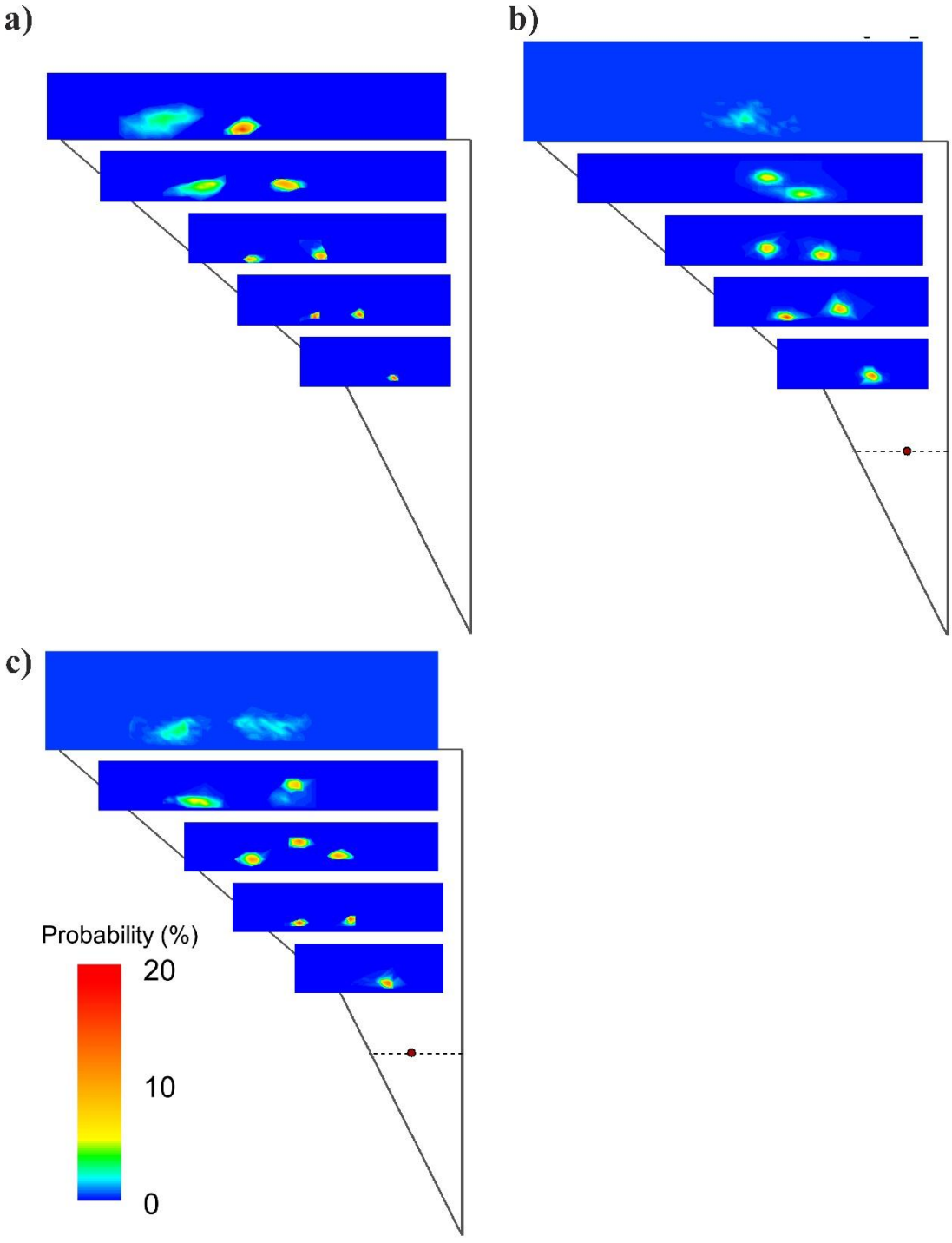


Figure 96. Meandering probability for α = 12º at a) baseline case, b) bleed hole #4 and c) bleed hole #5.

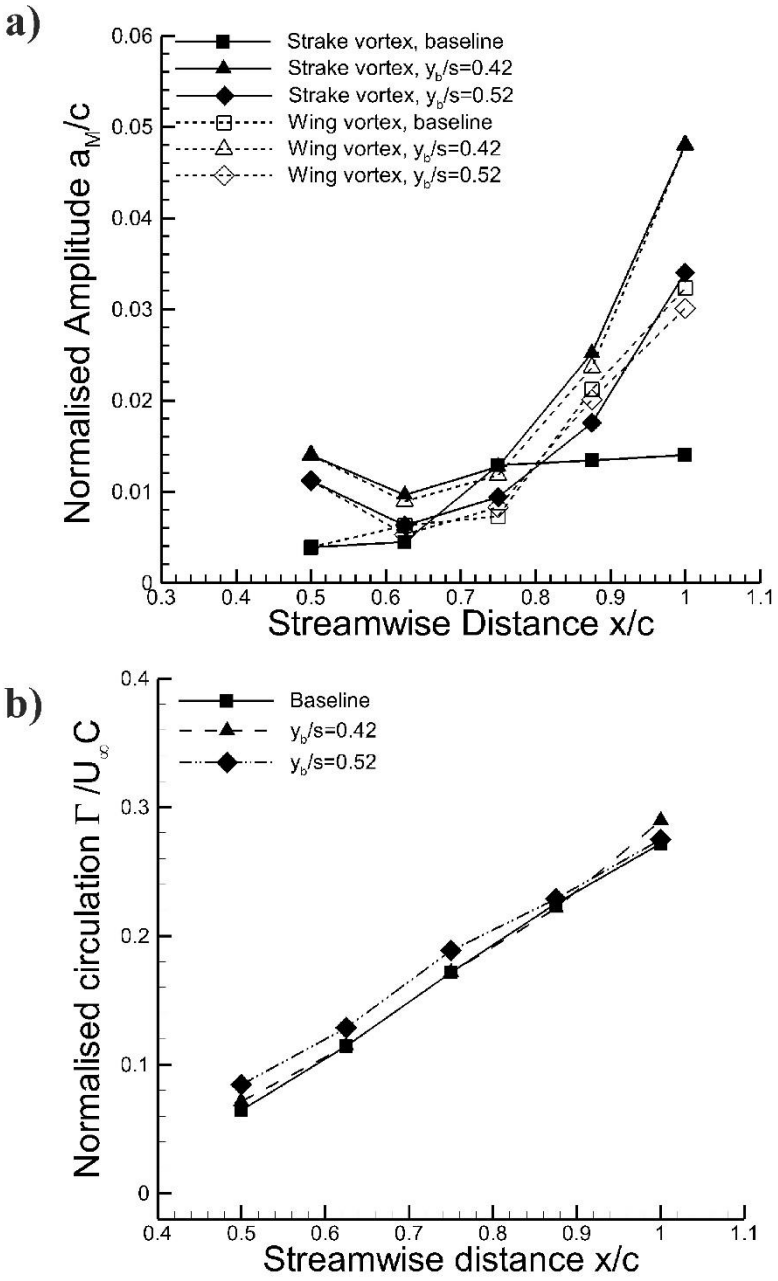


Figure 97. a) Normalised meandering amplitude at α = 12º and b) normalised total circulation.

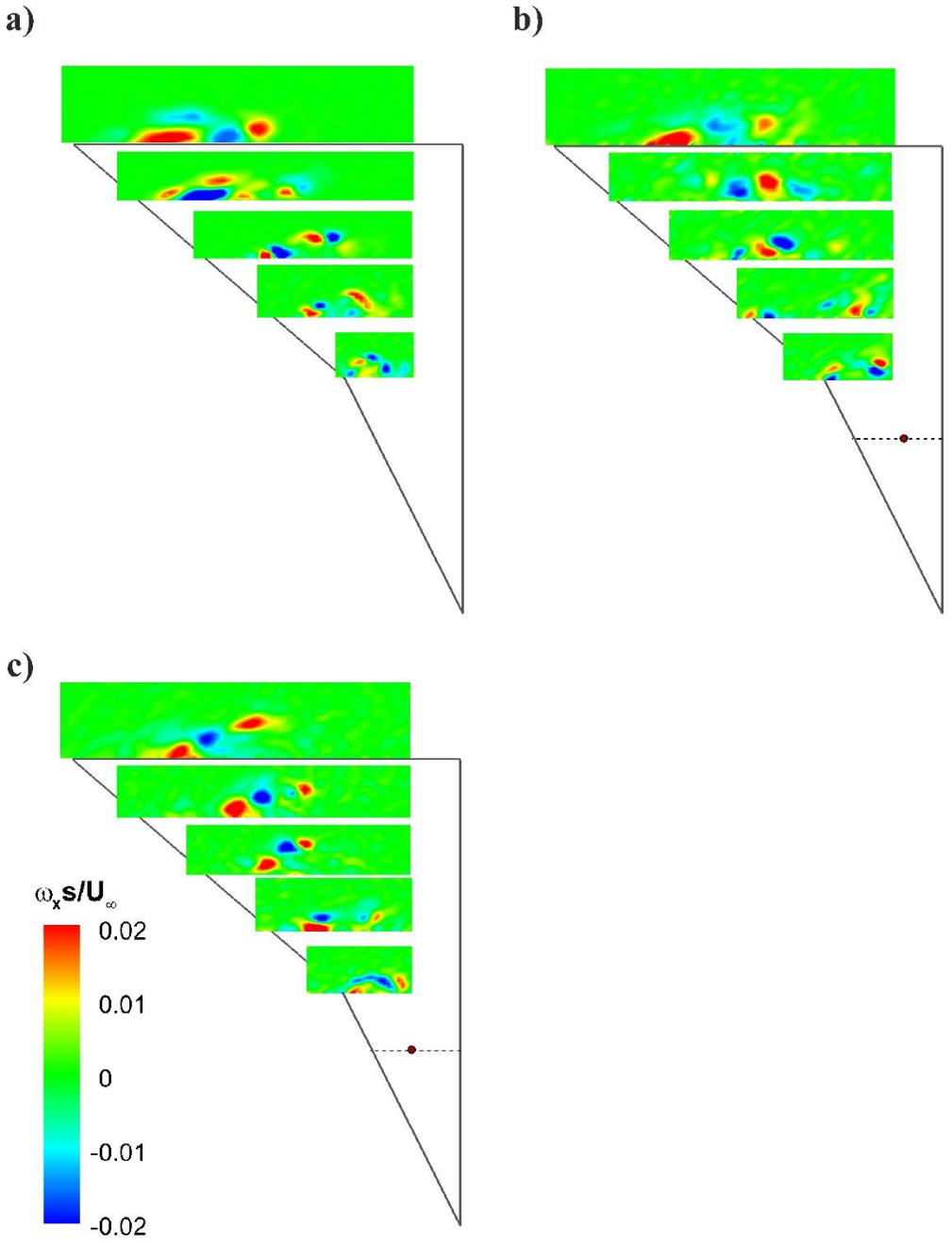


Figure 98. POD 1st mode for α = 12º at a) baseline case, b) bleed hole #4 and c) bleed hole #5.

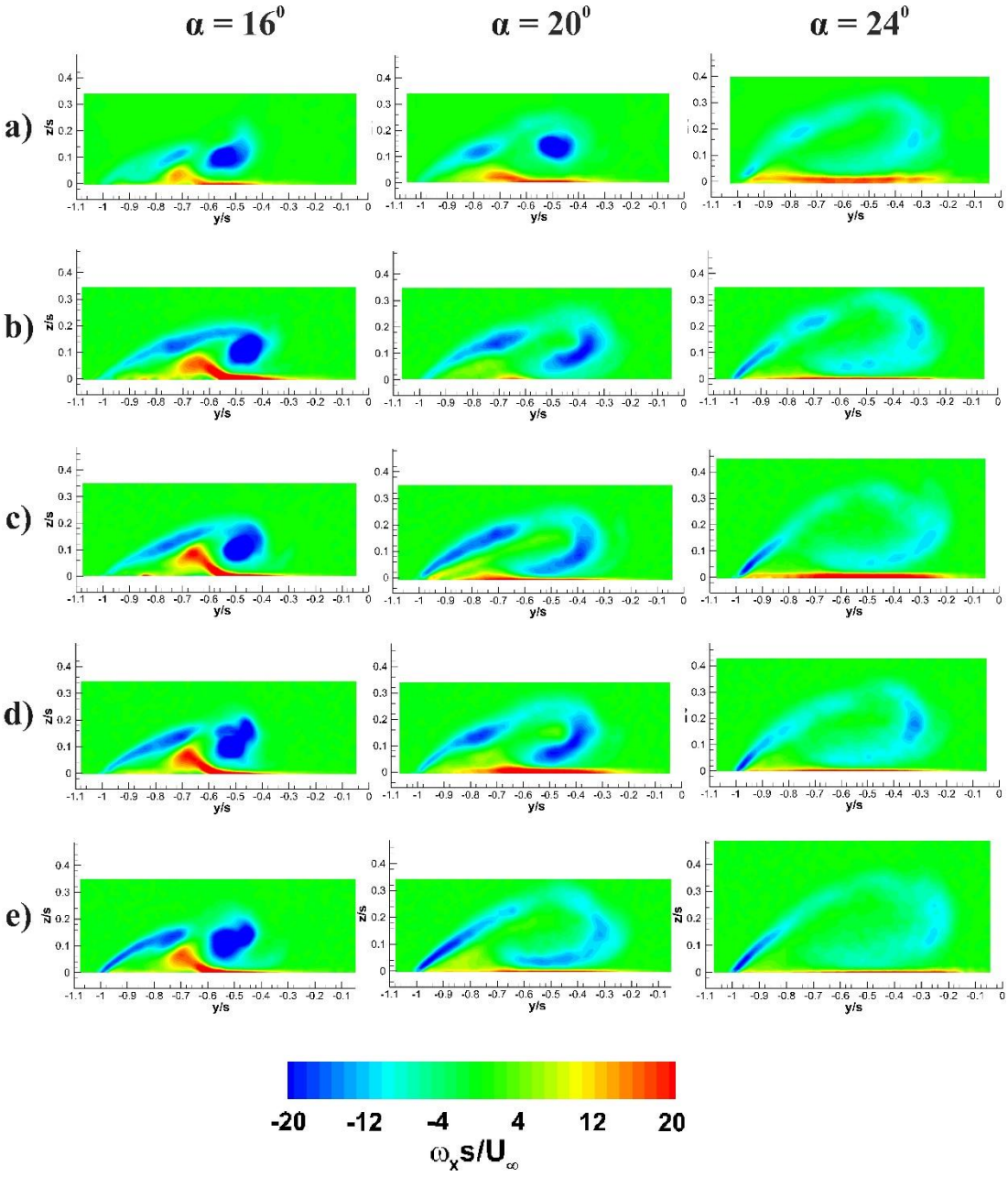


Figure 99. Time-averaged vorticity at x/c = 87.5% for a) baseline case, b) bleed hole #1, c) bleed hole #3, d) bleed hole #5 and e) bleed slot.

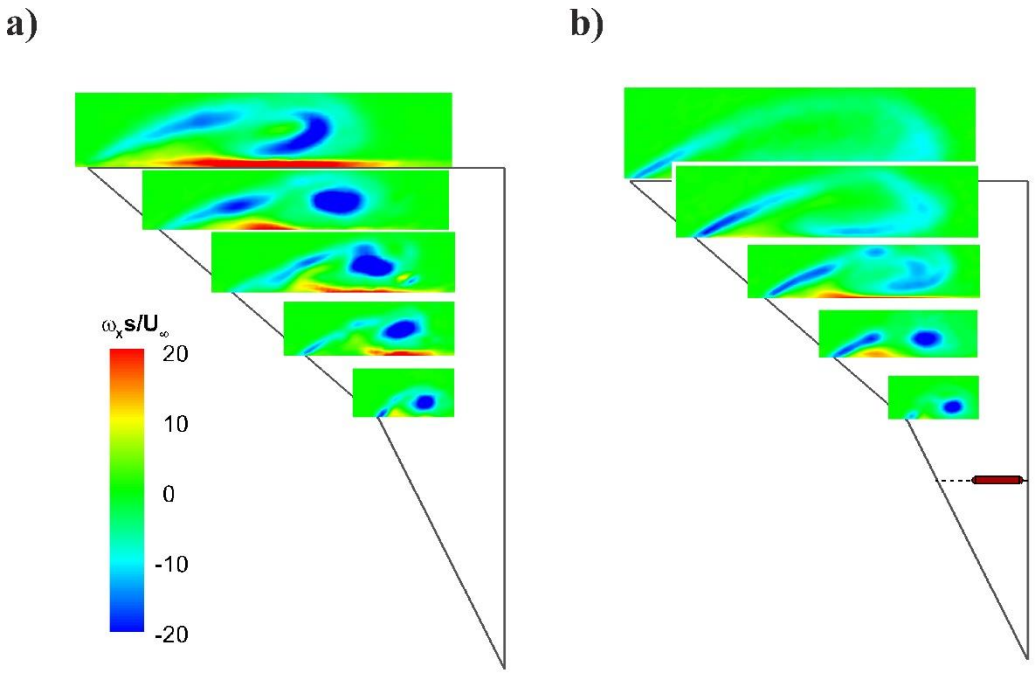


Figure 100. Time-averaged vorticity for α = 20º at a) baseline case, b) bleed slot.

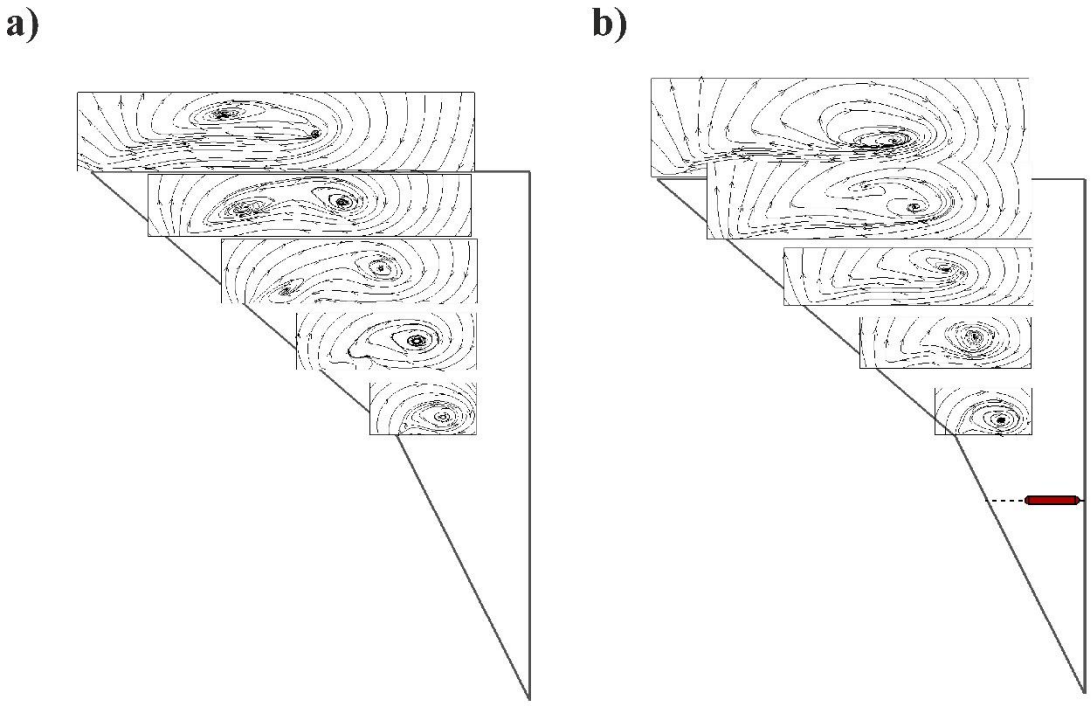


Figure 101. Streamline for $\alpha = 20^{o}$ at a) baseline case, b) bleed slot.

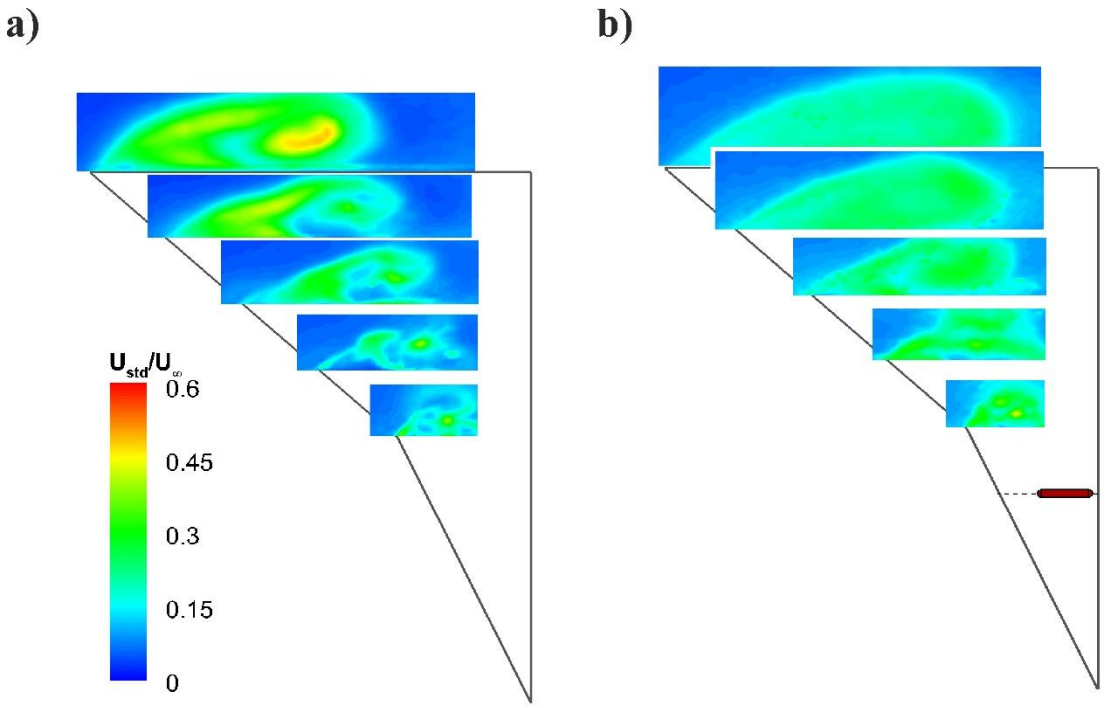


Figure 102. Standard deviation for α = 20º at a) baseline case, b) bleed slot.

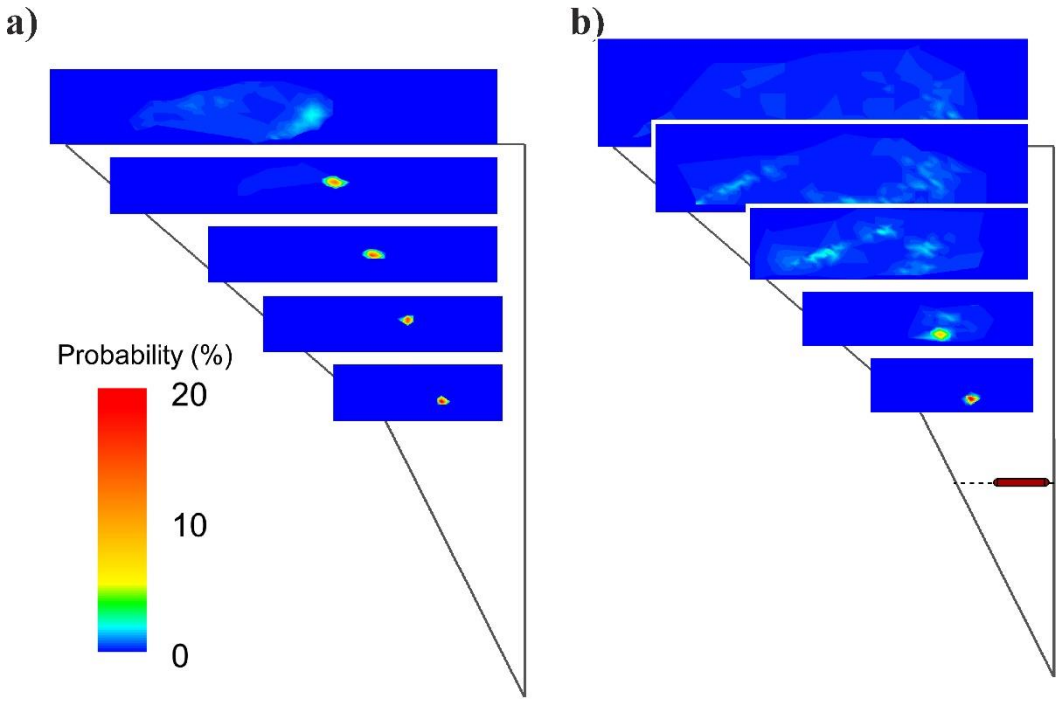


Figure 103. Meandering probability for α = 20º at a) baseline case, b) bleed slot.

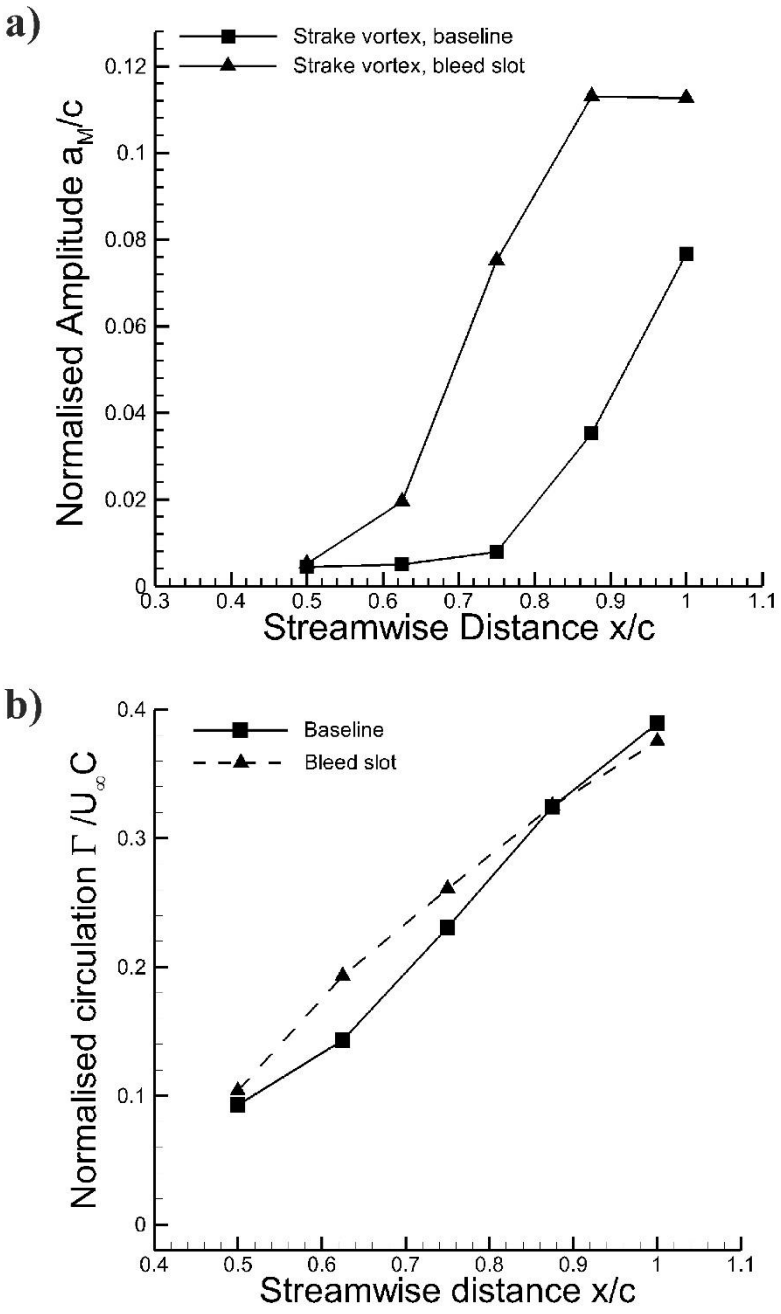


Figure 104. a) Normalised meandering amplitude at $\alpha = 20^{o}$ and b) normalised total circulation.

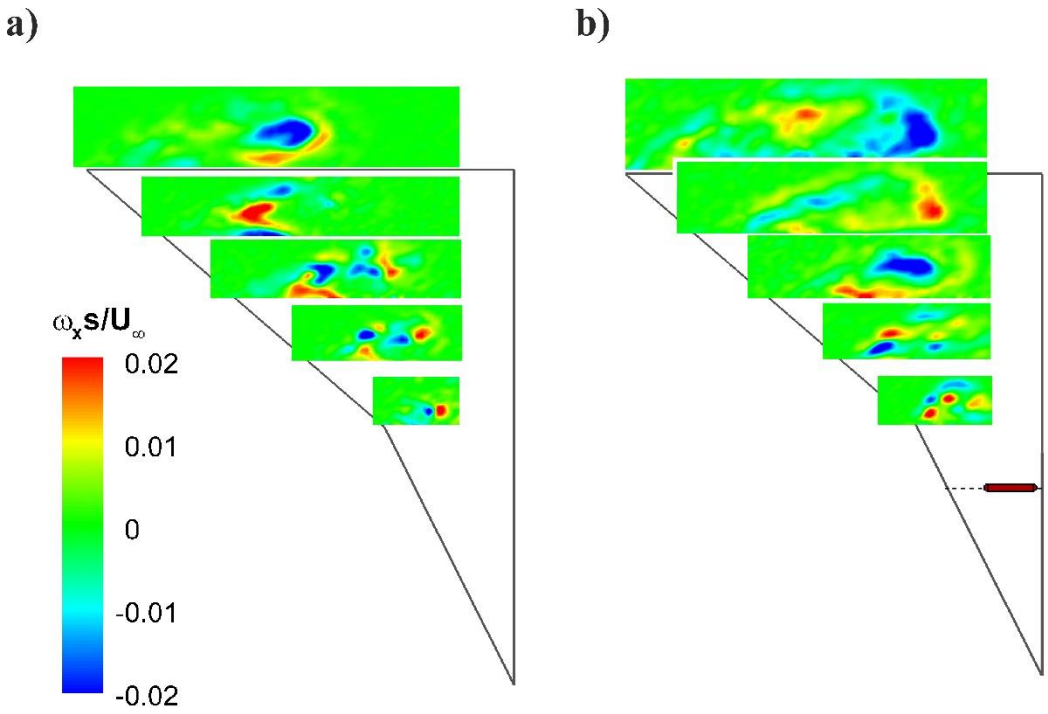


Figure 105. POD 1st mode for α = 20º at a) baseline case, b) bleed slot.

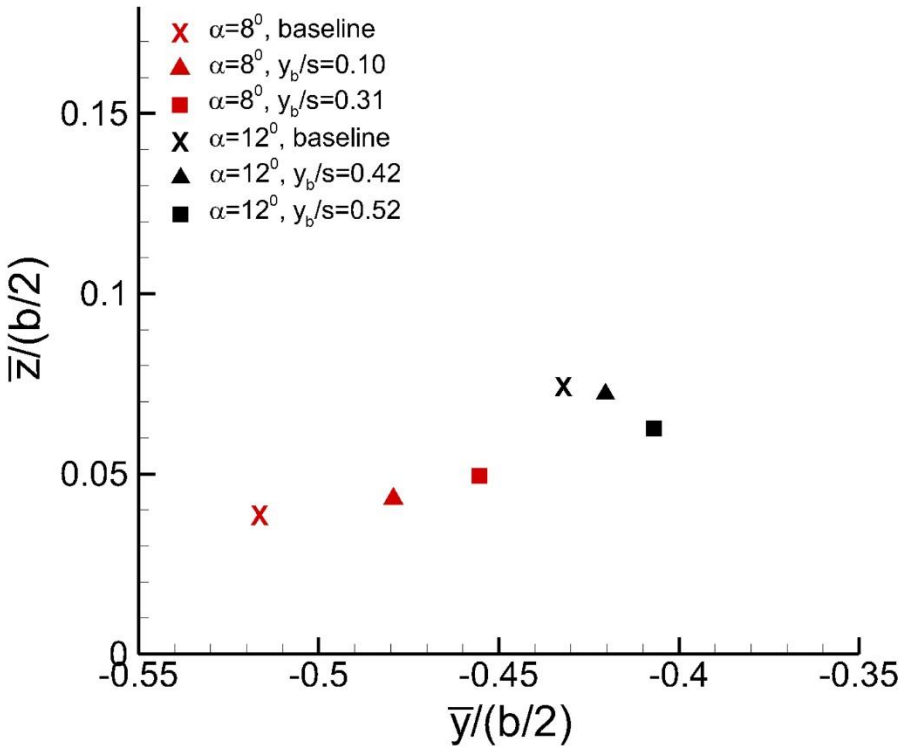


Figure 106. Global vortex centroids over the double delta wing at various wing incidences without and with bleed.

# CHAPTER 7.

# CONCLUSION AND FUTURE WORK

## 7.1 Conclusion

Double delta wings are widely employed for jet fighters, supersonic aircraft and Unmanned Air Vehicles (UAVs) due to their superior aerodynamic performance at high angles of attack. They achieve this superior performance due to the primary vortices generated over its upper surface. However, the interactions of multiple vortices and the breakdown of them are highly problematic. Recent studies have shown that the prediction of the unsteady flow over double delta wings needs improvement and there are requirements for additional experimental data to be contributed. Gursul also noted that there was little research emphasis on the unsteady aspects of the vortex interactions previously. Moreover, previous flow control studies were mainly focused on modifying the wing geometries, there have been little focus on the fluidic control methods. Therefore, this thesis presented the study on the interaction and control of multiple vortices over double delta wings, covering both steady and unsteady characteristics, active blowing and passive bleed were also studied extensively.

The first phase of the study (chapter 3 and first half of chapter 4) investigated the vortical flow over simple and double delta wings at different angles of attack and Reynolds numbers. Chapter 3 studied the effect of angle of attack on the flow pattern over a 70º/50º double delta wing and a 70º simple delta wing in a wind tunnel at Re = $2.34 \times 10^5$. It was found that the time-averaged vorticity field over the double delta wing exhibited a very distinctive 'dual-vortex' structure at mid-chord before the wing section across all angles of attack, however such structure was not seen on the simple delta wing with the same sweep angle, this indicated there was an upstream effect of the wing vortex on the formation of the strake vortex. As angle of attack increased, both the strake and wing vortices gained strength and size, and moved away from the wing surface, meanwhile vortex breakdown also occurred more upstream. Prior to vortex breakdown, both vortices meandered in relatively small areas with high

probability concentration at the vortex centres. The correlation of the displacement of the two vortices was generally small, highest correlation was seen at $\alpha = 12^{\circ}$.

Chapter 4 then compared the results between two different Reynolds numbers, and further investigated the effect of active and passive flow control methods. The first part of the chapter illustrated the comparison between the two Reynolds numbers ($Re = 2.34 \times 10^5$ from wind tunnel experiments, and $Re = 2.80 \times 10^4$ from water tunnel experiments). It was shown that the dual-vortex structure seen on the wind tunnel data was no longer present in the water tunnel data. For water tunnel case, the wing vortex broke down first, whereas for the wind tunnel case, the strake vortex broke down first. Higher Reynolds number resulted in greater interactions between the two vortices, the peak standard deviation and meandering amplitude were also greater at higher Reynolds number.

The next phase of this study (second part of chapter 4 and chapter 5) investigated the effects of active blowing and passive bleed on the vortical flow over the same 70º/50º double delta wing configuration. It was found that, at lower wing incidences, jet blowing at an upstream location could separate the wing and strake vortices apart and discourage the interaction or it could cause the merge of the vortices, depending on the jet yaw angle. On the other hand, at higher wing incidences, the jet blowing at downstream locations could encourage the interaction between the wing and strake vortices and, as a result, the two vortices may merge into one coherent vortex when evolving downstream. The physical mechanism of the accelerated merging appeared to be due to the ingestion of the jet turbulence. The strength, interactions, and relative spatial positions of the wing and strake vortices could be controlled effectively by changing the jet blowing momentum coefficient as well. Generally, the jet blowing was less effective at higher angles of attack. However, the jet blowing could substantially modify the global vortex centroid over the double delta wing up to $\alpha = 24^{\circ}$. It is therefore expected that significant changes in the lift or rolling moment of double delta wings could be achieved effectively by means of jet blowing. The present PIV measurements indicated that passive bleed could enhance the strength of the vortices and the counter-rotating secondary vortex, which was observed near the wing surface between the wing and strake vortices. For optimised locations of bleed, the wing and strake vortices merged into one coherent vortex. This appeared to be aided

by the ingestion of turbulence from the bleed. The secondary vortex, which developed outboard of the merged vortex, induced the roll-up of another wing vortex from the shear layer separated from the leading-edge. It was found that, with bleed, the global vortex centroid moved significantly inboard for estimated momentum coefficients of the order of 0.1%.

## 7.2 Future work

Although this study has constituted a large amount of experiments investigating several different variables and combinations of double delta wings, there is the potential for enormous amount of future experiments to further extend the findings.

1) It is still unclear the exact conditions that will cause the dual-vortex phenomenon observed at the mid-chord location. Therefore, it is worth adding more testing configurations (such as adding more combinations of different Reynolds number and angle of attack) to investigate the critical conditions for the dual-vortex structure to develop.
2) In order to examine the helical structure suggested by the POD results, 3D PIV data of the vortices is desired, it will provide opportunity for the helical structure to be quantified.
3) Current study mainly focused on the properties of the flow field, force and pressure measurement data could be acquired for promising cases to investigate the effect on aerodynamic loads
4) The sampling frequency of the PIV equipment used in current study was limited to 3.75Hz, it would be advantageous to use higher sampling frequency to uncover a wider range of flow patterns.
5) The current study investigated the effect of a single blowing hole at different locations and blowing angles. It is also a possible further research topic to study the effect of multiple blowing holes based on the current findings.

# LIST OF PUBLICATIONS

## JOURNAL ARTICLES

Zhang, X., Wang, Z., and Gursul, I., "Interaction of Multiple Vortices over a Double Delta Wing", *Aerospace Science and Technology*, Vol. 48, 2016, pp. 291-307.

## CONFERENCE PAPERS

Zhang, X., Wang, Z., and Gursul, I., "Interaction of Multiple Vortices over a Double Delta Wing", *45th AIAA Fluid Dynamics Conference*, AIAA-2015-2308, AIAA, Dallas, 2015.

Zhang, X., Wang, Z., and Gursul, I., "Control of Multiple Vortices over a Double Delta Wing", *47th AIAA Fluid Dynamics Conference*, AIAA-2017-4122, AIAA, Denver, 2017.

# REFERENCES


1. Lee, M., and Ho, C. M.,. "Lift force of delta wings," *Applied Mechanics Reviews* Vol. Vol. 43, No. No. 9, 1990, pp. pp. 209-221.

2. Kohlman, D. L., and Wentz, J. W. H. "Vortex breakdown on slender sharp-edged wings," *Journal of Aircraft* Vol. 8, No. 3, 1971, pp. 156-161.

3. Ekaterinaris, J. A., Coutley, R.L., Schiff, L.B., and Platzer, M.F.,. "Numerical Investigation of High Incidence Flow over a Double-Delta Wing," *Journal of Aircraft* Vol. Vol. No 32, 1995.

4. Sohn, M. H., and Chung, H. S. "Effects of Strake Planform Change on Vortex Flow of a Double-Delta Wing," *Journal of Aircraft* Vol. 44, No. 6, 2007, pp. 1842-1848.

5. Grismer, D. S., and Nelson, R. C. "Double-delta-wing aerodynamics for pitching motions with and without sideslip," *Journal of Aircraft* Vol. 32, No. 6, 1995, pp. 1303-1311.

6. Hebbar, S. K., Platzer, M. F., and Chang, W.-H. "Control of High-Incidence Vortical Flow on Double-Delta Wings Undergoing Sideslip," *Journal of Aircraft* Vol. 34, No. 4, 1997, pp. 506-513.

7. Ericsson, L. E. "Vortex characteristics of pitching double-delta wings," *Journal of Aircraft* Vol. 36, No. 2, 1999, pp. 349-356.

8. Verhaagen, N. G. J., L.N.; Kern, S.B.; Washburn, A.E. "A Study of The Vortex Flow Over 76-40-deg Double-Delta Wing." Vol. ICASE Report No. 95-5, Institute for Computer Applications in Science and Engineering, NASA Langley Research Center, 1995.

9. Boelens, O. J., Badcock, K.J., Elmilgui, A., Abdol-Hamid, K.S., Massey, S.J.,. "Comparison of Measured and Block Structured Simulation Results for the F-16XL Aircraft," *Journal of Aircraft* Vol. vol. 46, No. no. 2, 2009, pp. pp. 377-384.

10. Gursul, I. "Review of Unsteady Vortex Flows over Slender Delta Wings," *Journal of Aircraft* Vol. 42, No. 2, 2005, pp. 299-319.

11. Anderson, J. D. *Fundamentals of Aerodynamics*, 2001.

12. Gad-El-Hak, M., and Blackwelder, R. F. "The discrete vortices from a delta wing," *AIAA Journal* Vol. 23, No. 6, 1985, pp. 961-962.

13. Gursul, I., Wang, Z., and Vardaki, E. "Review of flow control mechanisms of leading-edge vortices," *Progress in Aerospace Sciences* Vol. 43, No. 7-8, 2007, pp. 246-270.

14. Lambourne, N., Bryer, DW. "The bursting of leading edge vortices: some observation and discussion of the phenomenon.," No. Aeronaut Res Council R&M 1962;3282.

15. Delery, J., Horowitz, E., Leuchter, O., Solignac, JL. "Etudes fondamentales sur les ecoulements tourbillonnaires," No. La Rech Aerospatiale 1984(2):81–104.

16. Polhamus, E. C. "Predictions of vortex lift characteristics by a leading edge suction analogy," *Journal of Aircraft* Vol. Vol. 8, 1971, pp. pp. 193-199.

17. Erickson, G. E. "Water-Tunnel Studies of Leading-Edge Vortices," *Journal of Aircraft* Vol. 19, No. 6, 1982, pp. 442-448.

18. Gursul, I., Gordnier, R., and Visbal, M. "Unsteady aerodynamics of nonslender delta wings," *Progress in Aerospace Sciences* Vol. 41, No. 7, 2005, pp. 515-557.

19. Taylor, G. S., and Gursul, I. "Buffeting Flows over a Low-Sweep Delta Wing," *AIAA Journal* Vol. 42, No. 9, 2004, pp. 1737-1745.

20. Ol, M. V., and Gharib, M. "Leading-edge vortex structure of nonslender delta wings at low Reynolds number," *AIAA Journal* Vol. 41, No. 1, 2003, pp. 16-26.

21. Yaniktepe, B., and Rockwell, D. "Flow Structure on a Delta Wing of Low Sweep Angle," *AIAA Journal* Vol. 42, No. 3, 2004, pp. 513-523.

22. Wang, J. J., and Zhang, W. "Experimental investigations on leading-edge vortex structures for flow over non-slender delta wings," *Chinese Physics Letters* Vol. 25, No. 7, 2008, pp. 2550-2553.

23. Gordnier, R. E., and Visbal, M. R. "Compact Difference Scheme Applied to Simulation of Low-Sweep Delta Wing Flow," *AIAA Journal* Vol. 43, No. 8, 2005, pp. 1744-1752.

24. Erickson, G. "Flow studies of slender wing vortices," *13th Fluid and PlasmaDynamics Conference*. American Institute of Aeronautics and Astronautics, 1980.

25. Verhaagen, N. G. "Effects of Reynolds Number on Flow over 76/40-Degree Double-Delta Wings," *Journal of Aircraft* Vol. 39, No. 6, 2002, pp. 1045-1052.

26. Gursul, I. "Vortex flows on UAVs: Issues and challenges," *The Aeronautical Journal*, 2004, pp. 597-610.

27. Gonzalez, H., Erickson, G., McLachlan, B., and Bell, J. "Effects of Various Fillet Shapes on a 76/40 Double Delta Wing from Mach 0.18 to 0.7," *Advanced Flow Management: Part A – Vortex Flows and High Angle of Attack for Military Vehicles*, 2001.

28. Rom, J. *High angle of attack aerodynamics: subsonic, transonic, and supersonic flows*: Springer-Verlag, 1992.

29. Verhaagen, N., and Maseland, J.E.J. "Investigation of the vortex flow over a 76/60-deg double delta wing at 20 deg incidence," *9th Applied Aerodynamics Conference*. American Institute of Aeronautics and Astronautics, 1991.

30. Gai, S. L., Roberts, M., Barker, A., Kleczaj, C., and Riley, A. J. "Vortex interaction and breakdown over double-delta wings," *Aeronautical Journal* Vol. 108, No. 1079, 2004, pp. 27-34.

31. Sohn, M. H., Lee, K. Y. "Effects of Sideslip on the High-Incidence Vortical Flow of a Delta Wing with the Leading Edge Extension," *41st Aerospace Sciences Meeting and Exhibit*. American Institute of Aeronautics and Astronautics, 2003.

32. Yu, F., Young, K., Chang, R. "An investigation on the coiled-up of vortices on a double delta wing," *28th Aerospace Sciences Meeting*. American Institute of Aeronautics and Astronautics, 1990.

33. Pamadi, B. N. *Performance, Stability, Dynamics, and Control of Airplanes*: American Institute of Aeronautics & Astronautics, 2004.

34. Hebbar, S. K. "A Visualization Study of the Vortex Flow around Double-Delta wing in Dynamic Motion," *AIAA-93-3425-CP*, 1993.

35. Hebbar, S. K., Platzer, M. F., and Fritzelas, A. E. "Reynolds number effects on the vortical-flow structure generated by a double-delta wing," *Experiments in Fluids* Vol. 28, No. 3, 2000, pp. 206-216.

36. Gursul, I., Taylor, G., and Wooding, C. "Vortex flows over fixed-wing micro air vehicles," *40th AIAA Aerospace Sciences Meeting & Exhibit*. American Institute of Aeronautics and Astronautics, 2002.

37. Rao, D. M. "Vortical Flow Management for improved Configuration Aerodynamics – Recent Experiences," *AGARD Symposium on Aerodynamics of Vortical Type Flows in Three Dimensions*. Rotterdam, Netherlands, April 1983, p. Paper No.30.

38. Yang, H., and Gursul, I. "Vortex Breakdown over Unsteady Delta Wings and Its Control," *AIAA Journal* Vol. 35, No. 3, 1997, pp. 571-574.

39. Hummel, D., Oelker, HC. "Vortex interference effects on closecoupled canard configuration at low speed," No. Aerodynamics of combat aircraft controls and of ground effects, CP-465, AGARD, 1989. p. 7-1–7-18.

40. Myose, R. Y., Hayashibara, S., Yeong, P.-C., and Miller, L. S. "Effect of Canards on Delta Wing Vortex Breakdown During Dynamic Pitching," *Journal of Aircraft* Vol. 34, No. 2, 1997, pp. 168-173.

41. Landahl, M., Widnall, SE. "Vortex control. In: Olsen JH, Goldburg A, Rogers M, editors," *Aircraft wake turbulence and its detection*, No. New York-London: Plenum Press; 1971. p.137–55.

42. Deng, Q., and Gursul, I. "Effect of leading-edge flaps on vortices and vortex breakdown," *Journal of Aircraft* Vol. 33, No. 6, 1996, pp. 1079-1086.

43. Rao, D. M., and Campbell, J. F. "Vortical Flow Management Techniques," *Progress in Aerospace Sciences* Vol. 24, 1987, pp. 173-224.

44. Klute, S. M., Rediniotis, O. K., and Telionis, D. P. "Flow control over a maneuvering delta wing at high angles of attack," *AIAA Journal* Vol. 34, No. 4, 1996, pp. 662-668.

45. Lee, G.-B., Shih, C., Tai, Y.-C., Tsao, T., Liu, C., Huang, A., and Ho, C.-M. "Robust Vortex Control of a Delta Wing by Distributed Microelectromechanical-Systems Actuators," *Journal of Aircraft* Vol. 37, No. 4, 2000, pp. 697-706.

46. Johari, H., Olinger, D. J., and Fitzpatrick, K. C. "Delta wing vortex control via recessed angled spanwise blowing," *Journal of Aircraft* Vol. 32, No. 4, 1995, pp. 804-810.

47. Sreenatha, A. G., and Ong, T. K. "Wing Rock Suppression Using Recessed Angle Spanwise Blowing," *Journal of Aircraft* Vol. 39, No. 5, 2002, pp. 900-903.

48. Hong, J. S., Celik, Z. Z., and Roberts, L. "Effects of leading-edge lateral blowing on delta wing aerodynamics," *AIAA Journal* Vol. 34, No. 12, 1996, pp. 2471-2478.

49. Wood, N. J., and Roberts, L. "Control of vortical lift on delta wings by tangential leading-edge blowing," *Journal of Aircraft* Vol. 25, No. 3, 1988, pp. 236-243.

50. Gu, W., Robinson, O., and Rockwell, D. "Control of vortices on a delta wing by leading-edge injection," *AIAA Journal* Vol. 31, No. 7, 1993, pp. 1177-1186.

51. Bradley, R. G., and Wray, W. O. "A Conceptual Study of Leading-Edge-Vortex Enhancement by Blowing," *Journal of Aircraft* Vol. 11, No. 1, 1974, pp. 33-38.

52. Mitchell, A. M., Barberis, D., Molton, P., Dé, J., and lery. "Oscillation of Vortex Breakdown Location and Blowing Control of Time-Averaged Location," *AIAA Journal* Vol. 38, No. 5, 2000, pp. 793-803.

53. Wang, Z.-J., Jiang, P., and Gursul, I. "Effect of Thrust-Vectoring Jets on Delta Wing Aerodynamics," *Journal of Aircraft* Vol. 44, No. 6, 2007, pp. 1877-1888.

54. Parmenter, K., and Rockwell, D. "Transient response of leading-edge vortices to localized suction," *AIAA Journal* Vol. 28, No. 6, 1990, pp. 1131-1133.

55. McCormick, S., and Gursul, I. "Effect of shear-layer control on leading-edge vortices," *Journal of Aircraft* Vol. 33, No. 6, 1996, pp. 1087-1093.

56. Badran, B., McCormick, S., and Gursul, I. "Control of Leading-Edge Vortices with Suction," *Journal of Aircraft* Vol. 35, No. 1, 1998, pp. 163-165.

57. Wang, Z., and Gursul, I. "Lift Enhancement of a Flat-Plate Airfoil by Steady Suction," *AIAA Journal* Vol. 55, No. 4, 2017, pp. 1355-1372.

58. Glezer, A., and Leonard, A. "Aero-Effected Flight Control Using Distributed Active Bleed." Woodruff School of Mechanical Engineering, Georgia Institute of Mechanical Engineering, Atlanta, GA, 2012.

59. Han, Y. O., and Leishman, J. G. "Investigation of Helicopter Rotor-Blade-Tip-Vortex Alleviation Using a Slotted Tip," *AIAA Journal* Vol. 42, No. 3, 2004, pp. 524-535.

60. Hu, T., Wang, Z., and Gursul, I. "Passive control of roll oscillations of low-aspect-ratio wings using bleed," *Experiments in Fluids* Vol. 55, No. 6, 2014.

61. Kirkpatrick, D. L. I. "Analysis of the Static Pressure Distribution on a Delta Wing in Subsonic Flow." MInistry of Technology, Aerodynamics Dept., R.A.E., Farnborough, 1970.

62. Rinoie, K., Fujita, T., Iwasaki, A., and Fujieda, H. "Experimental Studies of a 70-Degree Delta Wing with Vortex Flaps," *Journal of Aircraft* Vol. 34, No. 5, 1997, pp. 600-605.

63. Prasad. Ajay K. "Particle Image Velocimetry," *Current Science* Vol. 79, No. 1, 2000, pp. 51-60.

64. Graftieaux, L., Michard, M. and Grosjean, N. "Combining PIV, POD and vortex identification algorithms for the study of unsteady turbulent swirling flows," *Measurement Acience and Technology* Vol. 12, 2001, pp. 1422-1429.

65. Morgan, C., Babinsky, H., and Harvey, J. "Vortex Detection Methods for Use with PIV and CFD Data," *47th AIAA Aerospace Sciences Meeting including The New Horizons Forum and Aerospace Exposition*. American Institute of Aeronautics and Astronautics, 2009.

66. Moffat, R. J. "Contributions to the Theory of Single-Sample Uncertainty Analysis," *Journal of Fluids Engineering - Transactions of the ASME* Vol. 104, No. 2, 1982, pp. 250-260.

67. Moffat, R. J. "Using Uncertainty Analysis in the Planning of an Experiment," *Journal of Fluids Engineering - Transactions of the ASME* Vol. 107, No. 2, 1985, pp. 173-178.

68. Cleaver, D. J. "Low Reynolds Number Flow Control Through Small-Amplitude High-Frequency Motion," *Department of Mechanical engineering*. Vol. Ph.D, University of Bath, Bath, 2011.

69. Keane. Richard D., A. R. J. "Theory of cross-correlation analysis of PIV images," *Applied Scientific Research* Vol. 49, 1992, pp. 191-215.

70. Marles, D., and Gursul, I.,. "Effect of an Axial Jet on Vortex Merging," *Physics of Fluids* Vol. 20(4), 2008, 047101.

71. Cerretelli, C., and Williamson, C. H. K. "The physical mechanism for vortex merging," *Journal of Fluid Mechanics* Vol. 475, 2003.

72. Lumley, J. L. "Stochastic Tools in Turbulence," *Applied Mathematics and Mechanics* Vol. Vol. 12, No. Academic Press, 1970.

73. Hinze, J. O. *Turbulence*. McGraw Hill, New York, 1975.

74. Berkooz, Z., Holmes, P., and Lumley, J.L.,. "The proper orthogonal decomposition in the analysis of turbulent flows," *Annu Rev Fluid Mech*, 1993, pp. 25:539–575.

75. Sirovich, L. "Turbulence and the Dynamics of Coherent Structures Parts I–III," *Quarterly of Applied Mathematics* Vol. Vol. 45, No. No. 3, 1987, pp. pp. 561–590.

76. Rockwell, D. O., Cipolla, K. M., and Liakopoulos, A. "Quantitative Imaging in Proper Orthogonal Decomposition of Flow Past a Delta Wing," *AIAA Journal* Vol. 36, No. 7, 1998, pp. 1247-1255.

77. Kim, Y., Rockwell, D., and Liakopoulos, A. "Vortex Buffeting of Aircraft Tail: Interpretation via Proper Orthogonal Decomposition," *AIAA Journal* Vol. 43, No. 3, 2005, pp. 550-559.

78. Roy., C., and Leweke, T. "Experiments on vortex meandering," *FAR-Wake Technical Report AST4-CT-2005-012238* Vol. CNRS-IRPHE, also presented in International Workshop on Fundamental Issues related to Aircraft Trailing Wakes, 2008.

79. Del Pino C, Lopez-Alonso J.M., Parras L., and R.., F.-F. "Dynamics of the wing-tip vortex in the near field of a NACA 0012 airfoil," *The Aeronautical Journal* Vol. vol. 115, No. No. 1166, 2011, pp. pp. 229-239.

80. Heiland, R. W. "KLTOOL: A Mathematical Tool for Analyzing Spatiotemporal Data," *Arizona State University* Vol. Dept of Mathematics, No. December, 1992.

81. Wang, Z., and Gursul, I. "Unsteady characteristics of inlet vortices," *Experiments in Fluids* Vol. 53, No. 4, 2012, pp. 1015-1032.

82. Zhang, X., Wang, Z and Gursul, I. "Interaction of multiple vortices over a double delta wing," *Aerospace Science and Technology* Vol. 48, 2016, pp. 291-307.

83. Menke, M., and Gursul, I.,. "Unsteady Nature of Leading EdgeVortices," *Physics of Fluids* Vol. Vol. 9, No. No. 10, 1997, pp. pp. 1–7.